



Lawrence Berkeley Laboratory

UNIVERSITY OF CALIFORNIA

Physics Division

Mathematics Department

Phase Transitions and Connectivity in Three-Dimensional Vortex Equilibria

J.H. Akao
(Ph.D. Thesis)

May 1994



REFERENCE COPY
Does Not Circulate
Bidg: 50 Library.
Copy 1
LBL-35630

DISCLAIMER

This document was prepared as an account of work sponsored by the United States Government. While this document is believed to contain correct information, neither the United States Government nor any agency thereof, nor the Regents of the University of California, nor any of their employees, makes any warranty, express or implied, or assumes any legal responsibility for the accuracy, completeness, or usefulness of any information, apparatus, product, or process disclosed, or represents that its use would not infringe privately owned rights. Reference herein to any specific commercial product, process, or service by its trade name, trademark, manufacturer, or otherwise, does not necessarily constitute or imply its endorsement, recommendation, or favoring by the United States Government or any agency thereof, or the Regents of the University of California. The views and opinions of authors expressed herein do not necessarily state or reflect those of the United States Government or any agency thereof or the Regents of the University of California.

LBL-35630
UC-405

**Phase Transitions and Connectivity in
Three-Dimensional Vortex Equilibria**

James H. Akao

Department of Mathematics
University of California

and

Physics Division
Lawrence Berkeley Laboratory
University of California
Berkeley, California 94720

May 1994

Abstract

Phase Transitions and Connectivity in Three-dimensional Vortex Equilibria

by

James H. Akao

Doctor of Philosophy in Mathematics

University of California at Berkeley

Professor Alexandre J. Chorin, Chair

The statistical mechanics of collections of closed self avoiding vortex loops on a lattice are studied. The system is related to the vortex form of the three dimensional XY model and to lattice vortex equilibrium models of turbulence. The system exhibits vortex connectivity and screening effects, and models in vorticity variables the superfluid transition. The equilibrium states of the system are simulated by a grand canonical Monte Carlo method. A set of geometric transformations for self-avoiding loops is developed. The numerical method employs histogram sampling techniques and utilizes a modification to the Metropolis flow which enhances efficiency.

Results are given for a region in the temperature-chemical potential plane, where the chemical potential is related to the vortex fugacity. A line of second order transitions is identified at low temperature. The transition is shown to be a percolation threshold at which connected vortex loops of infinite size appear in the system. The nature of the transition supports the assumption that the lambda transition in bulk superfluid helium is driven by vortices.

An asymptotic analysis is performed for the energy and entropy scaling of the system as functions of the system size and the lattice spacing. These estimates indicate that the infinite temperature line is a phase boundary between small scale fractal vortices and large scale smooth vortices. A suggestion is made that quantum vortices have uniform structure on the scale of the lattice spacing and lie in the positive temperature regime, while classical vortices have uniform structure on the scale of the domain and lie in the negative temperature regime.

Contents

List of Figures	vii
List of Tables	xi
List of Symbols	xiii
Acknowledgments	xv
1 Introduction	1
1.1 Background	1
1.2 Overview of the Thesis	4
1.3 Vorticity in Classical and Quantum Systems	6
1.4 Vortex Equilibria and Phase Transitions	9
1.5 The Self-avoiding Loops System	11
1.6 Numerical Simulation	12
1.7 Phase Transitions in the Self-avoiding Loops System	12
2 Thermodynamics	14
2.1 Thermodynamic Ensembles	15
2.2 Finite Size Effects	17
2.3 Entropy and Energy/Entropy Arguments	21
3 Vorticity Models of Physical Systems	25
3.1 Classical Vorticity and Lattice Vorticity Discretization	27
3.2 Definition of the Self-avoiding Loops Model	34
3.3 The XY Model and the Lambda Transition	40
3.4 Percolation and the Lambda Transition	49
3.5 Applications of the Self-avoiding Loops Model	53
4 Numerical Thermodynamic Simulation	55
4.1 Monte Carlo Simulation	55
4.2 The Metropolis Method	58
4.3 Histogram Sampling	61
4.3.1 The Density of States	62

4.3.2	The Histogram Monte-Carlo Method	66
4.3.3	Combining Multiple Histograms	68
4.3.4	Observations on Combining Histograms	79
5	Numerics for the Self-avoiding Loops System	84
5.1	Transformations	86
5.1.1	Pivots	87
5.1.2	Translates	90
5.1.3	Reconnections	92
5.1.4	Elementary Addition/Deletion	94
5.1.5	Elementary Excitations	96
5.2	Ergodicity	99
5.3	The Split-phase Metropolis Method	101
5.3.1	Review of the Metropolis Sampling Method	102
5.3.2	Description of the Split-phase Metropolis Method	103
5.3.3	A Simple One-step Example	105
5.3.4	Final Acceptance Probability in a Split-phase Step	108
5.3.5	Proof of Detailed Balance for Split-phase Metropolis	110
5.3.6	Implementation of Split-phase Sampling for Self-avoiding Loops	118
5.3.7	Energy Well Escapes	120
5.4	Performance	122
5.4.1	Implementation and Runtime	122
5.4.2	Histogram Convergence	128
5.4.3	Split-phase Effectiveness	133
6	Phase Transitions in the Self-avoiding Loops System	136
6.1	Micro-canonical Ensemble	138
6.2	“Lambda” Percolation Transition	146
6.3	Fractal-Smooth Transition	159
6.4	Conclusions	172
	Bibliography	175

List of Figures

2.1	$P(E)$ vs. E as $L \rightarrow \infty$	19
2.2	Order Parameter $O(\beta)$ vs. β as $L \rightarrow \infty$	19
2.3	Order Parameter $O(\beta)$ vs. β in thermodynamic limit	20
2.4	Energy in a first order phase transition	21
2.5	Energy in a continuous phase transition	22
2.6	Specific heat in a continuous phase transition	22
3.1	Two-dimensional patch of vorticity	28
3.2	Vortex tube	28
3.3	Lattice terminology	30
3.4	Two vortex "particles"	30
3.5	Vorticity constraint $\nabla \cdot \xi = 0$	31
3.6	Vorticity constraint $\nabla \cdot \xi = 0$	31
3.7	Intersecting vortex loops	32
3.8	Self-avoiding loops	32
3.9	Single self-avoiding walk	35
3.10	Self-avoiding loops configuration	36
3.11	Periodic vortices	38
3.12	XY vortex loops	44
3.13	Vortex pair in the XY model	45
3.14	Percolation achieved by reconnections	50
3.15	Site percolation cluster	51
3.16	Percolation probability finite size scaling	52
3.17	Percolating vortex loop	53
4.1	$P_{\beta^*}(E)$	65
4.2	$P_{\beta^*}(E) \exp((\beta^* - \beta)E)$	65
4.3	$P_{\beta^*}(E)$ and $P_{\beta}(E)$	65
4.4	Logarithmic view of probabilities	68
4.5	$P_{\beta^*}(E)$ and $P_{\beta}(E)$	69
4.6	Unshifted histograms	76
4.7	Shifted probabilities	77
4.8	Combined probability	77

4.9	Combined probability	78
4.10	Unshifted histograms	79
4.11	Shifted probabilities	80
4.12	Combined probability	80
4.13	Combined probability	81
4.14	Shifted probabilities	83
5.1	Pivot preserving link order	88
5.2	Arc inversion	89
5.3	Pivot reversing link order	89
5.4	Pivot in three dimensions	90
5.5	Two reconnection moves	93
5.6	Link addition/deletion	95
5.7	Vortex dipole	97
5.8	A crystal of stacked elementary loops	97
5.9	Polarized vortices with high energy	98
5.10	Adding an elementary loop	99
5.11	Single "canonical" loop	101
5.12	Partitioned loops	101
5.13	Energy calculation time vs. number of vortices	127
5.14	Transformation and statistics time vs. number of vortices	127
5.15	Single histogram	130
5.16	Multi-histogram probability density	130
5.17	Sum squared error by M trials	131
5.18	Sum squared error proportional to $1/M$	132
5.19	Autocorrelation time estimators	132
6.1	Log of density of states	140
6.2	Contours of log of density of states	140
6.3	Density of states, $d(\mathcal{E}, \mathcal{D} = 0.4)$	141
6.4	Self-avoiding vortex loops at infinite temperature	143
6.5	Single vortex loop at infinite temperature	143
6.6	Loop crystals	144
6.7	Dipole loops	144
6.8	Density of states extended to high energies	145
6.9	Micro-canonical percolation probability	147
6.10	Micro-canonical percolation probability $\mathcal{D} = 0.4$	147
6.11	Phase plane	148
6.12	Total energy by system size	150
6.13	Specific heat by system size	150
6.14	Loop density by system size	151
6.15	Percolation probability by system size	152
6.16	Percolation threshold and specific Heat	152
6.17	Energy per link across transition	154
6.18	Size of a lone loop vs. number of links	156

6.19	Log-log size of a lone loop vs. number of links	156
6.20	Size of loops in a collection at $\beta = 0$	157
6.21	Size of a loops in a collection at $\beta = \beta_c$	158
6.22	Base loop configuration	162
6.23	Copied and thickened configurations	162
6.24	Dilation of a vortex configuration	164

List of Tables

5.1	Arc pivot/invert algorithm	91
5.2	Translation algorithm	92
5.3	Reconnection algorithm	93
5.4	Link addition/deletion algorithm	94
5.5	Dipole algorithm	99
5.6	Crystal algorithm	100
5.7	Split-phase acceptance functions	120
5.8	Monte Carlo algorithm	121
5.9	Runtime per Trial (sec)	126
5.10	Energy calculation time per trial (sec)	126
5.11	Fraction of runtime calculating energy (%)	126
5.12	Averages from Monte Carlo runs at $L = 6$	129
5.13	Runs by number of intermediate steps k	134
5.14	Autocorrelation and efficiency	135

List of Symbols

Thermodynamics

c	configuration	15
\mathcal{C}	state space of configurations $\{c\}$	15
$\rho(c)$	equilibrium weight of $c \in \mathcal{C}$	15
T	Temperature	16
β	inverse temperature parameter $\frac{1}{k_B T}$	16
\mathcal{Z}_β	partition function at temperature β	15
S	Entropy of a set of configurations	21
F_β	free energy (up to a factor of β): $F_\beta = -\log \mathcal{Z}_\beta$	64
$A(c)$	observable quantity of configuration c	14
$\langle A \rangle_\beta$	canonical ensemble average of A at temperature β	15
$\bar{A}(E)$	micro-canonical average of A at energy E	63
$D(E)$	density of states at energy E	63
$P_\beta(E)$	probability density function of E at temperature β	64

Histogram Monte Carlo

M	number of configurations (trials) in Monte Carlo run	66
$n(E)$	number of configurations falling in bin $[E, E + \Delta E)$	66
$A_{\text{acc}}(E)$	accumulator $\sum A(c)$ over configurations in energy bin E ..	66
$\bar{a}(E)$	numerical approx. to micro-canonical average $\approx \bar{A}(E)$...	66
$p_\beta(E)$	numerical approx. to probability density $\approx P_\beta(E)\Delta E$	66
$\Delta F_\beta^{\beta^*}$	approx. free energy diff. $F_\beta - F_{\beta^*}$ calculated from $p_{\beta^*}(E)$..	67

Multi-histogram Monte Carlo

R	number of separate Monte Carlo runs	70
β^i	inverse temperature of i th Monte Carlo run $i = 1 \dots R$...	70
M^i	number of trials in i th Monte Carlo run	70
$n^i(E)$	histogram taken on i th Monte Carlo run	70
$p^i(E)$	unshifted numerical density from M.C. run i at temp. β^i	70
$p_\beta^i(E)$	density from M.C. run i shifted to temp. β	70
$w^i(E)$	optimal weight of i th shifted probability	70
ΔF^i	approx. free energy diff. $F_\beta - F_{\beta^i}$ fixed point value	67

Metropolis Sampling

$P(c \Rightarrow c^*)$	transition probability from c to c^* in Markov chain	56
c_i	i th member of Markov chain	56
Q_α	random function $Q_\alpha : \mathcal{C} \rightarrow \mathcal{C}$	59
$\pi_\alpha(c_i)$	conditional probability for function Q_α given current conf. c_i	59
c'	candidate configuration for c_{i+1} , given by $c' = Q_\alpha c_i$	59
$\Theta(c_i, c')$	probability that c' is accepted as c_{i+1} in Markov step i	60
$\eta_\alpha(c_i, c_{i+1})$	conditional probability of conf. c_{i+1} from c_i through Q_α	60

Split-phase Metropolis

c'	final candidate configuration for c_{i+1}	104
$\Theta_\alpha(c_i, c')$	final acceptance probability in Markov step i	109
k	number of intermediate steps in each Markov step	104
\tilde{c}^j	j th intermediate configuration	104
\tilde{Q}_α^j	random function $Q_\alpha : \mathcal{C} \rightarrow \mathcal{C}$ chosen at j th sub-step	104
$\tilde{\pi}_\alpha^j(\tilde{c}^j)$	conditional probability of function \tilde{Q}_α^j given conf. \tilde{c}^j	104
\tilde{c}'	intermediate candidate configuration given by $\tilde{c}' = \tilde{Q}_\alpha^j \tilde{c}^j$	105
Δ_α^j	prob. of accepting intermediate candidate \tilde{c}' as \tilde{c}^{j+1}	105
F_α^j	intermediate acceptance weight	104
δ_α^j	factor of ratio of Gibbs weights $\rho(c')/\rho(c_i)$	109
$\tilde{\eta}_\alpha^j(\tilde{c}^j, \tilde{c}^{j+1})$	conditional probability conf. \tilde{c}^{j+1} from \tilde{c}^j through \tilde{Q}_α^j	110
\tilde{H}_α^j	random intermediate step $\tilde{c}^{j+1} = \tilde{H}_\alpha^j \tilde{c}^j$	110

Self-avoiding Loops

$\vec{u}(\vec{x})$	velocity field	27
$\vec{\xi}(\vec{x})$	vorticity field	27
E^H	kinetic energy of continuum flow	33
$G(\vec{x})$	Green function for Laplacian	33
h	lattice step size	37
L	period length of periodic domain	37
V	volume of one period L^3	37
$\tilde{\xi}_i$	discretized vorticity value	29
\vec{x}_i	discretized vorticity position	29
N	number of vortices in a configuration	33
ν	self-energy of a discretized vortex	33 37
E^{int}	discretized vortex-vortex interaction energy	33 37
E^{tot}	total discretized energy	33 37
\mathcal{E}	interaction energy density E^{int}/V	39
D	vortex line length density Nh/V	39
\mathcal{P}	percolation probability	39
$\text{Perc}(c)$	1 if c has a percolating loop	52
C	specific heat $-\beta\partial\langle\mathcal{E}\rangle_\beta/\partial\beta$	149

I wish to thank Prof. Alexandre Chorin for scientific, professional and personal support during the writing of this thesis and during the whole of my time as a graduate student. I also wish to thank Prof. James Demmel, Prof. Phillip Colella, and Prof. James Sethian for assistance with this thesis and for professional support and advice.

I gratefully acknowledge the generous financial support of the Office of Naval Research through the American Society for Engineering Education (ONR/ASEE) Graduate Fellowship Program, and of the Alfred P. Sloan Foundation through the Doctoral Dissertation Fellowship program. This work was also supported in part by the Applied Mathematical Sciences Subprogram of the Office of Energy Research, Department of Energy, under contract # DE-AC03-76SF00098.

I finally wish to thank the members of the mathematics and numerical analysis group at LBL for maintaining a stimulating and friendly environment, and Valerie Heatlie for bailing me out of administrative difficulties.

Chapter 1

Introduction

1.1 Background

A full understanding of the physics of turbulent flow is one of science's great open problems, and has been sought by mathematicians, physicists and engineers for many decades. The Navier-Stokes equations are an accurate model of flow in an incompressible fluid, and many satisfactory computational algorithms exist for the solution of smooth flows. See for example [5] [11] [35] [24] [58]. Three dimensional turbulent flows, however, are not currently well simulated. Since high Reynolds number turbulence contains motions on length scales covering perhaps five to fifteen orders of magnitude, a direct Navier-Stokes computation of the entire flow field would require something like $(10^{5-15})^4 = 10^{20} - 10^{60}$ points in a space-time volume. This computational effort is far beyond the reach of even the fastest parallel machines. A physical understanding of turbulence itself, beyond the underlying partial differential equations, is required for the effective simulation of fluid flow problems in complex machinery and in the oceanic and atmospheric environments.

Turbulence is also of interest in quantum systems such as superfluid helium. Superfluids exhibit motions which are not subject to viscous energy loss; a superflow once started will continue indefinitely [52] [139] [121]. This phenomena is of particular interest for its relation to resistanceless electric currents in superconductors [140] [104] [30]. In the superfluid case, even the underlying equations of motion have yet to be satisfactorily determined [20] [21] [6] [95]. It is apparent in these low temperature flows that mechanical and thermal motions are coupled, and that thermal effects can cause resistance and disrupt superfluid motion. The disruption of the superflow has been linked to the onset of

turbulence in the fluid [52] [59]. Thermal effects cause a phase transition in liquid helium known as the lambda transition which divides the superfluid phase from the normal fluid phase. A theoretical understanding of quantum turbulence may further the general theory of resistanceless flows and aid in the technological utilization of these quantum phenomena.

There is experimental and theoretical evidence for the existence of a universal behavior of turbulence in classical fluids. Fully developed turbulence exhibits an inertial range of scales spanning the lengths at which viscosity effects are important to the lengths at which the large scale geometry dominates the flow. The inertial range has a characteristic structure and energy spectrum which is largely independent of the type of fluid and of the large scale flow [102] [94] [41] [129]. The universal properties of the inertial range suggest that the concept of large eddy simulation is basically sound; one may be able to explicitly compute the large scale, geometry dependent, portion of the flow and employ a sub-grid model to account for turbulent motions below the desired resolution.

A sub-grid model should predict the response of the inertial range flow to outside stresses without resolving the specific turbulent motions. One way to simulate the inertial range without explicitly computing it is to make a stochastic model, in which the sub-grid flow is probabilistic. The average effects on the grid scale can be computed from the probabilistic model, with the probability distribution depending in some way on the external stresses.

While many approaches can be taken to study the probabilistic properties of turbulence, the thermodynamic equilibrium approach is a natural starting point for several reasons. Formulating the thermodynamic equilibrium model is relatively uncomplicated; the equilibrium depends on the energy and the constraints in the system but not on the details of the time evolution [92] [122] [138]. While the equilibrium assumption is a great simplification, it by no means trivializes the resulting model. Studies of various hydrodynamic equilibria have demonstrated a rich set of behaviors including order/disorder transitions and negative temperature states [23] [38] [39] [41] [61] [88] [97] [108] [109]. Thermodynamic equilibrium is well understood for many systems, so general experience with these systems can be brought to bear on the turbulence problem. The equilibrium model is also the foundation of more complex theories of critical behavior in statistical physics. See for example [64] [54]. While both classical and quantum turbulence are likely to be more complex than a thermodynamic equilibrium model, an understanding of hydrodynamic equilibria can be useful in concert with other techniques in the construction of a full stochastic theory.

The assumption of thermodynamic equilibrium leaves considerable freedom in formulating the model for turbulent flow. For example, both real-space and spectral variables have been used in theories and computations [116] [77] [41]. Vorticity variables in real-space have proved useful in dynamic computations of classical flows in the smooth regime and in turbulent approximations. See for example [4] [5] [120] [35] [67]. Vorticity can also be measured in physical experiments [47] [83] [103] [52] [117] [147], and figures in a number of non-equilibrium approaches to turbulence [8] [10] [14] [94] [84]. There is a considerable knowledge of the energetic properties of, and constraints satisfied by, vorticity representations of incompressible flow [7] [91] [44] [101]. Vorticity variables are therefore a reasonable choice for formulating an equilibrium model. Much is known of the vortex equilibria of two-dimensional flow [23] [41] [55] [80] [108] [123], and investigations of hydrodynamic vortex equilibria have been extended to higher dimensions [31] [32] [38] [41].

The study of turbulence in classical and in quantum fluids is an effort proceeding on many fronts. These nonlinear problems have aspects in a number of mathematical fields including, but not restricted to, differential equations, dynamical systems, numerical analysis, and statistical mechanics. Turbulence has given rise to a numerous and diverse collection of models whose properties have been compared to physical and computational experiments. The equilibrium properties of vorticity are only a small component of the turbulence problem. Vortex equilibria nevertheless exhibit rich and complex behavior, much of which has direct applicability to turbulence in classical and quantum fluids. A better understanding of the statistical mechanics of vorticity may improve the theoretical understanding, and practical modeling of turbulent fluids and quantum devices.

In this I have attempted to place the work of the present thesis in context, in particular by presenting classical and quantum turbulence as separate but not unrelated problems. The reader may refer to the references [41] [94] [102] for an overview of classical turbulence, and to [5] [11] [24] [35] [58] for a discussion of computational methods for the Navier-Stokes equations. Coverage of superfluidity and resistanceless quantum flows in general may be found in [51] [139] [121] [136]. Topics in statistical physics and critical phenomena are reviewed in [28] [78] [64] [92]. The list of references is not encompassing, but represents an introduction to place the present study in a wider scientific framework.

1.2 Overview of the Thesis

I consider in this thesis the properties of collections of three dimensional vortex loops in thermal equilibrium. Examination of this system brings together and extends several lines of research. The thesis extends to three dimensions a body of work on the equilibrium states of collections of point vortices in two dimensions [23] [61] [88] [108] [109]. It addresses issues of vortex geometry which are absent in the two dimensional setting. Numerical experiments on single three dimensional vortex filaments have been carried out for several years [32] [34] [33] [36] [43] [38]. The thesis extends these experiments to a dense collection of filaments having variable connectivity. The present simulation addresses the effects of connectivity among the loops in a vortex system on energy screening and on vortex geometry. The dense three dimensional system can also be compared to thermally excited vortices in liquid helium. Quantum vortices are observed experimentally in liquid helium [52] [117] [147], and are thought to drive a phase transition in the system [59] [127] [143] [145] [131] [86]. The XY model, which is believed to represent helium at the lambda transition, has been simulated in spin variables in three dimensions [75] [53] [85], and in vortex variables in $2\frac{1}{2}$ dimensions [39] [42]. A vorticity variable simulation of the three-dimensional XY model has yet to be performed. The model simulated in the thesis differs from the vortex form of three-dimensional XY model only in that it constrains vortices to be self-avoiding, while XY vortices can intersect. The thesis simulation can therefore clarify the effects of self-avoidance in dense vortex equilibria. While some previous theories assume that XY vortices have self-avoiding properties [130] [131], other considerations [39] [42] cast doubt on the validity of the assumption. A comparison of the behavior of the self-avoiding model studied in the thesis to the properties of the XY model can cast light on self-avoidance and the relationship between classical and superfluid vortices. The dense three dimensional vortex system studied in this thesis provides a direct look at the effects of connectivity and self-avoidance in vortex equilibria.

I present in this thesis a computational method for determining the equilibrium properties of the vortex system. The method is a Monte Carlo simulation generating a random sequence of vorticity configurations. The algorithm employs a set of transformations which change vortex geometry, position, connectivity, and density. A modification to the Metropolis sampling method is introduced which enhances the efficiency of the algorithm. Histogram methods for thermodynamic simulation are employed; their performance and

reliability is analyzed.

I demonstrate two phase transitions in the dense vortex model. The numerical simulation reveals a low temperature phase transition analogous to the superfluid lambda transition. Like the lambda transition, the vortex transition has no latent heat; the energy of the system is continuous across the critical temperature. The specific heat, however, grows with the system size at the transition. This indicates the presence of a divergence or cusp in the specific heat in the thermodynamic limit. This evidence is the first numerical demonstration of a three dimensional lambda-like transition in pure vorticity variables. The transition, furthermore, is shown to be a percolation threshold dividing systems containing infinite vortex loops from those containing only finite loops. I present observations on vortex connectivity, screening, and geometry at the transition, and place them in relation to existing vorticity-based theories of the lambda transition.

A scaling analysis of the system indicates the existence of another transition at infinite temperature. This transition divides states with fractal vortices from states with smooth vortices. I make a conjecture on the nature of classical and quantum vortices in equilibrium, and present a speculation on the development of turbulence in classical fluids.

The thesis is divided into six chapters. Chapter 1 contains an overview of the subject and a summary of the rest of the thesis. Chapter 2 summarizes relevant background and terminology of thermodynamics. It also describes the effects of finite system size on general equilibrium models. Chapter 3 concerns the physics of vorticity and vortex equilibria. The chapter first defines the present self-avoiding vortex loops model in terms of classical flow. The discussion then turns to quantum mechanical vortices in liquid helium and the XY model. Theories of the role which vortices play in the lambda transition are reviewed. The relationship of the self-avoiding loops model to the XY model is discussed.

Chapter 4 covers basic techniques for numerical simulation of thermodynamic systems. It reviews in detail histogram sampling methods, and gives an analysis of the Ferrenberg-Swendsen multi-histogram technique. Chapter 5 describes my application of the numerical techniques to the self-avoiding loops system. It lists the transformation set employed by the algorithm. It then describes my modification to the Metropolis sampling method, and comments on the performance of the resulting algorithm.

Chapter 6 describes the thermodynamic behavior of the system of self-avoiding vortex loops. It first presents numerical evidence of a phase transition at low temperature. It describes the nature of the transition and shows how thermodynamic quantities vary with

the system parameters and the system size. It relates the observations to vortex theories of the lambda transition in the XY model. The chapter then presents an scaling analysis for the energy and entropy of the system of self-avoiding loops as the system size diverges. The analysis indicates that the infinite temperature line is a transition dividing fractal vortex loops from smooth vortex loops. Finally, comments are made on the nature of classical and quantum vortices, and on the nature of a universal equilibrium state.

The remainder of this introduction presents an overview of topics discussed at greater length in the body of the thesis. The nature of vorticity and its relation to the energy of the system are reviewed. Previous work which on vortex equilibria and phase transitions is briefly discussed. The model studied in the thesis is described, and is related to the previous work. An introduction to the numerical method employed is given. Finally, the results of the thesis study are summarized.

1.3 Vorticity in Classical and Quantum Systems

The term *vorticity* arises from fluid mechanics [7] [44]; there the vorticity field $\vec{\xi}(\vec{x})$ is defined as the curl of the velocity field $\vec{u}(\vec{x})$:

$$\vec{\xi} = \nabla \times \vec{u}$$

The vorticity can be identified with rotation in the flow. Envision fluid circulating around in an eddy. Stokes' theorem indicates that the line integral of $\vec{u} \cdot d\vec{\ell}$ around the eddy is equal to the integral of vorticity penetrating a surface through the eddy. The presence of circulation, $\oint \vec{u} \cdot d\vec{\ell}$, implies the presence of vorticity. Thus the common notion of a "vortex" such as a tornado or whirlpool can be thought of in terms of a concentration of vorticity on the axis of rotation.

Since vorticity is a derivative of velocity, the presence of vorticity even in a small region may correspond to a flow in a large region. A flow in \mathfrak{R}^3 can be expressed up to the gradient of a scalar function in terms of the vorticity field $\vec{\xi}(\vec{x})$ [91]:

$$\vec{u}(\vec{x}) = \frac{1}{4\pi} \int \frac{(\vec{x} - \vec{y}) \times \vec{\xi}(\vec{y})}{|\vec{x} - \vec{y}|^3} d\vec{y}$$

Note that the velocity at a point depends on the vorticity strength and direction throughout all space. This formula also allows the energetic properties of the flow to be described in

terms of the vorticity. The kinetic energy of incompressible fluid in \mathfrak{R}^3 can be re-written as the Lamb integral [91]:

$$\frac{1}{2} \int |\vec{u}(\vec{x})|^2 d\vec{x} = \frac{1}{8\pi} \int \int \frac{\vec{\xi}(\vec{x}) \cdot \vec{\xi}(\vec{y})}{|\vec{x} - \vec{y}|} d\vec{x} d\vec{y}$$

While the integrand $|\vec{u}(\vec{x})|^2$ in the velocity form is positive definite, the integrand $\frac{\vec{\xi}(\vec{x}) \cdot \vec{\xi}(\vec{y})}{|\vec{x} - \vec{y}|}$ in the vorticity form can be negative if $\vec{\xi}(\vec{x})$ and $\vec{\xi}(\vec{y})$ are anti-parallel. This can be physically interpreted as regions of anti-parallel vorticity screening each other to reduce the kinetic energy of the flow.

Because of this screening effect, the energetic properties of a flow field characterized by the vorticity are dependent on the direction of $\vec{\xi}(\vec{x})$ and $\vec{\xi}(\vec{y})$ at pairs of points \vec{x}, \vec{y} in space. The spatial correlations of the vorticity field determine the average energy of a random flow. Some general characteristics of the vorticity correlation structure follow from the discretized form of the vorticity. Of course, in the full equilibrium problem the relative weights of the different configurations affect the correlation statistics. Nevertheless, an examination of the vorticity configurations alone gives some information on the statistical nature of the flow which they represent.

A direct study of the infinite dimensional set of continuous vorticity fields $\vec{\xi}$ presents significant difficulties. One can model the continuous problem by first discretizing the vorticity field and then taking a continuum limit. An appropriate discretization of the vorticity field follows from constraints on the field in space and in time. Since vorticity is a curl, it must at all times be divergence free in space.

$$\nabla \cdot \vec{\xi}(\vec{x}) = \nabla \cdot [\nabla \times \vec{u}(\vec{x})] = 0$$

The time evolution of an inviscid flow, furthermore, has an interpretation in which vorticity of conserved “strength” is physically moved by the flow [44]. The conserved strength is more precisely expressed as the circulation around closed curves which move with the flow. Recall that the circulation is related by Stoke’s Theorem to the integral of vorticity passing through the curve. A proper discretization of vorticity should consist of objects which satisfy the zero divergence condition and have constant circulation.

Consider first the degenerate case of two dimensional flow in which the velocity is independent of the \hat{x}_3 coordinate direction and in which the \hat{x}_3 component of velocity is zero. The vorticity field in a dynamic calculation may be discretized into a collection of

pointlike vortices [35] which move with the fluid and whose circulation is constant in time. In two-dimensional flow, the zero divergence condition is trivially satisfied. Configurations in a random model may consist therefore of independently positioned pointlike vortices. The energy in the model then depends on the circulations and distributions of the points.

In three dimensions, however, the vorticity field generated by a collection of pointlike vortices may not satisfy the divergence free condition. This constraint can be satisfied by a discretization of vorticity into a collection of linelike objects having vorticity aligned along their axes. Helmholtz's Theorem indicates that a discretized line of vorticity can neither end nor change strength; it must therefore either close on itself to form a vortex loop or stretch to infinity [44]. The circulation around any curve encircling the loop is constant along the loop and in time in a dynamic flow. Configurations in a random model may consist therefore of collections of closed vortex loops or infinite vortex lines having conserved circulation.

These vortex lines may be described on a lattice as directed walks which either return to their origin to form a vortex loop or stretch to infinity in both directions. Lattice vorticity points in the direction of the steps of the walks. The vortex-vortex correlations in the configuration are thus correlations among steps of the directed walks. In a random model, these correlations may depend significantly on connectivity and self-avoidance properties of the vortices. The vorticity at two points may correspond to two steps of the same walk: belonging to the same connected vortex loop, or to steps on different walks: belonging to different unconnected vortex loops. Steps of lattice walks may be allowed to revisit sites: vortex self-intersection, or may be constrained to visit a site no more than once: vortex self-avoidance. Suppose for the moment that the degree of folding along a vortex loop is limited so that the loop tends to remain fairly straight. Then nearby steps along a lattice walk will tend to point in the same direction. A nearby portion of a separate, unconnected walk, however, may have a direction almost independent of the direction of the first walk. The connectivity pattern among different loops, therefore, affects the vortex-vortex correlations and thus the energy. The self-avoidance property of vortex loops also affects the vorticity correlations. If a vortex loop is allowed to fold back on itself, it typically forms an extremely crumpled object similar to a random walk in which successive steps have independent directions. If, on the other hand, the vortex loop cannot revisit any site, it will tend to straighten out. The statistics of random walks which obey the self-avoidance constraint have been studied in the context of polymers [63]; the self-avoiding walks exhibit

fractal geometries. Studies of self-avoiding random walks as models of turbulent vortex filaments indicate power law correlations between successive steps of the walk, as opposed to the uncorrelated behavior of the purely random walk [34] [33] [36] [43] [38]. These fractal self-avoiding vortices are straighter than self-intersecting vortices but more crinkled than smooth vortices. The self-avoiding vortices accordingly have average energies between those of self-intersecting and smooth vortices.

The vortex-vortex correlations of collections of three dimensional linelike vortices have a complex geometric character absent in the two dimensional setting. Vortex folding and changes in connectivity can significantly alter the expected energies of a random collection of vortex configurations. Local connectivity and avoidance constraints can have significant effects on the overall flow.

A vortex discretization for classical fluid flow is given in Section 3.2; classical vortices are self-avoiding. Vortices in quantum mechanical systems such as superfluid helium have a natural discretization. These vortices possess quantized circulation and are thus physically discrete entities [51] [121]. In the superfluid case, as in the classical case, vortices are pointlike in two dimensions and linelike with conserved circulation in three dimensions. While the hydrodynamics of superfluid helium is not fully understood, the XY spin model is believed to represent the configurational and energetic properties of the superfluid [88] [13]. The XY model can be transformed into a vortex system [127]. The energy of a vortex state, furthermore, has the same form for XY vortices as for hydrodynamic vortices. The XY vortices, however, can self-intersect. The suggestion has been made [130] that there is no significant difference between the self-avoiding and weakly self-avoiding models, but arguments have been made to the contrary [39] [42]. Since the vortex configurations in the thesis model differ from the configurations in the XY model only in the self-avoidance condition, the thesis simulation may shed light on the effect of self-avoidance on dense vortex equilibria.

1.4 Vortex Equilibria and Phase Transitions

The thermal equilibria of vortex systems have been studied in several physical contexts. Thermally excited vortices are conjectured to underly the lambda transition of ^4He from a superfluid to a normal phase [59] [52]. Vortices have also been shown to play a role in the analogous transition in the three-dimensional XY model [86]. A number of

theories of thermally excited vortices in helium and in the XY model have been developed [88] [127] [143] [146] [130]. Onsager [115] suggested that two dimensional vortex equilibria could represent the turbulence of a classical fluid in the plane. He furthermore indicated that negative temperature was characteristic of the system. The negative temperature states of two dimensional vortex systems have since been studied by a number of researchers [23] [55] [80] [97] [108]. Chorin [32] [34] [33] [36] [38] has studied vortex equilibria in three dimensions as models for classical and quantum turbulence. For classical turbulence, Chorin and Akao [43] demonstrated a class of equilibria in a single-filament model which exhibits the universal Kolmogorov energy spectrum and gave evidence that the infinite temperature equilibrium is an asymptotically stable state.

Vortex equilibrium models are known to exhibit several types of phase transition. Kosterlitz and Thouless [88] [87] described a transition in the low temperature vorticity form of the XY model in two dimensions. The transition is thermodynamically weak, with all derivatives of the free energy remaining continuous, but is a threshold at which vortex pairs unbind to form a gaseous state. Caglioti [23] described a transition in two-dimensional negative temperature systems between smooth vorticity distributions and a collapsed state. Chorin [38] showed that a lone vortex in three dimensions undergoes a phase transition at infinite temperature. The vortex is collapsed into a three-dimensional object below the transition, and extends into a smooth one-dimensional object above the transition. The vortex is a fractal self-avoiding walk at the transition. Work by Shenoy et. al. [130] [146] indicates that the vortex form of the three-dimensional XY model undergoes second order transition analogous to the lambda transition in bulk superfluid helium. While the XY transition has been observed in spin variables [75] [53], and related to the existence of vortices [86] [131], it has not been directly observed in a vortex variable computation.

Phase transitions can arise in stochastic models other than thermal systems. The transitions in other models, furthermore, can sometimes be related to transitions in thermal systems. An example of a class of non-thermal systems having phase transitions is percolation [66] [134]. Percolation theory examines how collections of objects having random positions cluster into large structures. An example of a percolation system which typifies the phase transition behavior follows. Suppose each site of an infinite lattice is occupied by a particle with probability q , and empty with probability $1 - q$. There exists a critical probability q_c which the system undergoes a phase transition. For all occupation probabilities $q < q_c$ the probability of the existence of an infinite cluster of nearest neighbor particles is

zero, while for occupation probabilities $q > q_c$ the probability of an infinite cluster is one. This percolation transition displays a set of scaling behaviors analogous to transitions in thermal systems. The probabilities for different sites to be occupied need not be independent as in the example; the particles could have an interaction for instance. Dependent percolation has been linked to vortex equilibria by Chorin [39]. Percolation ideas are used in this thesis to describe the vortex behavior at a thermodynamic phase transition.

1.5 The Self-avoiding Loops System

This thesis considers the equilibria of dense collections of vortex loops in three dimensions. Individual vortices in the model trace out closed self-avoiding walks on a periodic lattice. Each vortex configuration contains a collection of vortex loops obeying the self-avoidance condition that no site can be visited more than once, hence no two loops can touch. A typical configuration contains loops of many different lengths at separations comparable to the size of the loops. The model extends research done [32] [34] [33] [36] [38] on a model of single three dimensional self-avoiding vortices. The single vortex model simulates vortices whose separation is much greater than their characteristic length. Allowing multiple loops exposes energy screening effects and addresses the impact of loop connectivity on the energy and on vortex-vortex correlations.

In addition to allowing vortex lines to arrange themselves in many ways to form collections of loops, the multiple vortex simulation has a definite spatial volume and thus allows the definition of vortex line density. Variable density vortex systems have been studied in two dimensions, but the current work is the first three dimensional variable density simulation. Since vortex length and density are not conserved in either classical or quantum turbulence, the effect of density on the equilibrium states is of physical interest.

The vortex system simulated in this thesis differs from the vortex form of the three-dimensional XY model only in that the vortices in the thesis model are self-avoiding while XY vortices can intersect. A simulation of the self-avoiding system is useful with regard to the XY system in several ways. To the extent that the models are similar, general characteristics of the phase transitions in the self-avoiding loops system may apply to the XY transition as well. The difference between the two models can clarify the effects of self-avoidance on vortex equilibria. A theory of the phase transition in the XY model [130] employs an assumption that large XY vortices have the same equilibrium statistics at the

critical temperature as equal probability (infinite temperature) self-avoiding walks. Other studies [38] [39] [42], however, indicate that self-avoidance has a significant impact on vortex statistics. The simulation of a model in which vortex self-avoidance is explicitly enforced can explore the distinction between self-avoiding vortices and self-intersecting XY vortices. Finally, the relation of the self-avoiding system to superfluid helium transition may cast light on the approximation process used to derive the XY model from physical considerations.

1.6 Numerical Simulation

The equilibrium states of the system of self-avoiding loops are simulated in this thesis by a grand canonical Monte Carlo algorithm. The algorithm employs a set of transformations which change vortex loop geometry, position, number, and connectivity. The vortex geometry transformations are adapted from the self-avoiding walk computations of Madras and Sokal [100] [99] [25] [26]. The set of transformations consists of both local and global moves. A modified Metropolis acceptance algorithm is developed to efficiently handle different types of transformations. The modified algorithm allows the probability of accepting a move to depend on the type of transformation producing the move, while still preserving the detailed balance condition. This freedom allows the algorithm to make efficient use of expensive configuration energy computations. The modification may also be of use in general Monte Carlo simulations which must overcome probability barriers near energy ground states.

Histogram sampling and histogram merging methods are employed. The methods enable a single computation to provide information on the micro-canonical, canonical, and grand canonical ensembles. They also allow average quantities to be examined as functions of the thermodynamic potentials, rather than values at discrete potentials. A theoretical analysis is given of the Ferrenberg-Swendsen multi-histogram method [56] [57], and suggestions are made for improving the algorithm.

1.7 Phase Transitions in the Self-avoiding Loops System

Two transitions are described for the system of self-avoiding loops. The first is a phase transition at low temperature. While the energy and vortex density are continuous as functions of temperature across the transition, the specific heat has a peak at the critical

temperature. The phase transition is shown to be a percolation threshold; the probability of the existence of an infinite connected vortex loop is zero below the transition and one above the transition. The transition in the self-avoiding loops system is similar in nature to the lambda transition in superfluid helium and to the phase transition in the XY model. The observation of percolation behavior at the transition supports the use of percolation ideas in developing renormalization theories of the lambda transition. While the phase transition in the self-avoiding system has a similar character to the phase transition in the XY model, the two models may lie in different universality classes. Estimates of the fractal dimension of self-avoiding vortex loops did not match estimates [53] of the fractal dimension of XY vortices. A definitive conclusion on the difference between the self-avoiding and the XY phase transitions is not presently available; although a computation of the critical exponents for the self-avoiding system could help resolve the issue.

The second transition occurs at infinite temperature. Vortex loops are shown to be fractal with structure of the size of the lattice spacing at positive and infinite temperatures. The negative temperature states, however, contain smooth composite vortices made of parallel bundles of lattice vortices. These regions of aligned vorticity are of the size of the domain. A suggestion is made that negative temperature states correspond to classical vortices, while positive temperature states correspond to quantum vortices. The infinite temperature state may be accessible to both quantum and classical systems, and may represent a generic turbulent state insofar as the equilibrium model holds for true turbulence.

Chapter 2

Thermodynamics

Thermodynamics provides a simplifying framework for studying systems having many degrees of freedom and complicated dynamical interactions. It gives information on average quantities for a system in its generic, or typical “state”. It is applicable for systems where the properties of interest are essentially constant on a coarse enough measurement scale in space and time. I present the barest essentials of thermodynamics in this section. A physical view of thermodynamics and statistical physics is available in Reif [122], while a more mathematical introductory treatment is given in Thompson [138].

Consider as an example a gas of N molecules in a box. The most straightforward way of examining the behavior of an observable quantity would be to construct a dynamical model. The instantaneous configuration of the collection can be described by a vector $c(t)$ with $6N$ coordinates: the positions (x, y, z) and momenta (p_x, p_y, p_z) of all the particles at time t . One could begin with a configuration $c(0)$ and then evolve the system forward to a time \mathcal{T} , tracking the orbit in $6N$ dimensional phase space:

$$c(t) \Big|_{t \in [0, \mathcal{T}]}$$

An observable function $A(c)$ of the system could then be computed instantaneously, or averaged over the time period:

$$\langle A \rangle = \frac{1}{\mathcal{T}} \int_{t=0}^{\mathcal{T}} A(c(t)) dt$$

Although this approach is useful for simple systems, the difficulty of obtaining an appropriate starting point, understanding the time evolution, and solving the model, is immense

when N is on the order of 10^{23} . Even storing the information on 6×10^{23} degrees of freedom is wholly impractical.

The thermodynamic approach replaces the temporal evolution and averaging with a probabilistic formulation. The set \mathcal{C} of all possible configurations of the system is formed. In the example \mathcal{C} is the collection of all possible vectors c of positions and momenta. The “state” of a system is defined not in terms of a path through the space of configurations but in terms of probabilities assigned to the configurations. The dynamic orbit $c(t)|_{t \in [0, T]}$ is replaced with a probability distribution $\rho(c)|_{c \in \mathcal{C}}$. The form of the probability distribution is determined by defining an entropy functional on the space of all suitable distributions and choosing the Gibbs Distribution ρ which maximizes that entropy [92]. The underlying physical principle is that a system with many degrees of freedom and complicated dynamic properties will quickly reach an equilibrium state which has maximum entropy. The implication of this assumption is that averages over a sufficiently long time period are equal to probabilistic averages over \mathcal{C} :

$$\langle A \rangle = \frac{1}{Z} \int_{c \in \mathcal{C}} A(c) \rho(c) dc$$

The probability of a configuration is in practice expressed as a relative weight $\rho(c)$ and normalized by a factor $1/Z$.

$$Z = \int_{c \in \mathcal{C}} \rho(c) dc$$

The normalization Z is known as the *partition function*. The thermodynamic equilibrium formulation eliminates the temporal component of the problem and replaces the dynamic average with a more tractable probabilistic average. Furthermore, the probabilities depend simply on quantities which are preserved by dynamics of the system.

2.1 Thermodynamic Ensembles

Differences in the manner of constituting \mathcal{C} lead to different probability distributions. The pair $\{\mathcal{C}, \rho\}$ is called the thermodynamic ensemble. Consider first an isolated system, such as a box with insulating walls. Since the energy of the system remains constant, \mathcal{C} should consist of all sets of N positions and N momenta with a particular energy density \mathcal{E} . The probability distribution with maximum entropy is then $\rho(c) = 1$; all the listed configurations are equally likely. This choice of $\{\mathcal{C}, \rho\}$ is known as the *micro-canonical ensemble*.

Suppose, though, that the system can exchange energy with another (infinitely large) reference system of energy density \mathcal{E} . The set \mathcal{C} thus contains configurations of any energy $E(c)$. The probability function corresponding to equilibrium with the reference system is then:

$$\rho(c) = e^{-\frac{1}{k_B T} E(c)} = e^{-\beta E(c)}$$

where $\beta = \frac{1}{k_B T}$ is a parameter which depends on the energy per unit volume \mathcal{E} of the reference system. This choice of $\{\mathcal{C}, \rho\}$ is known as the *canonical ensemble*. Here T is the temperature of the system; β is inverse temperature. I wish to emphasize that temperature is an arbitrary parameter arising through the equilibrium condition. While the familiar temperature corresponding to energy in the small scale motions of individual molecules is always positive, the temperature of equilibrium systems where other types of energy are present may be infinite or negative. In two-dimensional inviscid turbulence, for instance, where the internal molecular motions of the fluid are uncoupled from the the bulk velocity $\bar{u}(\vec{x})$, the temperature corresponding to the energy

$$E^H(\bar{u}) = \frac{1}{2} \int \|\bar{u}(\vec{x})\|^2 d\vec{x}$$

is typically negative [115] [109]. In this case the averaged “hydrodynamic” motions contributing to the bulk fluid velocity \bar{u} can come to an equilibrium which is decoupled from the equilibrium of the small scale molecular motions. The hydrodynamic system, therefore, can have two temperatures, the familiar temperature corresponding to individual molecular motions, and a different temperature defined for the equilibria of the bulk flow.

Some qualities of general temperature do follow a familiar pattern. For instance, higher positive temperature systems have a larger average energy, and energy will flow from a hotter system to a colder system if the two are placed in contact and allowed to come to equilibrium [92]. Since the parameter β is the inverse of the usual temperature T , systems become hotter as β decreases. The behavior for infinite and negative temperature may be seen from the expression for the average energy in the canonical ensemble:

$$\langle E \rangle = \frac{1}{Z} \int_{c \in \mathcal{C}} E(c) e^{-\frac{1}{k_B T} E(c)} dc = \frac{1}{Z} \int_{c \in \mathcal{C}} E(c) e^{-\beta E(c)} dc$$

The coldest systems have small positive T , or large positive β . The configuration weights in this case quickly decrease with increasing energy. The systems warm up as $T \rightarrow \infty^+$, and as $\beta \rightarrow 0^+$; high energy configurations are less severely discouraged. At infinite temperature,

$T = \pm\infty$, $\beta = 0$, all configurations have equal weight and the average energy depends only on the space of configurations. At negative temperatures, configurations with large energies have a weight which is exponentially *increasing* with increasing energy. The highest energy configurations, therefore, are the most favored. Negative temperatures are thus hotter than positive and infinite temperatures. The hottest states correspond to $T \rightarrow 0^-$, which is $\beta \rightarrow -\infty$. I use throughout most of this thesis the inverse temperature parameter β . The average energy of a system is always increasing as β moves down from $\beta = \infty$ through $\beta = 0$ toward $\beta = -\infty$.

If the dynamics of the system conserve the number of particles $N(c)$ as well as the energy, it makes sense to consider an open subsystem which can exchange energy and particles with a reference system of energy density \mathcal{E} and particle density \mathcal{D} . The set of subsystem configurations then contains configurations c of arbitrary energy $E(c)$ and arbitrary number of particles $N(c)$. In this case, the equilibrium probability function has two parameters: β and μ :

$$\rho(c) = e^{-\beta E(c) + \beta \mu N(c)}$$

This pair $\{\mathcal{C}, \rho\}$ is known as the *grand canonical ensemble*. The parameter β is the inverse temperature and the parameter μ is the “chemical potential” of the system.

2.2 Finite Size Effects

The thermodynamic ensemble $\{\mathcal{C}, \rho\}$ is formulated for a fixed system size, or volume V . We are interested, however, in the bulk properties of the system when the number of degrees of freedom is huge, on the order of 10^{23} . We therefore need to take the thermodynamic limit:

$$\langle A \rangle^\infty = \lim_{V \rightarrow \infty} \langle A \rangle^V$$

Under most conditions, the thermodynamic limit is independent of the choice of ensemble. The physical behavior of the macroscopic system is well represented by any of the ensembles.

In practice, computer simulations are conducted for extremely small systems with tens to a few thousands of degrees of freedom. These systems, viewed probabilistically, attach significant probability to configurations with observable values away from the mean. This may be formalized as follows. Think of c as a random variable with probability distribution ρ/Z ; we may then derive a corresponding random variable for an observable

A. Define the distribution function $F_A(x) : \mathfrak{R} \rightarrow \mathfrak{R}$:

$$F_A(x) = \text{Prob}(A(c) \leq x) = \int_{c' \in \mathcal{C}} \chi(A(c') \leq x) \rho(c') / \mathcal{Z} dc'$$

Then let $P_A(x) = \frac{\partial}{\partial x} F_A(x)$ in the distribution sense. Now A can be thought of as a random variable with probability density $P_A(x)$. The thermodynamic average is the mean, or expected value of A :

$$\langle A \rangle = \frac{1}{\mathcal{Z}} \int_{c \in \mathcal{C}} A(c) \rho(c) dc = \int_{\mathfrak{R}} x P_A(x) dx$$

We may now consider the variance of A which gives an indication of the magnitude of fluctuations about the mean:

$$\text{Var}(A) = \langle (A - \langle A \rangle)^2 \rangle$$

The typical asymptotic behavior for the variance of an observable for V large is given by:

$$\text{Var}(A) \propto e^{-V}$$

where the volume of the system V is proportional to the number of degrees of freedom. That is, the magnitude of fluctuations decreases exponentially with the system size. A schematic view of the probability density for the energy E/V is given in Figure 2.1. The density becomes more sharply peaked as the volume of the system increases. For the very large systems observed in most physical situations, the magnitude of the fluctuations is tiny compared to the mean value of an observable. In most numerical calculations, however, the scaling of the fluctuations with the volume of the system is quite noticeable.

The effect of taking the thermodynamic limit goes beyond the convergence of the mean values and the narrowing of the probability distribution. While the behavior of observables in a finite system is a smooth (even analytic) function of the equilibrium parameters $\{\beta, \mu\}$, this need not be the case in the thermodynamic limit. In fact, many systems exhibit *phase transitions* in which the behavior of certain thermodynamic functions changes abruptly. Consider an order parameter O which is a function of the configuration c and which characterizes the phase of a system. For instance, a system of molecules may have $O(c) = 0$ for a liquid configuration and $O(c) = 1$ for a solid configuration. While the temperature dependent behavior of $\langle O \rangle_\beta$ is smooth for any fixed system size, it can exhibit sharper and sharper gradients in larger and larger systems. A schematic example is given in Figure 2.2. After taking the thermodynamic limit, $\langle O \rangle_\beta^\infty$ exhibits a discontinuity

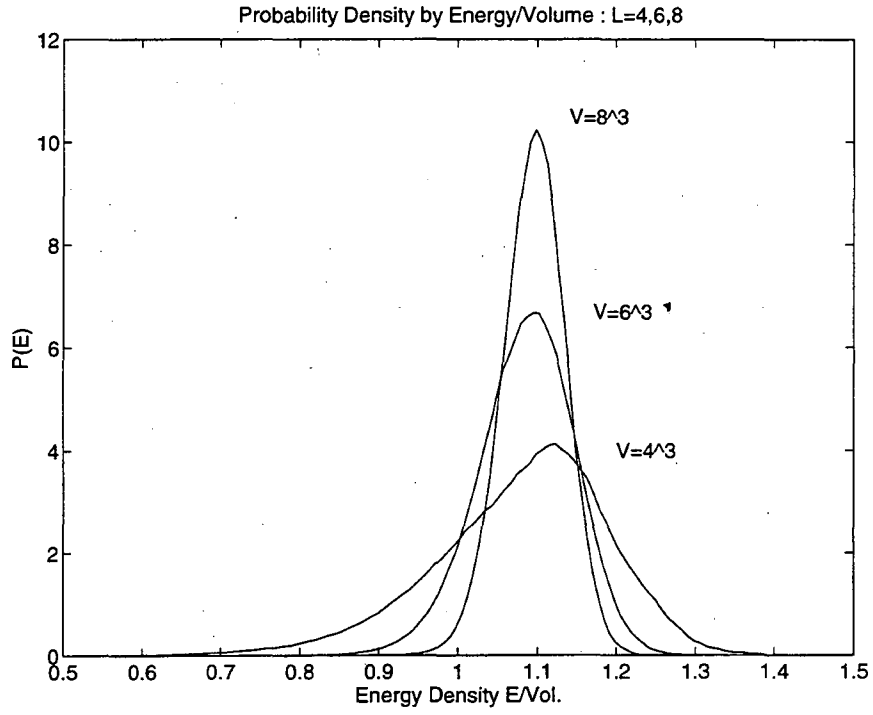


Figure 2.1:

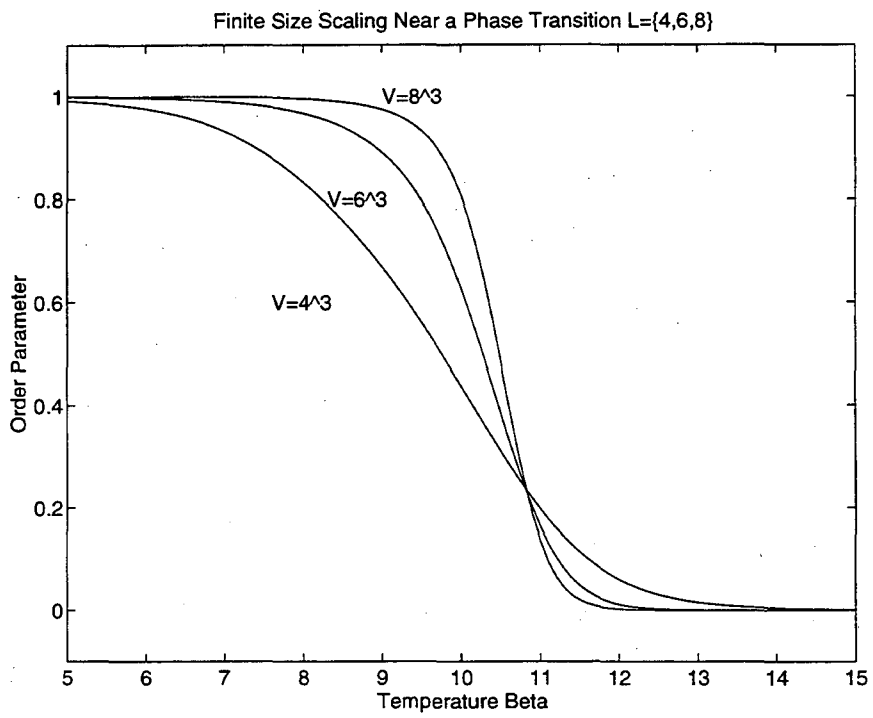


Figure 2.2:

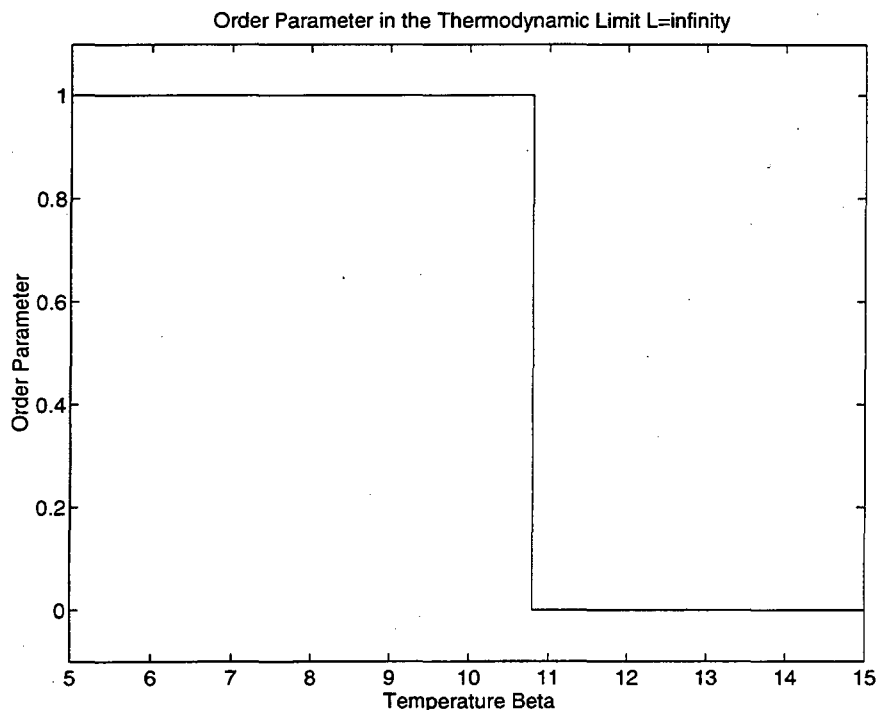


Figure 2.3:

at a critical temperature β_c where the order parameter jumps from 0 to 1. See Figure 2.3

The thermodynamic parameters such as the average energy and its derivatives are also analytic as a function of β at any finite size but can have discontinuous behavior in the thermodynamic limit. Refer to [138] [133] [119] for a more quantitative presentation of finite size effects in thermodynamic systems.

A phase transition at a critical temperature β_c is termed a first order transition if it has a latent heat associated with it; that is, if the energy $\langle E \rangle_\beta^\infty$ has a jump discontinuity at $\beta = \beta_c$. See Figure 2.4. Even if $\langle E \rangle_\beta$ is a continuous function of temperature, so there is no latent heat, a derivative of $\langle E \rangle_\beta$ may be unsmooth. Consider, for example the specific heat:

$$\langle C \rangle = -\beta \frac{\partial \langle E \rangle}{\partial \beta}$$

If the specific heat has a divergence or cusp at the critical temperature the transition is called continuous, or second order. See Figures 2.5 2.6.

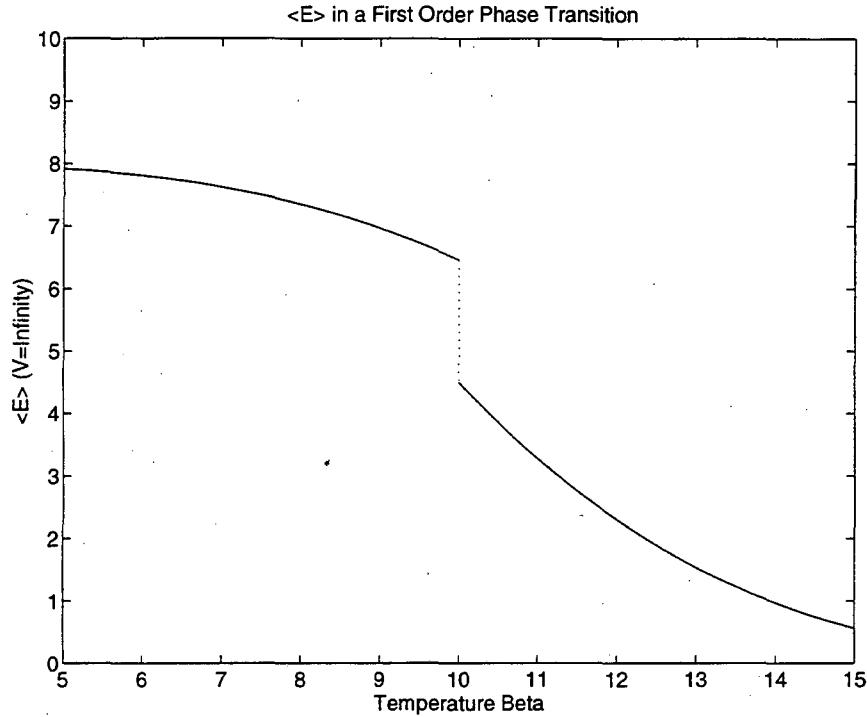


Figure 2.4:

2.3 Entropy and Energy/Entropy Arguments

A broad class of analytical techniques known as energy/entropy arguments [138] [64] are used to make general statements about the nature of thermodynamic systems. The arguments have several variations, but all examine the balance between the number of configurations having a given property and the Gibbs weight attached to those configurations. The arguments indicate if the configurations have a high probability or a low probability, and thus if the system as a whole has the property associated with the configurations.

A quantity called entropy [122] [138] is used to indicate the number of configurations having a particular property. Let the subset of configurations of interest be C_* , so:

$$C_* \subseteq C$$

Define the entropy S of the subset to be:

$$S = \log \left(\int_{c \in C_*} dc \right)$$

The entropy is the log of the measure of the subset of configurations C_* or, in the case

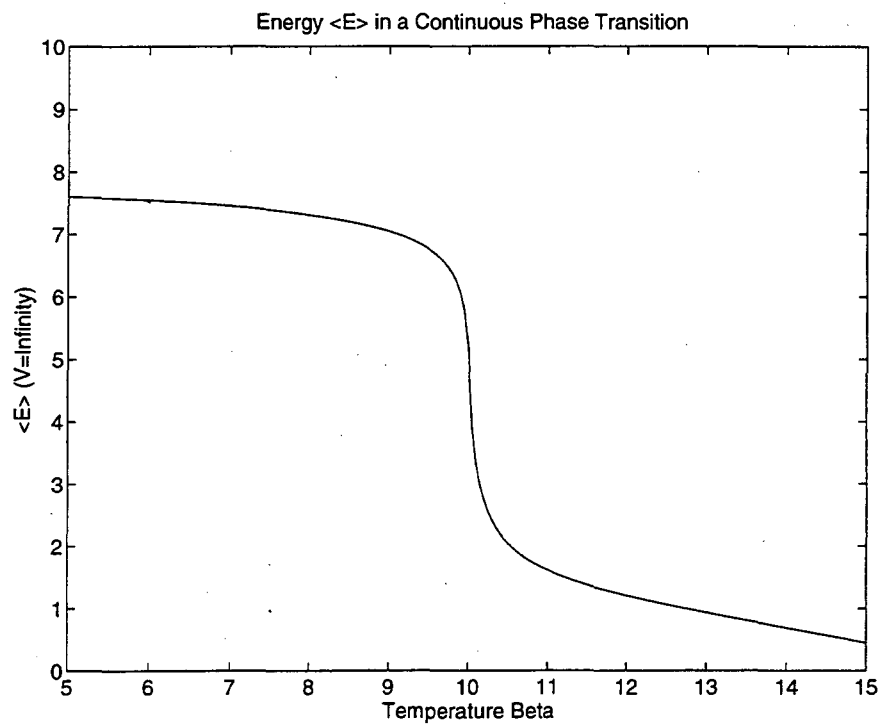


Figure 2.5:

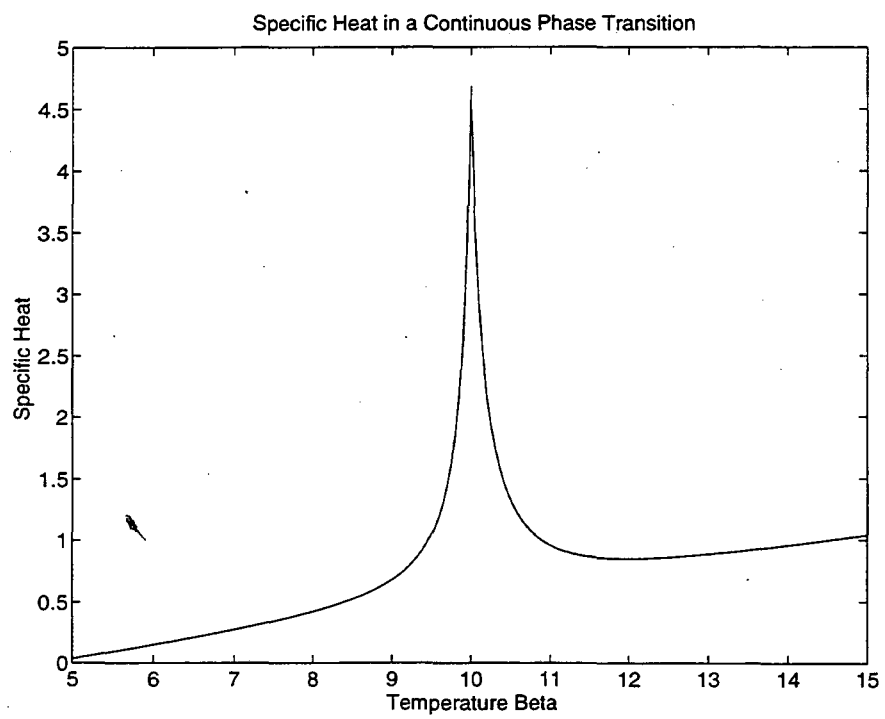


Figure 2.6:

of a discrete state space \mathcal{C} , the log of the number of configurations in the subset. The energy/entropy argument is named for its application in the canonical ensemble, but can be generalized to the grand canonical ensemble. The argument states, in essence, that if the quantity:

$$S - \beta E$$

increases as the system volume V increases, then the subset \mathcal{C}_* will have a high probability and the configurations of \mathcal{C}_* will characterize the system in the thermodynamic limit. If, on the other hand, the quantity $S - \beta E$ decreases as V increases, the subset will have a low probability and the configurations of \mathcal{C}_* will be insignificant in the thermodynamic limit.

A sketch of the energy entropy argument follows. Suppose the space of configurations is divided into two disjoint subsets:

$$\mathcal{C} = \mathcal{C}_1 \cup \mathcal{C}_2$$

Also suppose that the energy $E(c)$ of all configurations $c \in \mathcal{C}_1$ is E_1 , and that the energy of all configurations in \mathcal{C}_2 is E_2 . Let the observable quantity A indicate the property of interest; let $A(c)$ take the value A_1 for all $c \in \mathcal{C}_1$ and the value A_2 for all $c \in \mathcal{C}_2$. Now the canonical ensemble average of A is:

$$\langle A \rangle = \frac{1}{\mathcal{Z}} \int_{c \in \mathcal{C}} A(c) e^{-\beta E(c)} dc$$

The integral can be broken up over the two subsets \mathcal{C}_1 and \mathcal{C}_2 :

$$\langle A \rangle = \frac{1}{\mathcal{Z}} \int_{c \in \mathcal{C}_1} A_1 e^{-\beta E_1} dc + \int_{c \in \mathcal{C}_2} A_2 e^{-\beta E_2} dc$$

The expression can be rewritten in terms of the entropies S_1 and S_2 of the two subsets, since the exponential of the entropy is the measure of the subset:

$$e^{S_1} = \int_{c \in \mathcal{C}_1} dc$$

Making the substitutions for the entropy gives:

$$\langle A \rangle = \frac{1}{\mathcal{Z}} [A_1 e^{S_1 - \beta E_1} + A_2 e^{S_2 - \beta E_2}]$$

The relative probabilities of the subsets \mathcal{C}_1 and \mathcal{C}_2 are expressed as the weights, $\exp(S_1 - \beta E_1)$ and $\exp(S_2 - \beta E_2)$. Now suppose that the difference in energies and entropies between the two subsets can be estimated in terms of the volume V of the system:

$$E_2 - E_1 \approx JV$$

$$S_2 - S_1 \approx qV$$

The average of A is proportional to:

$$\langle A \rangle_{\beta}^L \propto \left[A_1 + A_2 e^{(S_2 - S_1) - \beta(E_2 - E_1)} \right] = \left[A_1 + A_2 e^{(q - \beta J)V} \right]$$

Now if the quantity $q - \beta J$ is positive, then the weight of C_2 will increase in relation to the weight of C_1 as $V \rightarrow \infty$ and thus $\langle A \rangle_{\beta}^{\infty} \approx A_2$. If, on the other hand, $q - \beta J$ is negative, then configurations in C_1 will dominate the system and $\langle A \rangle_{\beta}^{\infty} \approx A_1$. This argument indicates the presence of a critical value of the inverse temperature, $\beta_c = q/J$, at which the behavior of $\langle A \rangle$ changes from A_2 for $\beta < \beta_c$ to A_1 for $\beta > \beta_c$.

This example of an energy/entropy argument indicates the presence of a phase transition in the system at a critical temperature β_c . The example is simplified by assuming that the configurations in the system have only two different energies. The energy/entropy argument can also be shown to hold in more general situations. Analyses based on the balance of energy and entropy form a basic class of tools for making general statements about thermodynamic systems.

Chapter 3

Vorticity Models of Physical Systems

Much of the vorticity terminology and context used in this thesis comes from incompressible fluid dynamics. A number of physical systems, however, can be expressed in terms of vorticity. While the specific properties of each system are relevant to the formulation and interpretation of a vortex equilibrium model, the properties of the model may be considered separately from the individual systems. The physics of thermodynamic equilibrium depends only on the configurational and energetic properties of the model. In this regard, a vortex equilibrium model applies to any system having a description in terms of variables $\vec{\xi}(\vec{x})$ which are topologically linelike, which satisfy a zero divergence condition $\nabla \cdot \vec{\xi} = 0$, and for which the energy takes the form:

$$\int \int \frac{\vec{\xi}(\vec{x}) \cdot \vec{\xi}(\vec{y})}{|\vec{x} - \vec{y}|} d\vec{x} d\vec{y}$$

Systems to which a vorticity model applies include magnetic field lines in plasmas [45] [142] and in super-conductors [49] [104] [30], and topological defects in melting solids [72] [110] [112] [111] and in liquid crystals [62] [71]. Vortices have also been identified with monopoles in four-dimensional lattice gauge theories [90]. While vortex equilibria are pertinent to a wide range of physical systems, this thesis discusses only two: turbulence in incompressible fluids and the superfluid transition in the XY model of liquid helium.

This chapter both reviews the formulation of vortex models for the two systems and describes how the equilibria of the models can be applied to the physical systems. The first part of this chapter, Section 3.1, formulates a class of lattice vorticity models of classical flow

following Chorin [32] [34]. The section gives a description of the lattice configurations and explains how vorticity conservation laws govern the set of realizable configurations. It also formulates an energy functional on the lattice vortices. The vortex self-avoidance condition natural to classical fluids is presented. The formulation of a similar lattice vorticity model for superfluid helium will be given later in Section 3.3 following Savit et. al. [127].

The second part of the chapter, Section 3.2, describes the self-avoiding loops model employed in the thesis. The model is a member of the class formulated in Section 3.1; the distinction between the present instance of the class and previous instances is detailed. In particular, the thesis model allows multiple vortex loops in a periodic volume. Previous models investigated by Chorin [32] [34] [33] [36] [38] and Chorin and Akao [43] allowed only a single vortex filament in free space. The extrinsic and intrinsic observable quantities in the thesis model are defined in this section. An order parameter based on ideas from percolation theory is also given. The relation of the thesis model to the physics of slightly viscous turbulent flow is briefly discussed.

The third part of the chapter, Section 3.3, describes the XY spin model of superfluid helium. It reviews the vortex form of the model in terms of a low temperature duality transformation [128] and in terms of topological defects [13] [88] [113]. It then discusses the Kosterlitz-Thouless [88] theory of a vortex driven phase transition in the two-dimensional XY model. The phase transition in the three-dimensional XY model which is analogous to the lambda transition in bulk ^4He is presented, and analysis and computations in the spin variables are cited [124] [93] [75]. Efforts to extend the Kosterlitz-Thouless type vorticity analysis from two dimensions to three dimensions are reviewed [127] [143] [144] [146] [130] [131] [29] [43] [38]. Numerical evidence of vortex effects in spin based simulations of the three-dimensional XY model is given [53] [86] [85].

The fourth part of the chapter, Section 3.4, reviews the nature of percolation transitions. It discusses work by Chorin [39] [41] on vortex percolation in a $2\frac{1}{2}$ -dimensional model and indicates how percolation ideas may be used to develop a theory of the lambda transition.

The last part of the chapter, Section 3.5, outlines how the model simulated in the thesis can be applied to the general theory of vortex equilibria, and how the model can address theories of turbulence and of phase transitions in superfluid helium and the XY model.

3.1 Classical Vorticity and Lattice Vorticity Discretization

Lagrangian methods in vorticity variables have proved effective for solving the evolution equations of incompressible flow [4] [5] [120] [35] [67]. Experience with these methods grounds the discretization of the vorticity field for a thermodynamic equilibrium model. The discrete model developed by Chorin [31] [32] [34] [33] [43] [38] respects invariants in space and time. Thermodynamics relates equilibrium averages in the discrete model to time averages in the physical system; hence the collection of vortex configurations should preserve the invariants of turbulent flow. The following discussion summarizes the formulation of a class of lattice vortex models; refer to [32] [38] [41] for the original treatments.

Consider an incompressible velocity field $\vec{u}(\vec{x})$. The vorticity $\vec{\xi}(\vec{x})$ is the curl of the velocity field:

$$\vec{\xi}(\vec{x}) = \nabla \times \vec{u}(\vec{x})$$

We desire for the equilibrium model a discretization of the vorticity field into “particles” whose positions \vec{x}_i and strengths $\vec{\xi}_i$ will determine the flow. Consider first the degenerate case of two dimensional flow, where the velocity is restricted to the (\hat{x}_1, \hat{x}_2) directions and is invariant in the \hat{x}_3 direction. Then vorticity points only in the \hat{x}_3 direction. Take a small patch S of the (\hat{x}_1, \hat{x}_2) plane, and denote its counterclockwise oriented boundary by ω . See Figure 3.1. The circulation Γ around the boundary is equal to the total strength of the vorticity through the patch:

$$\Gamma = \oint_{\omega} \vec{u} \cdot d\vec{\ell} = \int_S \vec{\xi} \cdot d\vec{A}$$

Now consider the patch as a material surface moving with the flow. The patch may deform but, assuming the flow is smooth, the patch cannot break apart. Furthermore, the area of the patch is conserved since the flow is incompressible. If the flow is also inviscid, the circulation Γ is preserved in time:

$$\frac{d\Gamma}{dt} = 0$$

The support of the vorticity field $\vec{\xi}(\vec{x})$ can be covered with a collection of disjoint patches S_i with associated circulations Γ_i . If the patches are sufficiently small, one can accurately represent them by discrete point-like “vortices” $\vec{\xi}_i$ with positions \vec{x}_i and fixed strengths Γ_i . The review in [120] summarizes the properties of discrete vortices in a discretization of the inviscid Navier-Stokes equations.

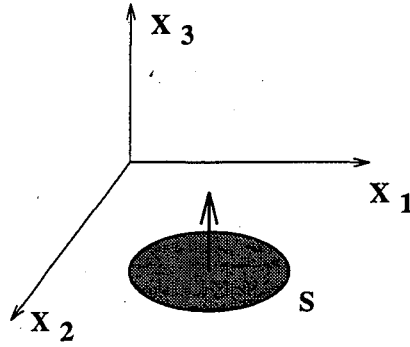


Figure 3.1: Two-dimensional patch of vorticity

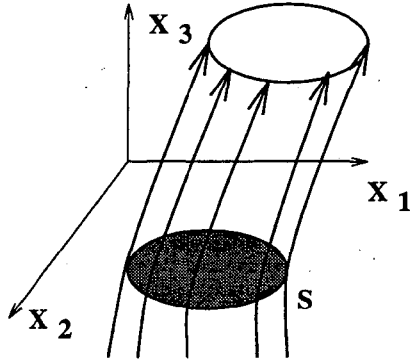


Figure 3.2: Vortex tube

For the purposes of an equilibrium model, two-dimensional flow can be represented by a collection of point vortices $\vec{\xi}_i$ with fixed strengths Γ_i . The model may be regularized by restricting the positions \vec{x}_i to the sites of a lattice. Since the patches S_i have in classical incompressible flow a fixed area, it is natural to associate with the discrete vortices an exclusive area. This gives rise to the self-avoidance condition that no two vortices can share a lattice site.

In three-dimensional flow the discretization is somewhat more complex. Consider again a small patch S in the fluid, and now extend it into a tube by following all the integral curves of $\vec{\xi}$ which pass through S . See Figure 3.2. Helmholtz's theorem [44] indicates that the circulations around any two closed curves ω, ω' encircling the tube are the same:

$$\oint_{\omega} \vec{u} \cdot d\vec{\ell} = \oint_{\omega'} \vec{u} \cdot d\vec{\ell} = \Gamma$$

This is a consequence of the constraint that the divergence of the vorticity is zero. The theorem furthermore indicates that the circulation about a tube is conserved in the dynamic

evolution of an inviscid fluid. Although the cross sections of the tube can vary in shape and size, the circulation and thus the strength of the tube are conserved. Vortex tubes are thus material objects which retain their identity in the flow.

The vorticity field in three dimensions may therefore be discretized as a collection of linelike objects with vorticity along the axis of the lines. The preservation of circulation along a line constrains the connectivity of the lines; vortex lines cannot end and must form collections of closed loops. The preservation of volume in a vortex tube leads to the self-avoidance condition on a lattice that no two vortex lines can pass through any lattice site.

Experience with the self-avoidance condition in the context of random walks on the lattice [63] indicates that self-avoidance has a significant effect on the statistics of the walks. The effects of avoidance constraints on vortex equilibria are of particular interest since vortices in the XY model are not self-avoiding. See Sections 3.2 3.3. Chorin has suggested that the self-avoidance condition is one of the most significant differences between classical and quantum vortices [39] [42].

While the circulation Γ is conserved along a single vortex, distinct vortex tubes in a classical flow can have arbitrary circulations. Physical vortices may be dynamically modeled as bundles of discrete vortex filaments having the same Γ , [68] [69] [9] [65] however. The effect of artificially quantizing vorticity in a model of classical fluid appears to be slight [42], and is physically appropriate for quantum mechanical systems, see Section 3.3. It is therefore reasonable to assume a lattice model of vorticity in which all vortices have the same circulation.

The properties of vorticity in incompressible, inviscid flow suggest a lattice discretization into collections of vortex lines of unit circulation. In order to make this picture rigorous, I define some terminology for the lattice. These terms are used to describe the lattice vortex configurations and later to describe a computational algorithm. I refer to points on the lattice as *sites* and the lines between sites as *bonds*. Vortex lines perform directed walks along the bonds of the lattice; occupied bonds are called vortex *links* and the visited sites at the ends of the links are termed *nodes*. The faces of cubes of sites are termed *plaquettes*. See Figure 3.3 for examples. The basic "particles" of the vortex model, vortex links, have vorticity vectors $\vec{\xi}_i$ lying on single bonds of the lattice and have positions \vec{x}_i at the bond centers. Vortex lines are collections of end-to-end links. Figure 3.4 shows a pair of vortex links on a (2 dimensional) lattice.

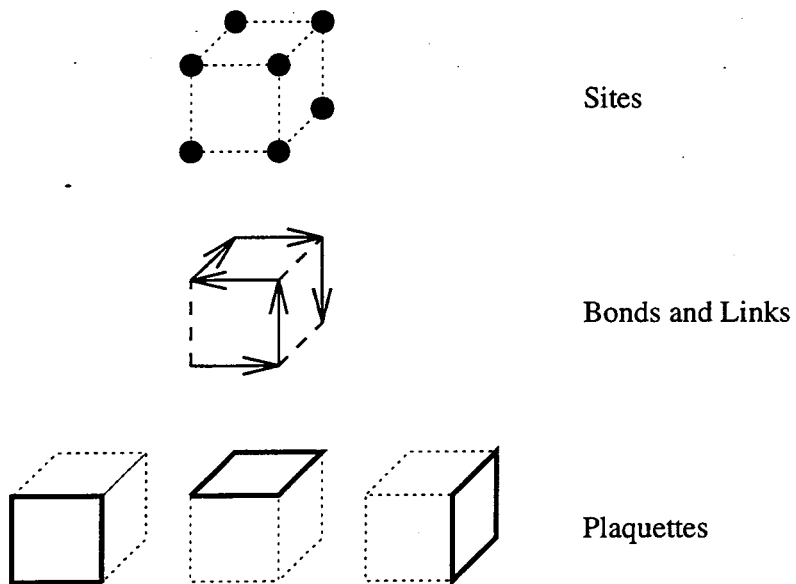


Figure 3.3: Lattice terminology

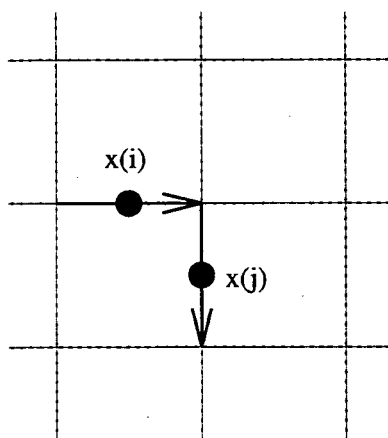
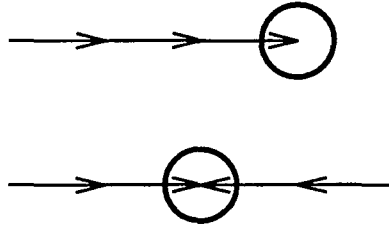
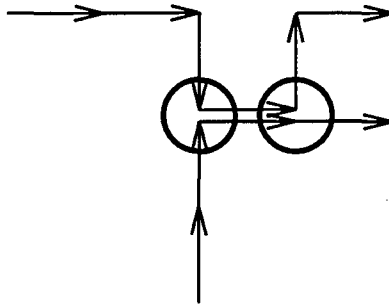


Figure 3.4: Two vortex "particles"

Figure 3.5: Vorticity constraint $\nabla \cdot \xi = 0$ Figure 3.6: Vorticity constraint $\nabla \cdot \xi = 0$

The conservation of circulation along a vortex tube in a continuous vorticity field follows from the constraint that $\nabla \cdot \vec{\xi} = 0$. In discrete vorticity configurations, the zero divergence constraint prevents vortex lines from ending or changing direction. See Figure 3.5. This implies that vortex lines form closed loops of head-to-tail links. The zero divergence constraint also prevents parallel links from sharing a lattice bond. See Figure 3.6. Vortex tubes in classical inviscid flow are material volumes which cannot intersect. This imposes an additional constraint, self-avoidance, on the lattice vortex lines. The self-avoidance condition prevents the situation in Figure 3.7 where two vortex loops touch at a lattice site. Note that the self-intersecting configuration is divergence free. A collection self-avoiding vortex loops is shown in Figure 3.8. Such collections form the basic class of discretized vortex configurations for classical flow.

An equilibrium model requires both a collection of configurations and an energy functional on the configurations. In incompressible, inviscid fluid flow, the internal energy is decoupled from the bulk kinetic energy and may be neglected. Since the kinetic energy is conserved by the time evolution of the fluid, it is an appropriate measure of the energy for formulating the thermodynamics of the system. While the kinetic energy for a fluid of

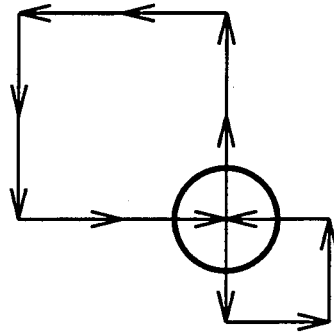


Figure 3.7: Intersecting vortex loops

Self Avoiding Loops on a 3-D Lattice

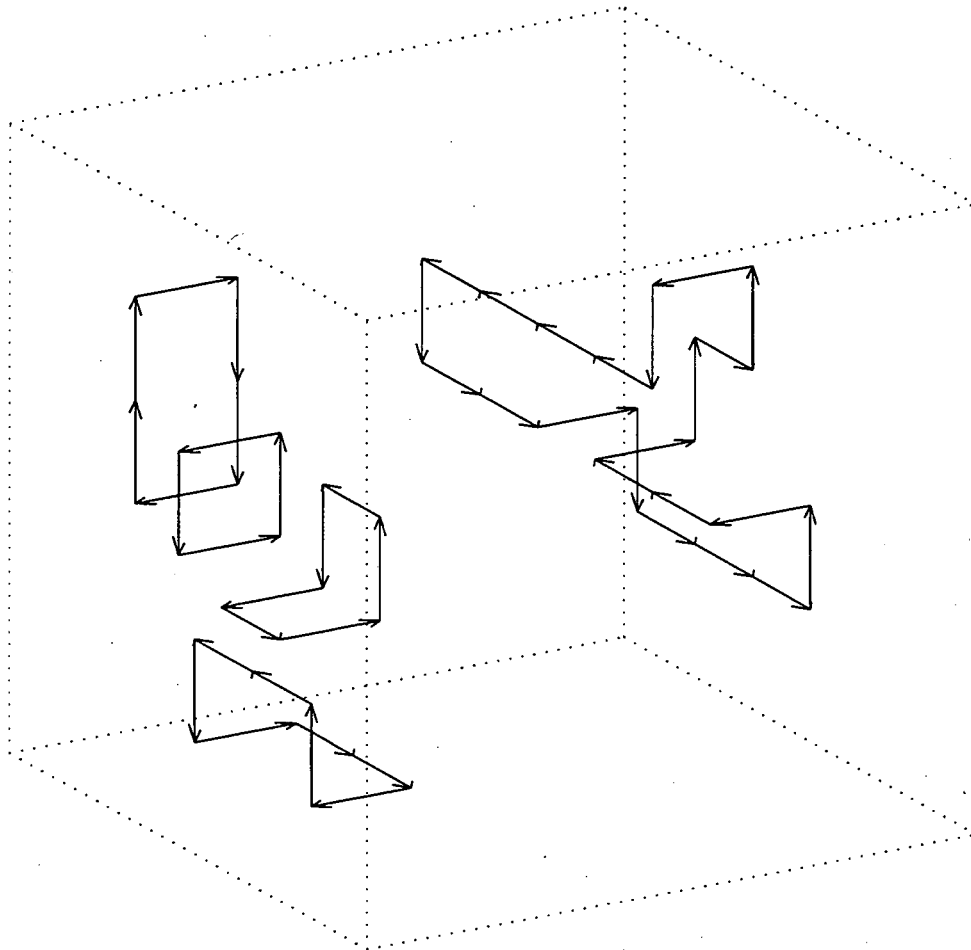


Figure 3.8:

uniform density is generally defined in terms of the velocity [91],

$$E^H = \frac{1}{2} \int |\vec{u}(\vec{x})|^2 d\vec{x}$$

integration by parts can be carried out over a suitable domain to give an expression for the kinetic energy in terms of the vorticity [91]:

$$E^H = \frac{1}{2} \int \int \vec{\xi}(\vec{x}) \cdot \vec{\xi}(\vec{y}) G(\vec{x} - \vec{y}) d\vec{x} d\vec{y}$$

where $G(\vec{x})$ is the Green function for the Laplacian on the domain. In free space,

$$G(\vec{x}) = \frac{1}{4\pi} \frac{1}{|\vec{x}|}$$

If the vorticity field is divided into a collection of thin vortex tubes $\{L_m\}$, with circulations Γ_m , the energy of the flow can be approximated by:

$$E = \frac{1}{2} \sum_m \sum_n \int_{\vec{x} \in L_m} \int_{\vec{y} \in L_n} \Gamma_m \Gamma_n G(\vec{x} - \vec{y}) d\vec{\ell}(\vec{x}) \cdot d\vec{\ell}(\vec{y})$$

up to some sort of regularization of the model as $|\vec{x} - \vec{y}| \rightarrow 0$.

In the lattice model, the integrals along the tube can be discretized into a sums over the links. Suppose there are a total of N vortex links in the configuration, This leads to a discrete energy [36]:

$$E = \left[\frac{1}{2} \sum_{i=1}^N \sum_{j \neq i} \vec{\xi}_i \cdot \vec{\xi}_j G(\vec{x}_i - \vec{x}_j) \right] + N\nu$$

The first term is a vortex-vortex interaction approximating the line integrals over distinct links (i, j) . The double integrals over the same link depend on the regularization, and will be assumed to be equal to a parameter ν , a vortex "self-energy". The total energy

$$E = E^{tot} = E^{int} + \nu N$$

is a positive quantity, but note that the interaction energy can be positive or negative. Each pair parallel of vortex links contributes a positive term to E^{int} while each anti-parallel pair contributes a negative term. This property makes the total energy strongly dependent on the geometry of the vortices. Although the Green function is long range, decaying as $1/r$ with distance, vortex links can arrange themselves so that anti-parallel pairs produce a long range cancellation or screening effect.

Consider as a final note on the class of lattice vortex models the number, N , of vortex links in the system. While the kinetic energy in a flow is preserved by the dynamics, the total length of vortex lines is not. Vortex links may be created spontaneously by stretching. One may consider, therefore, N as a free parameter, even in the “canonical” ensemble. The Gibbs weight ρ then has as variable parameters the interaction energy and the number of links in a configuration:

$$\rho = e^{-\beta E^{\text{tot}}} = e^{-\beta[E^{\text{int}} + \nu N]}$$

Although the system can exchange only energy and not links with the outside reference system, the Gibbs weight has the grand canonical form:

$$\rho = e^{-\beta E + \beta \mu N}$$

where the interaction energy E^{int} takes the place of the energy and the loop self-energy ν takes the place of the negative chemical potential.

3.2 Definition of the Self-avoiding Loops Model

The vortex model studied previously by Chorin in [32] [34] [33] [35] [36] [38] and Chorin and Akao in [43] is a dilute limit of the class of lattice vortex models defined in the previous section. The limiting model is defined by restricting configurations to those in which all the vortex links connect into a single loop: a closed self-avoiding walk. See Figure 3.9. In practice, the equilibria of an open self-avoiding walk are computed; the closure condition does not significantly effect the statistics of a system containing large number of links [63]. The single self-avoiding walk represents a collection of loops whose spacing is large compared to the individual loop size.

The single self-avoiding walk models a vortex tube which can reduce its interaction energy by folding but not by breaking apart. Indeed, in inviscid flow vortex tubes retain their connectivity [44] [41]. The presence of even a small viscosity, however, allows nearby anti-parallel vortices to reconnect. [41] [94]. This process allows a sharply folded vortex tube to smooth itself by shedding vortex loops [37] [38] [40]. Chorin proposes vortex reconnection as a mechanism for preserving the infinite temperature “polymeric” state in turbulent vortex filaments [41] [40].

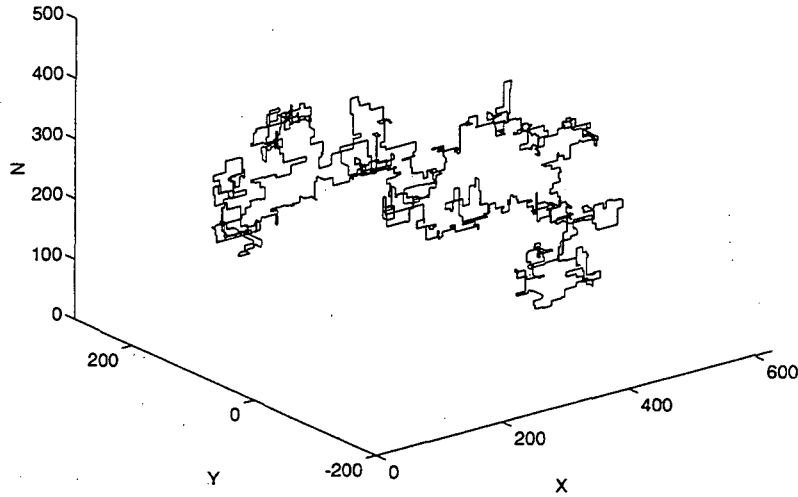


Figure 3.9: Single self-avoiding walk

The lattice model studied in this thesis allows a dense collection of vortex loops having arbitrary connectivity in a periodic volume. The model can thus manifest the equilibrium effects of vortex loops breaking apart or joining together. The model is also able to explore the equilibrium interactions between loops whose separation is of the order of the individual loop size. Finally, by enclosing the collection in a fixed volume and allowing the number of vortex links N to vary, the model can simulate density related effects in vortex equilibria. While the single self-avoiding walk computations were of a fixed- N ensemble, the number of links in the self-avoiding loops model may be allowed to come to equilibrium under the Gibbs weight:

$$\rho = e^{-\beta E^{int} - \beta \nu N}$$

In this manner the effect of the inverse temperature β and the loop self-energy ν on the equilibrium density can be exhibited.

The system simulated in this thesis will be referred to as the *self-avoiding loops system* to distinguish it from the single-loop self-avoiding walk system. Allowable vortex configurations in the self-avoiding loops model consist of arbitrary collections of vortex loops in a three dimensional periodic volume. The periodic boundary conditions are employed to reduce edge effects on the domain walls. See Figure 3.10 for a sample configuration over one

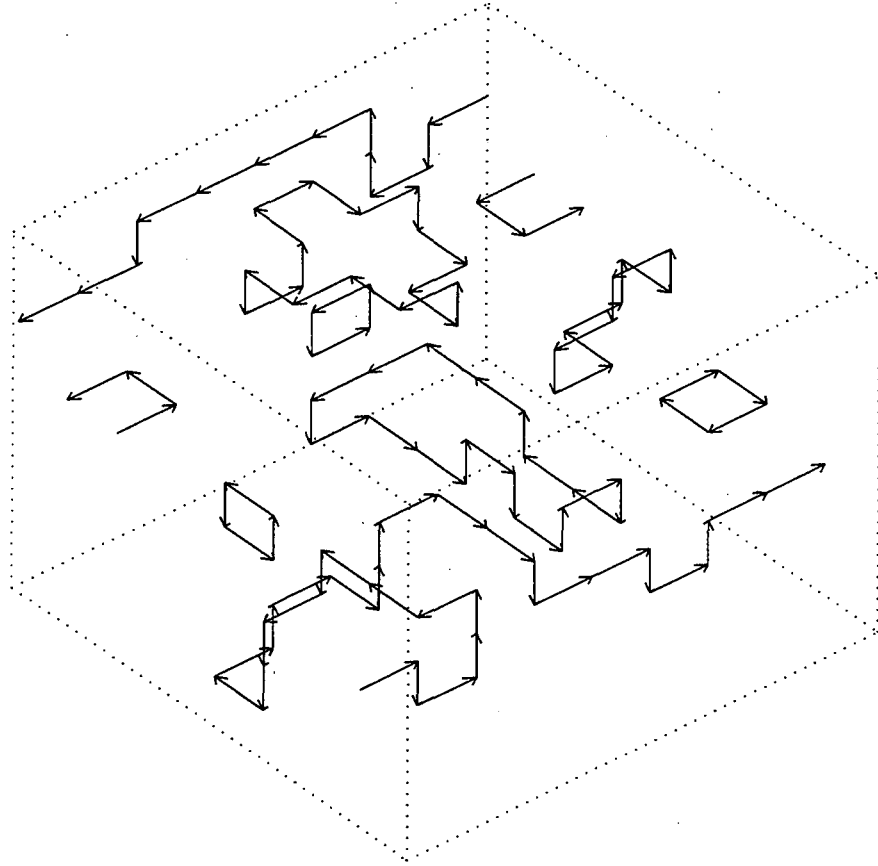


Figure 3.10: Self-avoiding loops configuration

period. A vortex loop can “end” on the boundary of the domain by exiting and re-entering on the other side. If the periodic copies of the configuration are combined on an infinite lattice, though, vortex loops always remain connected and the zero divergence condition is satisfied.

The Green function for the Laplacian is calculated for a cubic region with periodic boundary conditions. The Lamb integral for the hydrodynamic kinetic energy on a periodic cube is the energy of the fluid in one period. It follows that the discretized energy is the energy in the cubic domain. The use of a periodic boundary also imposes a consistency condition on the vorticity, namely that the sum of the vorticity in the domain must be zero in order for the energy to be finite [1] [79].

$$\sum_{i=1}^N \vec{\xi}_i = 0$$

Each link in a particular direction must have a corresponding anti-parallel link somewhere in the domain.

The self-avoidance and connectivity ($\nabla \cdot \vec{\xi} = 0$) constraints on vortex links are local. The consistency condition for the energy constrains the directions of vortex links but not their connectivity pattern. Figure 3.11 represents in light of these constraints possible vortex loop behaviors in two dimensions. The figure shows four connected loops on an 8×8 periodic lattice; they are labeled $\{ A, B, C, D \}$. The boundary of the periodic domain is marked by a dotted line, and vortices belonging to other periods are drawn with dashes. Loop B is a single closed loop, and loop A is closed when the periodicity of the lattice is taken into account. The sum of the vortex links in each of loops A and B is zero. Loops C and D, however, form infinite lines through the periodically copied lattice. The vortex links in loop C which are contained in the period sum to $(0, 8, 0)$. The consistency constraint is still satisfied, however, since the vortex links in loop D sum to $(0, -8, 0)$. Hence the total sum of $\vec{\xi}_i$ over all the vortex links in the period is zero.

Let the length of a period in the cubic domain be L , and let the lattice step size be h . The domain $[0, L) \times [0, L) \times [0, L)$ thus contains $(L/h)^3$ lattice sites in a volume $V = L^3$.

The interaction energy in a configuration c of N vortex links is:

$$E^{int}(c) = \frac{1}{2} \sum_{i=1}^N \sum_{j \neq i} \vec{\xi}_i \cdot \vec{\xi}_j G(\vec{x}_i - \vec{x}_j)$$

Each vortex has length h (the lattice step size) and thus strength $|\vec{\xi}_i| = \Gamma h = h$. The Green function for Laplacian on the domain approximates the free-space Green function as $L \rightarrow \infty$:

$$G(\vec{x}) \approx \frac{1}{4\pi} \frac{1}{|\vec{x}|} \text{ for } |\vec{x}| \ll L$$

The total energy is given by :

$$E^{tot} = E^{int} + \nu N$$

where $\nu = h\epsilon$ for some fixed filament self-energy per unit length ϵ .

The computational algorithm described in Chapter 5 simulates both the variable N ensemble and the fixed N ensemble. In the former case, the Gibbs weight for a configuration c having $N(c)$ vortex links is:

$$\rho(c) = e^{-\beta E^{int}(c) - \beta \nu N(c)}$$

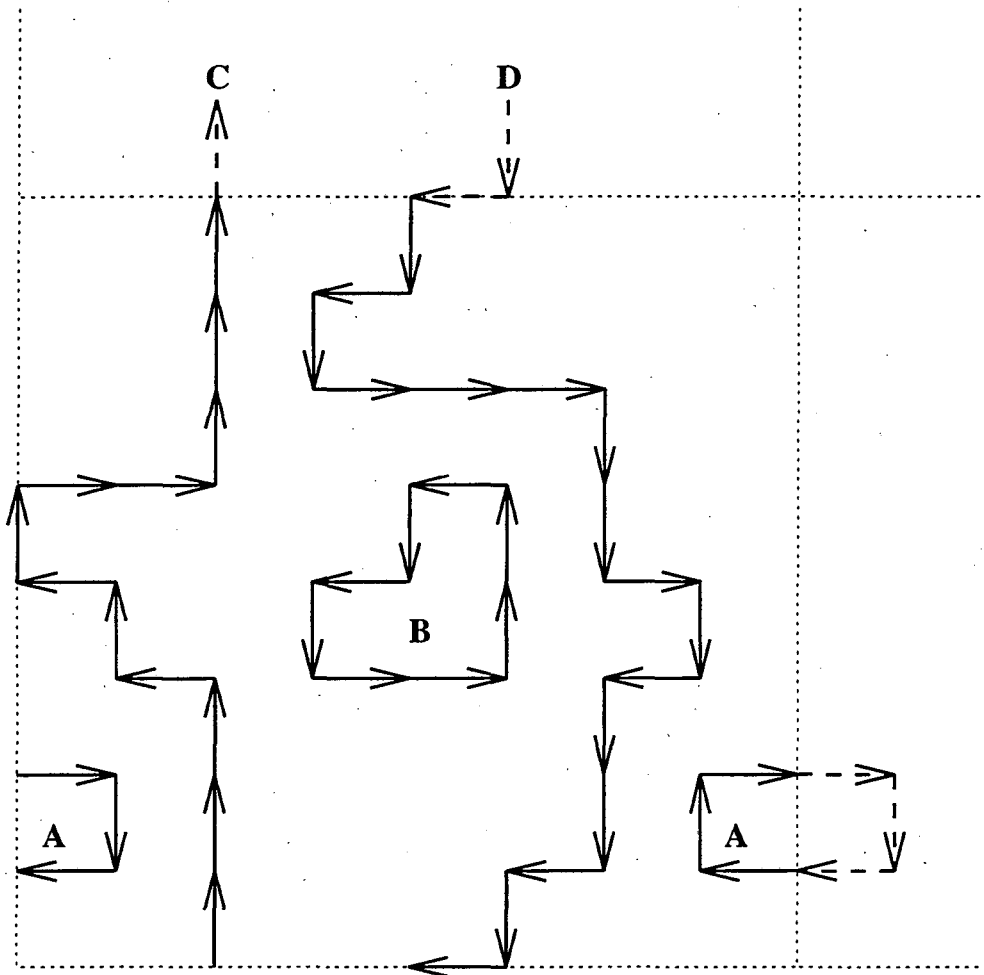


Figure 3.11: Periodic vortices

In the latter case, the self energy term νN is a fixed constant which is irrelevant to the equilibrium. In this ensemble, the Gibbs weight reduces to:

$$\rho(c) = e^{-\beta E^{int}(c)}$$

The interaction energy E^{int} , total energy E^{tot} , and number of vortex links N are extrinsic quantities which grow with the period volume $V = L^3$. A pair of intrinsic quantities are defined as follows. The interaction energy density is given by,

$$\mathcal{E} = E^{int}/V$$

while the vortex line density (or just density) is,

$$\mathcal{D} = Nh/V$$

I also wish to characterize the size of a loop in the periodic setting. I define the *extent* of a loop having k links in the period to be the smallest cube needed to enclose the loop when it is followed for k steps, even across periodic boundaries. Consider the four loops { A, B, C, D } in Figure 3.11. Starting anywhere on loop A and moving 6 steps traces out a 1×2 loop with extent 2. Loop B also fits in a 2×2 cube and has extent 2. Loop C has 12 links in the period; following it for 12 steps forms an unclosed walk which fits in an 8×2 box. The extent of loop C is thus 8. Loop D likewise traces a walk which fits in an 8×4 box and has extent 8.

It is possible to consider a threshold on the extents of the loops in a configuration to define an observable $\text{Perc}(c)$ of a configuration c as follows:

$$\text{Perc}(c) = \begin{cases} 1 & \text{if any loop of } c \text{ has extent } \geq L \\ 0 & \text{otherwise} \end{cases}$$

If none of the loops of c have extent at least L , then $\text{Perc}(c) = 0$, but if at least one loop has extent greater than or equal to L then $\text{Perc}(c) = 1$. The notation reflects the concept of *percolation*, which will be reviewed in Section 3.4. The percolation observable is used to define an order parameter, the percolation probability:

$$\mathcal{P} = \langle \text{Perc} \rangle = \frac{1}{Z} \int_{c \in \mathcal{C}} \text{Perc}(c) \rho(c) dc$$

This completes the description of the self-avoiding loops model. A similar system, the vortex form of the XY model, is described in the next section.

3.3 The XY Model and the Lambda Transition

The lattice vorticity models discussed in Section 3.1 are derived from a discretization of classical flow. Vortex like physics is also observed in quantum mechanical systems such as superfluid flow in liquid helium and resistanceless electric currents in superconductors [121] [139] [140]. While the physics of superconductors is of greater practical interest than the physics of liquid helium, the superconducting behavior is more complicated than superfluidity. Since there is still much about superfluid helium that is not well understood, it is practical to study superfluidity. The lessons learned can then be applied to the more difficult superconducting case.

As liquid helium is cooled, it undergoes a phase transition at which non-dissipative superfluid currents begin to appear [139]. The transition is called the *lambda transition* after the lambda-like appearance of the specific heat curve as a function of temperature. The transition is a continuous [64], (sometimes called second order) phase transition in which the energy is continuous at the critical temperature but in which the specific heat has a cusp [96]. The order parameter for this transition is the superfluid mass fraction [139]. At zero temperature, all the helium atoms can move together in a supercurrent; the superfluid mass fraction is one. As the fluid is heated, however, the proportion of the atoms moving in the supercurrent drops. The remaining atoms can only flow with resistance as in a classical fluid. The mass associated with superfluid behavior is known as the superfluid component, while the remaining mass is known as the normal component. At the critical temperature, the superfluid mass fraction goes to zero and resistanceless currents no longer exist. The helium liquid above the lambda transition behaves as a normal, classical fluid with nonzero viscosity and energy dissipation.

The lambda transition has been conjectured by Onsager [115] and by Feynman [59] to be driven by thermally excited vortices. While resistanceless supercurrents are associated with quantum mechanical ordering, vortices are associated with disorder in the system [132] and can dissipate energy in the fluid [70] [141]. It is conjectured that a sparse "gas" of small vortex loops generates the normal component of the fluid below the lambda transition. Feynman suggested that vortices become larger and more numerous as the critical temperature is approached, until a tangle of infinite vortices destroys remaining superfluid currents at the lambda transition [59]. Physical experiments on the behavior of mechanically excited vortex lines in ^4He [52] [117] support the connection between vortex

turbulence and the breakdown of superfluid behavior. Study of the thermal equilibria of vortex systems may explain the behavior of thermally excited vortices. This can improve understanding of the physics of the lambda transition and the breakdown of resistanceless electric currents in superconductors.

One wishes to develop a lattice model in vorticity variables for superfluid helium. The lattice vortex models discussed in the previous sections, 3.1 and 3.2, were derived using knowledge of vorticity evolution in classical incompressible flow. The evolution of vorticity in liquid helium, however, is not fully understood. Superfluid vortices interact with other excitations, such as second sound waves, in a complex manner [70] [141] [21]. While vortices in superfluid helium are known to possess quantized circulation [51] [147] and are thus in most situations distinct physical entities, the behavior at vortex-vortex intersections is controversial [20]. Theoretical work on quantum vortices in complex fields [114] [27] is beginning to address these issues. Nevertheless, it is uncertain from these considerations if helium vortices are self-avoiding, as are classical vortices. Superfluid vortices can also be created both by thermal and by mechanical effects. The derivation of a thermodynamic equilibrium model directly from the vortex properties is therefore problematic.

In this thesis I circumvent these difficulties by considering a simplified lattice model for superfluid helium: the XY model. The XY model is believed to represent the configurational and energetic properties of superfluid helium [113], but disregards complex dynamical issues. It admits a vortex description in both an intuitive [73] [88] and in a rigorous manner [128]. This section discusses the XY model in its native spin and in its vortex forms. Theoretical descriptions of the phase transition in the XY model which is analogous to the superfluid lambda transition are reviewed. The issue of lack of self-avoidance in the rigorous definition of XY vortices is discussed; this distinction forms the difference between the self-avoiding loops model simulated in the thesis and the XY model. Computations which reveal vortices in the equilibrium states of the XY model are reviewed.

The XY model is a spin system in which each lattice site is occupied by a spin, \vec{S}_i , with $O(2)$ symmetry [78]: $\vec{S}_i = (\cos \theta, \sin \theta)$ for $-\pi \leq \theta < \pi$. The two-dimensional spins are believed to represent in some sense the complex quantum-mechanical wave function of the superfluid. The Hamiltonian is given by:

$$E(\{\vec{S}_i\}) = -J \sum_{\langle i,j \rangle} \vec{S}_i \cdot \vec{S}_j$$

where $\langle i, j \rangle$ denotes nearest neighbor sites. The thermodynamic Gibbs weight of a

configuration of spins $\{\vec{S}\}$ is thus:

$$\rho = e^{-\beta J \sum_{\langle i,j \rangle} \vec{S}_i \cdot \vec{S}_j}$$

The case of interest is the low temperature ferromagnetic regime, $J > 0$ and $\beta \gg 0$. At very low temperature the low energy states in which nearby spins are nearly aligned dominate the system. At higher temperatures, more disorderly configurations are allowed.

The XY model is known to have in three dimensions a continuous phase transition [93] [75] in which the energy is continuous but the specific heat has a cusp at $\beta = \beta_c$. Long range spin ordering occurs at the transition; the spontaneous magnetization

$$M = \left\langle \sum_i \vec{S}_i \right\rangle$$

is zero above the critical temperature and non-zero below. This phase transition is believed to lie in the same universality class as the superfluid lambda transition. Computations of scaling exponents [124] [130] [93] [75], while not definitive, tend to support that belief.

The ferromagnetic XY model admits stable topological excitations which can be heuristically identified with vortices in the following manner. Suppose the temperature in the system is cold enough that spins are locally almost aligned. Then the phase θ is a slowly varying function of position. Discontinuities over the $-\pi = \pi$ boundaries may be removed by allowing the phase to be multiply valued with $-\infty < \theta < \infty$. Now let \vec{u} denote a discrete gradient of the phase θ , this is a single valued function whose magnitude increases with increasing spin-spin interaction energy. The sum of \vec{u} around a closed contour of sites is analogous to a circulation, and takes integer values [88]:

$$\frac{1}{2\pi} \sum \vec{u} \cdot d\vec{l} = k, \quad k \in \{0, 1, 2, \dots\}$$

A non-zero circulation, or wrapping number, k indicates the presence of a topological defect, or "vortex" passing through the contour. These defects are stable in the sense that a small perturbation of the spins does not change the wrapping number. In three dimensions the vortices are linelike, while in two dimensions they are point vortices [128]. The configurational character of XY vortices is thus similar to that of hydrodynamic vortices. Since the circulation is stable to small oscillations of the spins, the line defects can be expected at low temperature to have a conserved circulation. This leads to a connectivity condition similar to the condition arising from $\nabla \cdot \vec{\xi} = 0$ constraint in classical flow.

Topological defects in the phase field are termed excitations because their presence places a lower bound on the energy of the system. Berezinskii [13] used variational methods to write the approximate minimum energy of the spin system in terms of the positions and strengths of vortices. Since vortices in the XY model are defined in a low temperature context, and since vortices with high wrapping number imply a much higher energy than simple vortices, one may consider only defects with unit circulation $k = \pm 1$. In this low temperature approximation, the minimum energy has the same form as the hydrodynamic energy:

$$E(\vec{\xi}) = \left[c_1 \sum_i \sum_{j \neq i} \vec{\xi}_i \cdot \vec{\xi}_j G(\vec{x}_i - \vec{x}_j) \right] + N c_2$$

where c_1, c_2 are positive constants depending on the coupling J .

While the vortex defects in the XY model have an overall configurational and energetic character similar to vortices in classical fluids, examination of the heuristically defined defects does not reveal an avoidance condition on XY vortices. Since the defects are defined only for sufficiently slowly varying spin configurations, only well separated vortices can be considered and no information is provided on properties over distances on the order of the lattice spacing. The view of vortices as topological excitations of the spin system was made rigorous, however, by Savit, et. al. in work on the duality transformation of the XY system [128] [127] [60]. Savit performed an exact transformation of the three-dimensional XY partition function into a sum over a set of one dimensional fields defined on lattice bonds. By making a low-temperature approximation and fixing an appropriate gauge, he identified the new fields with vortices of unit strength interacting through a hydrodynamic Hamiltonian. The vortices defined by this duality transformation lie on bonds of the lattice and satisfy the same connectivity constraints as do hydrodynamic vortices. The XY vortices, however, are not self-avoiding. No two XY vortices can share the same lattice bond, but two vortex lines can intersect at a single site, as shown in Figure 3.12. Whereas hydrodynamic lattice vortices are collections of closed self-avoiding walks, XY vortices are collections of closed non-repeating walks.

The only difference, therefore, between the self-avoiding loops model and the vortex form of the XY model is the avoidance condition. The physics of the two models may therefore be expected to be qualitatively similar. Experience with the self-avoidance condition in systems containing single vortex loops, however, indicates that the constraint has a significant impact on the statistics of the systems. One may expect, therefore, some

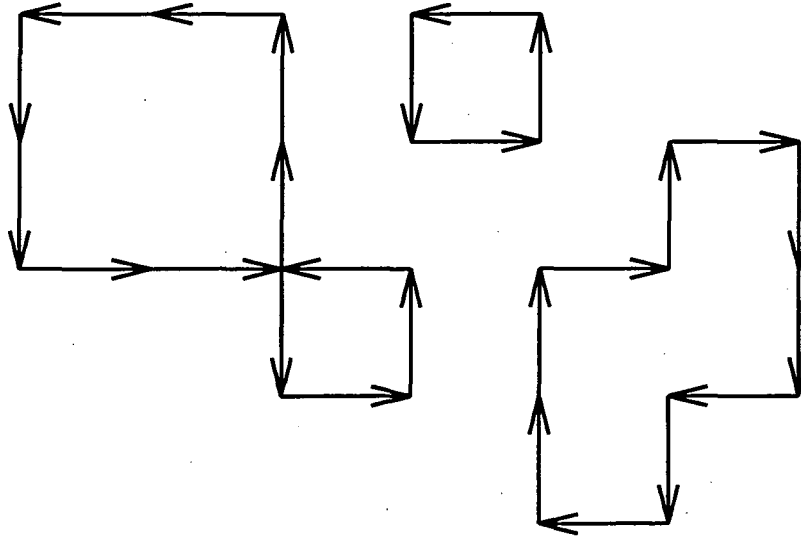


Figure 3.12: XY vortex loops

difference between the dense vortex systems with and without the self-avoidance constraint.

I note here that the self-avoidance condition places a different limit on the number of vortex links in the self-avoiding loops model than is present in the *XY* model. If we take the lattice step size $h = 1$, then there are in the domain L^3 lattice sites and $3L^3$ lattice bonds. Each lattice site in the self-avoiding model can have only one vortex link entering and one leaving. In the *XY* model, in contrast, three vortex links can enter a site and three can leave; thus filling all the bonds terminating at the site. The *XY* model therefore allows configurations with three times the number of vortex links as can exist in the self-avoiding loops model. The reader should be aware that vortex density is thus defined differently in *XY* calculations [53] [86] [85] [39] [42] than in the self-avoiding loops model studied in this thesis.

The *XY* model, which displays a continuous phase transition, transforms into a vortex system. One would like a theory of the phase transition in terms of the vortex variables. Such a theory would shed light on the role that vortices play in the superfluid lambda transition. While a vortex phase transition was described in the two-dimensional *XY* model by Kosterlitz and Thouless in 1972 [88], the role of vortices in the three-dimensional transition has been controversial. Nevertheless, theories and observations of vortices in superfluid helium have fueled interest in a vortex variable study of the three-dimensional *XY* model [127] [128] [143] [144] [145] [130] [131] [29] [86] [85].

The two dimensional *XY* model differs from the three dimensional *XY* model

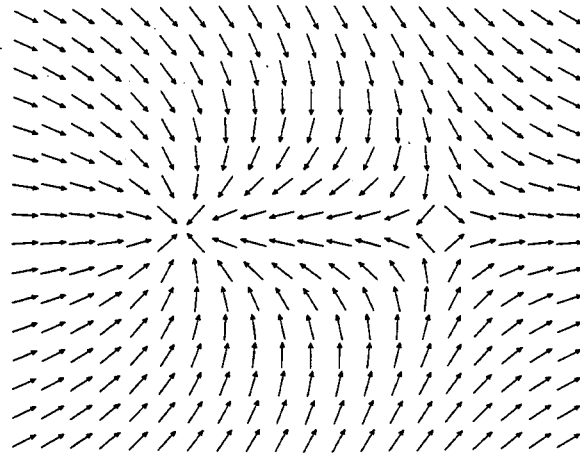


Figure 3.13: Vortex pair in the XY model

in that there can be no spontaneous magnetization or long range spin order at nonzero temperatures [76] [106] [105]. Kosterlitz and Thouless, however, described an infinite order phase transition in which the vortex behavior changes dramatically at a critical temperature. Below the transition, vortices are bound in anti-parallel pairs. Above the transition, the pairs disassociate into a plasma of free vortices.

Vortices in two dimensions are pointlike, with vorticity of positive or negative sign. Consider an anti-parallel vortex pair with separation R . The spin configuration corresponding to such a pair is given in Figure 3.13. The energy of a lone pair of anti-parallel vortices is approximately $\log(R/a)$ where a is a “core size” parameter on the order of the lattice spacing h into which the self-energy term is absorbed.

At low enough temperature, the likelihood of a lone vortex pair of separation R existing in the system decreases sharply with the separation distance. While a small pair can be excited with relatively little energy compared to the entropy of creating the pair, a large pair is too costly in energy to be frequently excited. Kosterlitz and Thouless realized, however, that small pairs can act like dipole charges to produce a screening effect and reduce the energy required to excite a large pair. They constructed a real-space renormalization treatment, the K-T renormalization, which gives the following characterization of the two-dimensional vortex unbinding transition [88] [87] [78]. A dipole gas of vortex pairs having separations less than a length R produces a dielectric screening effect which reduces the energy of a large vortex pair by a factor $\chi(R)$. The K-T renormalization calculates the density of vortex pairs with separations $R + \delta R$ by considering the entropy change of adding

such a pair to the system balanced against the screened energy required to excite the pair. The new screening effect $\chi(R + \delta R)$ is then calculated from the density of vortex pairs with separation $R + \delta R$. By integrating this system as $R \rightarrow \infty$, Kosterlitz and Thouless found that below a critical temperature the screened energy of a vortex pair of separation R scales as $\log(R)$ as $R \rightarrow \infty$. At the critical temperature, however, the screened energy of a vortex pair approaches a constant as $R \rightarrow \infty$. At the critical temperature, infinitely separated vortex pairs, free vortices, appear in the system.

Because of the geometric complexity of 3D vortex loops, as opposed to point vortices in 2D, the K-T renormalization argument cannot be simply extended to three dimensions. Nevertheless, there is great interest in a vortex theory of the ordering transition in the three-dimensional XY model. Such a theory is desirable in order to shed light on the role vortices play in the bulk superfluid lambda transition. A number of authors accordingly have considered a K-T like renormalization for vortices in the three-dimensional XY model [127] [128] [143] [144] [145] [130] [131] [29]. The theories follow the Kosterlitz-Thouless treatment for the two-dimensional system in that they consider the energetic and entropic balance of adding a single large vortex loop to the system. A critical temperature is sought, below which large loops are improbable and above which arbitrarily large vortex loops are possible. The probability of adding a large loop to the system can be increased by taking into account screening effects which reduce the energy of the loop.

Savit suggested in his papers on the dual transform of the XY model [127] [128] that if the interaction energy term in

$$E(\vec{\xi}) = \left[c_1 \sum_i \sum_{j \neq i} \vec{\xi}_i \cdot \vec{\xi}_j G(\vec{x}_i - \vec{x}_j) \right] + N c_2$$

could be ignored, a simple energy/entropy argument would indicate the presence of a phase transition from low vortex density to high density. The entropy of a closed walk of N links should scale as qN where q is a constant depending on the lattice coordination number [63] [98]. If the energy of a loop is simply the self-energy term $c_2 N$, then there should be a transition at $\beta_c = c_2/q$ at which vortex lines can grow to infinite length.

Wiegel studied the interaction energies of smooth vortex rings in three dimensions [143]. Following hydrodynamic treatments of vortex rings [91], he showed that the interaction energy of a smooth loop is $\log(R/a)$ where R is the radius of the ring and a is a small cutoff size.

Williams devised a K-T like renormalization procedure to incorporate the screening effects of small vortex rings on the energy of larger vortex rings [144] [145] [146]. The theory showed the existence of a transition at which infinite size vortex loops could be excited, although the critical exponents did not match the known values for the XY model, indicating that some aspects of the physics were not completely represented.

Shenoy in 1989 augmented the Williams procedure with the recognition of another kind of screening [130] [131] [29]. The Williams renormalization accounted for the effects of small polarizable loops upon the energy of large loops, but assumed that all loops were smooth. Shenoy supposed that the large loops might be crinkled along their length, so that screening along the folds of a single loop could occur. Shenoy used this idea to make a divergent-core ansatz where a_c was a screening length which diverged at the critical temperature. He then wrote the loop energy as $\log(R/a_c)$ and gave a renormalization treatment in which the energy per vortex link was logarithmic with R below the critical temperature where a_c remained finite, but was constant with R at and above β_c . The Shenoy renormalization recovers critical exponents quite close to the expected values.

One desires a theory of screening among the folds of a single vortex loop which can justify the divergent core ansatz. Shenoy suggested that the structure of a large vortex loop was that of a self-avoiding walk, and employed in the renormalization analysis the scaling behavior of the unweighted self-avoiding walk [130] [63]. Chorin [34] [33] [36] [43] [38] investigated the vortex-vortex interactions of a lone single self-avoiding walk. He found a phase transition at infinite temperature, $\beta_c = 0$, separating smooth vortices from fractal vortices [38]. At temperatures hotter than the critical temperature, $\beta < 0$, vortex lines are smooth one-dimensional objects with interaction energy scaling with $\log(N)$, where N is the number of vortex links. At the critical temperature, $\beta_c = 0$, vortices are fractal objects with interaction energy scaling linearly with N . See for example Figure 3.9. All possible self-avoiding walks are equally probable at infinite temperature; this state is termed the *polymeric* state for its relation to the configurations of dilute polymer chains [63]. The fractal dimension of the polymeric self-avoiding walk is

$$D = 1/\theta_{SAW} \approx 1.72$$

where $\theta_{SAW} \approx 0.58$ is the Flory exponent [63] [98].

The fractal dimension of XY vortices at criticality is of interest because the interaction energy per link has been shown to depend on the fractal dimension [43] [38]. Numerical

work by Chorin on self-avoiding walks with link interaction energies demonstrates that lone walks crumple up at low temperature and have higher fractal dimension than do polymeric self-avoiding walks. Increasing the fractal dimension allows different parts of the walk to screen long-range interactions more effectively, and reduces the interaction energy.

There are a number of differences between the polymeric self-avoiding walk and XY vortices at the critical temperature. The XY vortices are not self-avoiding, although a collection of XY vortices could be (not necessarily uniquely) split at the self intersection points into a number of self-avoiding vortices. The XY vortices are also fairly dense at the transition, so the statistics of large loops may be affected by the presence of other loops. Finally, the XY system favors configurations of low energy at the critical temperature. The structure of XY vortices may be expected to differ from the structure of infinite temperature self-avoiding walks. It is possible, however, that interactions among different XY vortex loops are such that the large vortices are screened at the critical temperature so that they have structure similar to infinite temperature walks. The critical exponents derived from the Shenoy renormalization do not depend strongly on the fractal dimension of vortex loops, so small deviations from the polymeric behavior may not be important.

Numerical simulations of the three-dimensional XY model have been carried out in the spin variables [75] [53] [86] [85]. Epiney [53] examined XY vortices in the spin configurations near the phase transition. Since the self-intersecting vortices do not form well-defined loops, Epiney employed a random method of resolving connectivity at multiply visited sites. The computations indicated that vortices indeed become more numerous as temperature is increased, and form a dense tangle of links at the phase transition. Epiney also measured the fractal dimension of individual loops at criticality. The computations indicated an inverse fractal dimension of $1/D \approx 0.5$, which is the value associated with random walks of independent unconstrained steps. The result is in contrast to the Shenoy suggestion of the behavior of vortex loops at criticality: that the inverse fractal dimension would be the Flory exponent $1/D \approx 0.58$. Nevertheless, Epiney's computation provides some of the first numerical evidence linking vortices to the phase transition in the three-dimensional XY model.

Kohring and Shrock [85] [86] investigated numerically the role which vortex excitations play in the transition by adding a term to the Hamiltonian which enhances or

suppresses vortices,

$$E(\{\vec{S}\}) = -J \sum_{\langle i,j \rangle} \vec{S}_i \cdot \vec{S}_j + \mu N$$

where N is the number of vortex links in the spin configuration. The computations showed that suppressing vortices suppresses the transition and allows the system to remain ordered, with nonzero spontaneous magnetization, at higher temperatures. If configurations containing vortex links are sufficiently suppressed, the system remains ordered even at infinite temperature. This behavior indicates that vortex defects are necessary to destroy the spin order at the XY phase transition.

While it appears that vortices indeed drive the order/disorder phase transition in the three-dimensional XY model as well as the K-T transition in the two-dimensional model, a number of questions remain open. Screening effects along the path of a large loop are important, but the structure of large XY vortices at criticality is unclear. There is conflicting evidence on the effects of low temperature and vortex self-intersection on the fractal dimension of the vortices. A three-dimensional computation in vorticity variables alone has not been performed for the self-intersecting vortices, although Chorin [42] has run a $2\frac{1}{2}$ -dimensional model. The vortex system simulated in the thesis differs from the vortex form of the XY model in that the self-avoidance constraint is imposed on the vortices, but is otherwise identical to the vortex form of the XY model. The results from the thesis model can cast light on the impact of the self-avoidance constraint on the vortex equilibria.

3.4 Percolation and the Lambda Transition

The success of the Kosterlitz-Thouless renormalization in the two-dimensional XY model has greatly influenced the vortex theories of the three-dimensional phase transition. Kosterlitz-Thouless type theories concentrate on a single large loop; the effects of smaller loops are incorporated in a screening effect. The renormalization proceeds by estimating the screened energy per vortex link and the entropy per vortex link of a large loop, the energy and entropy are used in turn to estimate the energy screening on even larger loops. These estimates are not without difficulties; the preceding section notes that the energy of a vortex loop may depend delicately on the loop structure. Entropy estimates also have uncertainty; for instance the number of ways of placing a large self-avoiding walk on the lattice may depend on the density of sites occupied by other vortices [63]. While K-T

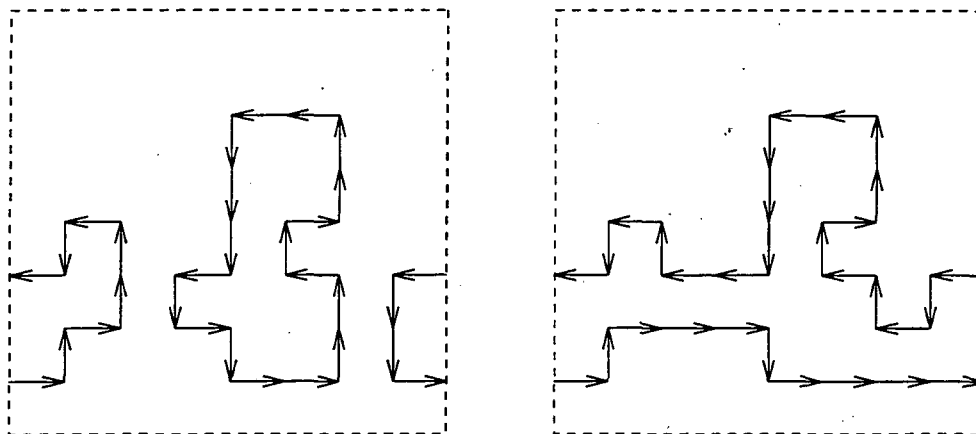


Figure 3.14: Percolation achieved by reconnections

style renormalization theories for the three dimensional XY model have provided valuable insights, it is desirable to have also other vorticity based theories of the transition.

The algorithmic progression in the K-T renormalization from smaller to larger vortex loops leads to a dynamic viewpoint of creating an infinite loop through a stretching process. An alternate viewpoint which considers vortex loops of all sizes simultaneously has been raised by Chorin [39] [42]. The appearance of an infinite loop in the system may be thought of as a *percolation* phenomenon. Percolation theory [134] [66] studies how particles in a system coalesce into large structures; an infinite system is said to have percolated if it contains an infinitely extended connected structure. The name “percolation” refers to random defects in a porous media connecting in a continuous path that allows liquid to flow through the material. Percolation is a type of critical phenomena which exhibits scaling properties and for which renormalization techniques exist [134] [66] [81] [50] [126] [2] [118] [82]. The use of percolation ideas may therefore lead to a vorticity variable renormalization distinct from the Kosterlitz-Thouless style approach.

Instead of taking the view of stretching a vortex loop to infinite size, one can consider reconnecting existing small loops into an infinite structure. Figure 3.14 shows two small loops on a periodic domain being reconnected to form a pair of loops each extending through the whole domain. Chorin has performed percolation computations and analysis for an XY model in which the vortices of a three-dimensional spin field are restricted to a plane [39] [42]. This leads to configurations such as the one shown in Figure 3.12. The $2\frac{1}{2}$ -dimensional model exhibits percolation phase transitions which can be identified with

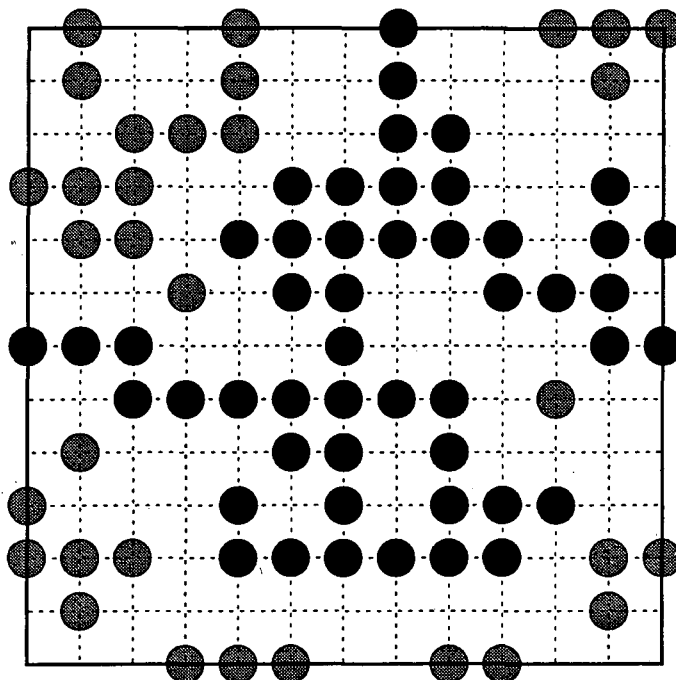


Figure 3.15: Site percolation cluster

the lambda transition.

Many percolation models display a particular sort of finite size scaling [134]. Consider the following simple model. Take a square lattice of side L and a parameter q , $0 \leq q \leq 1$. Create random configurations by taking each site independently and occupying the site with a particle with probability q , or leaving it empty with probability $1 - q$. Consider a configuration to have percolated if a connected set of nearest-neighbor occupied sites links opposite boundaries of the lattice. Such a connected cluster which is of the size of the lattice is called a percolating cluster. The black particles in Figure 3.15 are a percolating cluster. Let the percolation probability \mathcal{P} be the probability, taken over all random configurations, of a percolating cluster existing. If $q = 0$ the lattice is empty and $\mathcal{P} = 0$. If $q = 1$ the lattice is fully occupied and $\mathcal{P} = 1$. The percolation probability \mathcal{P} rises smoothly as a function of q from zero to one. As the lattice size L is increased, the function $\mathcal{P}_L(q)$ shifts more abruptly from zero to one. In the limit $L \rightarrow \infty$, the function $\mathcal{P}_L(q)$ approximates a step function at a critical value of the parameter q . See Figure 3.16 for a view of percolation finite size scaling. The percolation probability is shown as a function of the occupation probability q for square lattices of sizes $L = \{8, 16, 64\}$. Refer to Stauffer

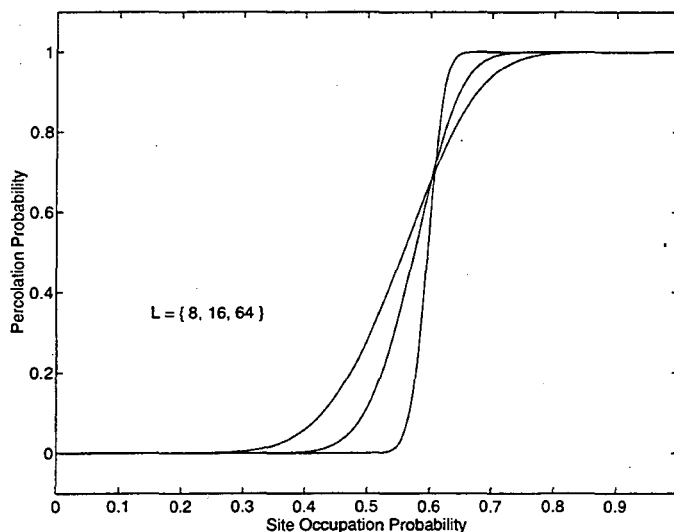


Figure 3.16: Percolation probability finite size scaling

[134] and Grimmett [66] for the general mathematical structure of the percolation problem.

The observable $\text{Perc}(c)$ of the self-avoiding loops configurations indicates if a percolating vortex loop exists in the configuration c . See Section 3.2. The percolation probability \mathcal{P} is thus the average value of $\text{Perc}(c)$. A connected loop is a percolating loop if it has extent at least the domain length. Loops C and D in figure 3.11 are percolating loops. Note that a loop can close in on itself and still be a percolating loop; the vortex loop in Figure 3.17 has extent 7 on a 6×6 domain. The finite size behavior of \mathcal{P} as a function of temperature can be used to test for the existence of a percolation threshold in the self-avoiding loops system.

As a final note on percolation in vortex systems, observe that the percolation view does not immediately appear to apply to the two-dimensional system of point vortices. Vortices in two-dimensional flow, or in the two-dimensional XY model, extend out of the plane of the flow and thus never span the domain horizontally. The percolation concept does apply to the two-dimensional systems, however, with the use of a magnetization representation [22] [48]. In magnetization variables an anti-parallel vortex pair is a connected string of tiny vortex dipoles, or “magnets”. It is therefore possible that a percolation renormalization would apply to the vortex disassociation transition in two dimensions as well as in three dimensions.

Note that while the self-avoiding loops model is defined by relaxing a constraint in the single self-avoiding walk model, it does not in practice subsume studies of the single walk. In fluid turbulence vortex reconnection may not be in equilibrium with vortex folding; the self-avoiding loops model may allow more breakup of vortex loops than is physically appropriate. Perhaps more importantly, the length scale for which computational simulations are feasible is significantly smaller in the dense collection of loops than in the single vortex model. The largest self-avoiding loops systems examined for this thesis were in a 16^3 volume containing about 2000 vortex links. The same number of links forms a single vortex walk stretching over perhaps 100 lattice sites. Since some vortex statistics can converge quite slowly with the linear dimension, the single walk model allows much greater accuracy from a comparable amount of computational work.

Regarding the XY model, the self-avoiding loops system provides a purely vorticity variable simulation of a system which differs from the vortex form of the XY model only by the imposition of the self-avoidance constraint. The thesis study is relevant to the theories of the phase transition in the XY model in several ways. It is first a verification that a phase transition can occur in a vortex system without other spin excitations. Although the low temperature approximations which produce the vortex form of the XY model [128] imply that non-vortical spin-waves are not important to the critical behavior, the thesis presents the first fully three dimensional computation of a dense vortex system without spin effects. The transition character in the self-avoiding loops model can support theories of a vortex driven lambda transition in liquid helium. The thesis model secondly brings into focus the effect of self-avoidance on the geometry of XY vortex loops at the phase transition. The scaling behavior of infinite temperature self-avoiding walks has been assumed, in producing a successful renormalization theory, to hold for low temperature XY vortices also [130] [29]. A comparison of the self-avoiding loops properties to simulations which revealed XY vortices [53] [86] [85] can clarify the importance of self-avoidance in theories of the XY transition. Finally, the self-avoiding loops simulation can produce information helpful to the search for renormalization treatments of the lambda transition besides the Kosterlitz-Thouless methods.

The simulation of the self-avoiding loops system can help answer questions on the nature of turbulence in classical fluids and on the breakdown of quantum order at the superfluid lambda transition. It can also expand the general understanding of vortex equilibria to aid in the study of more diverse defect systems.

Chapter 4

Numerical Thermodynamic Simulation

4.1 Monte Carlo Simulation

Monte Carlo methods provide an efficient numerical means of estimating thermodynamic averages. The name refers to games of chance at Monte Carlo; the methods compute estimates by averaging over a sequence of random trials. This section reviews the basics of Monte Carlo simulation and of Metropolis sampling; the implementation for the vortex model will follow later. A summary of Monte Carlo simulation from a physical point of view may be found in Itzykson & Drouffe [78]. A broad review of the subject complete with recent developments is contained in Binder [15] [16] [17] [18]. Several mathematical details are covered in Hammersley and Handscomb [74], and in Chung [46].

For simplicity of notation consider a discrete set of configurations \mathcal{C} . Sums then replace integrals in the expressions for the thermodynamic average and the partition function:

$$\langle A \rangle = \frac{1}{Z} \sum_{c \in \mathcal{C}} A(c) \rho(c)$$

$$Z = \sum_{c \in \mathcal{C}} \rho(c)$$

The thermodynamic sum could in theory be calculated by enumerating the configurations in \mathcal{C} , but since the cardinality of \mathcal{C} grows exponentially with the system size this is impractical. The essence of the Monte-Carlo method is the replacement of the sum over all configurations

with a sum over a random sequence of configurations $\{c_1, c_2, c_3, \dots, c_M\}$. The sequence is generated such that the eventual probability of each configuration c appearing is equal to its equilibrium weight $\rho(c)/\mathcal{Z}$. The estimate for the average of A is then:

$$\langle A \rangle^{(M)} = \frac{1}{M} \sum_{k=1}^M A(c_k)$$

If the configurations c_k are chosen independently with the distribution function ρ/\mathcal{Z} , then each $A(c_k)$ is an independent random variable with mean $\langle A \rangle$ and variance:

$$\text{Var}(A) = \langle A^2 \rangle - \langle A \rangle^2$$

Hence

$$\langle A \rangle = \lim_{M \rightarrow \infty} \langle A \rangle^{(M)} = \lim_{M \rightarrow \infty} \frac{1}{M} \sum_{k=1}^M A(c_k)$$

with the expected error decreasing as $1/\sqrt{M}$:

$$|\langle A \rangle - \langle A \rangle^{(M)}| < \frac{\sqrt{P_c \text{Var}(A)}}{\sqrt{M}} \text{ with probability } P_c$$

This algorithm is known as static Monte Carlo. In practice, it is difficult to generate independent configurations with the correct distribution. Rather, a Markov chain is computed by using the configuration c_i to generate the next configuration c_{i+1} . Successive steps in the chain are thus correlated, but under a reasonable set of conditions listed below, the occupation-time distribution in the chain still converges to the equilibrium probability ρ/\mathcal{Z} . Although the statistical errors in this dynamic Monte Carlo process decay more slowly than in static Monte Carlo simulation, practical algorithms for thermodynamic systems are almost exclusively of the dynamic variety.

The sequence $\{c_1, c_2, c_3, \dots, c_M\}$ has the Markov property if the conditional probability $P(c_i \Rightarrow c_{i+1})$ to choose a particular c_{i+1} as the next configuration given the current configuration c_i is independent of the chain's history $\{c_1, \dots, c_{i-1}\}$. The set of probabilities $\{P(c \Rightarrow c')\}_{c \in \mathcal{C}, c' \in \mathcal{C}}$ thus defines the Markov process. The following two conditions on the transition probabilities are sufficient, but not necessary, to assure that the limiting probability of c appearing in the chain is $\rho(c)/\mathcal{Z}$. [74]

Ergodicity: For each pair $\{c, c'\}$ there exists a finite number k and a sequence

$\{c = c_0, c_1, c_2, \dots, c_k = c'\}$ such that

$$\prod_{i=0}^{k-1} P(c_i \Rightarrow c_{i+1}) > 0$$

This states that every configuration should be eventually reachable from every other configuration.

Detailed Balance: For each pair $\{c, c'\}$,

$$\frac{P(c \Rightarrow c')}{P(c' \Rightarrow c)} = \frac{\rho(c')/\mathcal{Z}}{\rho(c)/\mathcal{Z}} = \frac{\rho(c')}{\rho(c)}$$

Although this condition may be relaxed, the symmetry proves to be extremely convenient. Furthermore, by expressing the probabilities as ratios, the need to know the partition function \mathcal{Z} is eliminated.

Note that these conditions still allow tremendous freedom in defining and implementing the Markov process. This point is emphasized in [78]. There are several known classes of algorithms which meet the conditions of ergodicity and detailed balance, but I only review Metropolis sampling in Section 4.2 and my modification to the Metropolis class in Section 5.3.

An important factor in the construction of the Markov process is its efficiency expressed in terms of the rate of convergence of the observables. While the average quantities $\langle A \rangle^{(M)}$ are guaranteed to converge to the thermodynamic average $\langle A \rangle$ in the limit $M \rightarrow \infty$, the rate of convergence can vary greatly. Convergence of dynamic Monte Carlo is typically slower than that of static Monte Carlo by a factor known as the autocorrelation time τ_A . A heuristic characterization is that the chain needs on the order of $2\tau_A$ steps in order to produce a statistically independent value for $A(c)$. The following formula for the error generally holds:

$$|\langle A \rangle - \langle A \rangle^{(M)}| \lesssim \frac{\sqrt{P_c \text{Var}(A)}}{\sqrt{M/(2\tau_A)}} \text{ with probability } P_c$$

Sokal [25] [26] has carefully characterized the autocorrelation time and has developed a number of methods to minimize the statistical error as a function of computer time. Note that the autocorrelation times for different observables may be different. A typical value for τ_A may be on the order of 100 to 100,000 steps and thus have a significant impact on the computational effort required.

In thermodynamic simulation, if the successive elements of the Markov chain differ only locally on the physical domain being modeled, the autocorrelation time increases as the domain size increases. This reflects the many steps needed to make changes all over the physical system. Furthermore if the system is being simulated near a phase transition

point, another factor known as *critical slowdown* may increase τ_A . This occurs as separated portions of the physical domain tend to become correlated. An enormous number of small changes may be needed to build and destroy these correlated structures in order reach an independent configuration.

As a final note on the efficiency of dynamic Monte Carlo, I wish to make an observation on the “generic” nature of the configurations in the Markov chain in an effective simulation. A typical Monte Carlo run may produce average values accurate to 1% after 1,000 steps of the Markov process. The configurations of such a system may contain perhaps 100 degrees of freedom. The number of possible configurations, the cardinality of \mathcal{C} , is thus on the order of $2^{100} \approx 10^{30}$! The sampled configurations in the Markov chain, therefore, are only an infinitesimal proportion of the state space \mathcal{C} . The quick convergence of the observables rests not on the fact that *each* configuration $c \in \mathcal{C}$ will be sampled in the Markov chain a number of times proportional to its weight $\rho(c)$, but on the property that the chain is a “representative” set of configurations. In a practical Monte Carlo simulation, the vast number of configurations which are not sampled should have the same statistics as the Markov chain when viewed in terms of the observables: the same energy distribution, the same density distribution, etc. Although the machinery for measuring the autocorrelation time is generally a reliable indicator of the rate of convergence, it does not in practice provide a certain bound on the error. The combined ergodicity and detailed balance conditions provide a convergence proof in the limit $M \rightarrow \infty$, but simulations are run far from this limit. Since the reliability of Monte Carlo simulation relies on the few sampled configurations having the same generic statistical properties as the system as a whole, and since this property is very difficult to prove mathematically, Monte Carlo simulations should be verified by multiple experiments and by theory, just as are physical experiments. When viewed in this light, Monte Carlo simulations are an effective experimental tool for the estimation of thermodynamic averages.

4.2 The Metropolis Method

The class of Markov processes known as Metropolis sampling methods satisfy the ergodicity and detailed balance conditions in a manner that leads to easily implemented algorithms. They separate the problem of creating a Markov chain which satisfies detailed balance into two simpler parts: transforming the configuration space and applying the

probability ρ . Metropolis methods first randomly transform the current configuration c into a candidate configuration c' which is then accepted or rejected depending on the weights $\rho(c)$, $\rho(c')$ of the current and candidate configurations.

Begin by considering a set of random transformations, $\mathcal{Q} = \{Q_\alpha\}$, and define $\pi_\alpha(c)$ as the conditional probability of performing transformation Q_α given the current configuration c . The probability should depend only on the current configuration and on the transformation Q_α so that the Markov property is retained. Denote the transformed configuration $c' = Q_\alpha(c)$; the process of creating a random candidate c' is called making a *move*. Suppose the $\{Q_\alpha\}$ and $\{\pi_\alpha\}$ satisfy versions of ergodicity and detailed balance:

Transformation Ergodicity: For each pair $\{c, c^*\}$ there exists a finite number k and a sequence of transformations $\{Q_0, Q_1, \dots, Q_{k-1}\}$ such that

$$Q_{k-1} \cdots Q_1 \cdot Q_0 c = c^*$$

with each $\pi_i(c_i) > 0$ where $c_i = Q_{i-1} \cdots Q_1 \cdot Q_0 c$ is the i th configuration visited by applying the sequence of transformations. This condition is satisfied if the transformations can change any configuration to any other configuration.

Transformation Detailed Balance: For each pair $\{c, c^*\}$, let $\{\alpha |_{Q_\alpha c = c^*}\}$ to be the set of transformations which take configuration c to configuration c^* . The transformation detailed balance condition is satisfied if:

$$\sum_{\alpha |_{Q_\alpha c = c^*}} \pi_\alpha(c) = \sum_{\alpha |_{Q_\alpha c^* = c}} \pi_\alpha(c^*)$$

This means that the probability of transforming $c \Rightarrow c^*$ is equal to the probability of transforming $c^* \Rightarrow c$. The condition is easily met if each transformation Q_α on c has an "inverse" $Q_{\alpha'}$ so that

$$Q_\alpha c = c^* \text{ and } Q_{\alpha'} c^* = c$$

with

$$\pi_\alpha(c) = \pi_{\alpha'}(c^*)$$

These conditions can be implemented by assuring that the probability of a particular transformation changing $c \Rightarrow c^*$ is equal to the probability of its inverse changing $c^* \Rightarrow c$. It is thus not necessary to enumerate all the possible ways of transforming one configuration into another in order to check the balance condition for the set of transformations, since the terms in the sums over α are pairwise equal.

Under these conditions, the chain created by choosing a transformation Q_i at the i th step and letting $c_{i+1} = Q_i c_i$ would eventually contain all configurations with equal probability. The following modification due to Metropolis [107] gives the configuration probability ρ/Z . At the i th step choose a transformation Q_i , and let

$$c_{i+1} = \begin{cases} Q_i c_i & \text{with probability } \min(1, \rho(Q_i c_i)/\rho(c_i)) \\ c_i & \text{otherwise} \end{cases}$$

This algorithm splits into a transformation step producing a candidate configuration $c' = Q_i c_i$ followed by an acceptance/rejection step. Either c' becomes new element c_{i+1} of the Markov chain or c_i is repeated. The transformation Q_i is chosen independently of the probability distribution ρ , while the acceptance step is independent of the specific transformation: depending only on the initial and candidate configurations.

Define the acceptance probability $\Theta(c, c')$ to be

$$\Theta(c, c') = \min\left(1, \frac{\rho(c')}{\rho(c)}\right)$$

Also define $\eta_\alpha(c, c')$ to be the conditional probability of choosing transformation Q_α given c and then of accepting or rejecting the candidate c' to produce the next step c' . The probability of producing the new configuration c' through the use of a transformation Q_α in a Metropolis step starting from configuration c is thus:

$$\eta_\alpha(c, c') = \pi_\alpha(c) \Theta(c, c')$$

The complete transformation probability in the Markov process is given by:

$$P(c \Rightarrow c') = \sum_{\alpha | Q_\alpha c = c'} \eta_\alpha(c, c') = \sum_{\alpha | Q_\alpha c = c'} \pi_\alpha(c) \min(1, \rho(c')/\rho(c))$$

with

$$P(c' \Rightarrow c) = \sum_{\alpha' | Q_{\alpha'} c' = c} \pi_{\alpha'}(c') \min(1, \rho(c)/\rho(c'))$$

In the detailed balance ratio for the Markov process, the summations are equal by transformation detailed balance and cancel:

$$\frac{P(c \Rightarrow c')}{P(c' \Rightarrow c)} = \frac{\min(1, \rho(c')/\rho(c))}{\min(1, \rho(c)/\rho(c'))}$$

Now, since if $\rho(c')/\rho(c) > 1$ then $\rho(c)/\rho(c') < 1$, either the numerator or the denominator will be one, so the min's drop out to give the detailed balance result:

$$\frac{P(c \Rightarrow c')}{P(c' \Rightarrow c)} = \left\{ \begin{array}{ll} \frac{\rho(c')/\rho(c)}{1} & \text{if } \rho(c') \leq \rho(c) \\ \frac{1}{\rho(c)/\rho(c')} & \text{if } \rho(c') > \rho(c) \end{array} \right\} = \frac{\rho(c')}{\rho(c)}$$

4.3 Histogram Sampling

Monte Carlo simulation generates a sequence of configurations with the property that the probability of each configuration c occurring in the sequence converges to its equilibrium probability $\rho(c)/\mathcal{Z}$ at temperature β . The simplest manner of utilizing this sequence is to store average values. Storing more information on the chain, however, can increase the efficiency of the method when thermodynamic averages are desired for a range of temperatures. The idea is to record information beyond the mean values of the probability density of observables. Note that numerically recording the probability of each configuration is an unmanageable task, but one can estimate the probabilities of suitable groups of configurations. Consider the Gibbs weight in the canonical ensemble:

$$\rho(c) = e^{-\beta E(c)}$$

Since the weight assigned to each configuration depends on the energy of the configuration, a natural way of grouping the configurations is by their energies E . A method taking statistics over configurations grouped by their energies allows the representation of the average observable quantities as *functions* of β , rather than as averages at a single value of β . Techniques using this idea are referred to as histogram methods because the programs store a histogram of the configurations over energy bins. The algorithm employed in this thesis implements the histogram in two dimensions (E, N) for the grand-canonical Gibbs weight,

$$\rho(c) = e^{-\beta E(c) + \beta \mu N(c)}$$

where $E(c)$ is the energy of the configuration c and $N(c)$ is the number of particles in the system. The following discussion is limited to one-dimensional histograms in E for the sake of clarity. The ideas presented here generalize simply to the two dimensional case.

Histogram type algorithms have seen occasional use for many years [3], [89], [12], [18] but have recently been revived and improved by Ferrenberg and Swendsen [57], [56]. The methods have been used to determine observables as functions of temperature in order to calculate critical exponents. They have also been employed to estimate thermodynamic quantities such as the free energy differences which are not average observables [12]. Histogram methods are used in this thesis to paint broad-brush pictures of phase space, to locate critical temperatures, and to monitor and diagnose the performance of the Monte Carlo algorithms. This section reviews the histogram idea in some detail, and gives an analysis of the error which highlights some assumptions which are unclear in the literature. My observations and comments on the implementation of histogram methods are included at the end of this section; I point out some difficulties and suggest improvements.

4.3.1 The Density of States

The histogram methodology represents observables as functions of temperature by separating the β dependent weight from the portion of the thermodynamic average which is dependent on the configurations. The probability distribution of the energies of the configurations, known in physics literature as the density of states [92], lies at the heart of the method. Consider the expression for the canonical ensemble average of an observable A at temperature β :

$$\langle A \rangle_{\beta} = \frac{1}{Z_{\beta}} \int_{c \in \mathcal{C}} A(c) e^{-\beta E(c)} dc$$

The density of states can be introduced by rewriting the expression for the average of A as follows. Begin with the partition function Z_{β} :

$$Z_{\beta} = \int_{c \in \mathcal{C}} e^{-\beta E(c)} dc$$

Split this expression by integrating first over configurations with a particular energy, and then integrating over the energies:

$$Z_{\beta} = \int_E \int_{E(c)=E} e^{-\beta E} dc dE$$

Now since the exponential no longer depends on the configurations, pull it outside of the integral dc :

$$Z_{\beta} = \int_E e^{-\beta E} \left[\int_{E(c)=E} dc \right] dE$$

The temperature independent integral is the density of states: the measure of the set $\{c \in \mathcal{C} | E(c)=E\}$

$$D(E) = \int_{E(c)=E} dc$$

This density of states condenses the information from the complicated configuration space into a function of the energy. Hence the process of factoring the integral for $\langle A \rangle_\beta$ has separated the temperature dependent from the configuration dependent portions of the integral:

$$Z_\beta = \int_E e^{-\beta E} D(E) dE$$

Now proceed with the numerator in the ensemble average:

$$\langle A \rangle_\beta = \frac{1}{Z_\beta} \int_{c \in \mathcal{C}} e^{-\beta E(c)} A(c) dc = \frac{1}{Z_\beta} \int_E e^{-\beta E} \left[\int_{E(c)=E} A(c) dc \right] dE$$

Introducing the density of states in the numerator and the denominator yields:

$$\langle A \rangle_\beta = \frac{1}{Z_\beta} \int_E e^{-\beta E} D(E) \left\{ \frac{\int_{E(c)=E} A(c) dc}{D(E)} \right\} dE$$

where the quantity in braces $\{ \}$ is the *micro-canonical average* of A . Let $\bar{A}(E)$ be the micro-canonical average of A in a restricted ensemble containing the configurations of energy $E(c) = E$:

$$\bar{A}(E) = \frac{\int_{E(c)=E} A(c) dc}{\int_{E(c)=E} dc}$$

Making this substitution gives:

$$\langle A \rangle_\beta = \frac{1}{Z_\beta} \int_E e^{-\beta E} D(E) \bar{A}(E) dE$$

Using the previously derived formula for Z_β yields a complete expression for the canonical ensemble average in terms of one dimensional integrals over E , with the integrals over configurations written as functions of E :

$$\langle A \rangle_\beta = \frac{\int_E e^{-\beta E} D(E) \bar{A}(E) dE}{\int_E e^{-\beta E} D(E) dE}$$

The dependence of $\langle A \rangle_\beta$ on β can be better related to the Monte-Carlo algorithm by writing the probability density for the energy E at temperature β in terms of the density of states:

$$P_\beta(E) = \frac{1}{Z_\beta} e^{-\beta E} D(E)$$

Then

$$\langle A \rangle_{\beta} = \int_E P_{\beta}(E) \bar{A}(E) dE$$

where $P_{\beta}(E)$ is a normalized probability distribution:

$$\int_E P_{\beta}(E) dE = 1$$

Suppose the probability distribution $P_{\beta^*}(E)$ is known at a reference temperature β^* ; then $D(E)$ can be expressed in terms of the known probability:

$$D(E) = Z_{\beta^*} e^{\beta^* E} P_{\beta^*}(E)$$

Now substitute into the formula for $P_{\beta}(E)$:

$$P_{\beta}(E) = \frac{Z_{\beta^*}}{Z_{\beta}} e^{(\beta^* - \beta)E} P_{\beta^*}(E)$$

The ratio of the partition functions can also be calculated from $P_{\beta^*}(E)$:

$$Z_{\beta} = \int_E e^{-\beta E} D(E) dE = Z_{\beta^*} \int_E e^{(\beta^* - \beta)E} P_{\beta^*}(E) dE$$

so finally:

$$P_{\beta}(E) = \frac{e^{(\beta^* - \beta)E} P_{\beta^*}(E)}{\int_{E'} e^{(\beta^* - \beta)E'} P_{\beta^*}(E') dE'}$$

Although combining terms into the probability function $P_{\beta}(E)$ may seem to complicate matters, it re-expresses the quantities $D(E)$ and Z_{β} in terms of a probability depending on their ratio. Furthermore, the shift in $P(E)$ from temperature β^* to β is simply the multiplication of the old probability density by an exponential weight and the normalization of the result; the integral over E' in the denominator of the expression for the shifted probability enforces the condition that $\int_E P_{\beta}(E) dE = 1$. See Figures 4.1, 4.2, 4.3 for a schematic view of this process on a numerical representation of $P_{\beta^*}(E)$. Note the change in axis in Figure 4.2 The notation for shifting the probability densities can be simplified somewhat by introducing the free energy at a temperature β :

$$F_{\beta} = -\log(Z_{\beta})$$

A factor of β is dropped in the definition of the free energy to reduce notational complexity.

Then

$$\frac{Z_{\beta^*}}{Z_{\beta}} = e^{F_{\beta} - F_{\beta^*}}$$

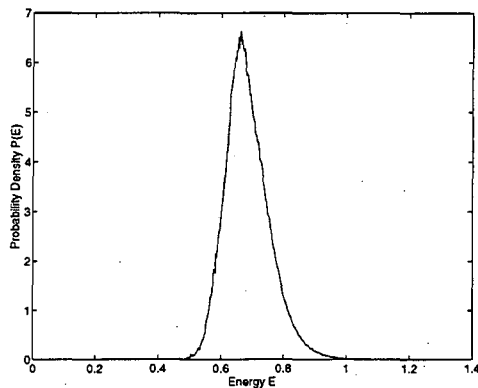


Figure 4.1: $P_{\beta^*}(E)$

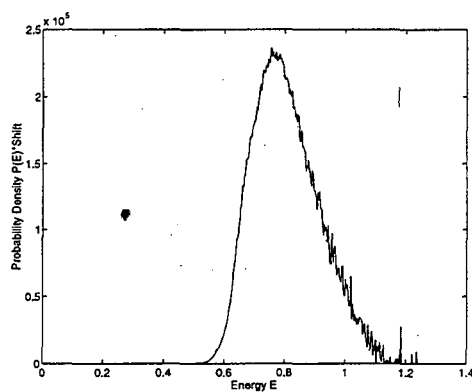


Figure 4.2: $P_{\beta^*}(E) \exp((\beta^* - \beta)E)$

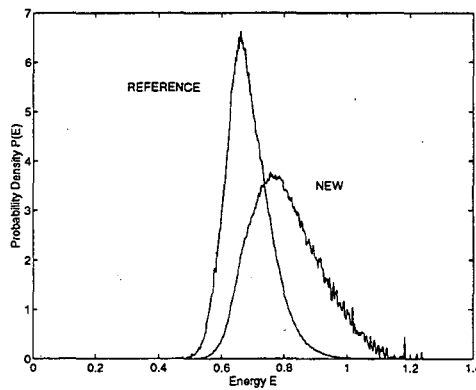


Figure 4.3: $P_{\beta^*}(E)$ and $P_{\beta}(E)$

The new probability can be written as the reference probability multiplied by exponential shifts:

$$P_{\beta}(E) = e^{F_{\beta} - F_{\beta^*}} e^{-(\beta - \beta^*)E} P_{\beta^*}(E)$$

4.3.2 The Histogram Monte-Carlo Method

Assuming that integration over the reals can be easily performed, the remaining numerical task is the estimation of the probability density and of the desired micro-canonical averages as functions of E . Recall that for a Markov process generating the sequence $\{c_1, c_2, \dots, c_M\}$ of configurations, the derived sequence $\{E(c_1), E(c_2), \dots, E(c_M)\}$ is assumed to have the probability distribution $P_{\beta}(E)$ in the limit $M \rightarrow \infty$. Thus the probability may be approximated by a histogram of the sequence of energies. Consider a Monte Carlo run of M configurations at temperature β^* . Break up the energy line into a collection of intervals of width ΔE centered at values E_i . Over the course of the run record a histogram $n(E_i)$ of the number of configurations which fall in each energy bin. Also keep track of the sum of $A(c)$ of configurations in each bin E_i in a list of accumulators $A_{acc}(E_i)$. This process gives the following estimates:

$$P_{\beta^*}(E_i) \Delta E \approx p_{\beta^*}(E_i) = \frac{n(E_i)}{M}$$

$$\bar{A}(E_i) \approx \bar{a}(E_i) = \frac{A_{acc}(E_i)}{n(E_i)}$$

Note that the normalization condition is automatically satisfied at β^* with $p_{\beta^*}(E_i)$ absorbing the factor of ΔE :

$$\sum_{E_i} p_{\beta^*}(E_i) = \frac{\sum_{E_i} n(E_i)}{M} = 1$$

The thermodynamic average may be approximated as follows:

$$\langle A \rangle_{\beta^*} = \int_E P_{\beta^*}(E) \bar{A}(E) dE \approx \sum_{E_i} p_{\beta^*}(E_i) \bar{a}(E_i)$$

Note that for $\beta = \beta^*$, this simply reduces to the standard Monte Carlo average:

$$\langle A \rangle_{\beta^*} \approx \sum_{E_i} \frac{n(E_i)}{M} \frac{A_{acc}(E_i)}{n(E_i)} = \frac{1}{M} \sum_{E_i} A_{acc}(E_i) = \frac{1}{M} \sum_{k=1}^M A(c_k)$$

The average may be approximated at $\beta \neq \beta^*$ by shifting the probability density to $p_\beta(E_i)$ and reapplying the summation formula for $\langle A \rangle_\beta$ in terms of $p_\beta(E)$:

$$\langle A \rangle_\beta \approx \sum_{E_i} p_\beta(E_i) \bar{a}(E_i)$$

where

$$p_\beta(E_i) = \frac{e^{(\beta^* - \beta)E_i} p_{\beta^*}(E_i)}{\sum_{E'_i} e^{(\beta^* - \beta)E'_i} p_{\beta^*}(E'_i)}$$

I will henceforth simplify the notation by dropping the subscript on E_i . Summations over E will implicitly be over the bins of the histogram. Now define the numerical free energy shift by :

$$\Delta F_\beta^{\beta^*} = -\log \left(\sum_E e^{(\beta^* - \beta)E} p_{\beta^*}(E) \right)$$

The shifted numerical probability density can then be written in terms of exponential weights:

$$p_\beta(E) = e^{\Delta F_\beta^{\beta^*}} e^{-(\beta - \beta^*)E} p_{\beta^*}(E)$$

If the numerical probability density $p_{\beta^*}(E)$ were equal to the true probability density $P_{\beta^*}(E)\Delta E$, then the following equivalence would hold up to numerical integration errors:

$$e^{\Delta F_\beta^{\beta^*}} = e^{-\Delta F_\beta^{\beta^*}} = e^{F_\beta - F_{\beta^*}} = \frac{Z_{\beta^*}}{Z_\beta}$$

In reality, free energy estimation can be one of the most troublesome aspects of the histogram method. The free energy difference may be viewed as the log of the average value of the function $g(E) = e^{(\beta^* - \beta)E}$ at temperature β^* . This function, however, can vary by many orders of magnitude over the support of the numerical distribution $p_{\beta^*}(E)$. Furthermore, over the range of the histogram, g takes its maximum value in the tail of the numerical distribution where statistical error is greatest. As a rule of thumb, the free energy difference can be considered accurate if the product of the probability $p_\beta(E)$ and the shift $e^{(\beta^* - \beta)E}$ falls off at the tails of the distribution. The peak of the shifted distribution is then within the sampling range of the original histogram. If this is not the case, and the new probability maximum is at the end of the original histogram, then the accuracy of the free energy difference and of the shifted probability are highly suspect. If the peak of the true shifted probability $P_\beta(E)$ lies outside of the histogram sampling range, then the histogram provides no information on the shifted distribution. The shifted numerical probability $p_\beta(E)$ and the free energy estimate $\Delta F_\beta^{\beta^*}$ will then be wildly inaccurate. Figure 4.4 is a representation

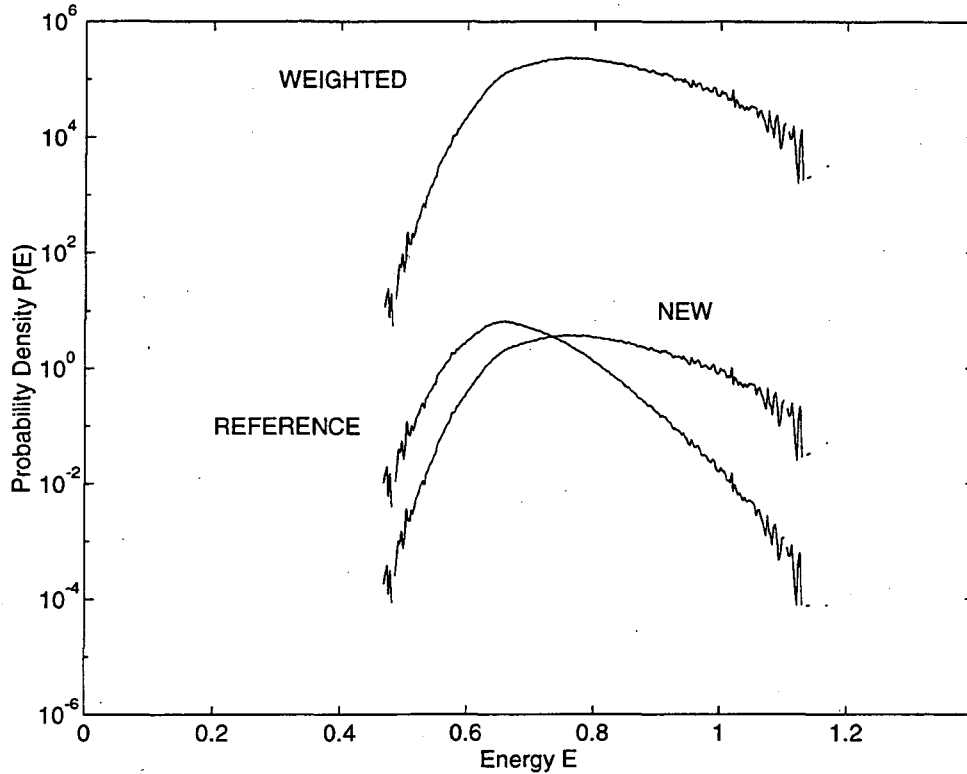
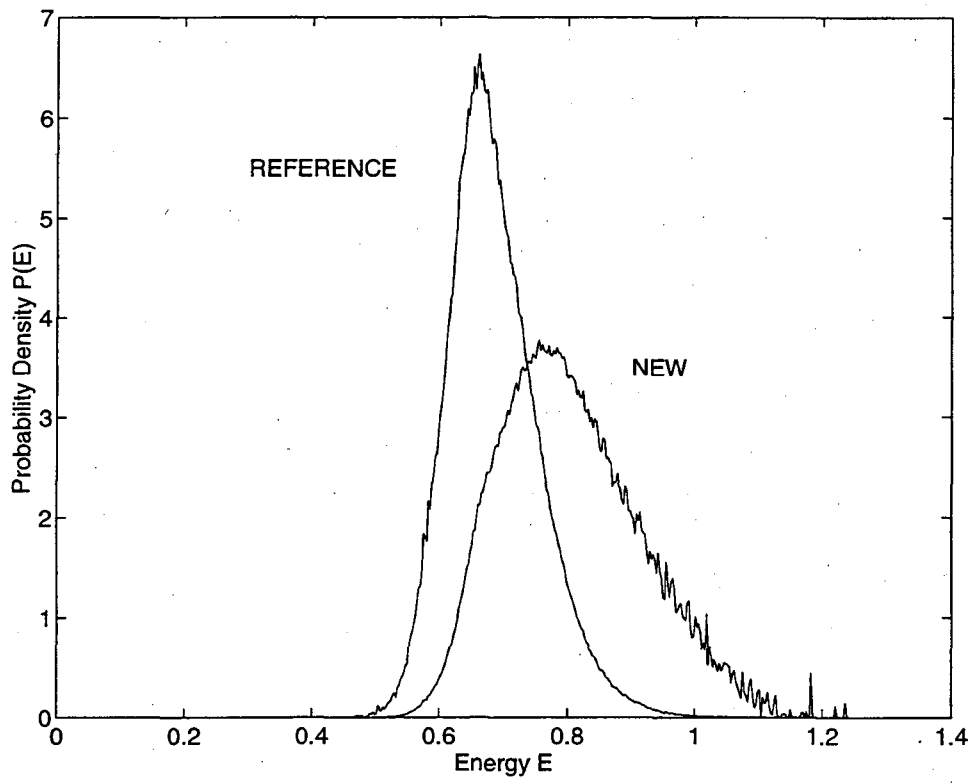


Figure 4.4: Logarithmic view of probabilities

of the shift shown in Figures 4.1, 4.2, and 4.3, on a single logarithmic axis. In terms of the logarithm of $p_\beta(E)$, the application of temperature shift is a the addition of the linear function $(\beta^* - \beta)E$, while the vertical distance between the weighted and new distributions is the free energy difference $\Delta F_\beta^{\beta^*}$. Note the evidence of statistical error near the tails of the distribution. Too large a temperature shift would significantly weight one tail and generate significant error in the observable averages. This error is already visible on the right side of the new distribution $p_\beta(E)$ in Figure 4.5, the reproduction of Figure 4.3.

4.3.3 Combining Multiple Histograms

Since a single Monte Carlo run can only provide accurate results over a limited region of temperature values, the need to make multiple runs at a set of temperatures spanning a region of interest still exists. Several questions then arise when using the his-

Figure 4.5: $P_{\beta^*}(E)$ and $P_{\beta}(E)$

togram method to compute average values over a large range of temperatures: for instance, how should the different values from various runs be interpreted? The numerical probability distribution functions from two Monte Carlo runs will differ when shifted to the same temperature because of statistical error. One desires a method of interpolation between histograms taken at different reference temperatures; furthermore, one would like to benefit from the sampling of multiple runs when histograms taken in the runs overlap. Ferrenberg and Swendsen have devised a method of making a weighted average of a collection of histograms which optimizes the use of computational effort and provides a smooth interpolation between reference histograms [57]. This section gives what I believe is an equivalent presentation of their method, along with my observations on its use and performance.

Suppose a sequence of R Monte Carlo simulations is performed at temperatures $\beta^1, \beta^2, \dots, \beta^R$, containing M^1, M^2, \dots, M^R trials respectively. Let $n^1(E), n^2(E), \dots, n^R(E)$ be the histograms collected over the same energy bins for the set of runs. Similarly, let $A_{acc}^1(E), A_{acc}^2(E), \dots, A_{acc}^R(E)$ be accumulators of the observable A for trials falling in bin E . The micro-canonical averages can simply be computed over all the runs for each bin E :

$$\bar{a}(E) = \frac{\sum_{i=1}^R A_{acc}^i(E)}{\sum_{i=1}^R n^i(E)} \approx \bar{A}(E)$$

Now for each run we have an approximation to the probability density at temperature β^i ,

$$p^i(E) = p_{\beta^i}^i(E) = \frac{n^i(E)}{M^i} \approx P_{\beta^i}(E)\Delta E$$

each of which may be shifted to any new temperature β :

$$p_{\beta}^i(E) = e^{\Delta F_{\beta}^{\beta^i}} e^{-(\beta - \beta^i)E} p^i(E)$$

The Ferrenberg-Swendsen algorithm constructs an approximation $p_{\beta}(E)$ as the weighted sum over the shifted approximations, where the weights $w^i(E)$ can be optimized for each energy bin E :

$$p_{\beta}(E) = \sum_{i=1}^R w^i(E) p_{\beta}^i(E)$$

where for each E :

$$\sum_{i=1}^R w^i(E) = 1$$

The following analysis gives an optimal choice for the weights. In order to minimize the error in each entry of $p_{\beta}(E)$, we should minimize the statistical variance $\text{Var}(p_{\beta}(E))$. Suppose

for the moment that the variance $V^i(E)$ of each component is known:

$$V^i(E) = \text{Var} \left(p_{\beta}^i(E) \right)$$

Then the quantity to minimize is:

$$\text{Var} \left(p_{\beta}(E) \right) = \sum_i \left(w^i \right)^2 V^i(E)$$

The method of Lagrange Multipliers gives the weights:

$$\begin{aligned} \frac{\partial}{\partial w^j} \left[\sum_i \left(w^i \right)^2 V^i - \lambda \left(\sum_i w^i - 1 \right) \right] &= 0 \\ 2 w^j V^j - \lambda &= 0 \\ w^j &\propto \frac{1}{V^j} \end{aligned}$$

So the weight of the i th density at each energy should be inversely proportional to the variance of the density. The normalization condition can be satisfied by taking:

$$w^i(E) = \frac{1/\text{Var} \left(p_{\beta}^i(E) \right)}{\sum_j 1/\text{Var} \left(p_{\beta}^j(E) \right)}$$

The following analysis, which duplicates the Ferrenberg/Swendsen result, assumes that the free energy differences $\Delta F_{\beta}^{\beta^i}$ can be computed *without statistical error*. In that case:

$$\text{Var} \left(p_{\beta}^i(E) \right) = \text{Var} \left(e^{\Delta F_{\beta}^{\beta^i}} e^{-(\beta-\beta^i)E} p^i(E) \right) = \left[e^{\Delta F_{\beta}^{\beta^i}} e^{-(\beta-\beta^i)E} \right]^2 \text{Var} \left(p^i(E) \right)$$

Now take the following model for the statistical error in $p^i(E)$. Associate with each trial k of the i th Monte Carlo run a random variable $\eta_k(E)$, which takes the following values:

$$\eta_k(E) = \begin{cases} 1 & \text{with probability } P_{\beta^i}(E)\Delta E \\ 0 & \text{otherwise} \end{cases}$$

For each trial k and each energy bin E , assume a hit in the E th histogram bin and increment $n^i(E)$ by one if $\eta_k(E) = 1$. So

$$n^i(E) = \sum_{k=1}^{M^i} \eta_k(E)$$

Now $\eta_k(E)$ has mean $\langle \eta \rangle = P_{\beta^i}(E)\Delta E$ and variance

$$\text{Var}(\eta) \approx P_{\beta^i}(E)\Delta E$$

when $P_{\beta^i}(E)\Delta E \ll 1$. If all the $\eta_k(E)$ were independent for successive trials k , we would have:

$$\text{Var}(n^i(E)) = M^i P_{\beta^i}(E)\Delta E$$

The effect of correlation between trials can be estimated by multiplying with the autocorrelation time τ_E :

$$\text{Var}(n^i(E)) = M^i P_{\beta^i}(E)\Delta E (1 + 2\tau_E)$$

Since the unshifted probability is:

$$p^i(E) = \frac{n^i(E)}{M^i}$$

the variance of the unshifted probability is:

$$\text{Var}(p^i(E)) = \frac{1}{(M^i)^2} \text{Var}(n^i(E)) = \frac{1}{M^i} P_{\beta^i}(E)\Delta E (1 + 2\tau_E)$$

Thus we have an estimate for the error in each element of the i th distribution where we have neglected the constraint $\sum_E n^i(E) = M^i$ in making the model for η . If $M^i \gg n^i(E)$ for each E , however, the model should be fairly accurate.

Now return to the formula for the variance of the shifted probability distribution:

$$\text{Var}(p_{\beta}^i(E)) = \left[e^{\Delta F_{\beta}^{\beta^i}} e^{-(\beta - \beta^i)E} \right]^2 \text{Var}(p^i(E))$$

Substituting in the expression for the variance of the unshifted probability gives:

$$\text{Var}(p_{\beta}^i(E)) = \left[e^{\Delta F_{\beta}^{\beta^i}} e^{-(\beta - \beta^i)E} \right]^2 \frac{1}{M^i} P_{\beta^i}(E)\Delta E (1 + 2\tau_E)$$

It is now helpful to use the formula for $P_{\beta}(E)$, which is exact if $\Delta F_{\beta}^{\beta^i} = F_{\beta} - F_{\beta^i}$,

$$P_{\beta}(E) = e^{\Delta F_{\beta}^{\beta^i}} e^{-(\beta - \beta^i)E} P_{\beta^i}(E)$$

to move the probability from β^i to β for all i , giving:

$$\text{Var}(p_{\beta}^i(E)) = \frac{1}{M^i} \left[e^{\Delta F_{\beta}^{\beta^i}} e^{-(\beta - \beta^i)E} \right] P_{\beta}(E)\Delta E (1 + 2\tau_E)$$

Returning to the formula for the weights:

$$w^i(E) = \frac{1/\text{Var}(p_{\beta}^i(E))}{\sum_j 1/\text{Var}(p_{\beta}^j(E))}$$

we have

$$w^i(E) = \frac{M^i \left[e^{\Delta F_\beta^{\beta^i}} e^{-(\beta-\beta^i)E} \right]^{-1} [P_\beta(E)\Delta E(1+2\tau_E)]^{-1}}{\sum_j M^j \left[e^{\Delta F_\beta^{\beta^j}} e^{-(\beta-\beta^j)E} \right]^{-1} [P_\beta(E)\Delta E(1+2\tau_E)]^{-1}}$$

where the probability densities at temperature β cancel to leave:

$$w^i(E) = \frac{M^i \left[e^{\Delta F_\beta^{\beta^i}} e^{-(\beta-\beta^i)E} \right]^{-1}}{\sum_j M^j \left[e^{\Delta F_\beta^{\beta^j}} e^{-(\beta-\beta^j)E} \right]^{-1}}$$

At this point pause to consider the degenerate case where all the $\beta^i = \beta$. Then the weights reduce to:

$$w^i(E) = \frac{M^i}{\sum_j M^j}$$

The formula for the probability density approximation is:

$$p_\beta(E) = \sum_{i=1}^R w^i(E) p_\beta^i(E)$$

so

$$p_\beta(E) = \frac{\sum_i M^i p^i(E)}{\sum_j M^j} = \frac{\sum_i M^i n^i(E)/M^i}{\sum_j M^j} = \frac{\sum_i n^i(E)}{\sum_j M^j}$$

The optimal combination of the histograms into a single probability gives the same result as if the runs were concatenated in a single long Monte Carlo run of $\sum_j M^j$ trials. The optimal combination results in the equal weighting of each trial's histogram hit over all the trials in the R runs.

Now, returning to the general case of arbitrary β^i 's, we can perform simplifications on the weighted densities:

$$w^i(E) p_\beta^i(E) = \frac{M^i \left[e^{\Delta F_\beta^{\beta^i}} e^{-(\beta-\beta^i)E} \right]^{-1} \left[e^{\Delta F_\beta^{\beta^i}} e^{-(\beta-\beta^i)E} p^i(E) \right]}{\sum_j M^j \left[e^{\Delta F_\beta^{\beta^j}} e^{-(\beta-\beta^j)E} \right]^{-1}}$$

$$w^i(E) p_\beta^i(E) = \frac{M^i p^i(E)}{\sum_j M^j \left[e^{\Delta F_\beta^{\beta^j}} e^{-(\beta-\beta^j)E} \right]^{-1}} = \frac{n^i(E)}{\sum_j M^j \left[e^{\Delta F_\beta^{\beta^j}} e^{-(\beta-\beta^j)E} \right]^{-1}}$$

Taking the summation over the different runs gives the complete expression for the probability density at temperature β :

$$p_\beta(E) = \sum_{i=1}^R w^i(E) p_\beta^i(E) = \frac{\sum_i n^i(E)}{\sum_j M^j \left[e^{\Delta F_\beta^{\beta^j}} e^{-(\beta-\beta^j)E} \right]^{-1}}$$

This is an optimal expression assuming that the free energy differences are known exactly, and that the histogram bins are sufficiently populated to justify the analysis of the variance of $n^i(E)$. The question remains of how to compute the free energy differences:

$$\{\Delta F_{\beta}^{\beta^j} \approx F_{\beta} - F_{\beta^j}\}$$

Experience with the single-histogram method indicates that the free energy calculated by shifting a single histogram is only accurate over a short range. Ferrenberg and Swendsen proposed to replace the estimate for the free energy difference,

$$\Delta F_{\beta}^{\beta^i} = -\log \left(\sum_E e^{(\beta^i - \beta)E} p^i(E) \right)$$

with its inverse calculated from the combined probability density $p_{\beta}(E)$, since the combined probability should be accurate over the entire range of temperatures.

$$-\Delta F_{\beta^i}^{\beta} = \log \left(\sum_E e^{(\beta - \beta^i)E} p_{\beta}(E) \right)$$

Since the combined probability density depends in turn on the free energy differences, the Ferrenberg-Swendsen method computes a set of free energy differences,

$$\{\Delta F^i \approx F_{\beta} - F_{\beta^i}\}_{i=1, \dots, R}$$

which are a fixed point of the following set of $R + 1$ equations:

$$\Delta F^i = \log \left(\sum_E e^{(\beta - \beta^i)E} p_{\beta}(E) \right) \text{ for } i = 1, \dots, R$$

$$p_{\beta}(E) = \frac{\sum_i n^i(E)}{\sum_j M^j e^{-\Delta F^j} e^{(\beta - \beta^j)E}}$$

The fixed point can in most cases be computed by iteration of the above set of free energy and probability equations, with initial free energy guesses ΔF_0^i computed from the individual histograms:

$$\Delta F_0^i = -\Delta F_{\beta}^{\beta^i} = \log \left(\sum_E e^{(\beta^i - \beta)E} p^i(E) \right)$$

This method has the convenient property that the fixed point $\{\Delta F^i\}$ is independent of the temperature β . It is therefore possible to apply the fixed point iteration once with a reference temperature $\beta = \beta^*$ to obtain a reference probability $p_{\beta^*}(E)$. The observable

averages can then be computed as functions of β by using the single histogram method to shift the combined reference probability $p_{\beta^*}(E)$ to each temperature β . The computational effort required for this shifting is modest compared to the original Monte Carlo runs, since it involves only multiplying the histogram by an exponential function and dividing by the new sum to normalize the new probability.

Figures 4.6, 4.7, 4.8, 4.9, show the results of combining three Monte Carlo runs into a single probability distribution. Figure 4.6 shows the three raw histograms $n^i(E)$ before shifting. Figure 4.7 shows on logarithmic axes the three shifted histograms adjusted with the fixed point free energy differences:

$$p_{\beta}^i(E) = e^{\Delta F^i} e^{-(\beta-\beta^i)E} p^i(E)$$

Figure 4.8 is a logarithmic view of the combined probability distribution: $p_{\beta}(E)$. Note that it is smooth over a larger range than any of the individual distributions. Figure 4.9 shows the new distribution on standard axes.

The fixed-point method does not always produce appropriate free energies, however. Indeed, it is possible that the fixed point is not unique for arbitrary histograms. My experience indicates that the iteration method can fail when attempting to incorporate histograms taken over a very large temperature range. Suppose some histograms come from runs near the reference temperature β^* at which the combined probability $p_{\beta^*}(E)$ is to be computed, while other histograms are taken at temperatures far from the reference. The histograms far from the reference temperature cover energy regions far into the tails of the reference probability $P_{\beta^*}(E)$ and should have little effect on the probability peak. Thus, the histograms $n^i(E)$ in the tails of the reference probability should be suppressed by a large negative free energy difference ΔF^i when shifted to the reference temperature:

$$p_{\beta}^i(E) = e^{\Delta F^i} e^{-(\beta-\beta^i)E} \frac{n^i(E)}{M^i}$$

Recall however, that the starting guesses for the free energy differences come from the original histograms and are extremely inaccurate for large shifts; refer to Section 4.3.2. The initial free energy inaccuracy can allow the greatly shifted histograms to produce a large error in the initial combined probability. The Ferrenberg-Swendsen iteration of the free energy and the combined probability equations cannot always recover from large initial errors.

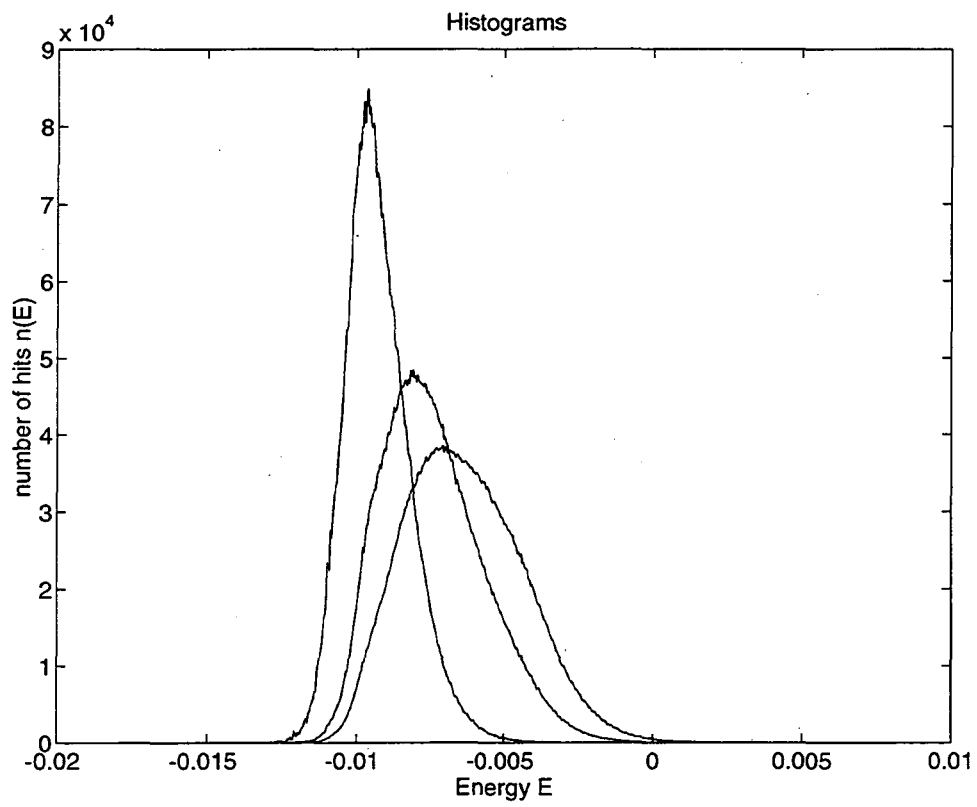


Figure 4.6: Unshifted histograms

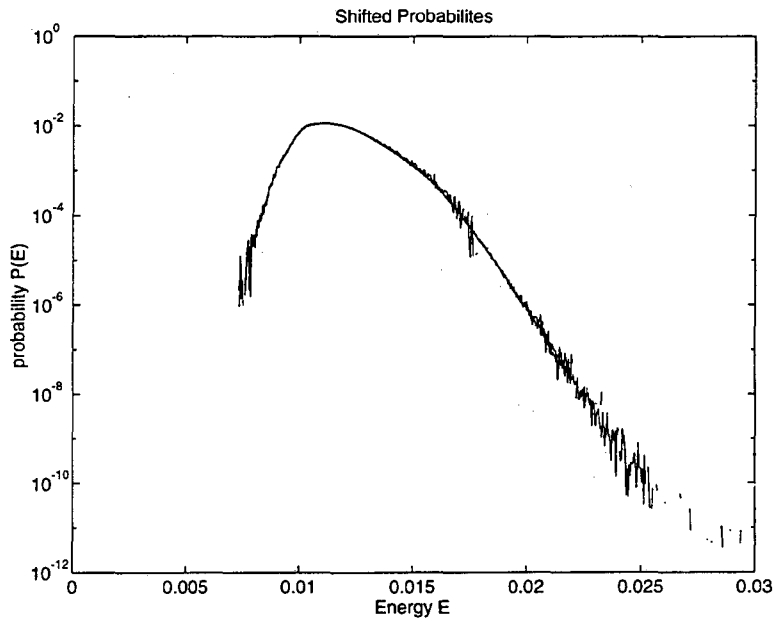


Figure 4.7: Shifted probabilities

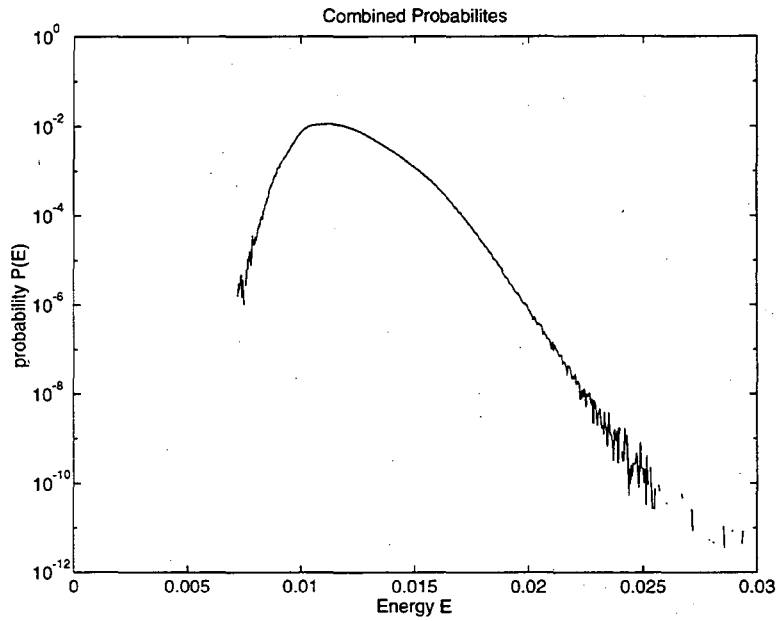


Figure 4.8: Combined probability

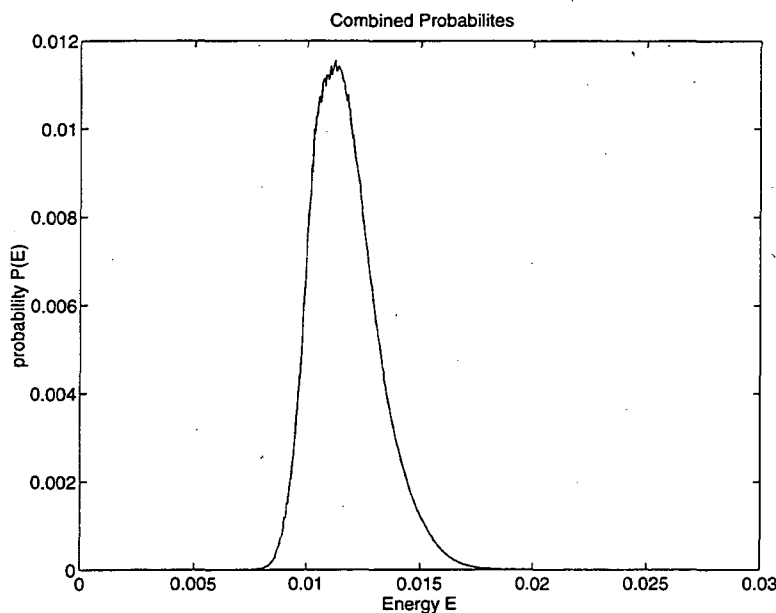


Figure 4.9: Combined probability

The problem of overly large temperature shifts can be circumvented by restricting the set of histograms to be combined to those taken at temperatures near the region of interest. The method is also sensitive, however, to very small errors in the tails of the individual histograms. This sensitivity makes it imperative to choose an initial configuration for the Monte Carlo run having energy near the peak of the expected histogram, or to discard enough initial trials to reach an equilibrium before beginning the histogram recording. If this procedure is not followed, the initial conditions can result in a few histogram hits far from the peak of the distribution. While these hits do not affect the average values at the temperature at which the histogram is taken, they can be exponentially magnified after shifting. The fixed point free energies can be sensitive to hits far from the probability peak; the following figures are an example of this sensitivity. Figure 4.10 shows a pair of histograms, each containing 5 million trials. Combining them with the fixed point method at a temperature between the two gives a reference probability visually identical to the result in Figure 4.9. Suppose the right histogram, however, is contaminated with a single hit at energy $E = 0.005$. One hit out of 5 million has no noticeable effect on the unshifted averages. Running the fixed point iteration to combine the histograms, however, results in a significant error in the free energies, evidenced by the vertical gap between the two shifted probability densities in Figure 4.11. The combined probability density then contains

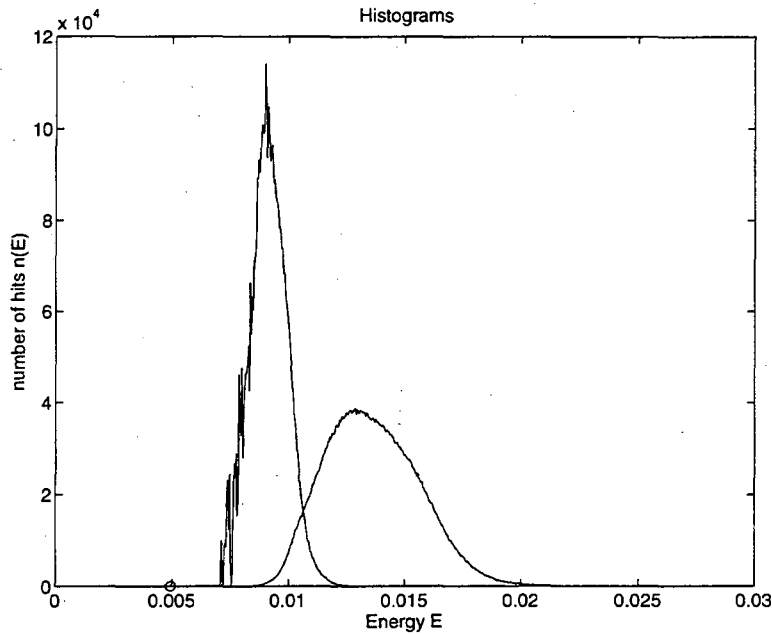


Figure 4.10: Unshifted histograms

an bump where the weight shifts from the right histogram to the left, Figure 4.12. This results in a significantly skewed probability, on the left of the correct result in Figure 4.13.

4.3.4 Observations on Combining Histograms

Although the histogram shifting and multi-histogram machinery is not highly robust, the methods still retain several advantages over traditional Monte Carlo algorithms which store only mean values. The process of extracting information from Monte Carlo simulation is in general an experimental science rather than a set procedure. One of the greatest advantages of using the histogram machinery is that it allows the easy creation of a broad-brush painting of parameter space. A few runs may be made for very small systems where finite size effects will broaden the histograms. A modest number of trials suffices since the autocorrelation time decreases in smaller systems, so the initial runs are very inexpensive compared to the effort required to do a thorough study. This first picture provides information on how to concentrate further runs with larger systems. Histograms for systems at the next size level give a somewhat more accurate view, and again guide the placement of longer runs. It is thus possible to build up a more and more refined map of pa-

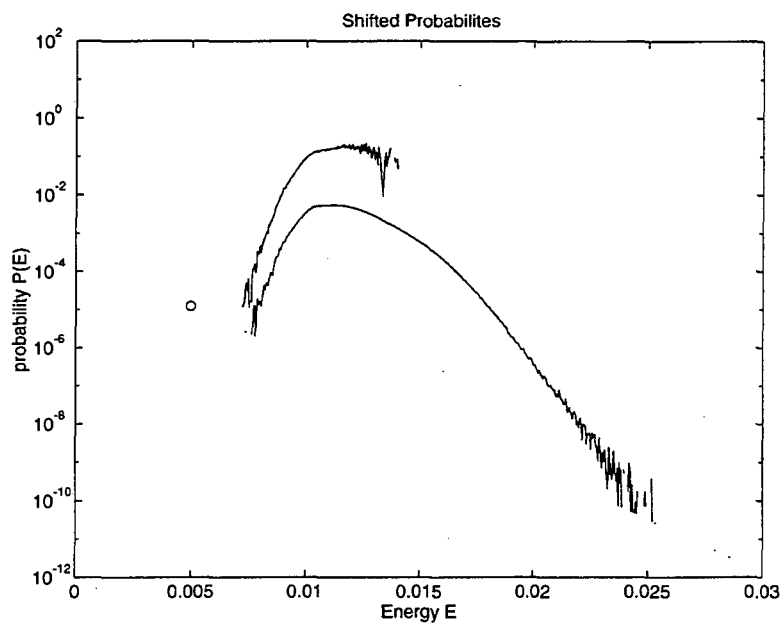


Figure 4.11: Shifted probabilities

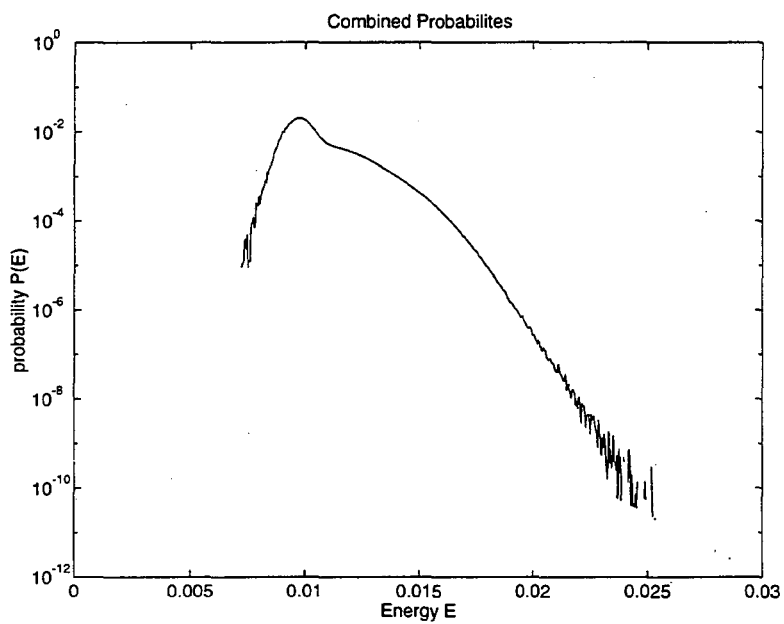


Figure 4.12: Combined probability

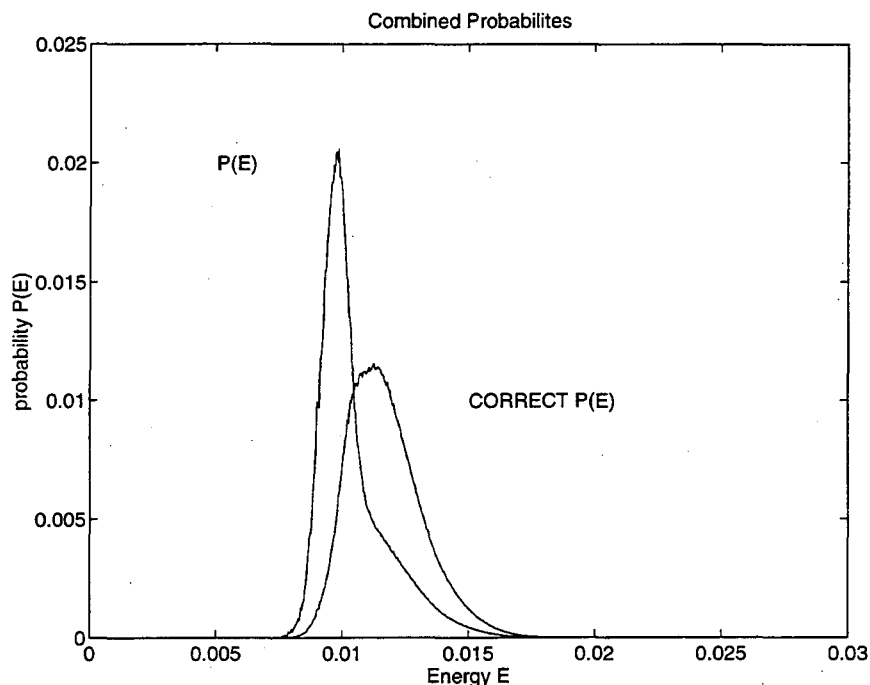


Figure 4.13: Combined probability

parameter space without wasting large, long runs in uninteresting regions. This is particularly useful in the process of identifying phase transition points.

The histograms also give a quick look at the performance of the Markov process in the Monte Carlo algorithm. The magnitude of statistical errors are more easily judged from the roughness of the histogram than from the drift of the mean values over the run. The shapes of shifted probability densities $p_{\beta}^i(E)$ also provide a check on the Metropolis sampling. I found an early violation of the detailed balance condition in my vortex algorithm by noting that shapes of histograms from different runs did not match up after shifting them to a reference temperature. The histogram sampling also gives an indication of the algorithm's performance over different regions of phase space.

If carefully monitored, the multi-histogram method can reduce the computational effort required to compute observable quantities to high precision. The accuracy of the free energy differences can be checked by viewing the shifted densities on a logarithmic scale. The shifted densities should lie on top of each other, as in Figure 4.7. Visual checks of shifted probabilities can also prevent the combined density from being shifted into the statistical tail at the ends of coverage. Convergence can be checked by comparing the results

obtained from different sets of parameter runs. If several histograms overlap, the removal of one from the combined density should not affect the results drastically.

Although the fixed point iteration of Ferrenberg and Swendsen seems to be the best method currently available for calculating the free energy differences and combining several histograms, I believe there are several avenues open for improvement. A re-examination of Figure 4.11, where the fixed point method failed, indicates that the *shape* of the curves is essentially the same over their regions of statistical confidence. On the logarithmic axes, an experimenter could determine the free energy shift by manually moving the shifted histograms up or down until they matched visually. See Figure 4.14. It is conceivable that an algorithm for determining the free energy shifts could be based on matching the shapes of the histograms, rather than the on the analytical formula:

$$\Delta F^i = \log \left(\sum_E e^{(\beta - \beta^i)E} p_\beta(E) \right)$$

One could take the idea further by assuming a degree of smoothness to the underlying density of states $D(E)$. In this case, the free energy differences could be determined from a statistical fit of the histograms to a smooth function. Something along these lines has been proposed by Bennett [12]. Such a fit would be less vulnerable to statistical outliers than the fixed point iteration. A representation of the probability distribution as a smooth function also raises the possibility of a higher order integration rule. Although the integration error from estimating the functions $P_\beta(E)$ and $\bar{A}(E)$ as step functions with step size ΔE is typically small compared to overall statistical error, a higher order representation could ensure that integration error is truly negligible and improve accuracy in the tails of the distribution.

Although the histogram methods require careful analytical and graphical monitoring to ensure their reliability, I believe they are an invaluable tool for thermodynamic simulation. The computational overhead involved in the histogram processing is minimal, and one always has the option of recovering the standard Monte Carlo averages as a degenerate case. Besides the potential savings in computer time, the density of states ideas can be useful in and of themselves. The histogram method gives approximations to the micro-canonical averages for free. The methods also give an approximation to the density of states; the density of states concepts can provide an additional avenue for coupling numerics to statistical mechanical theory.

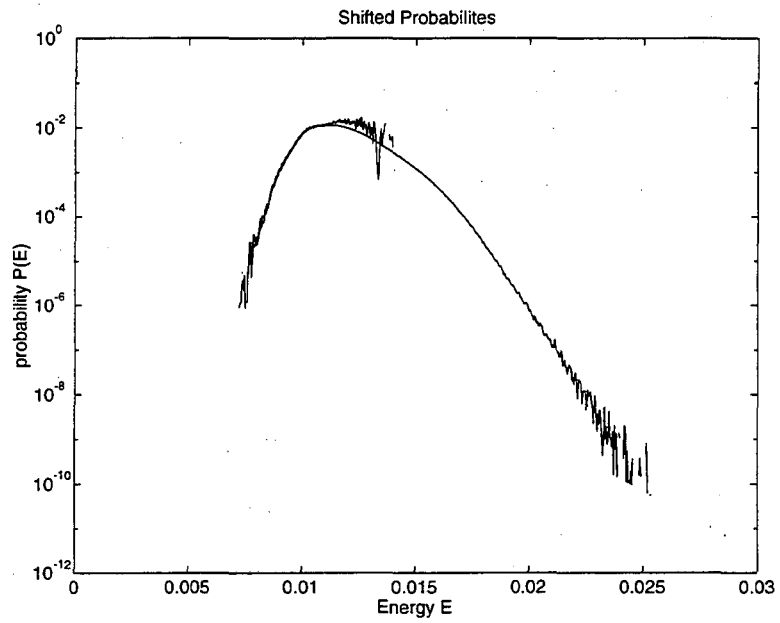


Figure 4.14: Shifted probabilities

Chapter 5

Numerics for the Self-avoiding Loops System

This chapter describes the implementation of a grand canonical Monte Carlo simulation for the self-avoiding loops system which was described in Chapter 3. The use of vorticity variables presents a set of challenges for numerical simulation very different than the problems of spin simulation. Section 4.1 described the construction of a Markov process for a Monte Carlo simulation. The process requires a suitable set of random transformations $Q_\alpha : \mathcal{C} \rightarrow \mathcal{C}$. These transformations Q_α must be able to generate a sequence of states through the region of representative, (that is probable), configurations with reasonable efficiency. Developing a set of transformations which move vorticity “particles” $\vec{\xi}_i$ while enforcing the geometric constraints on the vorticity field is a problem quite different from that of updating spin configurations.

For spin systems such as the XY model, the configurations are typically transformed by changing the direction of a single spin, which is a single degree of freedom, while keeping the other spins fixed. A few recent methods modify groups or blocks of spins [137] [19] [125] but they all rely on the relative independence of local spins to the configuration as a whole. In vorticity variables, however, the geometry of the configurations becomes of paramount importance. In particular, the zero divergence and self-avoidance constraints prevent the alteration of a single vortex link as an independent variable. While the modification of a single spin in a field model results in an acceptable configuration, a vortex link in the middle of a loop cannot simply be moved elsewhere or even have its direction changed

without violating the constraints. A set of transformations must therefore be developed which respect the geometric constraints of the problem. Fortunately, much of this geometric machinery has been developed for the simulation of the self-avoiding walk. In particular, the pivot algorithms used by Madras and Sokal [25] [26] [99] offer a highly efficient set of moves appropriate for changing the geometry of individual loops. These moves can serve as the base for a set of transformations which work on collections of loops.

A further complexity is introduced by the variability of N in the simulation. This leads to a “grand canonical” simulation which must include moves to increase and decrease the number of links in the configurations. Provisions must also be made for the re-arrangement of the links into configurations with different numbers of loops.

Finally note that a direct calculation of the interaction energy of a configuration requires on the order of N^2 operations, where N is the number of vortex links in the configuration. Since vortex links interact through a long range Green function, modifying a single link affects $N - 1$ interactions. If many links are altered by a transformation, the energy calculation is of order N^2 at each step. Although fast algorithms exist to calculate the energy in order N steps [135], the overall efficiency of the Monte Carlo simulation is strongly dependent on the efficient use of the energy calculations.

Section 5.1 of this chapter describes a set of transformations which change the shapes of individual vortex loops, re-arrange different loops, change loop connectivity, and change the number of vortex links in the configurations. Transformations which add or delete vortices to produce a particular effect on the energy of the system are also described. These transformations are shown to satisfy the transformation detailed balance condition given in Section 4.2. A possible lack of ergodicity for the set of transformations and its effect on the simulation is discussed in the Section 5.2 of this chapter.

Section 5.3 introduces a modification to the Metropolis sampling method of Section 4.2. The modification allows the computationally expensive energy calculations to be used efficiently in the presence of a diverse set of types of transformations. It employs composite transformations made of moves which need not individually satisfy the detailed balance condition. The generation of a new member of the Markov chain proceeds at each step in two phases: the first phase generates in several intermediate steps a candidate configuration, while the second enforces the detailed balance condition by accepting or rejecting the candidate. Transformation types which are not expected to greatly change the energy of the configuration can proceed in the first phase without the recomputation of the en-

ergy. Several of these transformations can occur in the first phase, producing collectively a configuration which differs greatly from the previous member of the Markov chain. Moves made in the first phase need not satisfy detailed balance, so the energy of intermediate steps need only be calculated when a move is expected to produce a large change. The second phase computes the energy and enforces the detailed balance condition of the Markov process. Energy calculations are thus used sparingly; the energy is recomputed only when the result of the calculation is expected to significantly effect the probability of accepting a configuration. The modified sampling method, termed *split-phase Metropolis*, is described in this section. A proof that the method preserves the detailed balance condition is given. The split-phase algorithm used for the simulation of the self-avoiding loops system is then described. Finally, the method is generalized and suggestions are made for its use in general Monte Carlo simulations.

Section 5.4 of this chapter discusses the implementation of the Monte Carlo algorithm and the performance of the method. The order of the number of operations required for portions of the algorithm is discussed, and the data structures required to achieve this performance are described. The convergence of the estimator for the probability density function is examined. Finally, the effectiveness of the split-phase method is discussed.

5.1 Transformations

Configurations in the self-avoiding loops model consist of collections of closed loops of vortex links. The links lie on the bonds connecting the sites of a periodic lattice; the self-avoidance condition prevents any lattice site from being visited more than once. The configurations are described in detail in Section 3.2.

This section gives an algorithmic description of the set of transformations on the set of self-avoiding loops configurations. Information on data structures and computational implementation will be given in Section 5.4. The entire Monte Carlo algorithm which employs the transformations will be described in Section 5.3. The transformations are divided into types: pivots, translates, reconnections, elementary addition/deletion, and elementary excitations. Pivots change the shape of individual loops, translates change the arrangement of loops in a collection, reconnections change the partitioning of vortex links into separate loops, and elementary addition/deletion changes the number of vortex links in the configuration. Elementary excitations add or delete vortices in a way that reduces

or increases the energy of the resulting configuration.

The action of each transformation type depends on random choices. The condition of transformation detailed balance presented in Section 4.2 states that each transformation should have an inverse such that the probability of moving configuration c to c' should equal the probability of moving c' back to c . The existence of an appropriate inverse will be given for each transformation and the probability balance will be justified. Algorithmic descriptions will be set in typewriter font where indentation and, if necessary, braces { } indicate dependent operations.

5.1.1 Pivots

The transformations in the “pivot” class described here are used to change the geometry of individual loops. They are adapted from the self-avoiding walk algorithm described and analyzed by Madras and Sokal in 1988 [100]. The transformations are modified to work on single vortex loops, which are closed self-avoiding walks. Madras in 1990 [99] studied an equivalent modification, and additionally gave a complete analysis. Pivots are augmented with moves called “inversions” after the terminology used by Sokal [26]. The pivot moves alter the loop by first choosing an arc: a connected sub-sequence of links. The loop is then “broken” into two rigid pieces at the endpoints of the arc, and the arc is “repositioned” at the endpoints to form a new loop which has been “bent” at the endpoints of the arc. By rigidly preserving the arc, and by reattaching at the endpoints, the connectivity of the loop is preserved. The self-avoidance of the bent loop is checked a-posteriori; if the repositioned arc intersects another part of the configuration then the move is rejected and the identity transformation is substituted in its place. In practice, the fraction of self-avoiding bends tends to a constant for large arcs, leading to an algorithm which can generate a nearly independent N link configuration in order of N computer time [100].

An arc of a loop can be described by the position of the first node in the arc and the list of vector steps $\{\vec{\xi}_i\}$ that trace out the arc. Figure 5.1 shows an arc of six steps between the nodes marked by black circles; the first node is at (a) and the list of steps is, from left to right:

$$\begin{bmatrix} 1 & 0 & 1 & 0 & 0 & 0 \\ 0 & 1 & 0 & -1 & -1 & -1 \\ 0 & 0 & 0 & 0 & 0 & 0 \end{bmatrix}$$

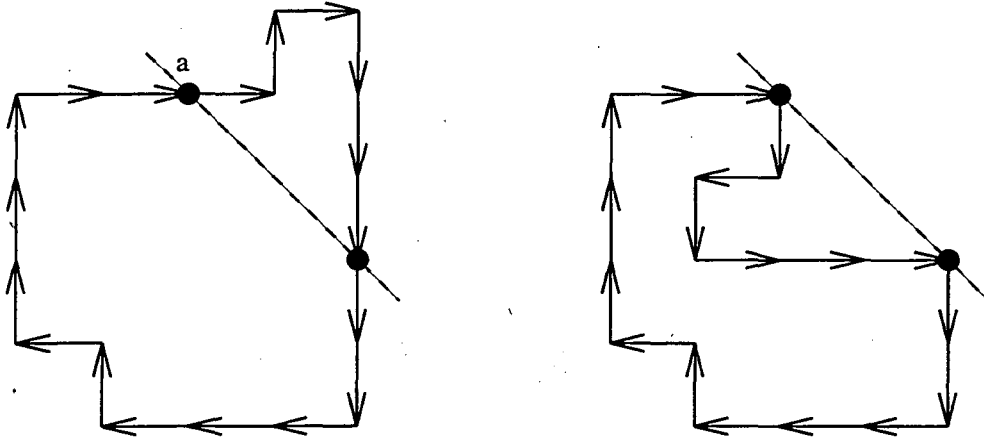


Figure 5.1: Pivot preserving link order

A pivot move changes only the selected arc of the loop, while the rest of the loop remains fixed in place. The movement of the arc can be expressed as an orthogonal matrix S . The new arc is formed by taking the list of link vectors $\{\vec{\xi}_i\}$ and making a new list $\{S\vec{\xi}_i\}$ by multiplying each link by S . The new positions of the nodes of the arc are calculated by starting at the first node and following the new list of steps, wrapping across periodic boundaries if necessary. In the example shown in Figure 5.1, the matrix S is:

$$\begin{bmatrix} 0 & -1 & 0 \\ -1 & 0 & 0 \\ 0 & 0 & 1 \end{bmatrix}$$

The new sequence of link vectors $\{S\vec{\xi}_i\}$ is:

$$\begin{bmatrix} 0 & -1 & 0 \\ -1 & 0 & 0 \\ 0 & 0 & 1 \end{bmatrix} \begin{bmatrix} 1 & 0 & 1 & 0 & 0 & 0 \\ 0 & 1 & 0 & -1 & -1 & -1 \\ 0 & 0 & 0 & 0 & 0 & 0 \end{bmatrix} = \begin{bmatrix} 0 & -1 & 0 & 1 & 1 & 1 \\ -1 & 0 & -1 & 0 & 0 & 0 \\ 0 & 0 & 0 & 0 & 0 & 0 \end{bmatrix}$$

The node positions for the arc are reconstructed by incrementing with the new vectors from point (a).

The matrix S is chosen from the set of 48 orthogonal matrices which preserve the cubic lattice. These matrices represent the symmetry group of the cubic lattice. In practice the choice of the matrix must be restricted so that the new arc fits back into the loop. The end-to-end vector $\vec{\Delta}$ of the arc is computed and a matrix S is chosen randomly from the set of matrices for which $S\vec{\Delta} = \vec{\Delta}$. In the example in Figure 5.1, S preserves the end-to-end vector $\vec{\Delta} = (2, -2, 0)$. If the vector $\vec{\Delta}$ does not lie on a symmetry axis of the lattice,

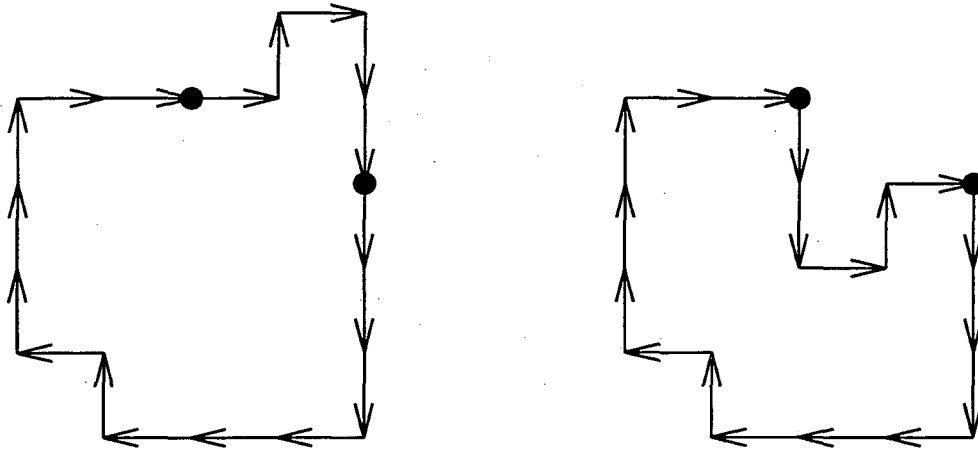


Figure 5.2: Arc inversion

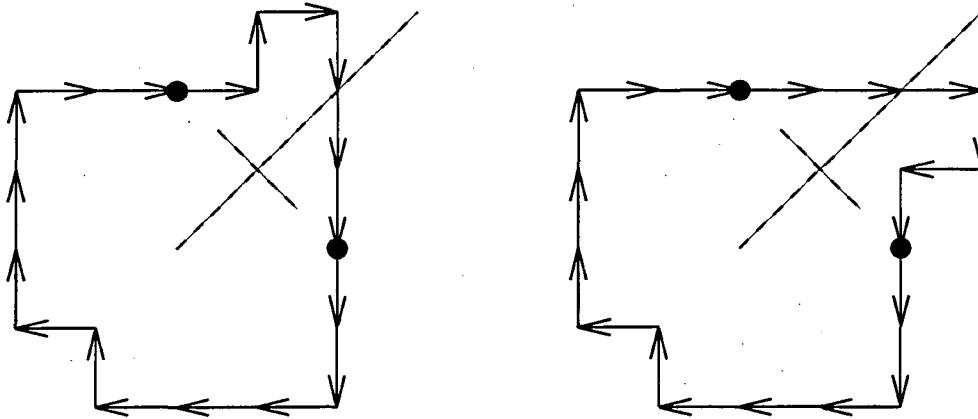


Figure 5.3: Pivot reversing link order

then only the identity matrix will preserve $\bar{\Delta}$. In this case, the arc is inverted by reversing the order of the steps in the arc before reconstructing the node positions. An example of arc inversion is given in Figure 5.2. Inversion may also be performed in concert with a non-trivial matrix transformation. An example of adding inversion to the pivot move of Figure 5.1 is given in Figure 5.3. Finally note that pivots can alter the shape of the loop in three dimensions, as in Figure 5.4. Note that all four examples produced self-avoiding configurations; if the alterations had caused two nodes to lie on the same lattice site the loop would revert to its original shape.

The full algorithm is given in Table 5.1. An explanation of detailed balance must show that for each transformation $c \rightarrow c'$ performed through the pivot/invert class on configuration c , there exists a pivot/invert transformation $c' \rightarrow c$ on c' which reverses the

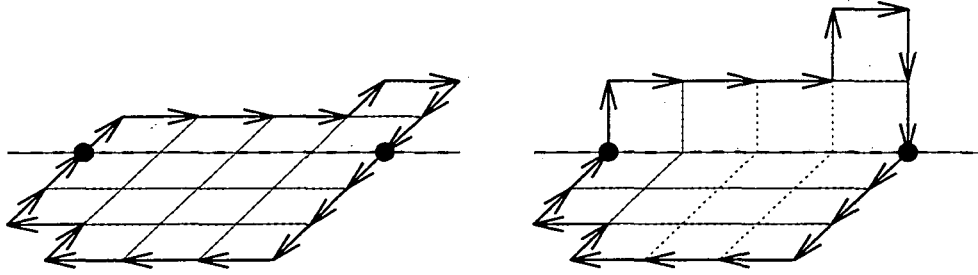


Figure 5.4: Pivot in three dimensions

move. Furthermore, the conditional probability of employing the forward transformation on c must equal the conditional probability of employing the reverse transformation on c' .

The probability of performing a non-trivial pivot move begins with the probability of choosing the pivot class. This is multiplied by the probability of choosing a particular loop and a particular arc. Since the pivot class moves do not change the number of loops nor the number of links in each loop, the probability of a pivot class move selecting an arc of a loop in c is equal to the probability of a pivot class move of selecting the same arc of the same loop in c' . If the endpoints of the arc, which are not changed by the original move, do not lie on a symmetry axis then inversion is performed by the pivot class on both c and c' . Since twice reversing the order of links in the arc recovers the original arc, the inversion step of the pivot class move is its own inverse and the probability of transforming c to c' by this class is equal to the probability of transforming c' back to c by the class.

If the endpoints of the arc do lie on a symmetry axis, the probability to perform a particular move is the probability of choosing the arc times the probability (50%) of inverting or preserving the link order, times the probability of choosing a particular S_α such that $S_\alpha \vec{\Delta} = \vec{\Delta}$. The group structure of $\{S\}$ guarantees the existence of a unique inverse matrix $S_{\alpha'}$ such that $S_{\alpha'} S_\alpha = I$. The since both S_α and $S_{\alpha'}$ preserve $\vec{\Delta}$, the probability of choosing $S_{\alpha'}$ during the reverse move is equal to the probability of choosing S_α during the forward move. The link order inversion commutes with multiplication of the links in the arc by an S , so the pivot class moves change c to c' and c' to c with equal probability.

5.1.2 Translates

Translates change the relative positions of individual loops by rigidly translating a single loop by a random lattice vector \vec{B} . The algorithm is described in Table 5.2. Translation does not change the number of loops in the configuration, so the probability

Table 5.1: Arc pivot/invert algorithm

```

(choose randomly a loop from the collection)
  (choose randomly an ordered pair of nodes in the loop:
the links between them are an arc)
    (compute the sum  $\vec{\Delta} = (\Delta X, \Delta Y, \Delta Z) = \sum_{i \in \text{arc}} \vec{\xi}_i$ )
    (if  $\vec{\Delta}$  lies along a symmetry axis of the cube then pivot)
      (choose randomly an  $S$  such that  $S\vec{\Delta} = \vec{\Delta}$  )
      (choose randomly to invert or not invert the arc)
      (if invert chosen then)
        (apply  $S$  to the  $\vec{\xi}_i$  in the arc)
        (reverse the order of the links in the arc)
        (construct new node positions by incrementing from
the first endpoint)
      (else)
        (apply  $S$  to the  $\vec{\xi}_i$  in the arc)
        (construct new node positions by incrementing from
the first endpoint)
    (else if  $\vec{\Delta}$  is not on on a symmetry axis then invert only)
      (reverse the order of the links in the arc)
      (construct new node positions by incrementing from
the first endpoint)

(if the resulting configuration is not self-avoiding then)
  (revert to original configuration)
(else)
  (take modified configuration)

```

Table 5.2: Translation algorithm

```

(choose randomly a loop from the collection)
  (choose randomly an translation vector  $\vec{B} \in [0, h, 2h, \dots, L - h]^3$  )
  (add  $\vec{B}$  to all node positions in the loop)
  (periodically wrap node positions back into the first period)
(if the resulting configuration is not self-avoiding then)
  (revert to original configuration)
(else)
  (take modified configuration)

```

of choosing the translation class times the probability of choosing a particular loop is unchanged by the forward move. The distribution of the random translation vectors $\{\vec{B}\}$ assigns equal weight to \vec{B} and to $-\vec{B}$ (modulo the periodicity of the domain) so moves in the translation class satisfy the balance condition. The probability of translating a loop of a configuration c to a new position is equal to the probability of translating it back in the changed configuration c' .

5.1.3 Reconnections

The pivot moves alter individual loop geometry and orientation, and translations alter the arrangement of the various loops. I have developed a set of reconnection moves which change the partitioning of links among the different loops. Reconnections change the connectivity pattern to break one vortex loop into two or merge two vortex loops into one. See Figure 5.5. The algorithm maintains a list of plaquettes which are “full”, that is, all four lattice sites at the corners of the plaquette are occupied with nodes (ends of vortex links). A full plaquette is classified as eligible for a reconnection move if its border is occupied by anti-parallel links on two sides and is unoccupied on the remaining two sides. A reconnection move relinks the nodes so that the links move to the previously empty sides of the plaquette.

If the anti-parallel links originally belonged to the same loop, a new loop is split off, while if they originally belonged to different loops the two are merged. Figure 5.5

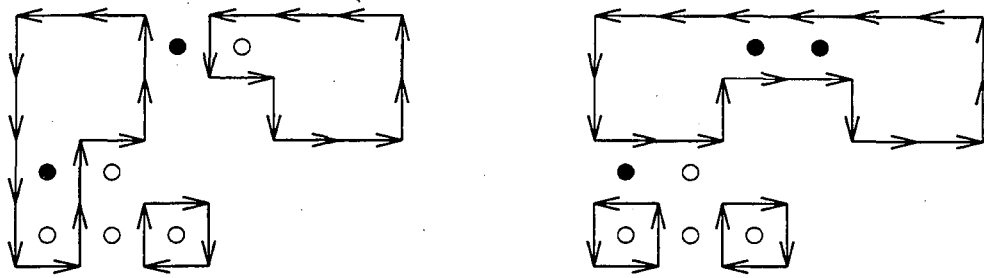


Figure 5.5: Two reconnection moves

Table 5.3: Reconnection algorithm

```

(do i = 1 to  $K_R$ ):
  {
    (choose randomly a plaquette from the set of full plaquettes)
    (if the plaquette is eligible then reconnect)
  }

```

shows on the left a loop configuration containing 7 full plaquettes, marked by circles. Two are bordered by only a pair of anti-parallel links and are eligible for reconnection moves. These are marked with filled circles. The configuration resulting from performing the two reconnections is shown on the right. Table 5.3 gives the reconnection algorithm. Since a reconnection event changes only two links, compared to the number of links in an arc changed by a pivot move and the number of links in a loop changed by a translation move, a number of reconnection attempts K_R are made at each invocation of the reconnection class. Note that while the number of full plaquettes is unchanged by a reconnection, the number of eligible plaquettes is not necessarily fixed. In the example, the merging of two loops makes a previously ineligible "hairpin turn" into an eligible plaquette. In order to preserve detailed balance, therefore, it is necessary to choose a plaquette randomly from the collection of full plaquettes, rather than from the collection of eligible plaquettes. This procedure insures that the probability of reconnecting a plaquette of a configuration c is equal to the probability of reconnecting at the same spot in configuration c' and of reversing the move.

Table 5.4: Link addition/deletion algorithm

```

(choose randomly a plaquette in the domain)
  (if the border has a single link then)
    (add a hairpin)
  (else if the border has a hairpin then)
    (delete the hairpin)
  (else if the plaquette is empty then)
    (choose randomly an orientation {CW or CCW})
    (add an elementary loop of chosen orientation)
  (else if the border is an elementary loop)
    (choose randomly an orientation {CW or CCW})
    (if the loop matches the orientation, delete it)
    (else leave it unchanged)
  (else the plaquette is ineligible for addition/deletion)

```

5.1.4 Elementary Addition/Deletion

Pivots and translations change the geometry of vortex loops, and reconnections change the partitioning of the existing vortex links into different loops. None of these transformations, however, change the number of links N in the configuration. I have developed a set of transformations for the variable- N simulation which add or delete links. In order to manage the detailed balance condition so that each addition and deletion should have an equal probability inverse, the “elementary” moves are restricted to adding or deleting links about a single plaquette. The additions and deletions fall into two classes, adding or deleting a “hairpin” which follows three sides of a plaquette, and adding or deleting an “elementary loop” which surrounds a plaquette on all four sides. Table 5.4 gives the algorithm, while Figure 5.6 shows the four possibilities around a single plaquette.

The probability of successfully performing an Addition/Deletion is the probability of choosing the Addition/Deletion class times the probability of choosing a particular plaquette of the lattice. If the plaquette is bordered by a single link, a hairpin, no links, or

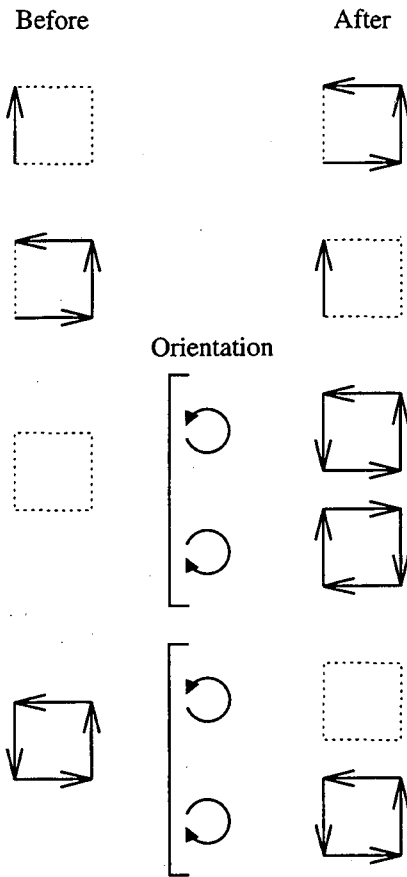


Figure 5.6: Link addition/deletion

an elementary loop then links are added or deleted. Otherwise no action is performed at the plaquette. A single link is transformed into a hairpin and vice versa. An empty plaquette is transformed into a clockwise loop with 50% probability and into a counter-clockwise loop with 50% probability. An elementary loop is deleted with 50% probability. Thus the probability of making a transformation is the same as the probability of reversing it.

5.1.5 Elementary Excitations

The pivot, translation, reconnection, and elementary addition/deletion classes of transformations suffice to change the geometry, connectivity, and number of links in the vortex configurations. These moves form a complete set of transformations for a grand canonical simulation of the self-avoiding loops system. The following transformation class is included not to change a particular aspect of the vortex configurations, but to increase computational efficiency. In some ranges of the parameter space (β, ν) , elementary addition/deletion moves are rarely accepted by Metropolis sampling. The equilibrium weight for a configuration is given in Section 3.2:

$$\rho = e^{-\beta E^{int} - \beta \nu N}$$

If, in a Metropolis step, the candidate configuration c' differs from the starting configuration c by $(\Delta E, \Delta N)$ in interaction energy and number of links, then the probability of accepting the move is $\min(1, \rho(c')/\rho(c))$ where

$$\frac{\rho(c')}{\rho(c)} = e^{-\beta \Delta E - \beta \nu \Delta N}$$

If $\beta \nu \gg 1$ then the addition of vortex links is strongly discouraged by the weight. It is sometimes desirable, therefore, to create transformations which add links to the domain in a manner that produces a particular effect on the interaction energy. Such a transformation may have a high probability of being accepted if a favorable change in interaction energy ΔE can offset an unfavorable change in the number of links ΔN . Transformations which are tailored to produce a large increase or decrease of the energy of the configuration are termed *elementary excitations* in this thesis. The use of such specialized transformations is similar to a technique used by Chorin [32] for sampling vortex filament configurations. This section describes two sorts of elementary excitations: one which raises the interaction energy of the configuration and one which lowers the interaction energy. The first sort are

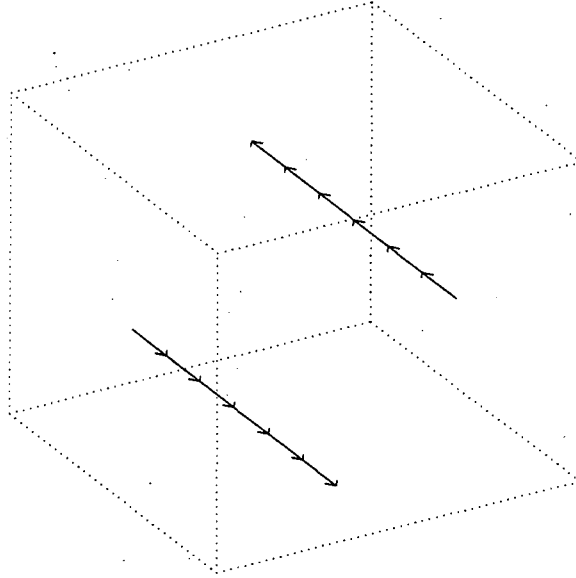


Figure 5.7: Vortex dipole

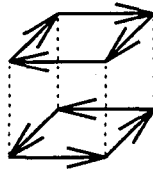


Figure 5.8: A crystal of stacked elementary loops

termed *dipole* transformations because the added vortices resemble two dimensional vortex dipoles when viewed along their axis, see Figure 5.7. The second sort are termed *crystal* transformations because they generate cubes of vortex loops which could fit together in a regular crystal, see Figure 5.8.

If temperature is negative so that high energy states are favored, while at the same time states with many vortex links are discouraged, configurations tend to become polarized with vorticity of one direction in one region of the domain and vorticity of the opposite direction in a separate region. See Figure 5.9. The addition of an elementary loop or a hairpin inserts a pair of nearest neighbor anti-parallel vortices which lowers the interaction energy of such a polarized configuration somewhat. Such additions, therefore, are penalized both for decreasing the energy and for increasing the number of links in the configuration. The addition of a pair of dipole vortices, however, such as those shown in Figure 5.7, can greatly increase the interaction energy in the system. If the favorable effect

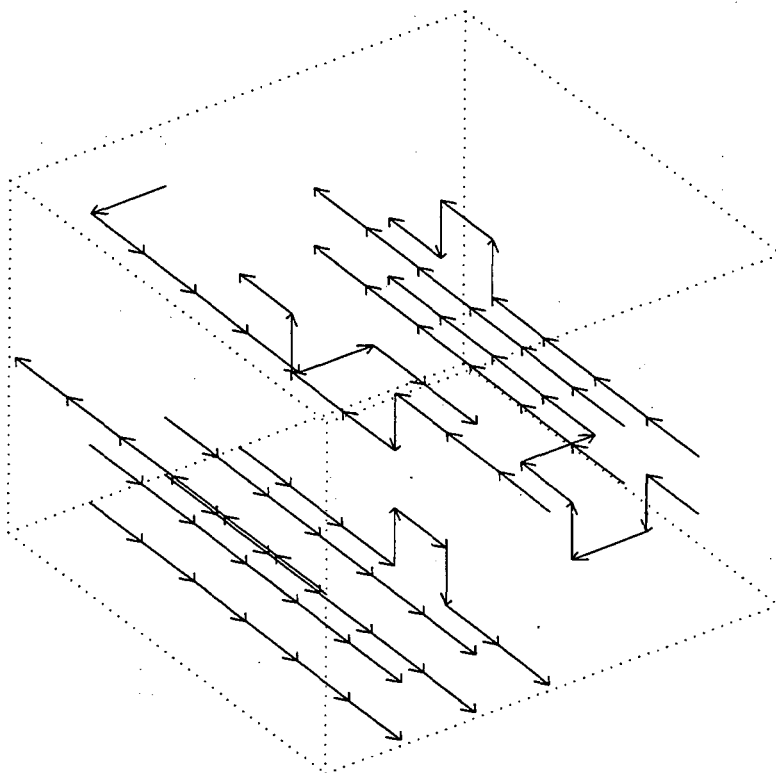


Figure 5.9: Polarized vortices with high energy

of the energy change nearly balances the penalty for increasing N , then dipole additions and deletions will be frequently accepted by Metropolis sampling. Table 5.5 gives the dipole addition/deletion algorithm. The sites for adding or deleting dipoles are chosen randomly to preserve the detailed balance condition.

The counterpart to dipoles are crystals, which lower the interaction energy rather than raise it. Crystals may be frequently accepted in systems at low positive temperature where low interaction energies are favored. Table 5.6 gives the crystal addition/deletion algorithm. If the randomly chosen sites are neither empty nor filled with a crystal, the algorithm attempts to add or delete an elementary loop. Figure 5.10 shows on the left a situation where one plaquette is empty and the other plaquette has a set of links which is not an elementary loop. The result of the crystal move adding an elementary loop is shown on the right. In order to maintain detailed balance, however, the addition or deletion of an elementary loop cannot create or break up a crystal of two counter-rotating loops. If the crystal algorithm visits the same site twice in a row, it should return the configuration

Table 5.5: Dipole algorithm

(choose randomly an anti-parallel pair of lines though the domain)
 (if all sites on both lines are empty then)
 (add two straight loops of the chosen directions)
 (else if a pair of straight loops of the chosen direction occupies the lines)
 (delete both loops in the dipole)
 (else the location is ineligible for a dipole move)

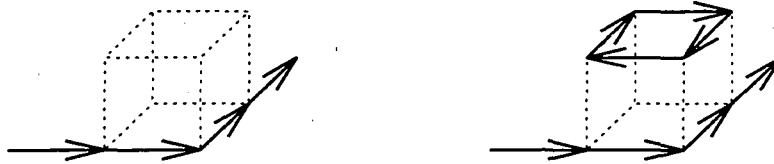


Figure 5.10: Adding an elementary loop

to the state before the visits. If the algorithm were to create a crystal by adding an elementary loop, and then were to remove both loops in the crystal on the second visit, the transformation detailed balance condition would not hold.

5.2 Ergodicity

The previous section describes the set of transformations on the self-avoiding loops configurations and shows that the transformation detailed balance condition given in Section 4.2 is satisfied. The proof that the Markov chain occupation time of each configuration $c \in \mathcal{C}$ converges to the equilibrium weight $\rho(c)/\mathcal{Z}$ also requires the ergodicity condition: that the transformations can change any state to any other state in a finite number of steps. I will not show that the ergodicity condition holds; in fact I believe that there exist high density states which are not reachable by this transformation set. Nevertheless I believe that at low and moderate densities the algorithm gives at least a representative set of configurations. The numerical results given in Chapter 6 are accordingly restricted to a region of parameter space (β, ν) in which vortices are discouraged so that the density is limited.

At low enough vortex density, a proof of ergodicity follows from the work of Madras

Table 5.6: Crystal algorithm

```

(choose randomly a stacked pair of plaquettes and an orientation)
  (if both plaquettes are empty then)
    (add two loops to make a crystal of the chosen orientation)
  (else if a crystal of the chosen orientation exists)
    (delete both loops in the crystal)
  (else if one plaquette is empty and the other
is not a loop of the correct orientation)
    (add an elementary loop of the chosen orientation)
  (else if one loop matches the orientation and the other plaquette
is not a loop of the correct orientation)
    (delete the elementary loop)
  (else the location is ineligible for a crystal move)

```

in his 1990 paper with Orlitsky and Shepp [99]. They showed that the pivot moves are ergodic for a single loop in free space. Therefore any geometry is realizable for a loop of a given number of links provided it is far enough away from other loops so that it may be folded freely. Given this fact, any configuration of N links can be reached from (or turned into) a single elementary loop by the following procedure. Add bumps onto the loop until the desired total number of links N is reached. Then shape the loop into a single long thin configuration, as demonstrated in Figure 5.11. Use reconnection moves to partition the loop as desired, Figure 5.12. Then employ translations to separate the loops and pivots to bend each one into the desired geometry. Finally, reassemble the configuration with translations. Note that both the pivot moves and the translations depend only on the final configurations being self-avoiding, so that loops can be freely knotted and linked by these transformations. As long as individual loops can be translated and pivoted freely enough to form any shape, any configuration can be reached through this procedure. The procedure may fail at high enough density, however, because pivots may be unable to transform a particular loop into the desired geometry in the presence of many sites which are occupied by other loops. Moves which would be possible on an infinite lattice may be blocked by the

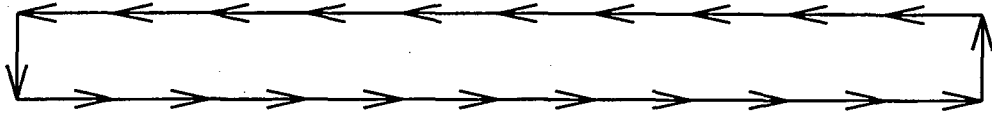


Figure 5.11: Single "canonical" loop

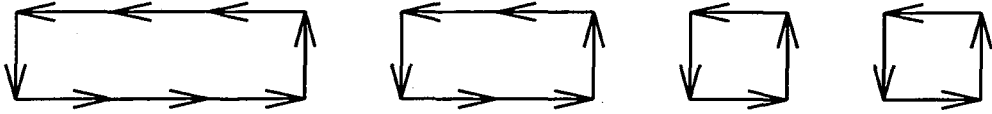


Figure 5.12: Partitioned loops

self-avoidance condition.

Although the possible lack of ergodicity in the algorithm is a serious matter, there is some reason to believe that the numerical results are not strongly affected. Recall that the effectiveness of practical Monte Carlo simulation rests not on the property that all configurations are visited with the correct frequency, but that the probability distributions of observable quantities converge quickly to their limiting distributions.

A number of numerical tests have been performed to search for indications that non-ergodicity effects the probability distributions at moderate density. Several runs with different initial conditions were taken at each set of parameters (β, ν) . No difference beyond statistical deviations was seen in either the resulting histogram distributions or the observable averages. Runs were performed in which the number of vortices N was held fixed. These runs produced histograms for a range of interaction energies and a single value of N . These histograms were compared to energy slices of two-dimensional histograms from variable- N runs. The results matched, indicating that the pivot, translation, and reconnection moves were sufficient to move configurations through a fixed- N subspace. The addition of addition/deletion moves did not seem to increase the space of accessible configurations at any particular value of N . These experiments lead me to believe that the numerical results are accurate for the self-avoiding loops system.

5.3 The Split-phase Metropolis Method

The separate operations of changing individual loop geometry, adding and subtracting links, and repartitioning links among different loops lead to an inhomogeneous set of transformations. In particular, some transformation types change N while others

leave N fixed, and some change E greatly while others make only modest changes to the energy. Because the energy calculations are computationally expensive compared to the transformations, an efficient algorithm would employ several transformations for each energy calculation. The use of several transformations would reduce the correlation between successive steps of the algorithm without incurring the cost of several energy calculations. I have used what I term a “split-phase Metropolis” method to balance work among the different transformations and the energy computations for the self-avoiding loops system. This method allows several minor transformations to proceed without an energy check, and splits the enforcement of detailed balance in the E and in N dependent portions of the Gibbs weight:

$$\rho(c) = e^{-\beta E(c)} e^{-\beta \nu N(c)}$$

The split-phase metropolis method maintains the detailed balance condition for the Markov process.

5.3.1 Review of the Metropolis Sampling Method

The description of Metropolis sampling was given in 4.2. The notation is reviewed here. Given a set of functions, also termed transformations, $\mathcal{Q} = \{Q_\alpha : \mathcal{C} \rightarrow \mathcal{C}\}$, each step of the Markov chain is generated as follows. Suppose the current configuration in the chain is c_i . Choose randomly one of the functions Q_α ; each function has conditional probability $\pi_\alpha(c_i)$ given the current configuration c_i . Thus for each $c \in \mathcal{C}$, since one transformation is chosen at each step, the following normalization condition holds:

$$\sum_{\alpha} \pi_{\alpha}(c) = 1$$

Apply Q_α to the current configuration to generate a candidate c' :

$$c' = Q_\alpha c_i$$

Now let the next member of the Markov chain be

$$c_{i+1} = \begin{cases} c' & \text{with probability } \Theta(c_i, c') \\ c_i & \text{otherwise} \end{cases}$$

where the acceptance probability $\Theta(c_i, c')$ is:

$$\Theta(c_i, c') = \min\left(1, \frac{\rho(c')}{\rho(c_i)}\right)$$

The probability $\eta_\alpha(c, c^*)$ is the probability, given current configuration c , of employing the transformation Q_α and of accepting or rejecting the candidate to select the next configuration c^* . If the step accepts the candidate, then:

$$\eta_\alpha(c, c^*) = \pi_\alpha(c) \Theta(c, Q_\alpha c)$$

otherwise:

$$\eta_\alpha(c, c^*) = \pi_\alpha(c) [1 - \Theta(c, Q_\alpha c)]$$

If the set $\{\alpha | Q_\alpha c = c^*\}$ contains all the transformations Q_α that map c to c^* , then the Markov transition probability,

$$P(c \Rightarrow c^*) = \sum_{\alpha | Q_\alpha c = c^*} \pi_\alpha(c) \Theta(c, c^*)$$

satisfies the detailed balance condition,

$$\frac{P(c \Rightarrow c^*)}{P(c^* \Rightarrow c)} = \frac{\rho(c^*)}{\rho(c)}$$

when the transformation set $\{Q_\alpha\}$ and the conditional probabilities $\{\pi_\alpha(c)\}$ satisfy for each c the transformation detailed balance condition given in Section 4.2. The transformation detailed balance condition is typically satisfied by insuring that for each α and for each c , there exists an α^* such that:

$$Q_{\alpha^*} Q_\alpha c = c$$

and

$$\pi_{\alpha^*}(Q_\alpha c) = \pi_\alpha(c)$$

If $c^* = Q_\alpha c$ then the probability $\pi_\alpha(c)$ of making the forward step Q_α from c equals the probability $\pi_{\alpha^*}(c^*)$ of making the inverse step Q_{α^*} from c^* .

5.3.2 Description of the Split-phase Metropolis Method

I introduce a modification to the Metropolis method which differs from the standard algorithm in two respects. First, the candidate configuration c' is generated from c_i in a sequence of intermediate steps:

$$c_i = \bar{c}^0, \bar{c}^1, \bar{c}^2, \dots, \bar{c}^k = c'$$

Second, the acceptance probability, $\Theta(c, c')$, of the candidate c' is modified to depend on aspects of the intermediate sequence. The "composite" transformations Q_α created through

the intermediate process need not satisfy transformation detailed balance; the acceptance probability $\Theta_\alpha(c, c')$ is adjusted so that the Markov transition probability

$$P(c \Rightarrow c^*) = \sum_{\alpha | Q_\alpha c = c^*} \pi_\alpha(c) \Theta_\alpha(c^*, c)$$

still satisfies the detailed balance condition.

Let $\{\tilde{Q}_\alpha : \mathcal{C} \rightarrow \mathcal{C}\}$ be a set of transformations, and let the conditional probability to use \tilde{Q}_α given current configuration \tilde{c} be $\tilde{\pi}_\alpha(\tilde{c})$. Suppose that this set $\{\tilde{Q}_\alpha, \tilde{\pi}_\alpha(\tilde{c})\}$ satisfies transformation detailed balance: for each \tilde{Q}_α such that $\tilde{Q}_\alpha \tilde{c} = \tilde{c}^*$, there exists a transformation \tilde{Q}_{α^*} which reverses the move,

$$\tilde{Q}_{\alpha^*} \tilde{Q}_\alpha \tilde{c} = \tilde{c}$$

with equal probability:

$$\tilde{\pi}_{\alpha^*}(\tilde{c}^*) = \tilde{\pi}_\alpha(\tilde{c})$$

Furthermore, associate with each \tilde{Q}_α an "acceptance function" $F_\alpha : \mathcal{C} \rightarrow \mathfrak{R}$. Let the same acceptance function be associated with inverse transformation \tilde{Q}_{α^*} as with the forward transformation:

$$F_{\alpha^*} = F_\alpha$$

This collection of transformations, conditional probabilities, and acceptance functions will be used to create the split-phase algorithm.

The split-phase algorithm employs intermediate Metropolis-like acceptance steps in the production of an intermediate sequence of configurations. Let k intermediate steps be taken at each step of the Markov process; an intermediate sequence of configurations leads to a candidate configuration c' from the current configuration c_i :

$$c_i = \tilde{c}^0, \tilde{c}^1, \tilde{c}^2, \dots, \tilde{c}^k = c'$$

The intermediate configurations are themselves selected by the two-step process of the generation of a candidate followed by an intermediate acceptance step. Let the first member of the intermediate sequence be $\tilde{c}^0 = c_i$. For each $j = 0, 1, \dots, k-1$, choose with conditional probability $\tilde{\pi}_\alpha^j(\tilde{c}^j)$ one of the transformations in $\{\tilde{Q}_\alpha\}$, call it \tilde{Q}_α^j . Generate an intermediate candidate:

$$\tilde{c}' = \tilde{Q}_\alpha^j \tilde{c}^j$$

Now accept this candidate with the intermediate acceptance probability Δ_α^j given by:

$$\Delta_\alpha^j = \min \left(1, \frac{F_\alpha^j(\tilde{c}')}{F_\alpha^j(\tilde{c}^j)} \right)$$

otherwise repeat \tilde{c}^j in the intermediate sequence:

$$\tilde{c}^{j+1} = \begin{cases} \tilde{c}' = \tilde{Q}_\alpha^j \tilde{c}^j & \text{with probability } \Delta_\alpha^j \\ \tilde{c}^j & \text{otherwise} \end{cases}$$

The acceptance function F_α^j plays the same role in the intermediate steps as the Gibbs weight ρ plays in a standard Metropolis step. Now, let the final candidate configuration c' be the last member of the intermediate sequence: $c' = \tilde{c}^k$. The candidate c' is then be accepted with the final probability $\Theta_\alpha(c_i, c')$, to generate the next member c_{i+1} of the Markov chain:

$$c_{i+1} = \begin{cases} c' & \text{with probability } \Theta_\alpha(c_i, c') \\ c_i & \text{otherwise} \end{cases}$$

The subscript α is used loosely here to indicate all the random choices involved in the generation of the candidate c' : the choice at each step of a transformation Q_α^j and the acceptance or rejection of the intermediate candidate. One could make a set of "composite" functions $\{Q_\alpha\}$ which correspond to all the different paths one could take from an initial configuration c to a candidate c' . Each function Q_α depends on the the sequence of intermediate transformations \tilde{Q}_α^j and on the outcomes of the intermediate acceptance steps producing the sequence $\{\tilde{c}^j\}$.

Note that the final acceptance probability $\Theta_\alpha(c, c')$ has not yet been defined. I begin by providing a concrete example in which the acceptance probabilities are defined and the Markov chain detailed balance condition is shown to hold. The example is then generalized to define the final acceptance probability used in the thesis. The detailed balance condition is shown to hold for this type of algorithm. Finally, the implementation for the self-avoiding loops system is described.

5.3.3 A Simple One-step Example

Consider as an example a system with grand canonical equilibrium weight:

$$\rho(c) = e^{-\beta E(c) + \beta \mu N(c)}$$

Let $k = 1$, so only one intermediate transformation \tilde{Q}_α^0 and one intermediate acceptance probability Δ_α^0 are employed in the generation of the final candidate c' . The intermediate chain between the current configuration c and the candidate c' therefore has only two elements:

$$c = \tilde{c}^0, \tilde{c}^1 = c'$$

A step of the Markov process involves first making a move, $\tilde{c}' = \tilde{Q}_\alpha^0 \tilde{c}^0$, by employing a random intermediate transformation \tilde{Q}_α^0 to generate an intermediate candidate \tilde{c}' . This intermediate candidate is accepted with the intermediate acceptance probability Δ_α^0 to determine if \tilde{c}' or \tilde{c}^0 is the last member of the intermediate chain and the final candidate c' . The final candidate is then accepted with probability $\Theta_\alpha(c, c')$ to determine if the next member of the Markov chain is c' or c .

Take a pair of configurations $\{c, c^*\}$ and abbreviate $E = E(c), E^* = E(c^*), N = N(c), N^* = N(c^*)$. Suppose there are only two intermediate transformations \tilde{Q}_1^0 and \tilde{Q}_2^0 which take c to c^* . Since the intermediate transformations set is assumed to satisfy the transformation detailed balance condition, there are two intermediate transformations $\tilde{Q}_{1^*}^0$ and $\tilde{Q}_{2^*}^0$ which take c^* back to c . The probabilities of selecting the forward and inverse steps are equal:

$$\bar{\pi}_1^0(c) = \bar{\pi}_{1^*}^0(c^*)$$

$$\bar{\pi}_2^0(c) = \bar{\pi}_{2^*}^0(c^*)$$

Now, for transformation $\alpha = 1$, let the acceptance function be constant, $F_1^0 = 1$, so intermediate acceptance is automatic:

$$\Delta_1^0 = \min\left(1, \frac{1}{1}\right) = 1$$

Then the intermediate step is:

$$\tilde{c}' = \tilde{Q}_1^0 \tilde{c}^0,$$

$$c' = \tilde{c}' \text{ (with probability 1)}$$

For this transformation let the final acceptance probability be:

$$\Theta_1(c, c') = \min\left(1, \frac{\rho(c')}{\rho(c)}\right) = \min\left(1, e^{-\beta(E(c')-E(c))+\beta\mu(N(c')-N(c))}\right)$$

Taking transformation $\alpha = 1$ results in a step corresponding to a regular Metropolis step; a candidate c' is generated and then accepted with probability $\rho(c')/\rho(c)$. Now suppose,

however, that for $\alpha = 2$ the acceptance function is:

$$F_2^0(\bar{c}) = \dot{e}^{\beta\mu N(\bar{c})}$$

Then the intermediate acceptance probability is:

$$\Delta_2^0 = \min \left(1, \frac{F_2^0(\bar{c}')}{F_2^0(\bar{c}^0)} \right) = \min \left(1, e^{\beta\mu(N(\bar{c}') - N(\bar{c}^0))} \right)$$

so the intermediate step is:

$$\bar{c}' = \tilde{Q}_2^0 \bar{c}^0,$$

$$c' = \begin{cases} \bar{c}' & \text{with probability } \min \left(1, e^{\beta\mu(N(\bar{c}') - N(\bar{c}^0))} \right) \\ c & \text{otherwise} \end{cases}$$

In this case c' is not an unweighted candidate. Adjust the final acceptance probability by taking:

$$\Theta_2(c, c') = \min \left(1, e^{-\beta(E(c') - E(c))} \right)$$

Now consider the Markov transition probabilities of moving from $c \Rightarrow c^*$ and of moving from $c^* \Rightarrow c$. Since in the example there is only one intermediate step, the only way to move from c to c^* is for all the candidates to be accepted at each step. Thus,

$$\bar{c}^0 = c, \bar{c}' = c^*, c' = c^*$$

The total probability $P(c \Rightarrow c^*)$ of transforming c to c^* is a sum over the two possible transformations $\alpha = 1, 2$:

$$P(c \Rightarrow c^*) = \sum_{\alpha=1,2} \tilde{\pi}_\alpha^0(c) \Delta_\alpha^0 \Theta_\alpha(c, c^*) =$$

$$\tilde{\pi}_1^0(c) \Delta_1^0 \Theta_1(c, c^*) + \tilde{\pi}_2^0(c) \Delta_2^0 \Theta_2(c, c^*) =$$

$$\tilde{\pi}_1^0(c) \min \left(1, e^{-\beta(E^* - E) + \beta\mu(N^* - N)} \right) + \tilde{\pi}_2^0(c) \min \left(1, e^{\beta\mu(N^* - N)} \right) \min \left(1, e^{-\beta(E^* - E)} \right)$$

Since the acceptance functions F_α^0 are the same for the forward and reverse steps, the reverse probability has the same form as the forward probability but with c and c^* exchanged:

$$P(c^* \Rightarrow c) = \tilde{\pi}_{1^*}^0(c^*) \Delta_{1^*}^0 \Theta_{1^*}(c^*, c) + \tilde{\pi}_{2^*}^0(c^*) \Delta_{2^*}^0 \Theta_{2^*}(c^*, c) =$$

$$\tilde{\pi}_1^0(c^*) \min \left(1, e^{\beta(E^* - E) - \beta\mu(N^* - N)} \right) + \tilde{\pi}_2^0(c^*) \min \left(1, e^{-\beta\mu(N^* - N)} \right) \min \left(1, e^{\beta(E^* - E)} \right)$$

The mins may be resolved in six cases; a case in which:

$$e^{-\beta(E^*-E)+\beta\mu(N^*-N)} > 1$$

$$e^{-\beta(E^*-E)} > 1$$

$$e^{\beta\mu(N^*-N)} < 1$$

follows. The other cases produce the same final result. In this case,

$$P(c \Rightarrow c^*) = \bar{\pi}_1^0(c) + \bar{\pi}_2^0(c) e^{\beta\mu(N^*-N)}$$

and

$$P(c^* \Rightarrow c) = \bar{\pi}_{1^*}^0(c^*) e^{-\beta(E-E^*)+\beta\mu(N-N^*)} + \bar{\pi}_{2^*}^0(c^*) e^{-\beta(E-E^*)} = e^{-\beta(E-E^*)+\beta\mu(N-N^*)} \left[\bar{\pi}_{1^*}^0(c^*) + \bar{\pi}_{2^*}^0(c^*) e^{\beta\mu(N^*-N)} \right]$$

The ratio of the forward to the reverse probabilities is:

$$\frac{P(c \Rightarrow c^*)}{P(c^* \Rightarrow c)} = \frac{1}{e^{-\beta(E-E^*)+\beta\mu(N-N^*)}} \frac{\bar{\pi}_1^0(c) + \bar{\pi}_2^0(c) e^{\beta\mu(N^*-N)}}{\bar{\pi}_{1^*}^0(c^*) + \bar{\pi}_{2^*}^0(c^*) e^{\beta\mu(N^*-N)}}$$

Since the transformation detailed balance condition is satisfied, $\bar{\pi}_1^0(c) = \bar{\pi}_{1^*}^0(c^*)$ and $\bar{\pi}_2^0(c) = \bar{\pi}_{2^*}^0(c^*)$. The summations over $\alpha = 1, 2$ and $\alpha^* = 1^*, 2^*$ in the numerator and the denominator are therefore equal and the detailed balance condition holds:

$$\frac{P(c \Rightarrow c^*)}{P(c^* \Rightarrow c)} = e^{-\beta(E^*-E)+\beta\mu(N^*-N)} = \frac{\rho(c^*)}{\rho(c)}$$

5.3.4 Final Acceptance Probability in a Split-phase Step

In the example the product of the arguments in the minimum functions of Δ_α^0 and $\Theta_\alpha(c, c')$ is the ratio $\rho(c^*)/\rho(c)$ for both transformations $\alpha = 1$ and $\alpha = 2$. For $\alpha = 1$,

$$[1] \left[e^{-\beta(E^*-E)+\beta\mu(N^*-N)} \right] = \frac{\rho(c^*)}{\rho(c)}$$

while for $\alpha = 2$,

$$\left[e^{\beta\mu(N^*-N)} \right] \left[e^{-\beta(E^*-E)} \right] = \frac{\rho(c^*)}{\rho(c)}$$

One can generalize the example to a class of methods in which $k > 1$ intermediate steps are taken. At each intermediate step $j = 0, 1, \dots, k-1$, the acceptance probability Δ_α^j is given by:

$$\Delta_\alpha^j = \min \left(1, \frac{F_\alpha^j(\tilde{c}')}{F_\alpha^j(\tilde{c}^j)} \right)$$

so at the j 'th intermediate step the next intermediate configuration is:

$$\bar{c}^{j+1} = \begin{cases} \bar{c}' = \bar{Q}_\alpha^j \bar{c}^j & \text{with probability } \Delta_\alpha^j \\ \bar{c}^j & \text{otherwise} \end{cases}$$

The sequence of acceptance functions

$$F_\alpha^0, F_\alpha^1, \dots, F_\alpha^{k-1}$$

determines the intermediate acceptance probabilities; one then must choose the final acceptance probability $\Theta_\alpha(c, c')$ so that the detailed balance condition holds for the Markov process. The final probability must depend on information from the intermediate chain. Record, therefore, for the sequence of k intermediate transformations and acceptance steps a sequence of factors:

$$\delta_\alpha^0, \delta_\alpha^1, \dots, \delta_\alpha^{k-1}$$

which are defined by:

$$\delta_\alpha^j = \begin{cases} \frac{F_\alpha^j(\bar{c}')}{F_\alpha^j(\bar{c}^j)} & \text{if the candidate } \bar{c}' \text{ is accepted this step} \\ 1 & \text{otherwise} \end{cases}$$

If, at the j 'th intermediate step the candidate \bar{c}' is accepted, then information on the intermediate acceptance probability Δ_α^j is stored in δ_α^j . If the candidate is rejected, a factor of unity is recorded. At the end of the intermediate sequence, in which the final candidate c' is set equal to \bar{c}^k , determine a final factor δ_α^k such that

$$\delta_\alpha^0 \times \delta_\alpha^1 \times \dots \times \delta_\alpha^{k-1} \times \delta_\alpha^k = \frac{\rho(c')}{\rho(c)}$$

Thus the final factor can be computed from the intermediate factors $\delta_\alpha^0, \delta_\alpha^1, \dots, \delta_\alpha^{k-1}$ and from the ratios of the Gibbs probabilities of the previous member c of the Markov chain and of the final candidate c' :

$$\delta_\alpha^k = \frac{\rho(c')}{\rho(c)} \left[\prod_{j=0}^{k-1} \frac{1}{\delta_\alpha^j} \right]$$

The final acceptance probability is defined from the final factor by:

$$\Theta_\alpha(c, c') = \min(1, \delta_\alpha^k)$$

The next member of the Markov chain is thus:

$$c_{i+1} = \begin{cases} c' & \text{with probability } \Theta_\alpha(c, c') \\ c & \text{otherwise} \end{cases}$$

This is the split-phase Metropolis sampling method which is used in this thesis. In the implementation for the self-avoiding loops system the intermediate transformations $\{\tilde{Q}_\alpha^j\}$ are members of the pivot/inversion, translation, reconnection, and elementary excitation classes. The acceptance functions F_α^j are determined by the transformation class. A thorough description of the acceptance functions will be given at the end of this section after the proof of detailed balance for the split-phase Metropolis method.

Note that the standard Metropolis method can be expressed as an instance of the split-phase Metropolis method by setting all the acceptance functions $F_\alpha^j = 1$. Then each intermediate configuration is automatically accepted and the final candidate c' is unweighted; that is, the probability to generate c' from c is equal to the probability to generate c from c' . Since each $F_\alpha^j = 1$, each corresponding factor $\delta_\alpha^j = 1$ and thus the final factor $\delta_\alpha^k = \rho(c')/\rho(c)$. The final acceptance step in this case proceeds with the standard Metropolis probability

$$\Theta_\alpha(c, c') = \min\left(1, \frac{\rho(c')}{\rho(c)}\right)$$

5.3.5 Proof of Detailed Balance for Split-phase Metropolis

A proof of detailed balance for the split-phase Metropolis method follows. Consider two configurations c and c^* . The Markov transition probability $P(c \Rightarrow c^*)$ is the sum, over all the possible ways α to go from c to c^* , of the probability of taking each path. Define notation for the intermediate steps as follows. Let the configuration at the beginning of the Markov step be c , let the result of the Markov step be c^* , and let the intermediate configurations be:

$$c = \tilde{c}^0, \tilde{c}^1, \tilde{c}^2, \dots, \tilde{c}^k = c'$$

Each \tilde{c}^{j+1} is produced from \tilde{c}^j by the generation of an intermediate candidate followed by an intermediate acceptance or rejection of the candidate. Name the intermediate step \tilde{H}_α^j , so that

$$\tilde{c}^{j+1} = \tilde{H}_\alpha^j \tilde{c}^j$$

The transformation Q_α generating the final candidate c' is thus the composition of the \tilde{H}_α^j s:

$$Q_\alpha = \tilde{H}_\alpha^{k-1} \circ \tilde{H}_\alpha^{k-2} \circ \dots \circ \tilde{H}_\alpha^1 \circ \tilde{H}_\alpha^0$$

Define the intermediate probability $\tilde{\eta}_\alpha^j(\tilde{c}^j, \tilde{c}^{j+1})$ to be the probability of selecting \tilde{Q}_α^j to transform \tilde{c}^j to \tilde{c}^j and then of accepting or rejecting the candidate to produce \tilde{c}^{j+1} . The

probability of generating the final candidate

$$c' = Q_\alpha c$$

through the sequence of intermediate transformations and acceptance/rejections is thus:

$$\pi_\alpha(c) = \prod_{j=0}^{k-1} \tilde{\eta}_\alpha^j(\tilde{c}^j, \tilde{c}^{j+1})$$

Since the probability of accepting the final candidate is $\Theta_\alpha(c, c')$, the probability of transforming $c \Rightarrow c'$ by path α is

$$\eta_\alpha(c, c') = \pi_\alpha(c) \Theta_\alpha(c, c')$$

Suppose $c^* \neq c$, then the final candidate c' must be accepted with probability $\Theta_\alpha(c^*, c)$ in order to produce c^* . Then the Markov transition probability is the sum over all the paths α for which $Q_\alpha c = c^*$ of the probability to take each path:

$$P(c \Rightarrow c^*) = \sum_{\alpha | Q_\alpha c = c^*} \pi_\alpha(c) \Theta_\alpha(c^*, c)$$

The Markov transition probability $P(c^* \Rightarrow c)$ is a similar sum over all the paths α^* for which $Q_{\alpha^*} c^* = c$.

In order to prove that the detailed balance condition holds, one wishes to identify each forward transformation Q_α with an inverse transformation Q_{α^*} . Each forward transformation can be written as the composition of intermediate steps:

$$Q_\alpha = \tilde{H}_\alpha^{k-1} \circ \tilde{H}_\alpha^{k-2} \circ \dots \circ \tilde{H}_\alpha^1 \circ \tilde{H}_\alpha^0$$

which produce the intermediate configurations:

$$c = \tilde{c}^0, \tilde{c}^1, \tilde{c}^2, \dots, \tilde{c}^k = c' = c^*$$

The corresponding inverse transformation can be written as:

$$Q_{\alpha^*} = \tilde{H}_{\alpha^*}^0 \circ \tilde{H}_{\alpha^*}^1 \circ \dots \circ \tilde{H}_{\alpha^*}^{k-2} \circ \tilde{H}_{\alpha^*}^{k-1}$$

where each intermediate step in the forward sequence is reversed. The reverse sequence begins from c^* and leads to the configuration c , which is taken as the final candidate of the inverse step.

$$c^* = \tilde{c}^k, \tilde{c}^{k-1}, \tilde{c}^{k-2}, \dots, \tilde{c}^0 = c$$

The ordering of the superscripts will be reversed when discussing the inverse Markov step Q_{α^*} so that $\tilde{H}_{\alpha^*}^{k-1}$ is the first of the inverse intermediate steps to be applied, followed by $\tilde{H}_{\alpha^*}^{k-2}$, and so on until $\tilde{H}_{\alpha^*}^0$. Therefore, the forward and inverse intermediate steps are:

$$\tilde{c}^{j+1} = \tilde{H}_{\alpha}^j \tilde{c}^j \text{ at the } j\text{'th forward intermediate step, and}$$

$$\tilde{c}^j = \tilde{H}_{\alpha^*}^j \tilde{c}^{j+1}, \text{ at the } (k-j)\text{'th inverse intermediate step.}$$

The inverse $\tilde{H}_{\alpha^*}^{k-j}$ of the intermediate step \tilde{H}_{α}^j is defined as follows. The probabilities for the forward and inverse intermediate steps are computed. Recall that for each j , the intermediate step \tilde{H}_{α}^j consists of applying an intermediate transformation \tilde{Q}_{α}^j with probability $\tilde{\pi}_{\alpha}^j(\tilde{c}^j)$ to produce an intermediate candidate \tilde{c}' which is then accepted as the next member of the intermediate chain with probability:

$$\Delta_{\alpha}^j = \min \left(1, \frac{F_{\alpha}^j(\tilde{c}')}{F_{\alpha}^j(\tilde{c}^j)} \right)$$

The acceptance or rejection of the intermediate candidate produces two cases. Consider the first case in which the intermediate candidate is accepted. Then $\tilde{c}^{j+1} = \tilde{c}'$ and the intermediate factor δ_{α}^j is set to

$$\delta_{\alpha}^j = \frac{F_{\alpha}^j(\tilde{c}^{j+1})}{F_{\alpha}^j(\tilde{c}^j)}$$

The probability $\tilde{\eta}_{\alpha}^j(\tilde{c}^j, \tilde{c}^{j+1})$ of choosing the particular transformation \tilde{Q}_{α}^j and accepting the step is:

$$\tilde{\eta}_{\alpha}^j(\tilde{c}^j, \tilde{c}^{j+1}) = \tilde{\pi}_{\alpha}^j(\tilde{c}^j) \Delta_{\alpha}^j = \tilde{\pi}_{\alpha}^j(\tilde{c}^j) \min \left(1, \frac{F_{\alpha}^j(\tilde{c}^{j+1})}{F_{\alpha}^j(\tilde{c}^j)} \right) = \tilde{\pi}_{\alpha}^j(\tilde{c}^j) \min(1, \delta_{\alpha}^j)$$

In this case, where the candidate in the forward intermediate step is accepted, define the inverse intermediate step $\tilde{H}_{\alpha^*}^j$ as follows. Choose the inverse transformation $\tilde{Q}_{\alpha^*}^j$ of \tilde{Q}_{α}^j so that the candidate in the inverse intermediate step is:

$$\tilde{c}^j = \tilde{Q}_{\alpha^*}^j \tilde{c}^{j+1}$$

Then accept candidate so that the step in the forward sequence from \tilde{c}^j to \tilde{c}^{j+1} is reversed in the inverse sequence. The probability of choosing the inverse transformation $\tilde{Q}_{\alpha^*}^j$ is $\tilde{\pi}_{\alpha^*}^j(\tilde{c}^{j+1})$ while the probability of accepting the candidate \tilde{c}^j in the inverse step is:

$$\Delta_{\alpha^*}^j = \min \left(1, \frac{F_{\alpha^*}^j(\tilde{c}^j)}{F_{\alpha^*}^j(\tilde{c}^{j+1})} \right)$$

The intermediate factor recorded for the inverse step is the ratio of the acceptance functions since the candidate is accepted in the inverse step,

$$\delta_{\alpha^*}^j = \frac{F_{\alpha^*}^j(\tilde{c}^j)}{F_{\alpha^*}^j(\tilde{c}^{j+1})} = \frac{1}{\delta_{\alpha}^j}$$

The probability of choosing this inverse step $\tilde{H}_{\alpha^*}^j$ is then:

$$\tilde{\eta}_{\alpha^*}^j(\tilde{c}^{j+1}, \tilde{c}^j) = \tilde{\pi}_{\alpha^*}^j(\tilde{c}^{j+1}) \Delta_{\alpha^*}^j = \tilde{\pi}_{\alpha^*}^j(\tilde{c}^{j+1}) \min(1, \delta_{\alpha^*}^j) = \tilde{\pi}_{\alpha^*}^j(\tilde{c}^{j+1}) \min\left(1, \frac{1}{\delta_{\alpha}^j}\right)$$

The transformation detailed balance indicates here that $\tilde{\pi}_{\alpha^*}^j(\tilde{c}^{j+1}) = \tilde{\pi}_{\alpha}^j(\tilde{c}^j)$, so the probabilities of taking the forward step \tilde{H}_{α}^j and of taking the reverse step $\tilde{H}_{\alpha^*}^j$ are:

$$\tilde{\eta}_{\alpha}^j(\tilde{c}^j, \tilde{c}^{j+1}) = \tilde{\pi}_{\alpha}^j(\tilde{c}^j) \min(1, \delta_{\alpha}^j)$$

and

$$\tilde{\eta}_{\alpha^*}^j(\tilde{c}^{j+1}, \tilde{c}^j) = \tilde{\pi}_{\alpha}^j(\tilde{c}^j) \min\left(1, \frac{1}{\delta_{\alpha}^j}\right)$$

The second case is when the intermediate candidate \tilde{c}' generated in the forward intermediate step is rejected. In this case, the configuration \tilde{c}^j is repeated in the forward intermediate sequence so that:

$$\tilde{c}^{j+1} = \tilde{c}^j$$

The intermediate factor δ_{α}^j is set to 1 for this j 'th step. The probability of rejecting the candidate \tilde{c}' is $1 - \Delta_{\alpha}^j$ where

$$\Delta_{\alpha}^j = \min\left(1, \frac{F_{\alpha}^j(\tilde{c}')}{F_{\alpha}^j(\tilde{c}^j)}\right)$$

Since the probability of choosing the intermediate transformation \tilde{Q}_{α}^j to create the intermediate candidate:

$$\tilde{c}' = \tilde{Q}_{\alpha}^j \tilde{c}^j$$

is given by $\tilde{\pi}_{\alpha}^j(\tilde{c}^j)$, the probability of taking the forward intermediate step \tilde{H}_{α}^j involving the rejection of this attempted move is:

$$\tilde{\eta}_{\alpha}^j(\tilde{c}^j, \tilde{c}^{j+1}) = \tilde{\pi}_{\alpha}^j(\tilde{c}^j) [1 - \Delta_{\alpha}^j] = \tilde{\pi}_{\alpha}^j(\tilde{c}^j) \left[1 - \min\left(1, \frac{F_{\alpha}^j(\tilde{c}')}{F_{\alpha}^j(\tilde{c}^j)}\right)\right]$$

Define for this case the inverse intermediate step $\tilde{H}_{\alpha^*}^j$ as follows. The step begins with \tilde{c}^{j+1} . Choose the *same* transformation \tilde{Q}_{α}^j that is used in the forward step \tilde{H}_{α}^j . Since the

intermediate configuration \tilde{c}^{j+1} at the start of the inverse step is the same as \tilde{c}^j , which is the intermediate configuration at the start of the forward step, the transformation \tilde{Q}_α^j produces the same candidate \tilde{c}' in the inverse step as in the forward step. Reject the candidate in the inverse step and set $\delta_{\alpha^*}^j = 1$. In this case,

$$\Delta_{\alpha^*}^j = \min \left(1, \frac{F_\alpha^j(\tilde{c}')}{F_\alpha^j(\tilde{c}^{j+1})} \right) = \min \left(1, \frac{F_\alpha^j(\tilde{c}')}{F_\alpha^j(\tilde{c}^j)} \right) = \Delta_\alpha^j$$

The probability $1 - \Delta_{\alpha^*}^j$ of rejecting the candidate in the inverse step is therefore equal to the probability of rejecting the candidate in the forward step. The total probability of taking the inverse intermediate step $\tilde{H}_{\alpha^*}^j$ is therefore the same as the probability of taking the forward intermediate step. Thus,

$$\tilde{\eta}_{\alpha^*}^j(\tilde{c}^{j+1}, \tilde{c}^j) = \tilde{\eta}_\alpha^j(\tilde{c}^j, \tilde{c}^{j+1})$$

in the case when the candidate is rejected in the forward step.

Now that the inverse intermediate steps $\tilde{H}_{\alpha^*}^j$ have been defined for both the case of acceptance and the case of rejection of the candidate in the forward step \tilde{H}_α^j , return to the composite moves Q_α and Q_{α^*} which generate the final candidates in the forward and inverse steps of the Markov process. The forward transformation Q_α is the composition of k intermediate steps:

$$Q_\alpha = \tilde{H}_\alpha^{k-1} \circ \tilde{H}_\alpha^{k-2} \circ \dots \circ \tilde{H}_\alpha^1 \circ \tilde{H}_\alpha^0$$

and acts on c to produce the candidate c^* :

$$c^* = Q_\alpha c$$

with probability:

$$\pi_\alpha(c) = \prod_{j=0}^{k-1} \tilde{\eta}_\alpha^j(\tilde{c}^j, \tilde{c}^{j+1})$$

The corresponding probability to select the inverse move Q_{α^*} when the current configuration is c^* is:

$$\pi_{\alpha^*}(c^*) = \prod_{j=0}^{k-1} \tilde{\eta}_{\alpha^*}^j(\tilde{c}^{j+1}, \tilde{c}^j)$$

The probability $\eta_\alpha(c, c^*)$ of choosing the transformation Q_α to apply to c and of accepting the resulting candidate c^* is:

$$\eta_\alpha(c, c^*) = \pi_\alpha(c) \Theta_\alpha(c, c^*) = \left[\prod_{j=0}^{k-1} \tilde{\eta}_\alpha^j(\tilde{c}^j, \tilde{c}^{j+1}) \right] \Theta_\alpha(c, c^*)$$

We have already defined the forward and inverse sequences of intermediate factors $\{\delta_\alpha^j\}$ and $\{\delta_{\alpha^*}^j\}$, and have computed the intermediate probabilities $\{\tilde{\eta}_\alpha^j(\tilde{c}^j, \tilde{c}^{j+1})\}$ and $\{\tilde{\eta}_{\alpha^*}^j(\tilde{c}^{j+1}, \tilde{c}^j)\}$ which depend on the $\{\delta_\alpha^j\}$. Note that the relation

$$\delta_{\alpha^*}^j = \frac{1}{\delta_\alpha^j}$$

holds for each j whether the candidate is accepted or rejected at that step. The final acceptance probability $\Theta_\alpha(c, c^*)$ depends on the final factor δ_α^k which is computed as follows:

$$\delta_\alpha^k = \frac{\rho(c^*)}{\rho(c)} \left[\prod_{j=0}^{k-1} \frac{1}{\delta_\alpha^j} \right]$$

The final acceptance probability in the forward step α is:

$$\Theta_\alpha(c, c^*) = \min(1, \delta_\alpha^k)$$

The final acceptance probability in the inverse step α^* is similarly:

$$\Theta_{\alpha^*}(c^*, c) = \min(1, \delta_{\alpha^*}^k)$$

where

$$\delta_{\alpha^*}^k = \frac{\rho(c)}{\rho(c^*)} \left[\prod_{j=0}^{k-1} \delta_{\alpha^*}^j \right] = \frac{1}{\delta_\alpha^k}$$

We wish to determine the relation between the probability $\eta_\alpha(c, c^*)$ of taking a particular forward path α and the probability $\eta_{\alpha^*}(c^*, c)$ of taking the corresponding inverse path α^* . Break up the indices $j = 0, 1, \dots, k-1$ corresponding to intermediate steps into two disjoint subsets:

$$I_a = \{j \in [0, k-1], \text{ such that the candidate is accepted at the } j\text{'th step}\}$$

and

$$I_r = \{j \in [0, k-1], \text{ such that the candidate is rejected at the } j\text{'th step}\}$$

Then the product of the intermediate probabilities $\tilde{\eta}_\alpha^j(\tilde{c}^j, \tilde{c}^{j+1})$ can be broken into two products in the composite probability, giving:

$$\eta_\alpha(c, c^*) = \left[\prod_{j \in I_r} \tilde{\eta}_\alpha^j(\tilde{c}^j, \tilde{c}^{j+1}) \right] \left[\prod_{j \in I_a} \tilde{\eta}_\alpha^j(\tilde{c}^j, \tilde{c}^{j+1}) \right] \Theta_\alpha(c, c^*) =$$

$$\left[\prod_{j \in I_r} \tilde{\eta}_{\alpha}^j(\tilde{c}^j, \tilde{c}^{j+1}) \right] \left[\prod_{j \in I_a} \tilde{\pi}_{\alpha}^j(\tilde{c}^j) \min(1, \delta_{\alpha}^j) \right] \Theta_{\alpha}(c, c^*)$$

Create another two sets of indices, I_{up} and I_{down} , such that $I_{up} \cup I_{down} = I_a \cup \{k\}$ as follows:

$$I_{up} = \{j \in I_a \cup \{k\}, \text{ such that } \delta_{\alpha}^j \geq 1\}$$

and

$$I_{down} = \{j \in I_a \cup \{k\}, \text{ such that } \delta_{\alpha}^j < 1\}$$

Then the products in $\eta_{\alpha}(c, c^*)$ can be further separated:

$$\eta_{\alpha}(c, c^*) = \left[\prod_{j \in I_r} \tilde{\eta}_{\alpha}^j(\tilde{c}^j, \tilde{c}^{j+1}) \right] \left[\prod_{j \in I_a} \tilde{\pi}_{\alpha}^j(\tilde{c}^j) \right] \left[\prod_{j \in I_{up}} \min(1, \delta_{\alpha}^j) \right] \left[\prod_{j \in I_{down}} \min(1, \delta_{\alpha}^j) \right]$$

The intermediate steps at which candidates are accepted are the same in the inverse sequence α^* as in the forward sequence. Write, therefore, the probability of taking the inverse path α^* from configuration c^* to configuration c as:

$$\begin{aligned} \eta_{\alpha^*}(c^*, c) &= \left[\prod_{j \in I_r} \tilde{\eta}_{\alpha^*}^j(\tilde{c}^{j+1}, \tilde{c}^j) \right] \left[\prod_{j \in I_a} \tilde{\pi}_{\alpha^*}^j(\tilde{c}^{j+1}) \min(1, \delta_{\alpha^*}^j) \right] \Theta_{\alpha^*}(c^*, c) = \\ &\left[\prod_{j \in I_r} \tilde{\eta}_{\alpha^*}^j(\tilde{c}^{j+1}, \tilde{c}^j) \right] \left[\prod_{j \in I_a} \tilde{\pi}_{\alpha^*}^j(\tilde{c}^{j+1}) \min\left(1, \frac{1}{\delta_{\alpha}^j}\right) \right] \min\left(1, \frac{1}{\delta_{\alpha}^k}\right) \end{aligned}$$

Now break up the products of the min's over the sets of indices I_{up} and I_{down} which were defined for the forward Markov step:

$$\eta_{\alpha^*}(c^*, c) = \left[\prod_{j \in I_r} \tilde{\eta}_{\alpha^*}^j(\tilde{c}^{j+1}, \tilde{c}^j) \right] \left[\prod_{j \in I_a} \tilde{\pi}_{\alpha^*}^j(\tilde{c}^{j+1}) \right] \left[\prod_{j \in I_{up}} \min\left(1, \frac{1}{\delta_{\alpha}^j}\right) \right] \left[\prod_{j \in I_{down}} \min\left(1, \frac{1}{\delta_{\alpha}^j}\right) \right]$$

Since for $j \in I_{up}$ the factor $\delta_{\alpha}^j \geq 1$, the results of the min functions may be calculated:

$$\min(1, \delta_{\alpha}^j) = \delta_{\alpha}^j \text{ and } \min\left(1, \frac{1}{\delta_{\alpha}^j}\right) = 1 \text{ for } j \in I_{up}$$

The min functions may be similarly resolved for $j \in I_{down}$. Performing this action yields the expressions for the probabilities of the forward and inverse paths:

$$\eta_{\alpha}(c, c^*) = \left[\prod_{j \in I_r} \tilde{\eta}_{\alpha}^j(\tilde{c}^j, \tilde{c}^{j+1}) \right] \left[\prod_{j \in I_a} \tilde{\pi}_{\alpha}^j(\tilde{c}^j) \right] \left[\prod_{j \in I_{up}} \delta_{\alpha}^j \right]$$

and

$$\eta_{\alpha^*}(c^*, c) = \left[\prod_{j \in I_r} \tilde{\eta}_{\alpha^*}^j(\tilde{c}^{j+1}, \tilde{c}^j) \right] \left[\prod_{j \in I_a} \tilde{\pi}_{\alpha^*}^j(\tilde{c}^{j+1}) \right] \left[\prod_{j \in I_{down}} \frac{1}{\delta_{\alpha}^j} \right]$$

The transformation detailed balance condition gives the equality:

$$\tilde{\pi}_{\alpha^*}^j(\tilde{c}^{j+1}) = \tilde{\pi}_{\alpha}^j(\tilde{c}^j)$$

for $j \in I_a$, and we have shown that

$$\tilde{\eta}_{\alpha^*}^j(\tilde{c}^{j+1}, \tilde{c}^j) = \tilde{\eta}_{\alpha}^j(\tilde{c}^j, \tilde{c}^{j+1})$$

for $j \in I_r$. The first two products in the forward and inverse probabilities are therefore equal; so write

$$\eta_{\alpha}(c, c^*) = \kappa_{\alpha} \left[\prod_{j \in I_{up}} \delta_{\alpha}^j \right]$$

and

$$\eta_{\alpha^*}(c^*, c) = \kappa_{\alpha} \left[\prod_{j \in I_{down}} \frac{1}{\delta_{\alpha}^j} \right]$$

where

$$\kappa_{\alpha} = \left[\prod_{j \in I_r} \tilde{\eta}_{\alpha}^j(\tilde{c}^j, \tilde{c}^{j+1}) \right] \left[\prod_{j \in I_a} \tilde{\pi}_{\alpha}^j(\tilde{c}^j) \right] = \left[\prod_{j \in I_r} \tilde{\eta}_{\alpha^*}^j(\tilde{c}^{j+1}, \tilde{c}^j) \right] \left[\prod_{j \in I_a} \tilde{\pi}_{\alpha^*}^j(\tilde{c}^{j+1}) \right]$$

Now since the δ_{α}^j and $\delta_{\alpha^*}^j$ are unity for $j \in I_r$, the condition:

$$\prod_{j=0}^k \delta_{\alpha}^j = \frac{\rho(c^*)}{\rho(c)}$$

implies that:

$$\prod_{j \in I_a \cup \{k\}} \delta_{\alpha}^j = \left[\prod_{j \in I_a \cup \{k\}} \delta_{\alpha}^j \right] \left[\prod_{j \in I_r} \delta_{\alpha}^j \right] = \frac{\rho(c^*)}{\rho(c)}$$

Since $I_a \cup \{k\} = I_{up} \cup I_{down}$, the previous expression can be rearranged by taking the factors for $j \in I_{down}$ to the right-hand side:

$$\left[\prod_{j \in I_{up}} \delta_{\alpha}^j \right] = \frac{\rho(c^*)}{\rho(c)} \left[\prod_{j \in I_{down}} \frac{1}{\delta_{\alpha}^j} \right]$$

Now substituting this equation into the forward probability gives the pair of equations:

$$\eta_{\alpha}(c, c^*) = \kappa_{\alpha} \frac{\rho(c^*)}{\rho(c)} \left[\prod_{j \in I_{down}} \frac{1}{\delta_{\alpha}^j} \right]$$

and

$$\eta_{\alpha^*}(c^*, c) = \kappa_{\alpha} \left[\prod_{j \in I_{down}} \frac{1}{\delta_{\alpha}^j} \right]$$

Hence for every path α and its corresponding inverse α^* , we have:

$$\eta_{\alpha}(c, c^*) = \frac{\rho(c^*)}{\rho(c)} \eta_{\alpha^*}(c^*, c)$$

The Markov transition probability $P(c^* \Rightarrow c)$ is the sum over all paths α such that $Q_{\alpha}c = c^*$ of the probability $\eta_{\alpha}(c, c^*)$ to take that particular path. That is:

$$P(c \Rightarrow c^*) = \sum_{\alpha | Q_{\alpha}c = c^*} \eta_{\alpha}(c, c^*)$$

and

$$P(c^* \Rightarrow c) = \sum_{\alpha^* | Q_{\alpha^*}c^* = c} \eta_{\alpha^*}(c^*, c)$$

where, for split-phase Metropolis we have:

$$P(c \Rightarrow c^*) = \sum_{\alpha | Q_{\alpha}c = c^*} \frac{\rho(c^*)}{\rho(c)} \eta_{\alpha^*}(c^*, c) = \frac{\rho(c^*)}{\rho(c)} \sum_{\alpha | Q_{\alpha}c = c^*} \eta_{\alpha^*}(c^*, c)$$

Since the forward and inverse paths α and α^* have a one-to-one relationship, the summations in the forward and reverse Markov transition probabilities are the same and thus:

$$\frac{P(c \Rightarrow c^*)}{P(c^* \Rightarrow c)} = \frac{\rho(c^*)}{\rho(c)}$$

The detailed balance condition is therefore satisfied for the Markov process defined by the split-phase Metropolis algorithm. Q.E.D

5.3.6 Implementation of Split-phase Sampling for Self-avoiding Loops

The first section of this chapter, Section 5.1, presented a list of types of transformations for the self-avoiding loops system. The split-phase Metropolis algorithm presented in the previous section is constructed from a collection of transformations $\{\tilde{Q}_{\alpha}\}$ to be used in generating the intermediate configurations along with a collection of acceptance functions F_{α} to be used in accepting or rejecting intermediate candidates. In the split-phase algorithm used in this thesis to compute the equilibria of the self-avoiding loops system, the set of intermediate transformations consists of the possible moves made by pivots, translates, reconnections, elementary additions/deletions, and elementary excitations. The random selection of a transformation for application to a configuration \tilde{c}^j begins by randomly choosing

one of the above transformation classes; the effect of the transformation class depends on further random choices as described in Section 5.1. The collection of transformations formed by the set of transformation classes has been shown to satisfy the transformation detailed balance condition. The acceptance functions F_{α}^j corresponding to each of the transformation classes are given in Table 5.7

The pivot, translate, and reconnection moves do not change the number of links N in the configuration and change the energy E^{int} moderately. They are accepted automatically in the intermediate steps. Elementary additions/deletions change N while changing the energy by only a relatively small amount. They are accepted in the intermediate steps only on the basis of the change in the N dependent portion of the complete Gibbs weight:

$$\rho = e^{-\beta E^{int} - \beta \nu N}$$

In regions of the parameter space (β, ν) in which $\nu \gg 1$ but $\beta \ll 1$, the change in N of two or four links often makes a greater difference in the Gibbs weight than the change in energy brought about by adding or deleting the links. The split-phase method allows the N dependent portion of the Gibbs weight to be checked immediately upon an addition/deletion move while deferring the computationally expensive energy check to the end of the intermediate sequence. The desire to split the N dependent and E dependent portions of the detailed balance condition was my original motivation for developing the split-phase Metropolis algorithm. Elementary excitations are used in regions of the parameter space in which both changes in energy and changes in N have significant effects on the Gibbs weight. The elementary excitations attempt to change both N and E^{int} greatly, but in a manner such that the effects cancel in the Gibbs weight. These moves are therefore subject to an immediate acceptance base on the full Gibbs weight, resulting in a standard Metropolis acceptance in the middle of the intermediate sequence. They thus require energy computations, but this class can be selected with a low probability in order to maintain the overall efficiency of the algorithm. The split-phase method does not eliminate the need for energy computations, but insures that they are only used when the change of energy can be expected to have a significant effect on the Gibbs probability.

A pseudo-code description of the main Monte-Carlo loop is given in Table 5.8. Aspects of the programming implementation of the algorithm are given in Section 5.4. The number of intermediate trials k was set so that the final candidate was accepted about 50% of the time. Employing more intermediate trials decreases the correlation between

Table 5.7: Split-phase acceptance functions

Transformation Class	Acceptance Function
pivots	1 (automatic acceptance)
translates	1
reconnections	1
elementary additions/deletions	$e^{-\beta\nu N(\bar{c})}$
elementary excitations	$e^{-\beta E^{int}(\bar{c}) - \beta\nu N(\bar{c})}$

the candidate configuration and the previous configuration in the Markov chain, but also decreases the probability that the candidate will be accepted. The 50% rule of thumb [78] seems to provide a good balance between the autocorrelation time and the computational work.

5.3.7 Energy Well Escapes

The numerical results which I show later in Chapter 6 employ the pivots, translations, reconnections, elementary additions/deletions, and elementary excitation moves with the acceptance functions given in Table 5.7. I have also experimented, however, with another application of the split-phase machinery which I believe bears mention. For simulations with very large $|\beta|$, positive or negative, the probable configurations sometimes break up into a collection of “ground states” [125]. In the vortex system at negative temperature for example, the probable configurations were collections of dipoles as shown in Figure 5.9. For a given number of dipoles there is some freedom to move the dipoles and to add small bumps or kinks. The states with different numbers of dipole vortices, however, are separated by gaps of $\sim 2L$ vortices in N . The probability of bridging such a gap through the process of building up a closed loop of $2L$ links with elementary additions and then breaking the loop into a pair of dipoles is very small. There is therefore a sort of “probability barrier” between states with different numbers of dipoles at negative temperatures. I was able for the self-avoiding loops system to identify an elementary excitation which allowed the algorithm to jump directly from one probability well into another. For general systems which break up into a set of ground states, however, such transformations may not be easily implemented.

An alternative to elementary excitation moves is a sort of “annealing” process whereby the temperature constraints are relaxed and then re-imposed. I experimented with

Table 5.8: Monte Carlo algorithm

```

(set Number of Trials M)
(set Number of Sub-Configurations k)
(set initial configuration  $c_0$ )
(do i = 0 to M:)
  {
    (set  $\bar{c}^0 = c_i$ )
    (do j = 0 to k-1:)
      {
        (choose randomly a transformation class)
        (perform transformation on  $\bar{c}^j$  to obtain candidate  $\bar{c}'$ )
        (calculate  $r = F_\alpha^j(\bar{c}')/F_\alpha^j(\bar{c}^j)$  depending on transformation class)
        (if RANDOM[01]  $\leq \min(1, r)$  then)
          (set  $\bar{c}^{j+1} = \bar{c}'$ )
          (set  $\delta_\alpha^j = r$ )
        (else)
          (set  $\bar{c}^{j+1} = \bar{c}^j$ )
          (set  $\delta_\alpha^j = 1$ )
      }
    (set candidate  $c' = \bar{c}^k$ )
    (calculate  $\rho(c')/\rho(c_i)$ )
    (calculate final factor  $\delta_\alpha^k$ )
    (if RANDOM[01]  $\leq \min(1, \delta_\alpha^k)$  then)
      (set  $c_{i+1} = c'$ )
    (else)
      (set  $c_{i+1} = c_i$ )
    (record statistics on  $c_{i+1}$ )
  }
(terminate)

```

this idea in the split-phase framework by taking a fairly large k and checking the complete probability for *each* transformation class, but with random temperatures $\tilde{\beta}$ which were less restrictive than the overall simulation temperature β . The intermediate acceptance functions are:

$$F_{\alpha}^j(\tilde{c}) = e^{-\tilde{\beta}E^{int}(\tilde{c}) - \tilde{\beta}\nu N(\tilde{c})}$$

The relaxed acceptance steps occasionally allowed large hops with a small value of $|\tilde{\beta}|$, which were then slowly pulled down into another well by the more probable temperatures nearer β . I have not carefully assessed the performance of this algorithm, as the elementary excitation method proved more useful in the self-avoiding loops system. Nevertheless, the random temperature process suggests an avenue for equilibrating systems in which the high-probability regions are separated by probability barriers.

5.4 Performance

This section discusses a number of issues related to the performance of the computational simulation. First, the computational work involved in the simulation is examined. The number of computer operations required to perform the transformations and to calculate the observable quantities is discussed, and the data structures employed are described. The runtime of the Monte-Carlo algorithm as a function of the system size and parameters is examined. Next, the performance of the histogram sampling method is discussed. Section 4.3 gave an overview of the histogram sampling technique and of the Ferrenberg-Swendsen method for combining multiple histograms. This section describes some results for the self-avoiding loops system. Finally, the effectiveness of the split-phase Metropolis sampling technique is discussed.

5.4.1 Implementation and Runtime

The computational algorithm has two distinct steps. In the first step the Monte Carlo algorithm generates a sequence of configurations which represent the self-avoiding loops system for particular values of the inverse temperature β and the loop self-energy ν . Observable quantities are computed for each configuration in the sequence; these values are stored in histograms over the configuration energy and number of links. A number of runs at different parameter values (β, ν) may be made during this step. The second step processes

the histogram data to generate values of the observable averages at arbitrary points in the (β, ν) plane. Plots of thermodynamic quantities as functions of β and ν can be generated in the second step.

The first step is more computationally intensive by far than the second step. A great number of configurations must be generated, as the statistical error in the final results decreases only as $\mathcal{O}(1/\sqrt{M})$ where M is the number of configurations sampled. Decreasing the statistical error by a factor of 10, therefore, requires 100 times as many configurations. Once the configurations have been generated and the results stored in histograms, however, determining the ensemble averages requires relatively little work. Computing the average value of an observable quantity at each point (β, ν) in parameter space requires a number of operations only on the order of the number of bins in the histogram. Hundreds of hours were spent running the Monte Carlo code which sampled the configurations, while the final pictures included in Chapter 6 required only a modest number of minutes of cpu time.

The Monte Carlo code which generated the configurations and created the histograms was written in ANSI-C. The the C code was not as easily optimized as FORTRAN would have been, but provided more flexibility in memory management and in data structures. The histogram processing routines were implemented in Matlab, a data language licensed by the The Mathworks, Inc. of Natick Mass. The Matlab language is interpreted rather than compiled and is therefore significantly slower than C or FORTRAN. This was not a severe handicap in the histogram processing step, however. The use of Matlab provided flexibility in handling the data and gave easy access to graphical output. As is stated in Section 4.3.4, graphical monitoring is important for insuring the integrity of the histogram merging process.

The code which generated the configurations must apply the transformations listed in Section 5.1, accept and reject candidate configurations in Metropolis steps, compute the energy, number of links, and desired observable quantities of the configurations, and store and output histograms. Algorithmic descriptions of the components of the Monte Carlo method are given in Sections 5.1 and 5.3.6. The main algorithm is given in Table 5.8, while the algorithms for pivots, translates, reconnections, elementary loop additions/deletions, and elementary excitations are given in Tables 5.1, 5.2, 5.3, 5.4, 5.5 and 5.6. A discussion of the computational work required for various operations and of the data structures employed in the algorithm follows.

Individual vortex links in the collection of vortex loops need to be referenced in

two ways. In order to identify the links in a loop or in an arc of a loop one should be able to reference the vortex links in head-to-tail order within each loop. On the other hand, in order to check vortex self-avoidance or to find sites for reconnection events one should be able to reference the links by their position in the domain. The first sort of referencing is accomplished by representing the configuration of vortex loops as a linked list of loops, with each loop possessing a linked list of nodes in head-to-tail order. Employing linked lists instead of arrays supports link additions, deletions, and connectivity changes efficiently. The lists are used to identify and move loops and arcs of loops in the pivot and translate class transformations. The second sort of link referencing, by position in the domain, is accomplished by maintaining two hash tables: one of occupied sites and one of plaquettes which are bordered by occupied sites. The entries of the tables contain pointers to the corresponding links. Referencing by position is used to check if the result of a pivot or translate is self-avoiding, and to locate sites for reconnection events or for the addition or deletion of elementary loops. The use of the hash tables allows each site to be searched in $\mathcal{O}(1)$ time, as opposed to searching the lists of vortex links looking for a link that matches a particular location. In checking the self-avoidance of a pivot move which alters the positions of n links, for instance, the hash table search requires $\mathcal{O}(n)$ operations to examine the n new locations, while searching the list of links would require examining on the order of N elements for each location, leading to a time of order $\mathcal{O}(nN)$ where N is the total number of vortex links in the configuration. The use of hash table referencing, as suggested in [100], greatly reduces the time required to check the self-avoidance of pivot and translation moves. Reconnection events are only possible at plaquettes which are bordered on all four sides by vortex links. The algorithm maintains a list of such plaquettes to facilitate quick selection of reconnection sites.

These data structures allow each transformation to be carried out in a number of operations proportional to the number of links which are changed by the transformation. The metropolis acceptance/rejection steps require copying a candidate configuration to the new configuration or copying the old configuration to the new configuration. This can be accomplished in $\mathcal{O}(N)$ operations where N is the number of vortex links in the configuration. Calculating and recording statistics such as loop sizes can also be performed in $\mathcal{O}(N)$ operations.

The one operation in the present algorithm for which the computational work does not scale linearly with the number of links in the system is the computation of the energy

of a configuration. The interaction energy is given by a double sum over all pairs of vortex links in the system:

$$E^{int}(c) = \frac{1}{2} \sum_{i=1}^N \sum_{j \neq i} \vec{\xi}_i \cdot \vec{\xi}_j G(\vec{x}_i - \vec{x}_j)$$

Since there are of the order N^2 such pairs, a direct calculation of the energy requires $\mathcal{O}(N^2)$ time. In the simulation of large enough systems, most of the runtime is consumed in the calculation of the energy. An $\mathcal{O}(N^2)$ scaling for the runtime implies that doubling the system length L , which increases the domain volume and the number of vortices by a factor of eight, would increase the runtime by a factor of sixty-four. The energy calculation is thus the limiting factor in simulating large vortex systems. For small to moderate system sizes, however, such as the $L = 4$ to $L = 16$ domains studied in this thesis, the energy calculation may be implemented in such a way that the time spent in energy calculations remains manageable. The use of the split-phase metropolis sampling reduces the number of energy calculations required by the algorithm, and tabulating the lattice Green function $G(\vec{x})$ reduces the time required to calculate each vortex-vortex interaction.

Table 5.9 shows the runtime per trial of the Monte Carlo algorithm by the number of vortex links N and the number of intermediate steps k taken in the split-phase process. The runs were executed on a collection of Sparc 2's at Lawrence Berkeley Laboratory. Table 5.10 shows the energy calculation time by the number of links in the configuration. A typical number of links in a domain of size $L = 8$ is $N = 128 - 256$, while a typical number of links in a domain of size $L = 16$ is $N = 2048$. Table 5.11 shows the percentage of the runtime which is consumed in the energy calculation. At $L = 8$, the energy calculation requires only 40% - 60% of the runtime, although this fraction rises to about 95% of the runtime at $L = 16$.

The scaling of the energy calculation time with the number of links is shown on log-log axis in Figure 5.13. The time scales with the square of the number of links. Figure 5.14 shows the remaining portion of the runtime: the runtime minus the energy calculation time. Plots for different values of k are shown with solid lines as functions of N ; a dotted line of slope one is plotted as a reference. The portion of the runtime not in the energy calculation scales linearly with N for large N .

The energy calculation time currently limits the size of the vortex systems which

Table 5.9: Runtime per Trial (sec)

k	$N = 32$	$N = 64$	$N = 128$	$N = 256$	$N = 512$	$N = 1024$	$N = 2048$
1	0.0020	0.0037	0.0088	0.0260	0.0968	0.3996	1.8467
2	0.0029	0.0047	0.0099	0.0273	0.1009	0.4012	1.8351
3	0.0039	0.0054	0.0110	0.0289	0.1011	0.4065	1.8515
4	0.0045	0.0064	0.0119	0.0297	0.1029	0.4084	1.8446
8	0.0081	0.0097	0.0156	0.0351	0.1109	0.4347	1.8679
16	0.0143	0.0165	0.0231	0.0449	0.1204	0.4574	1.9101

Table 5.10: Energy calculation time per trial (sec)

	$N = 32$	$N = 64$	$N = 128$	$N = 256$	$N = 512$	$N = 1024$	$N = 2048$
	0.0003	0.0011	0.0043	0.0178	0.0788	0.3654	1.7654

Table 5.11: Fraction of runtime calculating energy (%)

k	$N = 32$	$N = 64$	$N = 128$	$N = 256$	$N = 512$	$N = 1024$	$N = 2048$
1	20	30	48	68	82	91	97
2	10	23	44	65	79	90	96
3	8	20	39	60	78	88	96
4	7	19	35	59	77	88	95
8	5	12	29	52	71	86	94
16	3	7	18	41	64	82	92

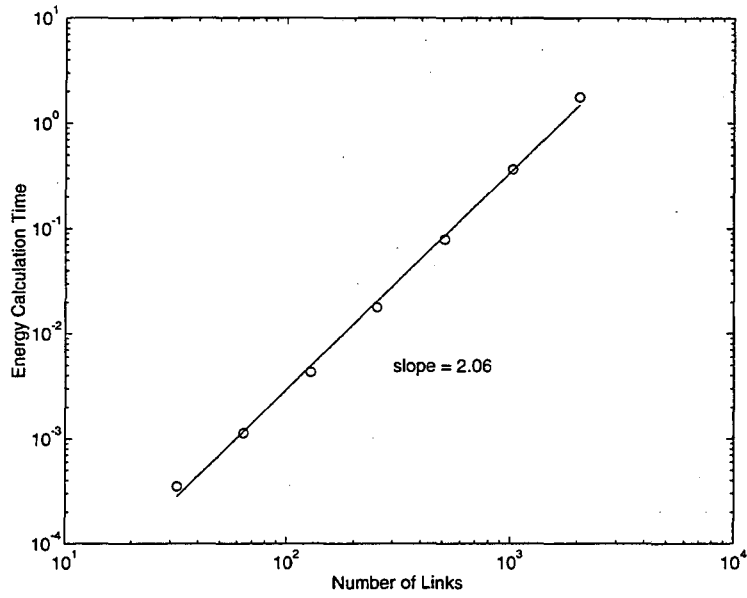


Figure 5.13: Energy calculation time vs. number of vortices

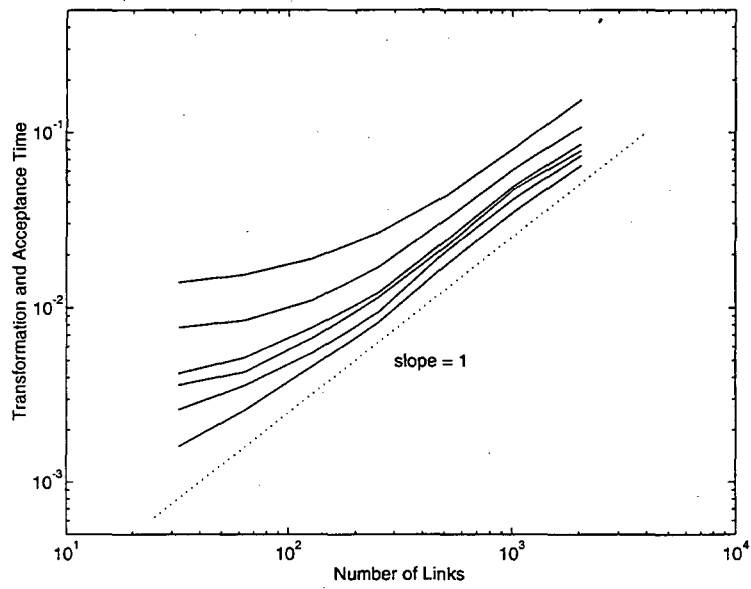


Figure 5.14: Transformation and statistics time vs. number of vortices

can be simulated. There exist, however, algorithms for calculating the energy sum

$$E^{int}(c) = \frac{1}{2} \sum_{i=1}^N \sum_{j \neq i} \vec{\xi}_i \cdot \vec{\xi}_j G(\vec{x}_i - \vec{x}_j)$$

in less than $\mathcal{O}(N^2)$ operations. In the current algorithm, the periodic Green function $G(\vec{x})$ was calculated by the Ewald summation technique [3] and stored in a lookup table. The Ewald summation technique represents the Green function in terms of a sum of Fourier modes and a sum of Gaussian functions. A method developed by Strain [135] employs fast Fourier transforms and fast Gauss transforms to calculate the energy sum. While the overhead involved in this method makes it impractical for use with small and moderate sized systems, the fast method could greatly reduce the time required to calculate the energy of large systems. Such a fast method is virtually necessary in order to study a system with a very large number of links.

5.4.2 Histogram Convergence

The histogram sampling method for calculating ensemble average values at arbitrary points in the (β, ν) plane is described in Section 4.3. Also described is a method of merging histograms taken during different Monte Carlo runs into a single dataset. These methods are used to collect data and produce the results of Chapter 6. This section discusses some aspects of accuracy and convergence in the histogram framework.

Histograms were sampled during a number of Monte Carlo runs simulating the self-avoiding loops system in the grand canonical ensemble at different (β, ν) values. The histograms were then merged into a single reference probability function using the Ferrenberg-Swendsen fixed point method described in Section 4.3.3. This reference function was then used to calculate the ensemble averages for the plots in Section 6.2. Table 5.12 lists positive temperature runs used for the $L = 6$ system size. The average interaction energy per unit volume \mathcal{E} , the average vortex density per unit volume \mathcal{D} , and the average percolation probability \mathcal{P} are calculated in two ways. The first group of averages is computed from the configurations in each run separately, as in a Monte Carlo simulation without the histogram method. The second group of averages is computed from the merged histograms. The percentage difference is given; the interaction energy and vortex density values match to within a few percent. The percolation probability converges more slowly in a single run than do the energy and vortex density, so the single-run averages differ from the combined

Table 5.12: Averages from Monte Carlo runs at $L = 6$

Parameters		Single Run Averages			Histogram Averages			Percent Difference		
β	ν	\mathcal{E}	\mathcal{D}	\mathcal{P}	\mathcal{E}	\mathcal{D}	\mathcal{P}	\mathcal{E}	\mathcal{D}	\mathcal{P}
7.0	0.20	-.0098	.3562	.35	-.0098	.3573	.39	-0.3	-0.3	-10.7
10.4	0.15	-.0088	.2761	.07	-.0085	.2635	.05	3.8	4.8	20.2
10.0	0.15	-.0099	.3231	.16	-.0099	.3204	.16	0.1	0.8	-4.5
9.6	0.15	-.0115	.3919	.38	-.0114	.3837	.36	1.3	2.1	4.4
9.6	0.15	-.0114	.3858	.34	-.0114	.3837	.36	0.4	0.6	-6.6
8.6	0.15	-.0140	.5046	.78	-.0143	.5115	.81	-2.2	-1.4	-4.1
13.0	0.12	-.0113	.3494	.15	-.0112	.3454	.14	0.5	1.1	1.1
16.0	0.10	-.0144	.4326	.31	-.0136	.4055	.22	5.5	6.7	37.9
21.0	0.08	-.0197	.5538	.53	-.0187	.5199	.42	5.2	6.5	24.1

averages by a greater amount.

As described in Section 4.3, each Monte Carlo run records each configuration c as a hit in a two-dimensional histogram $n(E^{int}, N)$ of the interaction energy $E^{int}(c)$ and the number of vortex links $N(c)$. Normalizing the histogram gives an estimate of the joint probability density function, $P_{\beta,\nu}(E^{int}, N)$, of E^{int} and N at the simulation parameters (β, ν) . If M is the number of trials in the Monte Carlo simulation, then the estimated probability density function is:

$$p_{\beta,\nu}(E^{int}, N) = \frac{n(E^{int}, N)}{M} \approx P_{\beta,\nu}(E^{int}, N) \Delta E^{int} \Delta N$$

Figure 5.15 shows the histogram $n(E^{int}, N)$ from a single run of one million trials. Figure 5.16 shows the estimated probability density created by combining histograms from multiple Monte Carlo runs listed in Table 5.12. Averaging histogram hits from a number of overlapping histograms reduces the statistical error and smooths the probability density.

Section 4.3.3 gives a statistical model for the error in the probability density function formed during a single Monte Carlo run. If M is the number of trials and τ is the autocorrelation time, then the variance of each entry $p(E^{int}, N)$ of the single-histogram probability estimate is:

$$\text{Var} \left(p(E^{int}, N) \right) = \frac{1 + 2\tau}{M} P_{\beta,\nu}(E^{int}, N) \Delta E^{int} \Delta N$$

The variance is the expected value of the square of the error between the estimated probability and the true probability. Define the error for each bin as:

$$e(E^{int}, N) = p(E^{int}, N) - P_{\beta,\nu}(E^{int}, N) \Delta E^{int} \Delta N$$

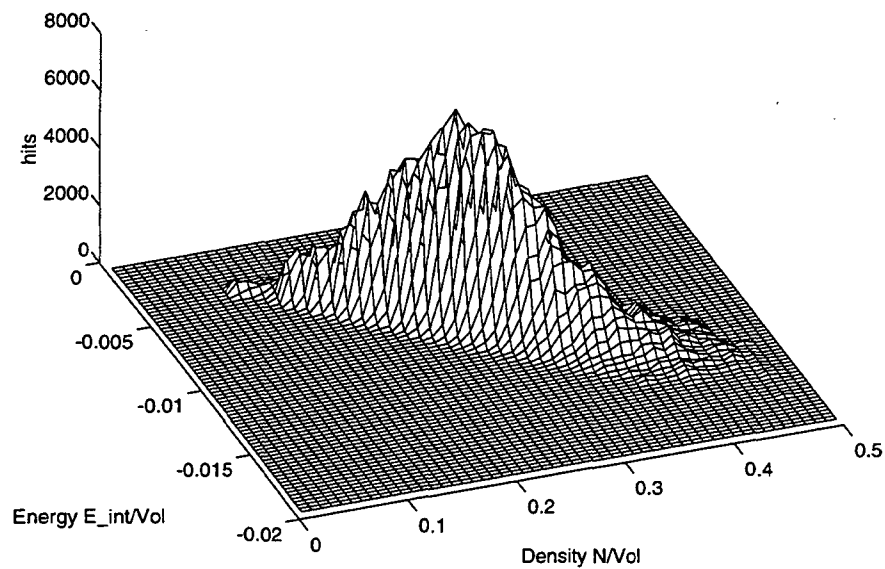


Figure 5.15: Single histogram

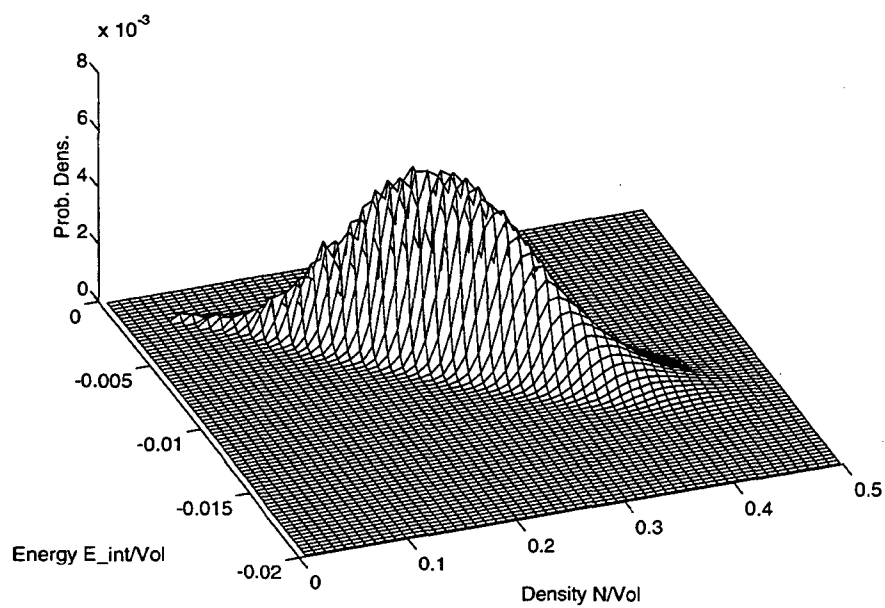
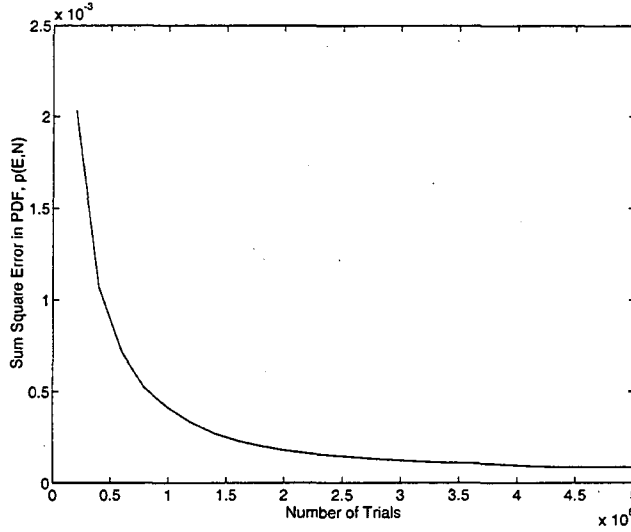


Figure 5.16: Multi-histogram probability density

Figure 5.17: Sum squared error by M trials

One can sum the squared errors over all the bins (E^{int}, N) in the histogram to obtain the statistical estimate:

$$\left\langle \sum_{E,N} \left(e(E^{int}, N) \right)^2 \right\rangle = \frac{1 + 2\tau}{M} \sum_{E,N} P_{\beta,\nu}(E^{int}, N) \Delta E^{int} \Delta N$$

Since the true probability function is normalized, the sum over all the histogram bins is equal to one, and the expected value of the sum squared error of the estimated probability function is:

$$\left\langle \sum_{E,N} \left(e(E^{int}, N) \right)^2 \right\rangle = \frac{1 + 2\tau}{M}$$

Figure 5.17 shows the sum squared error as a function of the number of trials averaged over a number of Monte Carlo runs at the same parameter values. The multi-histogram probability function generated from the combination of many Monte Carlo runs was used as the reference probability for the purpose of estimating the error. Figure 5.18 shows the error on log-log axis; the sum squared error indeed decreases as $1/M$. Figure 5.18 shows the estimator for the autocorrelation time τ given by:

$$\tau \approx \frac{M}{2} \sum_{E,N} \left(e(E^{int}, N) \right)^2$$

The estimated autocorrelation time is $\tau \approx 200$, so approximately 200 trials were required to generate an independent sample of the probability density function.

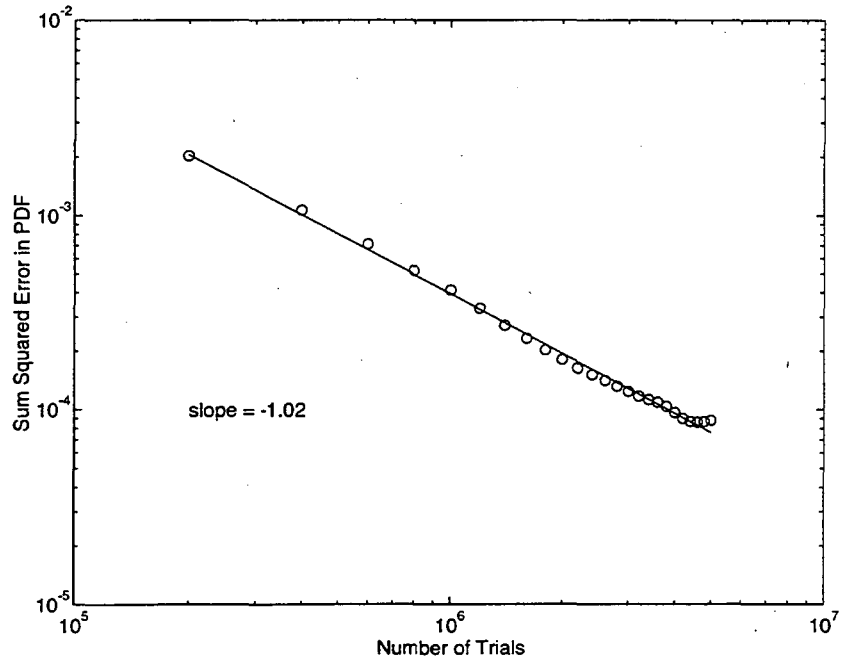
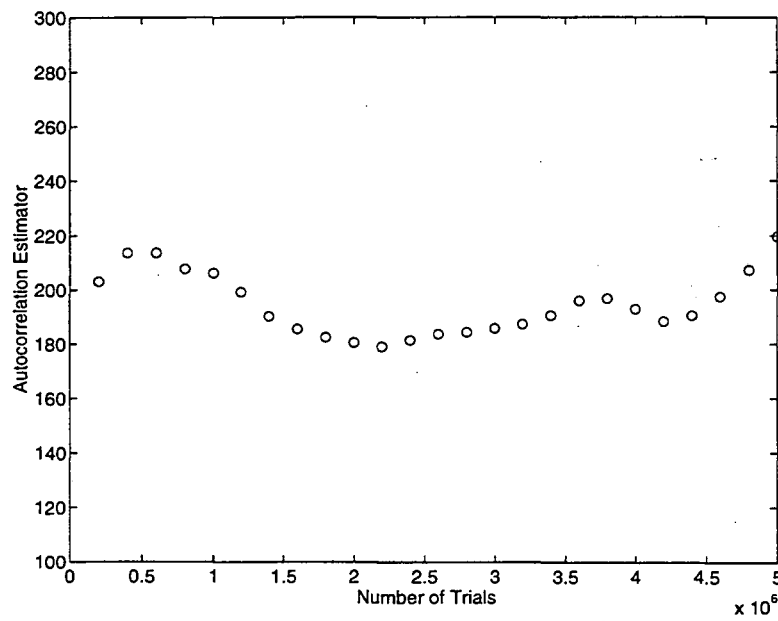
Figure 5.18: Sum squared error proportional to $1/M$ 

Figure 5.19: Autocorrelation time estimators

5.4.3 Split-phase Effectiveness

The split-phase Metropolis sampling described in Section 5.3 is implemented to reduce the proportion of the runtime spent in energy computations compared to the runtime spent transforming the configurations. In particular, the algorithm separates acceptance steps which depend on a change in the number of links N from acceptance steps which depend on the change in energy. The Gibbs weight of a configuration c in the grand canonical ensemble of the self-avoiding loops system is:

$$\rho(c) = e^{-\beta E^{int}(c)} e^{-\beta\nu N(c)}$$

Transformations which add or delete a few links change the configuration by a relatively small amount, only a few vortex links out of several hundred are changed. A number of such transformations are needed to make any significant change in the interaction energy E^{int} . A link addition, therefore, may change the portion of the Gibbs weight which depends on the number of links by a much greater amount than the portion of the Gibbs weight which depends on the change in energy. Allowing intermediate Metropolis steps to accept or reject a move which changes N only on the basis of the N dependent portion of the Gibbs weight can reduce the number of energy calculations needed in the overall algorithm.

The following is an example in which elementary loop additions and deletions have a greater effect on the N dependent portion of the Gibbs weight than on the E^{int} dependent portion of the weight. Let the inverse temperature be $\beta = 10.4$ and the self-energy per link be $\nu = 0.15$. The average interaction energy per link in the system at these parameter values is $\langle E^{int}/N \rangle = -0.0325$. In an average sense, therefore, adding an elementary bump of two links to the system produces the following changes:

$$\begin{aligned} \Delta E^{int} &\approx -0.065 \\ \Delta N &= 2 \end{aligned}$$

The change in the magnitude of Gibbs weight, therefore, is:

$$\frac{\rho(c')}{\rho(c)} \approx 0.08$$

So the addition of a bump reduces the weight of the new configuration by a factor of about 12. Most of the change comes from the N dependent portion of the weight:

$$\begin{aligned} e^{-\beta\Delta E^{int}} &\approx 2.0 \\ e^{-\beta\nu\Delta N} &\approx 0.04 \end{aligned}$$

Table 5.13: Runs by number of intermediate steps k

k	time/Trial (sec)	energy fraction (%)	final acceptance rate (%)
1	0.0206	25	78
2	0.0267	20	64
3	0.0330	16	54
4	0.0380	14	47
8	0.0501	11	34

The energy change increases the weight by a factor of 2, while the change in N decreases the weight by a factor of 25. This is a relatively low temperature example; the dominance of the N dependent portion of the Gibbs weight can be expected to increase as the temperature increases toward $\beta = 0$.

The following tables give an indication of how the split-phase algorithm performs for the example system. The algorithm is described in Section 5.3.6. For each trial, k intermediate steps are taken. Randomly chosen transformation types are used in the intermediate steps; the intermediate steps sometimes include the application of transformations which add or delete vortex links in the domain. Such transformations are accepted in the intermediate steps with the probability:

$$\min(1, e^{-\beta\nu\Delta N})$$

where ΔN is the change in the number of links in the system. The final acceptance step after the k intermediate steps always includes a calculation of the complete Gibbs probability and thus entails a computation of the energy. Table 5.13 lists the total runtime per trial, the fraction of the runtime spent computing the energy of configurations, and the probability that the candidate configuration was accepted in the final acceptance/rejection step. As more intermediate steps are employed, the time per trial increases, but the fraction of the time spent in the energy calculation routine decreases. The probability that the final configuration will be accepted also decreases with k , as the use of more intermediate steps allows a greater change in the configuration before the final acceptance step. Table 5.14 shows the autocorrelation time estimates as functions of k . These estimates may contain significant error, as the autocorrelation estimates converge more slowly than the probability density function itself. The approximate number of trials needed to obtain an independent sample of the probability density is given along with the time required to complete each trial. The product of these two columns is the runtime required to generate an independent

Table 5.14: Autocorrelation and efficiency

k	Autocorrelation time τ (trials/sample)	time/trial (sec)	Efficiency (sec/sample)
1	309	0.0206	6.4
2	195	0.0267	5.2
3	178	0.0330	5.9
4	126	0.0380	4.8
8	117	0.0501	5.9

sample. This measure of efficiency supports the use of the split-phase method in this example. Less cpu time is required to produce a given level of error when a number of intermediate steps are employed. The implementation of the split-phase Metropolis method for the self-avoiding loops system offers an even greater increase in efficiency near infinite temperature, $\beta = 0$.

Chapter 6

Phase Transitions in the Self-avoiding Loops System

This chapter contains computational results for the self-avoiding loops system and a scaling analysis of energy and entropy. Two phase transitions are shown to exist: one at low temperature which separates a phase containing only finite vortices from a phase containing infinite vortices, and one at infinite temperature which separates a phase containing fractal vortices from a phase containing smooth vortices. The first phase transition is related to the lambda transition and to the phase transition in the three-dimensional XY model. Similarities and differences between the self-avoiding vortices and the self-intersecting XY vortices are noted. Aspects of the self-avoiding loops transition are compared to XY theories, and a renormalization which is not based on the Kosterlitz-Thouless method is suggested. The second phase transition in the self-avoiding loops system is related to vortex breakdown in the development of classical turbulence. An argument supporting the notion that infinite temperature is the asymptotic state for vortex filaments is given.

The self-avoiding loops system is described in Section 3.2 of this thesis. The Monte Carlo algorithm for generating a representative sequence of random configurations is described in Sections 5.1 and 5.3, and the histogram sampling method for computing thermodynamic averages from the statistics of the sequence is discussed in Section 4.3. The Monte Carlo algorithm simulates the self-avoiding loops system in the variable- N , grand canonical ensemble with the Gibbs weight:

$$\rho(c) = e^{-\beta E^{int}(c) - \beta \nu N(c)}$$

A feature of the histogram method also allows the statistics to be interpreted for the microcanonical and canonical ensembles.

Section 6.1 of this chapter examines quantities in the micro-canonical ensemble as functions of E^{int} and N . The density of configurations at points in the (E^{int}, N) plane is shown; the density is proportional to the number of configurations c which have energy $E^{int}(c) = E^{int}$ and number of links $N(c) = N$. This examination reveals the most densely populated regions of the phase space and the high and low energy limits of the system.

Section 6.2 of this chapter examines thermodynamic averages of the self-avoiding loops system in the grand canonical ensemble as functions of inverse temperature β and of vortex link self-energy ν . A line of phase transitions is revealed at low temperatures. The phase transitions have no latent heat, but have a divergence or a cusp in the specific heat at the critical temperature. The transitions are also shown to be percolation thresholds; vortices are of finite length below the critical temperature, while infinite vortices exist above the critical temperature. In these respects the phase transition in the self-avoiding loops system resembles the lambda transition in superfluid helium and the ordering transition in the three-dimensional XY model. Estimates of the fractal dimension of the self-avoiding vortex loops at criticality, however, differ noticeably from previous estimates of the fractal dimension of self-intersecting XY vortices.

Section 6.3 of this chapter gives computational results and a scaling analysis for the self-avoiding loops system in the fixed- N ensemble in which vortex density is held constant. The use here of the canonical ensemble rather than the grand-canonical ensemble allows examination of the system at moderate vortex density near infinite temperature, since density tends toward one in the grand canonical ensemble as temperature goes to infinity. The computations and the scaling analysis of energy and entropy indicate an instability at any negative temperature to the formation of bundles of smooth vortex lines of the size of the domain. At positive and infinite temperature, vortices are fractal and have structure of size comparable to the lattice spacing. At hotter, negative, temperatures however, vortices are smooth and have structure of size comparable to the domain length. This transition at infinite temperature is analogous to the fractal/smooth transition which is observed in a system consisting of a single self-avoiding vortex [38].

The final section, Section 6.4 of this chapter, summarizes the behavior of the self-avoiding system. Comments are made on the relation of the system to the XY model, to Kosterlitz-Thouless renormalizations, and to classical turbulence. Suggestions are then

made for future investigations.

6.1 Micro-canonical Ensemble

The micro-canonical ensemble restricts the state space to those configurations c in which the energy $E(c)$ and the number of particles $N(c)$ take set values: $E(c) = E, N(c) = N$. Thermodynamic averages in the micro-canonical ensemble assign equal weights to all the configurations in this restricted set, as described in Section 2.1. The Monte Carlo Algorithm described in Chapter 5 simulates a variable E , variable N ensemble with the Gibbs weight:

$$\rho(c) = e^{-\beta E^{int}(c) - \beta\nu N(c)}$$

The histogram sampling method discussed in Section 4.3, however, breaks up the information from each run into bins by the energy E^{int} and the number of vortices N . Averaging the observable quantity A over the individual bins gives an estimate $\bar{a}(E^{int}, N)$ of the micro-canonical ensemble average. The histogram method also estimates a joint probability density $p_{\beta,\nu}(E^{int}, N)$ of the interaction energy and the number of vortex links at temperature β and vortex self-energy ν . As discussed in section 4.3, the probability density can be related to the density of states:

$$D(E^{int}, N) = \int_{E^{int}(c)=E^{int}, N(c)=N} dc = Z_{\beta,\nu} e^{\beta E^{int} + \beta\nu N} P_{\beta,\nu}(E^{int}, N)$$

The numerical estimate

$$d(E^{int}, N) = e^{\beta E^{int} + \beta\nu N} p_{\beta,\nu}(E^{int}, N)$$

is proportional to the number of configurations c in the variable- E , variable- N ensemble which have energy $E^{int}(c)$ in the interval $[E^{int}, E^{int} + \Delta E^{int})$ and number of links $N(c)$ in the interval $[N, N + \Delta N)$. An examination of this numerical density of states reveals the most populated regions of the (E^{int}, N) plane. This section describes the density of states and the micro-canonical averages in the variables (E^{int}, N) , or equivalently,

$$(\mathcal{E}, \mathcal{D}) = \left(\frac{E^{int}}{V}, \frac{N}{V} \right)$$

Recall that the interaction energy $E = E^{int}$ can be positive or negative, since the physical energy is decomposed as:

$$E^{tot} = E^{int} + \nu N$$

Lines of constant total energy, therefore, have slope $-\nu$ in the (E^{int}, N) or $(\mathcal{E}, \mathcal{D})$ planes.

This section notes several features of the self-avoiding loops system from the examination of micro-canonical averages and of the density of states. At infinite temperature $\beta = 0$ in the canonical and grand canonical ensembles, the Gibbs weight $\rho(c) = 1$, so all configurations in the appropriate phase space \mathcal{C} are equally likely. The infinite temperature behavior of the energy and of the vortex density can be deduced for these ensembles from the density of states $D(E^{int}, N)$; the maximum of the density of states in the region of the (E^{int}, N) plane which is accessible to the system will occur at the expected values $(\langle E^{int} \rangle_\infty, \langle N \rangle_\infty)$. In the grand-canonical ensemble, the entire (E^{int}, N) plane is accessible to the system and the infinite temperature point is the global maximum of $D(E^{int}, N)$. This maximum appears to occur at high density $\mathcal{D} \approx 1$ for the self-avoiding loops system. In the canonical ensemble, N is fixed and only a slice of the (E^{int}, N) plane is accessible to the system. In this ensemble, the infinite temperature interaction energy $\langle E^{int} \rangle_\infty$ is both finite and negative. Finite energy at infinite temperature is characteristic of other vortex systems such as two dimensional vortex turbulence and the single self-avoiding vortex filament. The negative vortex-vortex interaction energy, however, is unusual and reflects the allowance of vortex reconnections in the self-avoiding loops system.

High and low energy “ground states” are examined for the self-avoiding loops system. The high energy states are seen to have energies far above the infinite temperature energy at fixed N . This observation of the existence of rare but very high energy states in the self-avoiding loops system is quantified by the scaling analysis of Section 6.3.

The micro-canonical percolation probability is examined. Finite size scaling is observed in the probability that the self-avoiding loops system at fixed \mathcal{E} and fixed \mathcal{D} has a percolating loop, see Sections 3.2 and 3.4. The scaling indicates the existence of a percolation threshold: a line in the $(\mathcal{E}, \mathcal{D})$ plane below which the probability of an infinite vortex loop existing in the micro-canonical ensemble is zero, and above which the probability is one. Percolation occurs at lower vortex loop density \mathcal{D} for higher loop interaction energies \mathcal{E} .

As discussed in Section 4.3.1, the density of states is proportional to the number of configurations c having energy $E^{int}(c)/V = \mathcal{E}$ and vortex density $N/V = \mathcal{D}$. Figure 6.1 shows a portion of the surface generated by the logarithm of the density of states $\log_{10}(d(\mathcal{E}, \mathcal{D}))$ for the self-avoiding loops system of domain size $L = 6$. Figure 6.2 shows a contour plot of the surface; the lines are of constant population density d . The spacing

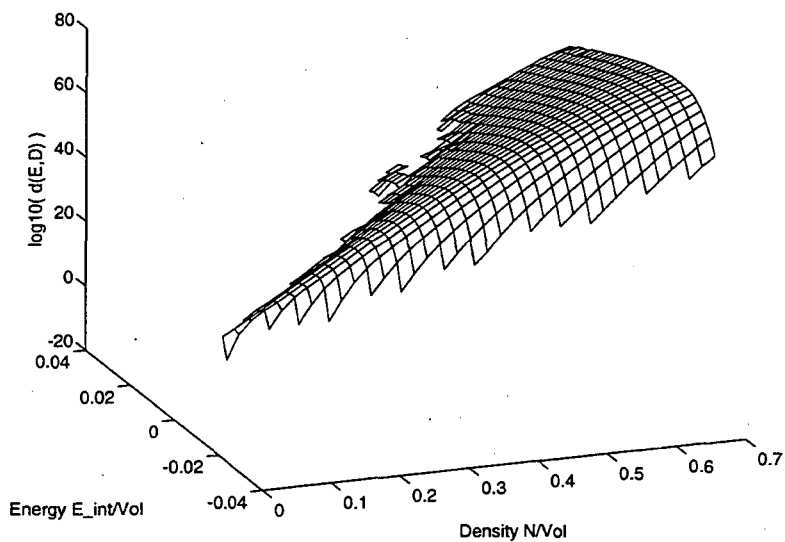


Figure 6.1: Log of density of states

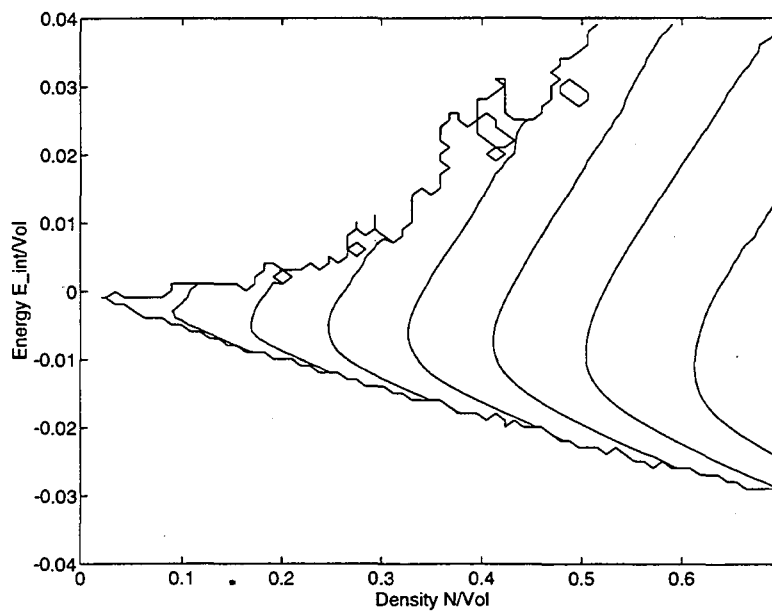
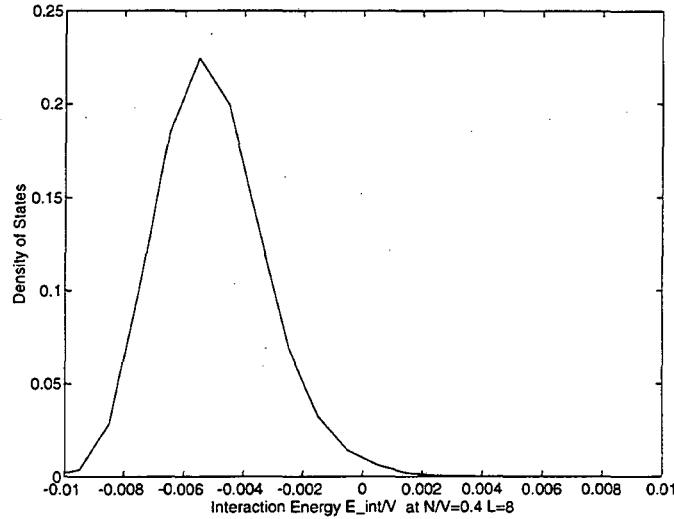


Figure 6.2: Contours of log of density of states

Figure 6.3: Density of states, $d(\mathcal{E}, \mathcal{D} = 0.4)$

between the contours represents factors of ten; crossing each line as one moves from left to right indicates that there are ten times as many configurations in the $L = 6$ ensemble which have a particular \mathcal{E} and \mathcal{D} as there were at the previous line.

Several features of the self-avoiding loops system can be noted from these figures. First, note that the most populated region of phase space is at high density. The surface is cut off in the figures at density $\mathcal{D} = 0.7$ since the computational algorithm used in the thesis may not be ergodic at high density. A lack of ergodicity at high density \mathcal{D} would result in an undercounting of states at high \mathcal{D} . Any difference between the true density of states $D(\mathcal{E}, \mathcal{D})$ and the numerical approximation $d(\mathcal{E}, \mathcal{D})$, therefore, can be expected to be positive and to increase with increasing \mathcal{D} . While the exact shape of the density of states and the thermodynamic behavior is unknown for the self-avoiding loops system at very high density, one may assume that the overall maximum of the density of states $d(\mathcal{E}, \mathcal{D})$ lies near $\mathcal{D} = 1$. This indicates that the variable- N system will tend toward high density as the temperature tends to infinity.

Secondly note that at fixed vortex density \mathcal{D} , the density of configurations decreases both for small \mathcal{E} and for large \mathcal{E} . This is in contrast to systems such as the ideal gas, in which the state space is described by both position and momentum variables. In the ideal gas, the number of configurations is monotonically increasing with the energy of the system at fixed molecular density, and the average energy becomes infinite as temperature

goes to infinity. In the vortex system, the number of configurations decreases at very high energies. At a fixed vortex density \mathcal{D} there are fewer ways to achieve a very high energy than there are to achieve a moderate energy. Figure 6.3 shows a slice through the density of states at fixed $\mathcal{D} = 0.4$. Note that the most populated region is of negative interaction energy. The interaction energy of the self-avoiding loops system in the canonical ensemble will therefore be negative even at infinite temperature. The total energy of the system,

$$E^{tot} = E^{int} + \nu N$$

which includes the self-energies of the vortex links is still positive, however. The negative interaction energy in the self-avoiding loops system is in contrast to the positive interaction energy of the single self-avoiding walk at infinite temperature [38].

Figure 6.4 shows a typical configuration from the most heavily populated energy region $\mathcal{E} = -0.0036$ at vortex density $\mathcal{D} = 0.16$. Contrast this configuration of multiple self-avoiding loops with the example of a single self-avoiding vortex loop in Figure 6.5. The principle difference in formulation between the single loop model and the multiple loop model of the thesis is the relaxation of the constraint that a vortex loop must remain connected. As can be seen from the figures, this relaxation leads to a breakup of vortex lines into many loops. While some large connected loops remain, the smallest loops are the most numerous. The existence of this “sea” of small loops plays a role in the reduction of the interaction energy of the system. An elementary loop consisting of four vortex links has negative interaction energy:

$$E^{int} = -\frac{1}{2\pi}$$

While the total energy interaction associated with the elementary loop includes its interactions with other vortex links in the domain, a collection of small vortex loops of independent orientations may be expected to contribute a negative term to the interaction energy. The collection of small vortex loops could reduce the interaction energy even further if the small loops were not independently oriented but were arranged to screen large vortex loops.

The density of states in Figures 6.1 and 6.2 is cut off at high \mathcal{D} , but the upper and lower energy limits reflect the extent of sampling by the Monte Carlo algorithm. Figure 6.6 shows a configuration with very low interaction energy per vortex link, while Figure 6.7 shows a configuration of very high interaction energy. The $(\mathcal{E}, \mathcal{D})$ locations of these two configurations are shown in the contour plot of the density of states in Figure 6.8. The energy

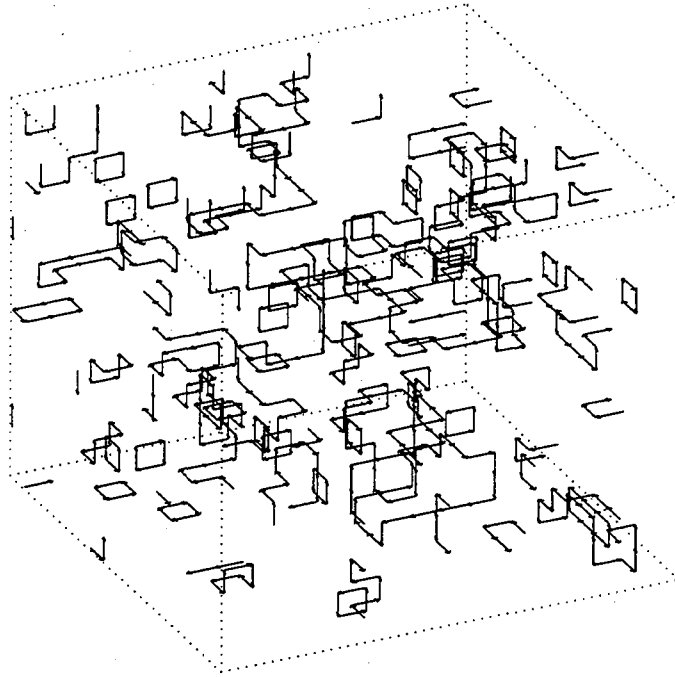


Figure 6.4: Self-avoiding vortex loops at infinite temperature

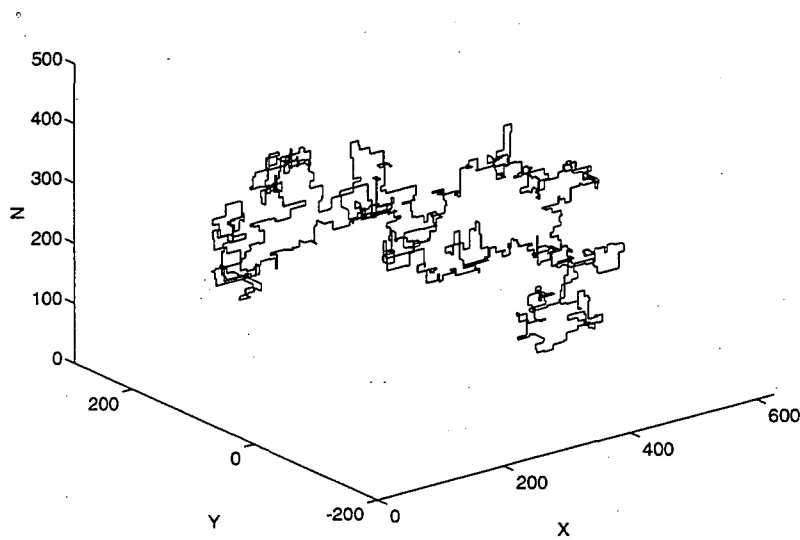


Figure 6.5: Single vortex loop at infinite temperature

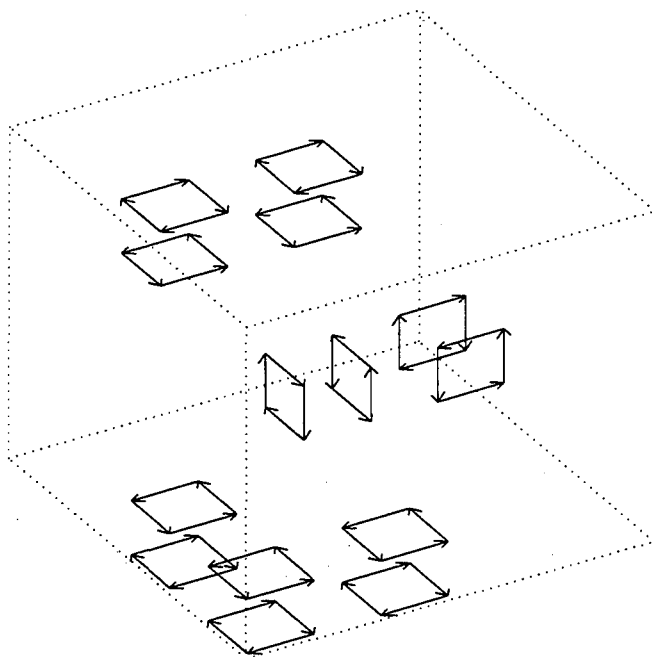


Figure 6.6: Loop crystals

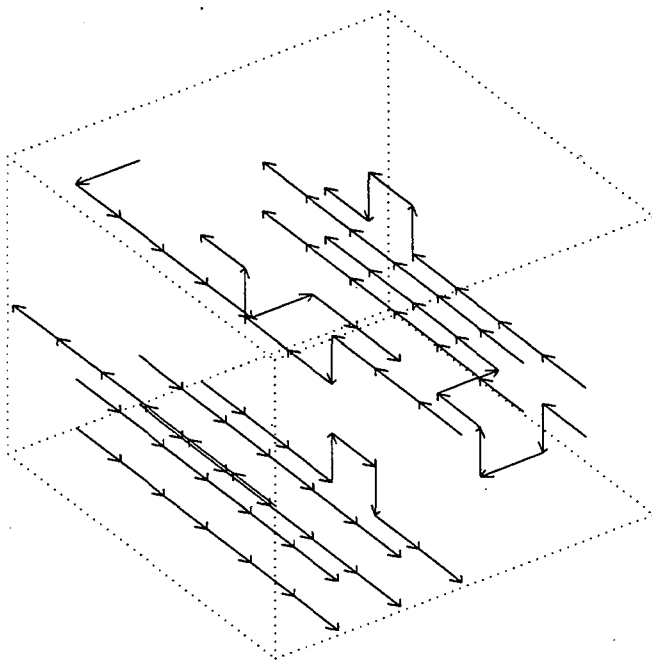


Figure 6.7: Dipole loops

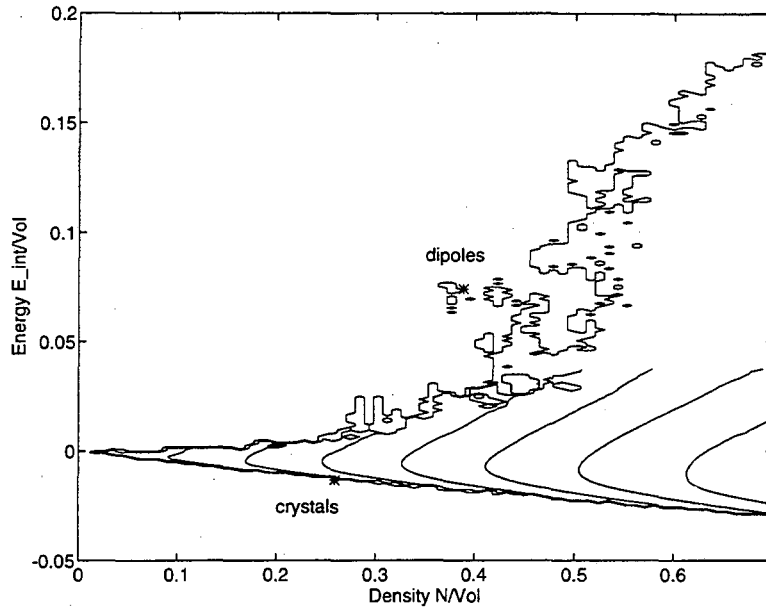


Figure 6.8: Density of states extended to high energies

axes in this figure have been expanded from the values in Figure 6.2 to include histograms taken at negative temperatures. Note that the low energy example configuration is much nearer in energy to the highly populated area of the $(\mathcal{E}, \mathcal{D})$ plane than is the high energy example configuration. The existence of very rare but extremely high energy configurations will be shown in Section 6.3 to have a significant impact on the system as the thermodynamic limit is taken.

The micro-canonical percolation probability is the micro-canonical average of the observable $\text{Perc}(c)$, which is defined in Section 3.2. The micro-canonical percolation probability is the fraction of configurations of fixed $(\mathcal{E}, \mathcal{D})$ which contain a connected loop spanning the length of the domain. In the thermodynamic limit $L = \infty$, the self-avoiding loops system has a micro-canonical percolation threshold in which the probability of the existence of an infinite loop jumps from zero to one over a line in the $(\mathcal{E}, \mathcal{D})$ plane. In micro-canonical systems of low interaction energy, large aligned vortex structures are rare and a percolating loop forms only at relatively high vortex density. As the interaction energy in the system increases a percolating loop forms at lower and lower density. At high enough interaction energy, dissociated loops pierce the system at arbitrarily low density. Figure 6.9 shows the micro-canonical percolation probability at $L = 6$ as a function of $(\mathcal{E}, \mathcal{D})$. The orientation of the transition shows how the percolation threshold occurs at a lower vortex density for

higher interaction energy. The probability shown in this figure is smoothed by finite size effects. Figure 6.10 shows a slice of the micro-canonical percolation probability through $\mathcal{D} = 0.4$ in domains of size $L = \{4, 6, 8\}$. The transition shows the typical percolation finite size behavior: becoming steeper as the system size increases. In an infinite system, the percolation probability would jump from 0 to 1 at a critical value \mathcal{E}_c of the interaction energy.

6.2 “Lambda” Percolation Transition

Section 4.3 shows how the density of states information and micro-canonical averages taken in the histogram sampling method can be used to approximate canonical or grand canonical averages. This section employs those techniques to describe the thermodynamic averages of the self-avoiding loops system in the variable- N grand canonical ensemble in terms of the inverse temperature β and the loop self-energy ν . The set of configurations, \mathcal{C} , here contains collections of loops c with arbitrary numbers of vortex links $N(c)$ and arbitrary interaction energies $E^{int}(c)$. The Gibbs weight of a configuration c is:

$$\rho(c) = e^{-\beta E^{int}(c) - \beta \nu N(c)}$$

The Gibbs weight indicates that the average interaction energy per unit volume \mathcal{E} decreases as β increases, and the average number of vortex links per unit volume \mathcal{D} decreases as $\beta \nu$ increases. Computational results reveal a line of phase transitions at low temperature. Finite size scaling indicates that the transition is a continuous phase transition; the energy of the system is continuous at the critical temperature but the specific heat shows peak whose height increases with the system size. The vortex density is also continuous at the phase transition, but the probability of an infinite connected loop existing in the system jumps from zero to one in a percolation threshold at the critical temperature. This phase transition is similar to the lambda transition in superfluid helium in that it is a continuous phase transition with a divergence or a cusp in the specific heat, and in that vortices are of finite size below the transition while vortices of infinite size exist above the transition.

Examination of the interaction energy per link across the transition reveals a change in the energy per link in the system. The energy per link rises more slowly with temperature above the transition than below. This qualitative behavior is consistent with the renormalization arguments of Shenoy [130] and Williams [144]. A modification to the

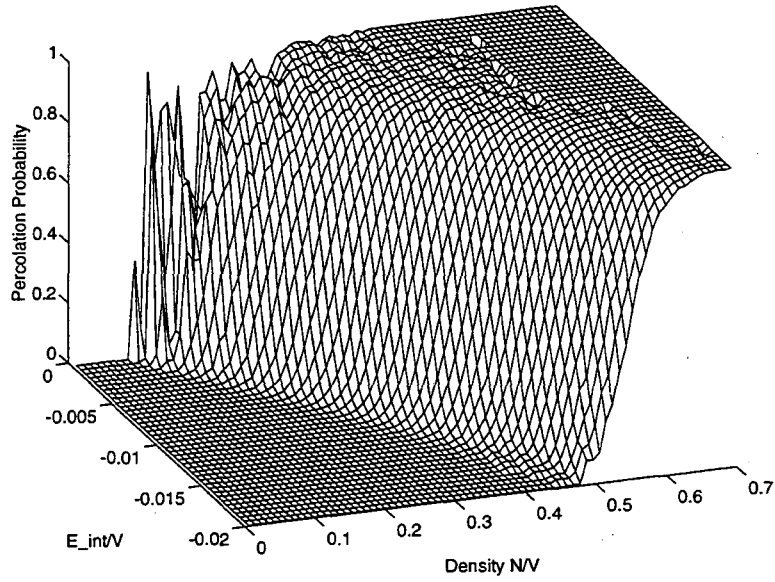


Figure 6.9: Micro-canonical percolation probability

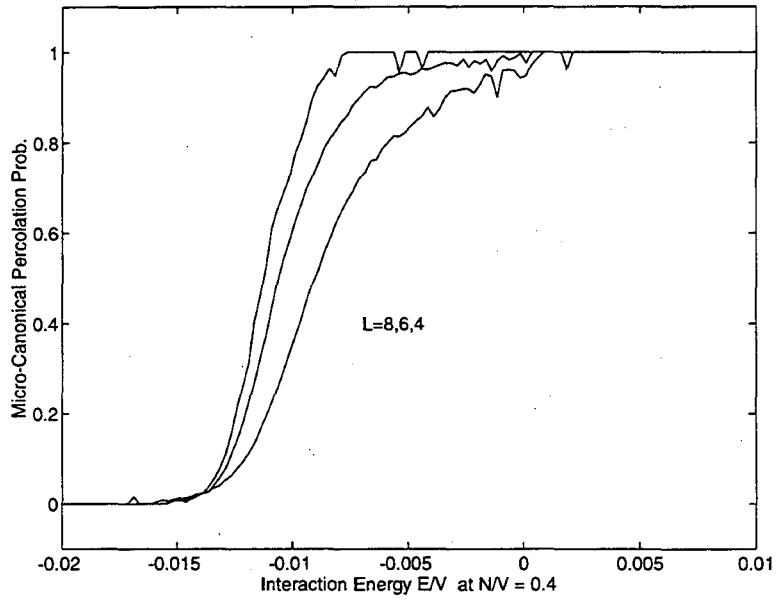


Figure 6.10: Micro-canonical percolation probability $\mathcal{D} = 0.4$

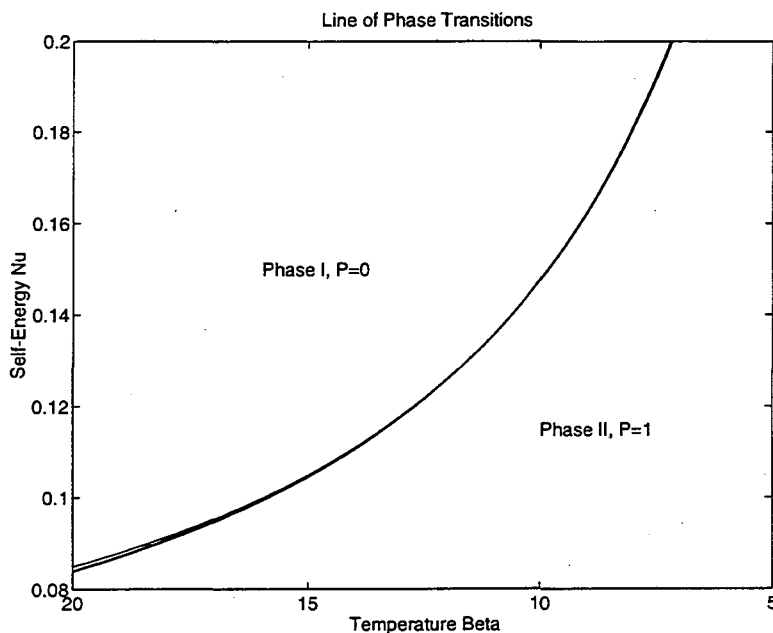


Figure 6.11: Phase plane

self-avoiding loops computation which would reveal more detailed information about the assumptions in the renormalization theories is described in this section.

The fractal dimension of individual vortex loops is estimated. The numerical values found for the fractal dimension do not accurately represent the thermodynamic limit, but serve as a comparison with the fractal dimension estimates for comparably sized XY systems in Epiney's computations [53]. The fractal dimensions of self-avoiding vortex loops are found to be significantly larger than the fractal dimensions of self-intersecting XY vortex loops. While altering the definition of distinct XY loops in the presence of intersections may give different fractal dimension values than those found by Epiney, the results tend to indicate that the self-avoidance condition significantly effects the fractal dimension of vortex structures.

Figure 6.11 shows the location of the line of phase transitions in the (β, ν) plane. Note that the β axis is reversed so that low temperature is on the left and high temperature is on the right. This orientation convention is retained in figures throughout this section. Phase I is the "cold" phase in which all vortex loops are of finite size. Phase II is the "hot" phase in which infinite vortex loops exist. The line between them is both a continuous thermodynamic phase transition and a percolation transition. In the analogy with the

lambda transition in liquid helium, phase I is identified with the superfluid phase while phase II is identified with the normal fluid phase. In the analogy with the XY model, phase I is identified with the ordered phase in which the XY spins are aligned over long distances, and phase II is identified with the disordered phase in which vortical excitations break up the alignment of the spins. The phase transition in the self-avoiding loops system occurs at hotter temperatures as the self-energy of a vortex link is increased. Higher self-energy ν discourages vortices from forming and suppresses the phase transition. This behavior is in agreement with numerical work done by Shrock and colleagues [86] [85] on the XY model in which a term was added to enhance or suppress vortex defects in the spin system.

Figure 6.12 shows a slice through the (β, ν) plane at a self-energy value of $\nu = 0.15$. The views presented by the fixed- ν slices in Figures 6.12, 6.13, 6.14 6.15 6.17 are qualitatively similar at different values of the self-energy. Figure 6.12 shows the average total energy per unit volume:

$$\langle E^{tot}/V \rangle = \langle \mathcal{E} + \nu \mathcal{D} \rangle$$

as a function of β at $\nu = 0.15$. The dotted line marks the critical temperature β_c for this value of the self-energy. Note that the curves for the system sizes $L = \{4, 6, 8\}$ show little difference beyond statistical error. This indicates that the energy is continuous across the critical temperature. The specific heat per unit volume,

$$C = -\frac{\beta}{V} \frac{\partial \langle E^{tot} \rangle_{\beta}}{\partial \beta}$$

however, shows in Figure 6.13 a peak which increases in height with the system size. This indicates the presence of a cusp or divergence in the specific heat in the thermodynamic limit and demonstrates that the system has a continuous phase transition.

The loop density, like the energy, appears continuous across the transition. See Figure 6.14. Although there is a sense in which the cold phase corresponds to low vortex density and the hot phase corresponds to high vortex density, the self-avoiding loops system does not exhibit a sudden increase in vortex line length at the transition. This is in contrast the the belief which is commonly held for the lambda transition in superfluid helium. There does exist, however, a sudden increase in the length of connected vortices at the critical temperature. The number of vortices in the system does not jump at β_c , but the connectivity pattern changes to allow infinitely extended vortices at and above the transition. Figure 6.15 shows the finite size scaling for the percolation probability \mathcal{P} as a function of β at

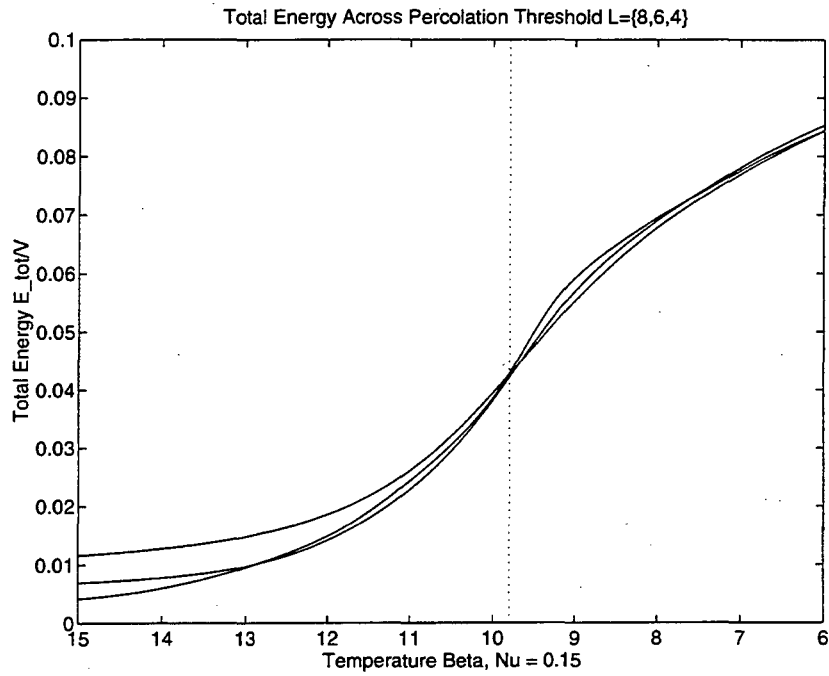


Figure 6.12: Total energy by system size

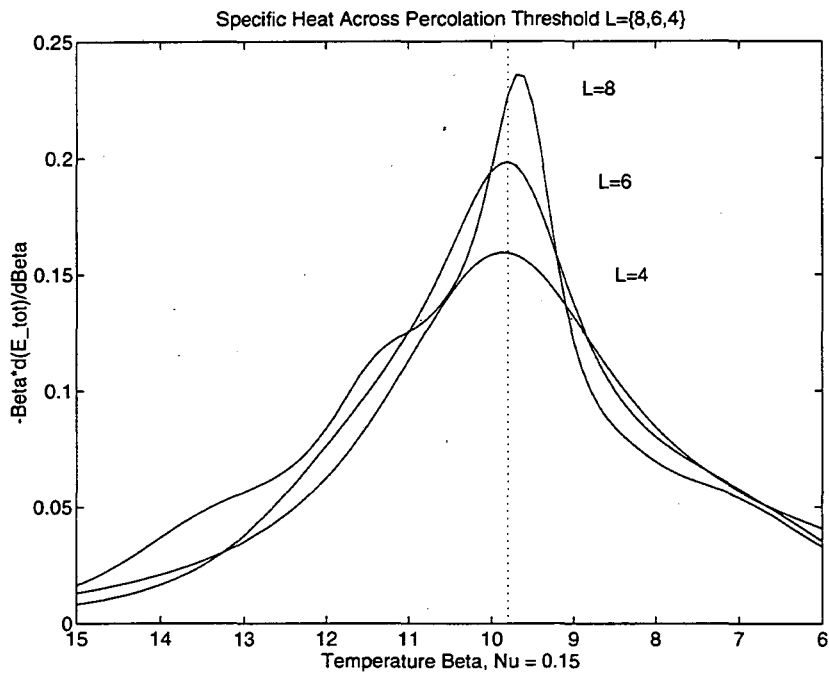


Figure 6.13: Specific heat by system size

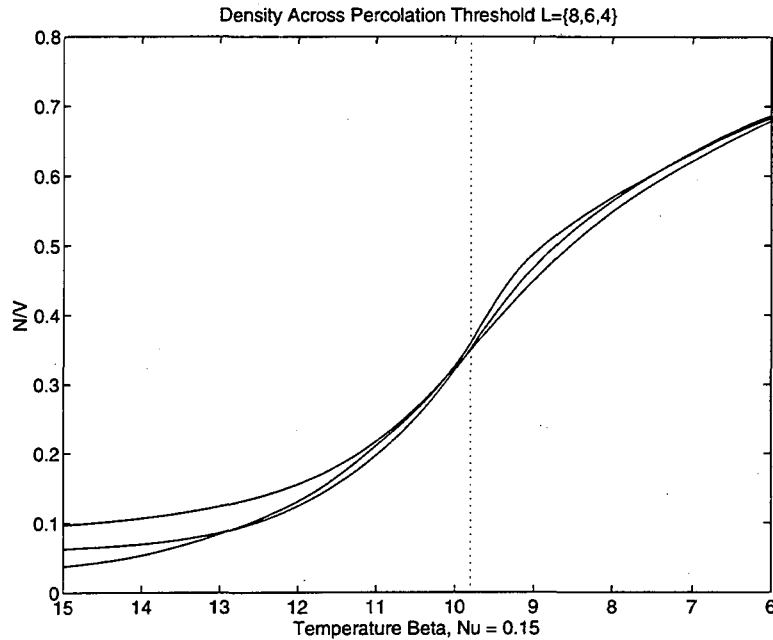


Figure 6.14: Loop density by system size

$\nu = 0.15$. The percolation probability is the expected value of the observable $\text{Perc}(c)$, which has the value one if the configuration c has a loop as large as the system size, and has the value zero if no loop in c is as large as the domain. The figure shows the curves \mathcal{P}_β for the system sizes $L = \{4, 6, 8\}$ plotted on the same graph. The threshold is the most gradual for $L = 4$ and the most steep at $L = 8$. This scaling indicates the presence of a discontinuity in the thermodynamic limit, so that the probability of an infinite vortex loop existing in the system is zero below the critical temperature and one above β_c .

The inverse temperature β for which $\mathcal{P} = 0.24$ is the same for the system sizes $L = \{4, 6, 8\}$, and assumably marks location β_c of the percolation threshold when $L \rightarrow \infty$. Above the crossing temperature the percolation probability increases with system size and may be expected to converge to one in the thermodynamic limit, while below the crossing temperature the percolation probability decreases with system size and may be expected to converge to zero. Figure 6.16 shows in the (β, ν) plane the location of the percolation probability crossing and the location of the peak of the specific heat. The percolation threshold is plotted with a solid line, while the specific heat peak is plotted with a dashed line. This figure demonstrates that the percolation threshold coincides with the thermodynamic phase transition.

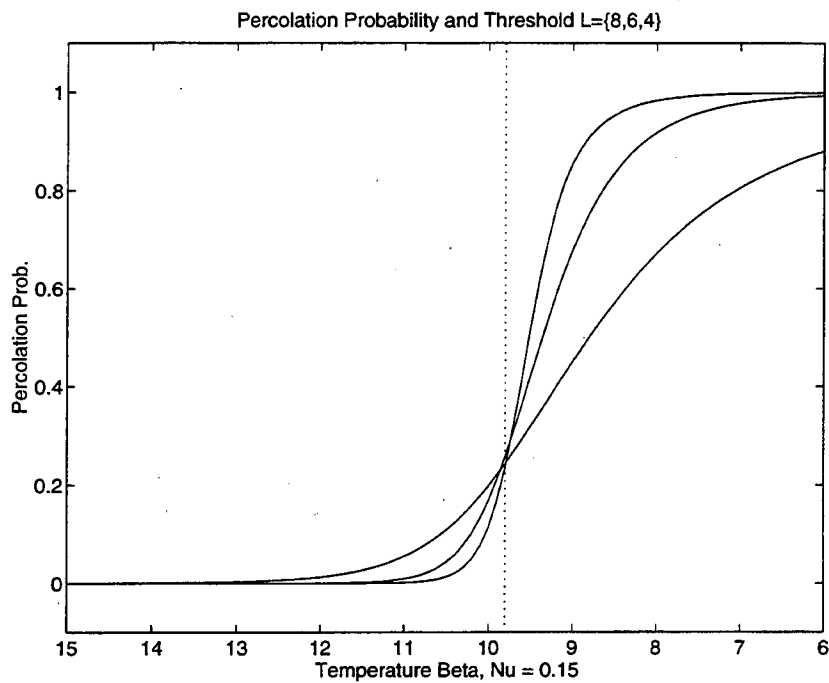


Figure 6.15: Percolation probability by system size

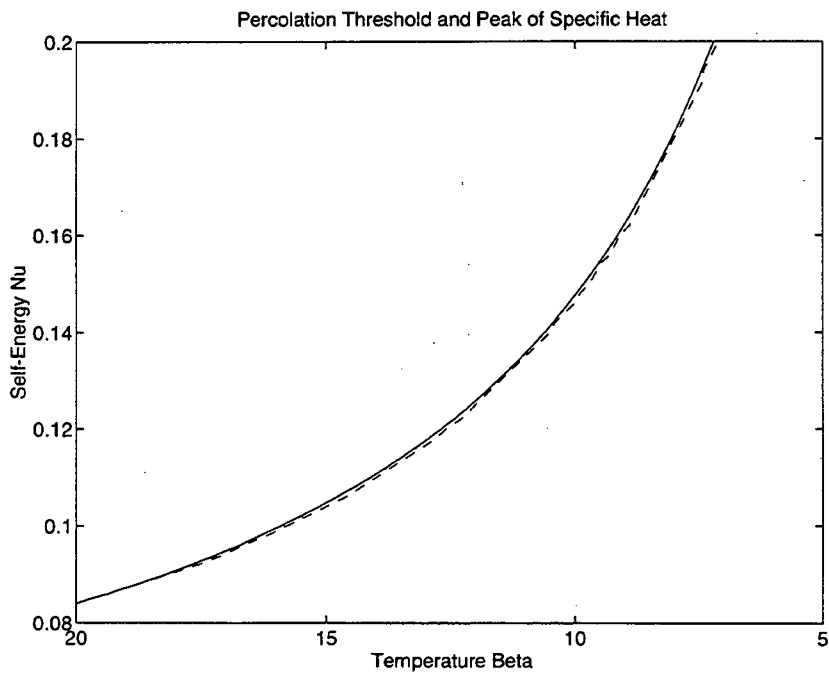


Figure 6.16: Percolation threshold and specific Heat

The computational data demonstrates the existence of a continuous phase transition in the self-avoiding loops system which is also a percolation threshold. The question remains to what extent the phase transition in the self-avoiding loops system describes the lambda transition in superfluid helium and the ordering transition in the XY model. The most conclusive evidence of the extent of the similarity of these transitions awaits a calculation of the critical exponents for the self-avoiding loops transition. A matching of the critical exponents for the self-avoiding loops system and the XY model would indicate that the transitions are in the same universality class and can be expected to have the same physics. A significant difference between the exponents for the two systems would be conclusive evidence that the transitions are in different universality classes although they are superficially similar. The finite size scaling of the percolation probability in the self-avoiding loops system may provide a means of determining the critical exponents for the system.

In any event, the phase transitions in the self-avoiding loops system and in the XY system are qualitatively similar. One can compare the behavior of the self-avoiding loops system with vorticity theories for the phase transition in the XY model. Since XY vortices are self-intersecting, while the vortices simulated in the thesis are self-avoiding, differences between the two systems can indicate the effect of the self-avoidance condition on dense vortex equilibria.

The Kosterlitz-Thouless style renormalization theories of Shenoy and Williams look for a phase transition in which the energetic cost of adding a very large loop to a system containing smaller loops changes behavior. Specifically, one expects from the theories that the additional energy of adding to the system a large vortex loop having n links should scale as $\log n$ below the phase transition but should be constant for large n above the transition. Figure 6.17 shows the interaction energy per link for $L = 8$ in the self-avoiding loops system. The critical temperature is marked by the dotted line. There is an indication that the behavior changes at the critical temperature as the energy curve flattens out. Note however, that the quantity shown represents the complete set of interactions within and among all the vortex loops in the system. Care should be taken when comparing to the incremental energy described in the Shenoy renormalization. Nevertheless, the figure illustrates the screening effect of multiple loops of varying sizes. The interaction energy per link is negative in this system, in contrast to the single connected vortex for which the interaction energy is typically positive [38]. The allowance of vortex reconnection in the self-avoiding loops model permits small loops to orient themselves in such a way that they

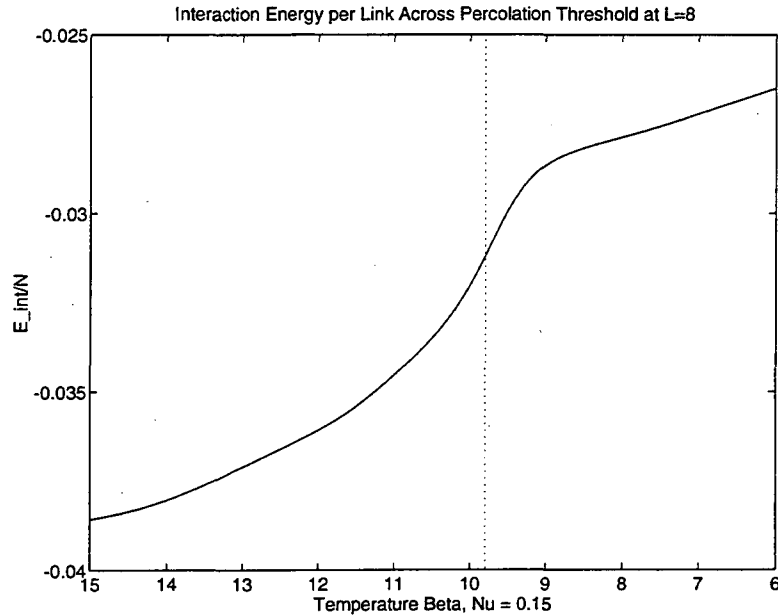


Figure 6.17: Energy per link across transition

reduce the total interaction energy in the system.

The computation could be modified in the following manner to test the energy scaling theory of Shenoy for the self-avoiding loops system. The largest loop in each configuration c could be identified. The total interaction energy, which is a sum over all $N(N-1)/2$ pairs of vortex links in c could then be decomposed into three parts: a “background” energy, a “bare” energy, and a “screening” energy. The background arises from all pairs of links not in the largest loop; this is the interaction energy of the configuration without the dominant loop. The bare energy arises from all pairs of links in the largest loop; this is the energy of a configuration containing *only* the dominant loop. The sum of these two is not the total interaction energy, since one must also consider pairs of links with one link in the dominant loop and the other in the background loops. The interaction energies of these pairs describes the screening effect which the background has on the dominant loop. Averaging of the three component energies separately along with the number of links n in the dominant loop would yield a set of quantities which could be directly compared with the Kosterlitz-Thouless type renormalization theories.

The fractal dimension of XY vortex loops at the critical temperature has been identified in the Shenoy renormalization theory [130] [29] with the fractal dimension of a

single self-avoiding walk in free space at infinite temperature. One is interested in the possible effects on the fractal dimension of XY vortex loops at criticality of the following three conditions: the reduction of temperature to β_c from $\beta = \infty$, the addition of many vortex loops to the system instead of a single walk, and the allowance of self-intersections in the XY vortices. Numerical estimates of the fractal dimension of self-avoiding vortex loops can shed light on the the difference between a single self-avoiding walk and a dense collection of loops, and on the difference between infinite temperature and low temperature. A comparison of the estimated fractal dimension of self-avoiding vortex loops to the estimated fractal dimension of self-intersecting XY vortices suggests the impact of the self-avoidance condition.

Several finite-size effects must be considered when estimating the fractal dimension of vortex loops in small systems, such as the $L = 16$ domains simulated in the thesis. Fractal dimension is computed from the following power-law scaling relation:

$$R = n^\theta$$

where R is a length scale of the loop and n is the number of links in the loop. The exponent θ is the inverse of fractal dimension; for a single open self-avoiding walk or a single self-avoiding loop, $\theta \approx 0.59$ for very large n . Computational fractal dimension estimators such as the end-to-end distance between the ends of an arc of n links converge rather slowly with the linear dimension R . For an open self-avoiding walk, two significant digits are obtained in θ at a length of $R = 50$. The largest self-avoiding loops simulations run for this thesis were $L = 16$; the three-dimension XY simulation run by Epiney [53] was also on an $L = 16$ domain. Finite size effects are therefore significant in the self-avoiding loops and in the XY simulations.

The length scale R employed for closed self-avoiding loops is the loop extent as defined in Section 3.2. The extent is essentially the side length of the smallest cube needed to enclose the loop. The average extent of a single self-avoiding loop at infinite temperature is shown versus the number of links n in the loop in Figure 6.18. The extents are calculated both for a loop in free space and for a loop in an $L = 16$ periodic domain; for numbers of links less than 100, enclosing the loop in the periodic domain has virtually no effect on the average size. Figure 6.19 shows the plot of loop size versus number of links on log-log axes, a linear fit to the curve has slope $\theta = 0.71$. The finite size error is:

$$\theta_{SAW} - \theta \approx 0.59 - 0.71 \approx 0.12$$

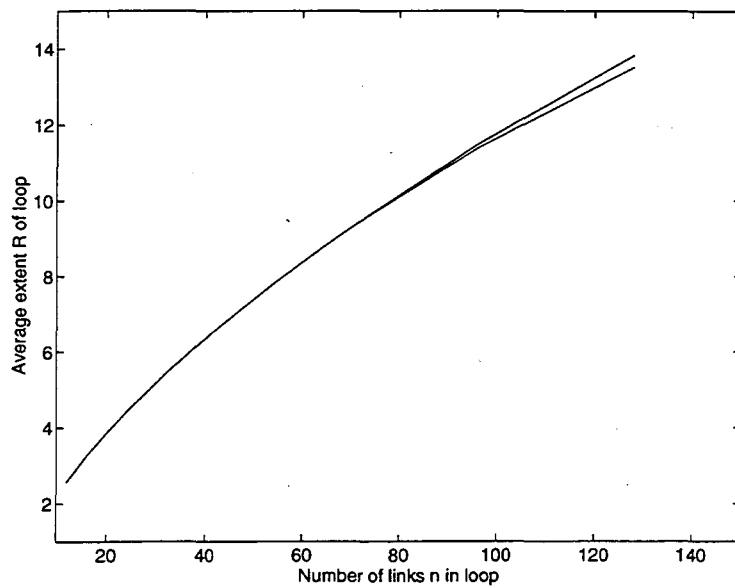


Figure 6.18: Size of a lone loop vs. number of links

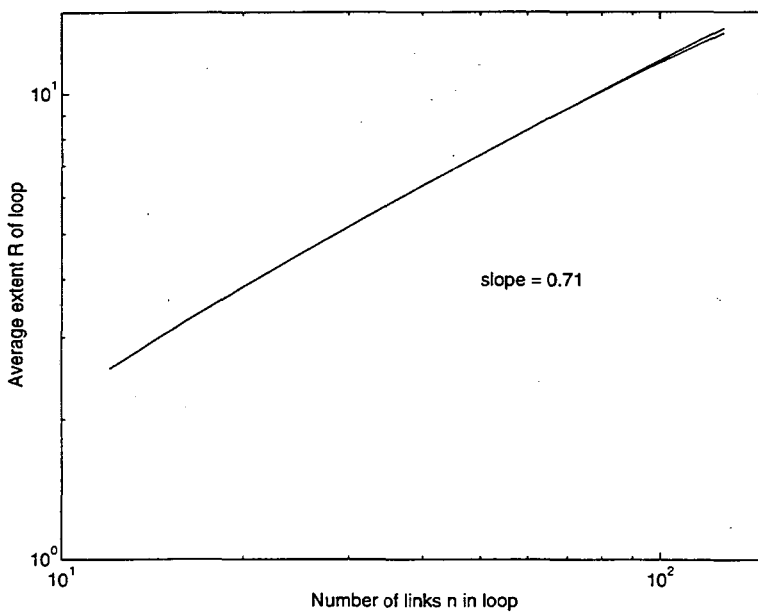


Figure 6.19: Log-log size of a lone loop vs. number of links

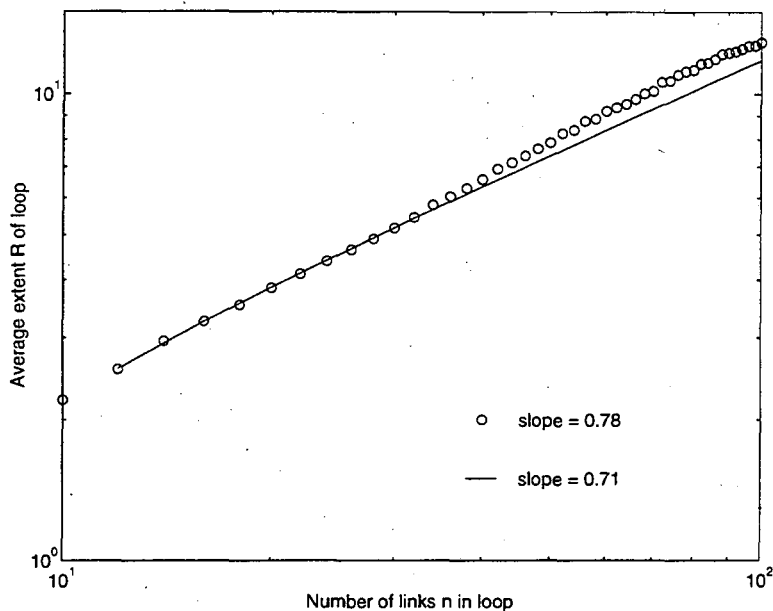
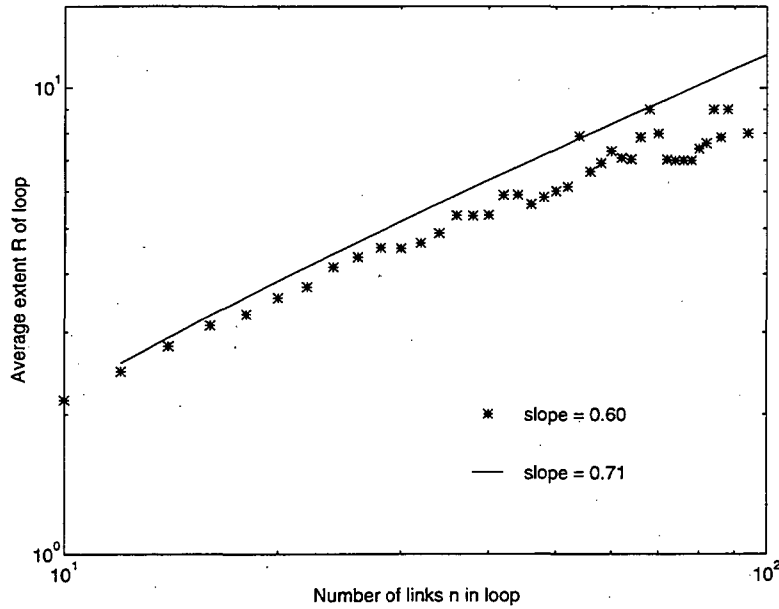


Figure 6.20: Size of loops in a collection at $\beta = 0$

This error is of the same order as the difference between the asymptotic value of the self-avoiding walk exponent $\theta_{SAW} \approx 0.59$ and the inverse fractal dimension of the purely random walk $\theta_{RW} = 0.5$. The numerical values of the $L = 16$ fractal dimension estimates therefore are not accurate enough to determine if vortex loops in the infinite system scale like random walks or like self-avoiding random walks. The average sizes of the small single self-avoiding loops at infinite temperature can serve as a finite size reference for the the infinite temperature self-avoiding walk.

The sizes of self-avoiding loops selected from dense collections at $L = 16$ can be compared to the sizes of single infinite temperature self-avoiding loops. Figure 6.20 shows on log-log axis the average sizes of self-avoiding vortex loops in a collection at infinite temperature in the canonical ensemble. The vortex line density was $\mathcal{D} \approx 0.15$. The sizes of loops from configurations containing many loops are plotted with circles; the single loop sizes are plotted with a solid line. Allowing many loops instead of a single loop slightly straightened the vortices; a linear fit to the circles gives an inverse fractal dimension of $\theta \approx 0.78$ as compared to the finite size value for lone infinite temperature loops of $\theta \approx 0.71$.

Figure 6.21 shows the average sizes of loops in a collection near the critical tem-

Figure 6.21: Size of a loops in a collection at $\beta = \beta_c$

perature. Here the sizes of loops in the collection, plotted with asterisks, are smaller than the sizes of lone infinite temperature self-avoiding loops. A linear fit gives an inverse fractal dimension of self-avoiding loops at criticality of $\theta \approx 0.60$. The closeness of this value to the asymptotic value for the self-avoiding walk is merely fortuitous, but the value does indicate that self-avoiding loops are somewhat more crinkled at low temperature than they are at infinite temperature.

Epiney [53] calculated the inverse fractal dimension of XY vortex loops at the XY critical temperature in a system with $L = 16$. His calculations gave a value of $\theta \approx 0.5$, significantly less than the $\theta \approx 0.60$ of self-avoiding loops at criticality. This difference seems to indicate that the self-avoidance condition has a significant effect on the fractal dimension of vortex loops at the critical temperature. The comparison is not definitive, however, since the fractal dimension of the self-intersecting XY vortex loops is difficult to define. Which links constitute a single loop is not uniquely determined in the presence of loop intersections. Epiney traced out individual loops by randomly picking a branch to follow at each intersection, he suggests that this method may reduce the value of the scaling exponent θ to the asymptotic random walk value of $\theta_{RW} = 0.5$. Shenoy suggests in

his renormalization argument [130] that a vortex loop should be defined by the process of removing all the sets of four end-to-end links which form a closed loop, and then removing all the sets of six link loops, and so on until only the largest loop remains. This alternate method of defining the identity of the largest loop may yield a different fractal dimension estimate than the $\theta \approx 0.5$ found by Epiney.

Because of the existence of significant finite size errors in the computational fractal dimension estimates, the following summary is somewhat speculative. Nevertheless, both the addition of a collection of loops to the domain and the reduction of temperature from $\beta = 0$ to $\beta = \beta_c$ appear to have significant effects on the fractal dimensions of self-avoiding vortex loops. The allowance of multiple loops in the domain seems to result in individual loops which are straighter than lone self-avoiding walks. The reduction in temperature from infinite to the critical temperature seems to have the opposite effect of producing more folding in individual loops. Self-intersecting XY loops at criticality appear to have a different fractal dimension than self-avoiding loops at criticality.

The low temperature phase transition described here resembles the lambda transition in superfluid helium and the ordering transition in the XY model in that it is a continuous phase transition at which infinite vortices appear as the system is heated. Percolation finite size scaling is observed at this transition; the percolation framework describes how infinite vortices can appear at the critical temperature without a sudden increase in vortex density. Aspects of Kosterlitz-Thouless renormalization theories for XY vortices are consistent with observations in the self-avoiding loops model. Fractal dimension estimates, however, indicate a difference between the self-avoiding vortex loops and the self-intersecting XY vortex loops.

Finally note that other positive temperature phases and phase transitions may exist in the self-avoiding loops system. In particular one may expect a "vortex solidification" transition at low temperature and very low values of the self-energy ν in which vortices pack into a regular lattice with very large negative interaction energy. Such a transition has been observed in a $2\frac{1}{2}$ -dimensional vortex model studied by Chorin [42].

6.3 Fractal-Smooth Transition

As the temperature becomes infinite, ($\beta \rightarrow 0$), in the variable- N ensemble of the self-avoiding loops model, the vortex loop density \mathcal{D} tends toward one. One may also

consider the temperature dependence of the system in a canonical ensemble in which the density is restricted to a fixed value. Such an ensemble may represent the equilibrium of a physical system in which the time scale of vortex stretching is much greater than the time scale of vortex folding and reconnection. The examination of the density of states in Section 6.1 indicates that the number of configurations having high energies decreases with increasing energy. The self-avoiding loops system may be therefore be expected to have non-trivial thermodynamics at infinite and negative temperatures, as do other vortex systems [115] [38] [80] [109]. Examination of the self avoiding loops system at infinite and negative temperatures may shed light on processes such as the development of turbulence in classical fluids [115] [43] [38] [41].

At positive temperatures, the thermodynamic limit $L \rightarrow \infty$ exists for the self-avoiding loops system and is the same in the micro-canonical, canonical, and grand canonical ensembles. At negative temperatures, however, the canonical and grand-canonical average energy $\langle \mathcal{E} \rangle^L$ is not finite in the thermodynamic limit $L \rightarrow \infty$; the ensemble average energy per unit volume increases indefinitely with increasing system length L . This instability of the self-avoiding loops system comes about through the existence of configurations whose interaction energy grows faster with L than does the entropy of the system. These configurations therefore dominate the negative temperature systems in which high energy configurations are encouraged by the Gibbs weight:

$$\rho(c) = e^{-\beta E^{int}(c)}$$

The high energy configurations are shown in this section to consist of aligned bundles of vortex lines which are smooth on the scale of the domain length. These smooth configurations are in contrast to self-avoiding loops configurations at positive and at infinite temperature which are fractal on the scale of the domain length. The scaling of the energy and of the entropy of certain groups of configurations as $L \rightarrow \infty$ and as the lattice step size $h \rightarrow 0$ is discussed in this section. The basic energy/entropy argument is discussed in Section 2.3. Analysis of the balance of energy and entropy between smooth configurations and fractal configurations is used in this section to demonstrate the presence of a phase boundary at infinite temperature, $\beta = 0$.

The thermodynamic limit is usually taken as the length L of the system goes to infinity. The lattice step size h may be held constant under the assumption that the physical system has a natural discretization. This is appropriate, for example, when modeling a

collection of gas molecules which have a certain size, or the atoms of a ferromagnetic material which form solid lattice. In the classical fluid flow system, however, physical considerations may not fix the lattice size. The discretization of the vorticity field is discussed in Section 3.1; the assumption is made that h is a scale on which the vorticity field is smooth. The development of turbulence in classical fluids is a process in which motions are generated on smaller and smaller length scales; one may therefore wish to consider the fluid system as $h \rightarrow 0$. The scaling analysis of this section will therefore be applied to the limit $h \rightarrow 0$ as well as to the limit $L \rightarrow \infty$. In both cases, the number of lattice sites and thus the number of degrees of freedom in the system go to infinity; so both cases represent a thermodynamic limit.

This section considers the energy of two classes of self-avoiding loops configurations: one class containing configurations having complex structure down to the lattice size h , and another class containing configurations having uniform structure on all scales below the domain length L . The first class represents the fractal vortices observed at positive and at infinite temperatures, while the second class represents the smooth vortices which dominate the system at negative temperatures. The asymptotic scaling of the interaction energy for configurations in these classes is given as $h \rightarrow 0$ and as $L \rightarrow \infty$. The relative numbers of configurations in the two classes are also approximated. Arguments based on the balance of energy and entropy show that fractal configurations have high probability at positive and at infinite temperatures, while smooth configurations have high probability at negative temperatures.

Members of the two classes of configurations are defined through a notion of "equivalent" configurations with having different numbers of vortex links N . I consider two types of equivalency which I refer to as *copying* and *thickening*. Configurations in the first class representing vorticity with structure on the lattice scale are related through the copying equivalency, while configurations in the second class representing smooth vorticity are related through the thickening equivalency. Figure 6.22 shows a reference configuration of eight vortex links. Figure 6.23 shows on the left the thirty-two node copied version of the reference and on the right the thirty-two node thickened version. Both the copying and thickening operations preserve the number of vortex links per lattice site; in the example the domain volume and the number of vortices each increase by a factor of eight. Copying, however, preserves the small scale structure of the configuration while thickening preserves the large scale structure. In the former case, repeating copying leads to a vorticity field

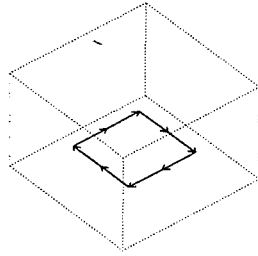


Figure 6.22: Base loop configuration

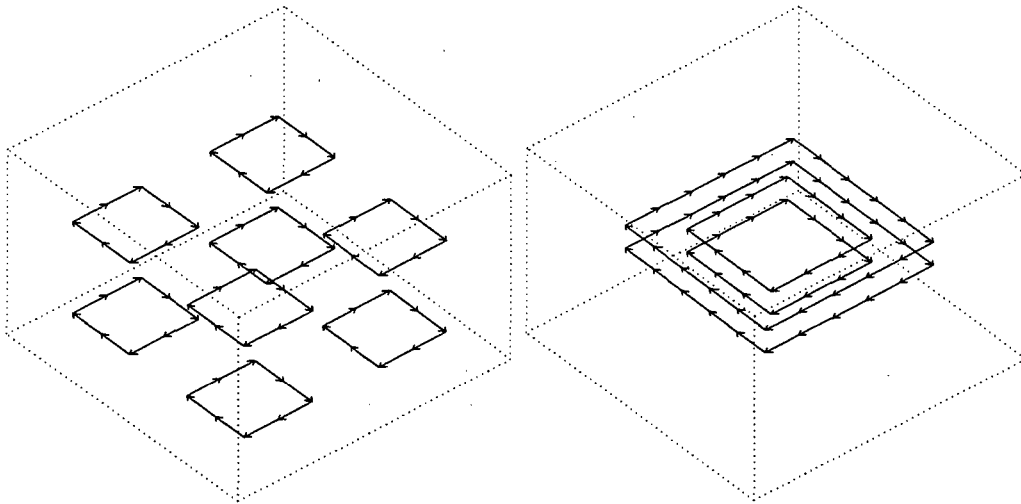


Figure 6.23: Copied and thickened configurations

having length scale h , so that macroscopic vortices in configurations of the first class are individual lattice vortices. In the latter case, repeated thickening leads to a vorticity field having length scale L . Macroscopic vortices in configurations of the second class are aligned bundles of smooth lattice vortices.

The following calculations give the scaling behavior of the energy of configurations which are equivalent through the copying or through the thickening relation. Section 3.2 discusses the energy and density definitions for the self avoiding loops model; I begin here by summarizing scaling with the lattice step size h . The total energy is the sum of an interaction term and a self-energy term:

$$E^{tot} = E^{int} + \nu N$$

where ν comes from a constant self-energy per length ϵ :

$$\nu = h\epsilon$$

and the interaction energy is given by:

$$E^{int}(c) = \frac{1}{2} \sum_{i=1}^N \sum_{j \neq i} \vec{\xi}_i \cdot \vec{\xi}_j G(\vec{x}_i - \vec{x}_j)$$

where

$$|\vec{\xi}_i| = h$$

The linear scaling of the vortex link self energy ν and the vortex link strength $|\vec{\xi}|$ with h is based on the view that the vortex tubes represented by the links have a circulation $\Gamma = 1$ which is fixed as h varies.

Consider as a preliminary step the dilation of a configuration and the domain by a factor b . Thus a reference lattice $[0, L^*]^3$ with step size h^* is mapped to a new lattice $[0, L]^3$ with step size h , where

$$b = \frac{L}{L^*} = \frac{h}{h^*}$$

Figure 6.24 shows a vortex configuration before and after dilation by a factor b . The domain length and the step size are increased together so that the number of vortices N in the original and in the dilated configurations is unchanged. Consider the interaction energies of the two configurations:

$$E_{L^*, h^*}^{int} \text{ and } E_{L, h}^{int}$$

In free space, the Greens function $G(\vec{x}) = \frac{1}{4\pi |\vec{x}|}$, transforms under dilation as follows:

$$G(b\vec{x}) = \frac{1}{4\pi |b\vec{x}|} = \frac{1}{4\pi |\vec{x}|} \frac{1}{b} = G(\vec{x}) \frac{1}{b}$$

The same law holds for the periodic domain:

$$G_L(b\vec{x}) = G_{L^*}(\vec{x}) \frac{1}{b}$$

Suppose $\vec{\xi}_i$ are vectors of length h^* and $\vec{x}_i \in [0, L^*]^3$. The vortex strength is increased in the dilated configuration to $b|\vec{\xi}_i|$. The interaction energy changes as follows:

$$E_{L, h}^{int} = \frac{1}{2} \sum_{i=1}^N \sum_{j \neq i} (b\vec{\xi}_i) \cdot (b\vec{\xi}_j) G_L(b\vec{x}_i - b\vec{x}_j) = \frac{1}{2} \sum_{i=1}^N \sum_{j \neq i} \vec{\xi}_i \cdot \vec{\xi}_j G_{L^*}(\vec{x}_i - \vec{x}_j) \frac{b^2}{b} = b E_{L^*, h^*}^{int}$$

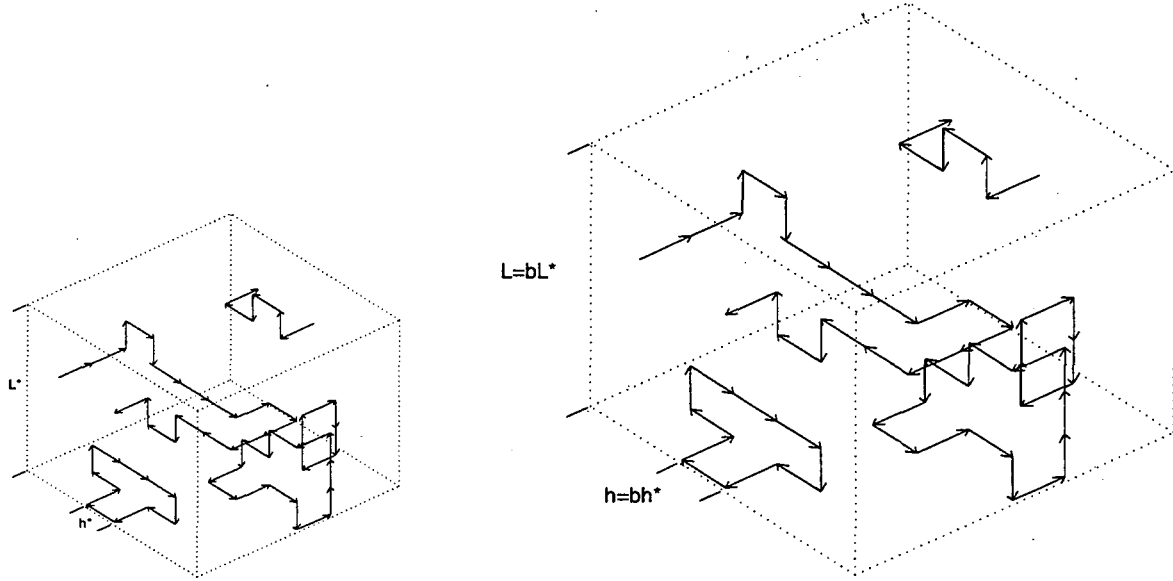


Figure 6.24: Dilation of a vortex configuration

so scaling L and h together by a factor of b gives the relation:

$$E_{bL^*,bh^*}^{int} = b E_{L^*,h^*}^{int}$$

The self energy term scales in the same way with b :

$$\nu_h N = h \epsilon N = bh^* \epsilon N = b \nu_{h^*} N$$

Now consider the periodic copying of a reference configuration of loops. Suppose a copies are added in each coordinate direction. Since the original domain is periodic, the energy of a^3 copies of a configuration in a domain of $[0, aL^*)^3$ is simply a^3 times the energy of the original configuration in $[0, L^*)^3$. Hence for copied configurations at a fixed h :

$$E_{aL^*,h^*}^{int} = a^3 E_{L^*,h^*}^{int}$$

Now if L and h are scaled separately,

$$\frac{L}{L^*} = ab \text{ and } \frac{h}{h^*} = b$$

combining the above energy relation with the dilation formula gives:

$$E_{L,h}^{int} = E_{abL^*,bh^*}^{int} = a^3 E_{bL^*,bh^*}^{int} = a^3 b E_{L^*,h^*}^{int}$$

The energy can be expressed in terms of L and h by substituting in for a and b .

$$E_{L,h}^{int} = (ab)^3 \frac{1}{b^2} E_{L^*,h^*}^{int} = \frac{L^3}{h^2} E_{L^*,h^*}^{int} \frac{h^{*2}}{L^{*3}}$$

Thus the functional form of the energy of configurations related by copying is:

$$E_{L,h}^{int} = \frac{L^3}{h^2} E_{L^*,h^*}^{*int}$$

where factors of h^* and L^* are absorbed into the reference interaction energy E_{L^*,h^*}^{*int} .

The number of vortex links per lattice site is preserved by copying, so the number of links is proportional to the number of sites in the domain,

$$N_{h,L} = \frac{L^3}{h^3} N_{L^*,h^*}^*$$

and the self energy, $\nu_h N_{h,L}$, scales in the same way as the interaction energy:

$$\nu_h N_{h,L} = \frac{L^3}{h^2} \nu^* N_{L^*,h^*}^*$$

The vortex line length hN follows the same pattern:

$$hN_{h,L} = \frac{L^3}{h^2} N_{L^*,h^*}^* h^*$$

The total energy, self energy, and line length are all proportional to L^3/h^2 for configurations related by copying. Since the domain volume is $V = L^3$, the the interaction per unit volume \mathcal{E} and the vortex line density per unit volume \mathcal{D} are constant under the copying relation as $L \rightarrow \infty$ but diverge as $\frac{1}{h^2}$ as $h \rightarrow 0$.

Now consider class of configurations related by thickening; these configurations are shown to have interaction energies which increase more quickly as $L \rightarrow \infty$ or as $h \rightarrow 0$ than do the energies of copied configurations. The thickening process, like the copying process, preserves the number of links per lattice site and thus the vortex line density \mathcal{D} as $L \rightarrow \infty$. The scaling of energy in the thickening process may be determined by examining a different discretization of the Lamb integral from the one used in the self-avoiding loops model. Consider a vorticity field $\vec{\xi}(\vec{x})$ on the periodic unit cube with $|\vec{\xi}(\vec{x})|$ equal to zero or to one. Then the Lamb Integral

$$E = \frac{1}{2} \int \int \vec{\xi}(\vec{x}) \cdot \vec{\xi}(\vec{y}) G(\vec{x} - \vec{y}) d\vec{x} d\vec{y}$$

for the energy is finite. The vortices produced in the thickening process as $h \rightarrow 0$ may be thought of as a discretization of this integral which converges if

$$|\vec{\xi}_i| = h^3$$

since the vortices represent volume elements instead of line elements. Thus the volume scaled interaction energy defined below in terms of the self-avoiding loops line vortices $\vec{\xi}_i$ having $|\vec{\xi}_i| = h$ converges as the configuration is thickened to finer and finer lattices:

$$E^{vol} = \frac{1}{2} \sum_{i=1}^N \sum_{j \neq i} (h^2 \vec{\xi}_i) \cdot (h^2 \vec{\xi}_j) G(\vec{x}_i - \vec{x}_j)$$

As $h \rightarrow 0$, the following relation holds:

$$E \approx E^{vol} = h^4 E^{int}$$

Therefore, solving for the interaction energy gives the scaling for small h :

$$E_{h,1}^{int} = \frac{1}{h^4} E^{vol}$$

The relation between thickened configurations at two discretization lengths $h = ah^*$ and h^* is thus:

$$E_{L^*,ah^*}^{int} = \frac{1}{a^4} E_{L^*,h^*}^{int}$$

This expression can be combined with the dilation formula to scale h and L separately. Let

$$\frac{L}{L^*} = b \text{ and } \frac{h}{h^*} = ab$$

Then

$$E_{L,h}^{int} = E_{bL^*,abh^*}^{int} = \frac{1}{a^4} E_{bL^*,bh^*}^{int} = \frac{b}{a^4} E_{L^*,h^*}^{int} = \frac{b^5}{(ab)^4} E_{L^*,h^*}^{int}$$

Substituting back the expressions for L and h for a and b gives:

$$E_{L,h}^{int} = \frac{L^5}{h^4} E_{L^*,h^*}^{int} \frac{h^{*4}}{L^{*5}}$$

The functional form of the interaction energy for configurations related by thickening is therefore:

$$E_{L,h}^{int} = \frac{L^5}{h^4} E_{L^*,h^*}^{*int}$$

where factors of h^* and L^* are absorbed into the reference interaction energy. The energy growth for the thickened configurations is much greater than the L^3/h^2 scaling for the

copied configurations. Physically, the thickening process represents the formation of a large scale correlated flow as $L \rightarrow \infty$, or vortex intensification as $h \rightarrow 0$.

The previous calculations show that the vortex line length $hN_{h,L}$ and the self energy term $\nu_h N_{h,L}$ scale as:

$$hN_{h,L} \propto \frac{L^3}{h^2} \text{ and } \nu_h N_{h,L} \propto \frac{L^3}{h^2}$$

with as $L \rightarrow \infty$ and as $h \rightarrow 0$ for configurations related both by copying and by thickening. The interaction energy term, $E_{L,h}^{int}$, however, scales differently for copied and thickened configurations:

$$E_{L,h}^{int} \propto \frac{L^3}{h^2} \text{ under the copying relation}$$

$$E_{L,h}^{int} \propto \frac{L^5}{h^4} \text{ under the thickening relation}$$

The following calculations estimate the number of configurations in three subsets of \mathcal{C} as functions of L for large L and as functions of h for small h . The first estimate is of the total number of self-avoiding loops configurations in \mathcal{C} . The second estimate is of the number of configurations related by a copying like process and having a particular interaction energy per unit volume \mathcal{E} and vortex line density \mathcal{D} . The second estimate is essentially an estimate of the density of states for some pair $(\mathcal{E}, \mathcal{D})$. The third estimate is of the number of "thick" configurations as functions of h and of L . These estimates of the entropies of the three subsets are employed in the final part of this section, along with the estimates of the energies of copied and thickened configurations, to describe thermodynamic features of the self-avoiding loops system. The system will be shown to be dominated by configurations with small-scale structure at positive and at infinite temperatures and to be dominated by configurations with smooth large-scale structure at negative temperatures. An argument will be made that the disordered, infinite temperature, state is generic as $h \rightarrow 0$.

Consider the set of self-avoiding loops configurations \mathcal{C} at fixed number of links N per lattice site. The vortex links in the self-avoiding loops configurations satisfy connectivity and self-avoidance constraints, and are a subset of the set of configurations in which links are arranged on the lattice without constraints. Since the number of ways of arranging the vortex links independently on the lattice scales as Q^N for some constant, the number of self-avoiding loops configurations at fixed N per site can grow no faster than a constant to the power N as $N \rightarrow \infty$. Thus the entropy of the entire system, which is the log of the number

of configurations, grows no faster than linearly with N . On the other hand, the set of single self-avoiding loops of N links is a subset of the self-avoiding loops configurations (at low enough density so that the periodic boundary conditions are not significant). The number of self-avoiding loops is also believed to scale asymptotically as q^N for some constant q [63], [98]. We may therefore conclude that the entropy of the self-avoiding loops system S_c at fixed N per site grows linearly with N . If the lattice step size h is fixed, then this scaling applies to the system of fixed vortex line density \mathcal{D} as $L \rightarrow \infty$.

Now consider the number of configurations at some fairly low interaction energy per vortex link and at fixed number of vortex links per lattice site. If the lattice step size h is fixed, these parameters translate into fixed interaction energy per unit volume \mathcal{E} and fixed vortex line density \mathcal{D} . A variation of the copying relation gives a heuristic argument for the scaling of the number of such configurations as $L \rightarrow \infty$. Consider first the collection of configurations on the domain $[0, L^*)^3$ which have a particular interaction energy E^{int} . Suppose that the vortices in the configurations have complex small-scale structure and appear disordered when viewed on the scale of the domain. Let n be the number of configurations in this set, so the entropy is given by:

$$S_{L^*} = \log n$$

Now consider an enlarged domain $[0, aL^*)^3$; it consists of a^3 copies of the smaller lattice. If we ignore loop connectivity constraints across the boundaries of the a^3 subcubes, n^{a^3} new configurations may be created on the large cube by placing independently one of the n small configurations on each subcube. The entropy thus increases to:

$$S_{aL^*} = a^3 \log n$$

The energy of a new configuration may be assumed to resemble the result from the periodic copying relation and thus be approximately $a^3 E^{int}$. These non-periodic copying operations increase the volume, the interaction energy, and vortex line length by the same factor a^3 , so the interaction energy density \mathcal{E} and the vortex line density \mathcal{D} are preserved. The entropy of the new set of configurations generated by the non-periodic copying also increases by a factor of a^3 . This, admittedly sketchy, argument implies that the entropy of the set of configurations having small-scale structure and having a particular \mathcal{E} and \mathcal{D} scales linearly with volume $V = L^3$ as $L \rightarrow \infty$.

Finally consider the “thick” configurations in which macroscopic vortices consist of aligned bundles of smooth lattice vortices. Whereas the non-periodic copying plausibly generates a set of configurations whose entropy is proportional to N , each thickened configuration corresponds to a single macroscopic vorticity field $\vec{\xi}(\vec{x})$. If the lower scale for the fields $\vec{\xi}(\vec{x})$ is fL , then f limits the number of distinct fields and thus the number of thick configurations to a constant as $L \rightarrow \infty$ or $h \rightarrow 0$. The thick configurations thus represent a vanishingly small proportion of the total number of self-avoiding loops configurations as $L \rightarrow \infty$ or as $h \rightarrow 0$.

The preceding arguments suggest that the entropy of the set of configurations having complex small-scale structure and a particular energy density $\mathcal{E} = E^{int}/(L^3)$ and vortex line density $\mathcal{D} = (hN)/(L^3)$ grows linearly with the volume $V = L^3$ as $L \rightarrow \infty$. The entropy of all configurations having vortex line density \mathcal{D} also grows linearly with the volume V as $L \rightarrow \infty$. The entropy of the thick configurations, however, remains essentially constant as $L \rightarrow \infty$. For a fixed number of vortex links per lattice site, if we denote the entropy of the whole system by S_c , the entropy of copied configurations of reference energy e_* at some reference size by $S_{cop}(e_*)$, and the entropy of thick configurations by S_{thick} , then the following asymptotic relations hold as $L \rightarrow \infty$ and as $h \rightarrow 0$:

$$\begin{aligned} S_c &\approx q_c \frac{L^3}{h^3} \\ S_{cop}(e_*) &\approx q(e_*) \frac{L^3}{h^3} \\ S_{thick} &\approx q_t \end{aligned}$$

Now consider the thermodynamic limit $L \rightarrow \infty$ in the canonical ensemble in which \mathcal{D} is held fixed. The Gibbs weight for each configuration is:

$$\rho(c) = e^{-\beta E^{int}(c)}$$

The estimates of the interaction energy and of entropy can be used to make assessments of which subsets of configurations dominate the self-avoiding loops system in the thermodynamic limit. Consider the thick configurations in relation to the rest of the configurations in the system. Copied configurations have entropy which scales in the same way as the entropy of the total system; it suffices to compare the set of all copied configurations to the set of all thick configurations. The entropy/energy balance is:

$$(S_{thick} - S_{cop}) - \beta(E_{thick} - E_{cop})$$

If this quantity increases as the thermodynamic limit is taken, then thick configurations dominate copied configurations, while if the quantity decreases then thick configurations are insignificant. Inserting the scaling forms for the entropies and the energies gives:

$$(S_{thick} - S_{cop}) - \beta(E_{thick} - E_{cop}) \approx \left(q_t - q_c \frac{L^3}{h^3} \right) - \beta \left(e_t \frac{L^5}{h^4} - e_c \frac{L^3}{h^2} \right)$$

For large L or for small h , this is approximately:

$$(S_{thick} - S_{cop}) - \beta(E_{thick} - E_{cop}) \approx \left(-q_c \frac{L^3}{h^3} \right) - \beta \left(e_t \frac{L^5}{h^4} \right)$$

First consider positive and infinite temperatures: $\beta \geq 0$. At positive temperatures, $\beta > 0$, high energy configurations are discouraged. At infinite temperature, $\beta = 0$, all configurations of vortex density \mathcal{D} are equally weighted. Both terms of the energy/entropy difference are non-positive and decrease as L increases. The probability of the subset of thick configurations therefore decreases with increasing L : the configurations become more rare and are penalized for their high energy. The typical configurations at positive and at infinite temperatures, therefore, come from the copied subset and have complex structure on the scale of the lattice step size. At negative temperatures, however, the Gibbs weight exponentially favors configurations of high energy. The entropy term of the energy/entropy difference is still negative and favors the copied configurations, but the energy term $-\beta\Delta E$ now favors the thickened configurations. The energy term, furthermore, grows as L^5 , while the entropy term grows only as L^3 . The relative probability of the thick configurations compared to the rest of the system, therefore, increases with increasing L . Thick configurations dominate the self-avoiding loops system in the thermodynamic limit and the canonical ensemble average energy increases without bound as $L \rightarrow \infty$.

The same situation holds with regard to the thickened configurations as $h \rightarrow 0$. In this case, the magnitude of the energy difference term in the energy/entropy difference grows as $1/h^4$, while the magnitude of the entropy term grows only as $1/h^3$. At positive or at infinite temperature, both terms are non-positive and thick configurations are suppressed. At any negative temperature, however, the energy term becomes positive. Since the energy term grows faster as $h \rightarrow 0$ than the entropy term, the system is dominated by thick configurations in the thermodynamic limit.

In both thermodynamic limits $L \rightarrow \infty$, h fixed, \mathcal{D} fixed, and $h \rightarrow 0$, L fixed, N/site fixed, infinite temperature marks a phase threshold. At positive and at infinite

temperatures, $\beta \geq 0$, the average interaction energy per unit volume \mathcal{E} converges in the canonical ensemble as $L \rightarrow \infty$. Vortices have complex structure down to the lattice spacing h . At all negative temperatures, $\beta < 0$, very large or very refined systems are dominated by configurations of smooth vorticity and very high energy. The average interaction energy grows as the thermodynamic limit is taken.

The preceding arguments indicate the behavior of the self-avoiding loops system at negative temperature as $L \rightarrow \infty$ or as $h \rightarrow 0$. Computational results at positive and at infinite temperature given in Sections 6.2 and 6.1 indicate that the average energy per unit volume $\langle \mathcal{E} \rangle_\beta$ converges in the thermodynamic limit $L \rightarrow \infty$ to a function of β . The scaling of the energy and of the entropy of copied configurations is consistent with a non-trivial thermodynamic limit; both the interaction energy and the entropy of copied configurations with fixed small-scale structure increase linearly with the volume $V = L^3$. As $h \rightarrow 0$, however, the energy of copied configurations grows only as $1/h^2$ while the number of links in the system and thus the entropy grows as $1/h^3$. This scaling indicates that the infinite temperature state dominates the system as $h \rightarrow 0$ at fixed number of links per lattice site. Consider as references two microcanonical subsets of a self-avoiding loops system at a fixed system size. Suppose one has average interaction energy e_{inf} corresponding to infinite temperature in the canonical ensemble at that system size. Suppose the other has average energy $e_* < e_{inf}$. Now consider the two classes formed by non-periodic copying of the two subsets. The difference in entropy and energy between the infinite temperature class and the low energy class of configurations is:

$$(S_{cop}(e_{inf}) - S_{cop}(e_*)) - \beta(E_{inf} - E_*) \approx \left([q_{inf} - q_*] \frac{L^3}{h^3} \right) - \beta \left([e_{inf} - e_*] \frac{L^3}{h^2} \right)$$

where $q_{inf} - q_*$ is the difference in entropies between the two reference systems. There are more configurations in the infinite temperature reference than there are in the finite temperature reference, so $[q_{inf} - q_*] > 0$. The reference energy difference $[e_{inf} - e_*]$ is positive by assumption. The energy/entropy difference between the two states represents a competition between the energy and the entropy terms at positive temperature β . As $L \rightarrow \infty$, both terms grow as L^3 , so there is a temperature,

$$\beta_* = \frac{q_{inf} - q_*}{e_{inf} - e_*} \frac{1}{h_*}$$

below which the lower energy state is encouraged over the state representing infinite temperature. As $h \rightarrow 0$, however, the entropy term grows as $1/h^3$ while the energy term

grows only as $1/h^2$. Entropy therefore dominates, and the configurations representing the infinite temperature system eventually dominate the other configurations at any value of β . The self-avoiding loops system at positive temperature, therefore, resembles the infinite temperature system in the limit $h \rightarrow 0$.

The infinite temperature state has been conjectured on other grounds, [43] [38] to be the asymptotic state of incompressible turbulence. To the extent that the self-avoiding loops system resembles classical turbulence, this conjecture is supported by the scaling behavior as $h \rightarrow 0$. One should note, however, that the linear scaling of the vortex link strength $|\bar{\xi}_i|$ and of the self-energy term ν_h with the lattice step size h is somewhat arbitrary. The linear scaling is appropriate for isolated vortex tubes of constant circulation. Other constraints not considered in the formulation given in Chapter 3 may regulate how the vortex strength and the self-energy term scale with h . More work is required to determine the physical meaning of the thermodynamic limits for vortex systems.

6.4 Conclusions

The self-avoiding loops model demonstrates several features of vortex equilibria. The model illustrates the effect of vortex loop connectivity on vortex screening at positive temperatures and on vortex intensification at negative temperatures. The model also demonstrates the effect which temperature and vortex self-energy have on the density of vortex loops. The model supports a non-trivial infinite temperature state. The self-avoiding loops system exhibits at least two phase transitions: one at low temperature which is similar to the lambda transition in liquid helium, and one at infinite temperature which may be related to the formation of inertial range turbulence in classical fluids.

The self-avoiding loops model has a line of continuous phase transitions in the (β, ν) plane at low temperature, $\beta \gg 0$. The energy and vortex density are continuous as functions of β at the critical temperature, but the specific heat has a peak whose height increases with increasing system size. In the thermodynamic limit, connected vortices of infinite size exist only above the critical temperature. In these respects, this phase transition in the self-avoiding loops system resembles the lambda transition in superfluid helium [139]; the two transitions may share a similar mechanism. The nature of the self-avoiding loops transition indicates that a lambda-like phase transition can be driven by vortices.

The properties of vortices in the self-avoiding loops model also support vorticity

based theories of the disordering transition in the three-dimensional XY model [130] [144]. A difference in the fractal dimension of self-avoiding vortices and of self-intersecting XY vortices is apparent, however. The self-avoiding loops system and the vorticity form of the XY model differ only in the self-avoidance constraint, but the difference may place the self-avoiding loops phase transition in a different universality class than the disordering transition of the XY model. A calculation of critical exponents for the self-avoiding loops system is required to resolve the issue.

The phase transition in the self-avoiding loops system exhibits percolation finite size scaling; the phase transition is also a percolation threshold. Renormalization treatments based on connectivity and percolation ideas may be possible for both the self-avoiding loops system and for the vorticity form of the XY model [39]. Such treatments would represent a departure from the Kosterlitz-Thouless style renormalizations and could complement existing theories.

The micro-canonical, canonical, and grand canonical ensembles of the self-avoiding loops system appear to be equivalent in the thermodynamic limit $L \rightarrow \infty$ at positive temperatures. This equivalence does not hold at infinite and at negative temperatures, however.

The canonical ensemble in which the number of vortex links per lattice site is held fixed supports a non-trivial infinite temperature state. The energy is finite in the thermodynamic limit $L \rightarrow \infty$. Screening among unconnected vortex loops reduces the energy of the system; vortex-vortex interactions contribute a negative term to the total energy. Vortices exhibit complex small-scale structure at infinite temperature, and long vortices have fractal geometry. The scaling of energy and entropy as the lattice size $h \rightarrow 0$ indicates that entropy dominates energy at positive temperatures as the lattice is refined. In this sense, the infinite temperature state may be the asymptotic state as vorticity in a classical flow breaks up into turbulence.

At any negative temperature, the energy of the self-avoiding loops system becomes infinite in the thermodynamic limit. High-energy configurations in which lattice vortices align into smooth bundles dominate the system as $L \rightarrow \infty$ or as $h \rightarrow 0$. Infinite temperature, therefore, marks a phase boundary between vortices with complex small-scale structure and vortices with smooth small-scale structure.

To the extent that the self-avoiding loops model simulates classical turbulence, the following picture may hold [38] [41]. At negative temperature, the flow is smooth and kinetic

energy is concentrated on large scales. As vortices stretch and fold, however, energy moves into smaller scales and the temperature moves toward infinity. Fractal structure forms at infinite temperature. Positive temperatures below infinite temperature are unreachable in the limit $h \rightarrow 0$, but can exist in a system in which a lower bound h_0 is placed on the refinement of the small scale.

Bibliography

- [1] D. J. Adams and G. S. Dubey. Taming the Ewald sum in the computer simulation of charged systems. *Journal of Computational Physics*, 72:156–176, 1987.
- [2] M. Aizenman and G. Grimmett. Strict monotonicity for critical points in percolation and ferromagnetic models. *Journal of Statistical Physics*, 63(5-6):817–835, 1991.
- [3] N. A. Alves, B. A. Berg, and R. Villanova. Ising-model Monte Carlo simulations: Density of states and mass gap. *Physical Review B*, 41(1), 1990.
- [4] C. Anderson and C. Greengard. On vortex methods. *SIAM Journal on Scientific and Statistical Computing*, 22:413–440, 1985.
- [5] C. Anderson and C. Greengard. *Vortex methods*, volume 1360 of *Lecture notes in mathematics*. Springer, 1988.
- [6] C. F. Barenghi, R. J. Donnelly, and W. F. Vinen. Friction on quantized vortices in helium II. *Journal of Low Temperature Physics*, 52:189–247, 1983.
- [7] G. K. Batchelor. *An Introduction to Fluid Mechanics*. Cambridge, 1967.
- [8] J. T. Beale, T. Kato, and A. Majda. Remarks on the breakdown of smooth solutions for the 3D Euler equations. *Communications in Mathematical Physics*, 94:61–66, 1984.
- [9] J. T. Beale and A. Majda. Vortex methods II: Higher order accuracy in two and three space dimensions. *Mathematics of Computation*, 32:29–52, 1982.
- [10] J. Bell and D. Marcus. Vorticity intensification and the transition to turbulence in the three dimensional Euler equations. *Communications in Mathematical Physics*, 147(2):371–394, 1992.

- [11] J. B. Bell, P. Colella, and H. M. Glaz. A 2nd-order projection method of the incompressible Navier Stokes equations. *Journal of Computational Physics*, 85(2):257–283, 1989.
- [12] C. H. Bennett. Efficient estimation of free energy differences from Monte Carlo data. *Journal of Computational Physics*, 22:245–268, 1976.
- [13] V. L. Berezinskii. Destruction of long-range order in one-dimensional and two-dimensional systems having a continuous symmetry group I. classical systems. *Soviet Physics, JETP*, 32:493–500, 1971.
- [14] P. Bernard, J. M. Thomas, and R. A. Handler. Vortex dynamics and the production of Reynolds stress. *Journal of Fluid Mechanics*, 253:385–419, 1993.
- [15] K. Binder, editor. *Applications of the Monte Carlo Method in Statistical Physics*. Springer, 1984.
- [16] K. Binder, editor. *Monte Carlo Methods in Statistical Physics*. Springer, 1986.
- [17] K. Binder. *Monte Carlo Simulation in Statistical Physics: An Introduction*. Springer, 1988.
- [18] K. Binder, editor. *The Monte Carlo Method in Condensed Matter Physics*. Springer, 1992.
- [19] A. Brandt, M. Galun, and D. Ron. Optimal multigrid algorithms for calculating thermodynamic limits. Technical Report CS90-29, Weizmann Institute of Science, Rehovot 76100, Israel, 1990.
- [20] T. F. Buttke. Numerical study of superfluid turbulence in the self-induction approximation. *Journal of Computational Physics*, 76:301–326, 1988.
- [21] T. F. Buttke. Turbulence and vortices in superfluid helium. In K. E. Gustafson and J. A. Sethian, editors, *Vortex Methods and Vortex Motion*. SIAM, 1991.
- [22] T. F. Buttke and A. J. Chorin. Turbulence calculations in magnetization variables. *Applied Numerical Mathematics*, 12(1-3):47–54, 1993.

- [23] E. Caglioti, P.L. Lions, C. Marchioro, and M. Pulvirenti. A special class of stationary flows for 2-dimensional Euler equations - a statistical mechanics description. *Communications in Mathematical Physics*, 143(3):501–525, 1992.
- [24] C. Canuto. *Spectral Methods in Fluid Dynamics*. Springer, 1988.
- [25] S. Caracciolo, A. Pelissetto, and A. Sokal. Nonlocal Monte Carlo algorithm for self-avoiding walks with fixed endpoints. *Journal of Statistical Physics*, 60:1–53, 1990.
- [26] S. Caracciolo, A. Pelissetto, and A. Sokal. Join-and-cut algorithm for self-avoiding walks with variable length and free endpoints. *Journal of Statistical Physics*, 67(1-2):65–111, 1992.
- [27] N. N. Carlson. *Topological Defect Model of Superfluid Vortex Filaments*. PhD thesis, University of California at Berkeley, Berkeley, CA 94720, 1991.
- [28] D. Chandler. *Introduction to Modern Statistical Mechanics*. Oxford, 1987.
- [29] B. Chattopadhyay, M. C. Mahato, and S. R. Shenoy. Vortex-loop crinkling in the 3-dimensional XY model - numerical evidence in support of an ansatz. *Physical Review B*, 47(22):15159–15169, 1993.
- [30] B. Chattopadhyay and S. R. Shenoy. Kosterlitz-Thouless signatures from 3D vortex loops in layered superconductors. *Physical Review Letters*, 72(3):400–403, 1994.
- [31] A. J. Chorin. The evolution of a turbulent vortex. *Communications in Mathematical Physics*, 83:517–535, 1982.
- [32] A. J. Chorin. Turbulence and vortex stretching on a lattice. *Communications on Pure and Applied Mathematics*, 39:S47–S65, 1986.
- [33] A. J. Chorin. Scaling laws in the lattice vortex model of turbulence. *Communications in Mathematical Physics*, 114:167–176, 1988.
- [34] A. J. Chorin. Spectrum, dimension, and polymer analogies in fluid turbulence. *Physical Review Letters*, 60(19):1947–1949, 1988.
- [35] A. J. Chorin. *Computational Fluid Mechanics: Selected Papers*. Academic Press, 1989.

- [36] A. J. Chorin. Constrained random walks and vortex filaments in turbulence theory. *Communications in Mathematical Physics*, 132(3):519–536, 1990.
- [37] A. J. Chorin. Hairpin removal in vortex interactions. *Journal of Computational Physics*, 91:1–21, 1990.
- [38] A. J. Chorin. Equilibrium statistics of a vortex filament with applications. *Communications in Mathematical Physics*, 141(3):619–631, 1991.
- [39] A. J. Chorin. A vortex model with superfluid and turbulent percolation. *Journal of Statistical Physics*, 69(1-2):67–78, 1992.
- [40] A. J. Chorin. Hairpin removal in vortex interactions II. *Journal of Computational Physics*, 107:1–9, 1993.
- [41] A. J. Chorin. *Vorticity and Turbulence*. Springer, 1993.
- [42] A. J. Chorin. Vortex phase transitions in 2.5 dimensions. *Journal of Statistical Physics*, 1994. in press.
- [43] A. J. Chorin and J. H. Akao. Vortex equilibria in turbulence theory and quantum analogues. *Physica D*, 52(2-3):403–414, 1991.
- [44] A. J. Chorin and J. E. Marsden. *A Mathematical Introduction to Fluid Mechanics*. Springer, 1990.
- [45] S. T. Chui and J. D. Weeks. Phase transitions in the two-dimensional coulomb gas and the interfacial roughening transition. *Physical Review B*, 14:4978–4982, 1976.
- [46] K. L. Chung. *Markov Chains with Stationary Transition Probabilities*. Springer, 1967.
- [47] P. Constantin, I. Procaccia, and K. R. Sreenivasan. Fractal geometry of isoscalar surfaces in turbulence - theory and experiments. *Physical Review Letters*, 67(13):1739–1742, 1991.
- [48] R. Cortez. The geometry of impulse flow. Manuscript, Mathematics Dept. U. C. Berkeley, 1993.
- [49] C. Dasgupta and B. I. Halperin. Phase transitions in a lattice model of superconductivity. *Physical Review Letters*, 47:1556–1560, 1981.

- [50] M. D. Demeo, D. W. Heermann, and K. Binder. Monte-Carlo study of the Ising model phase transition in terms of the percolation transition of physical clusters. *Journal of Statistical Physics*, 60(5-6):585–618, 1990.
- [51] R. J. Donnelly. *Quantized Vortices in Helium II*. Cambridge, 1991.
- [52] R. J. Donnelly and C. E. Swanson. Quantum turbulence. *Journal of Fluid Mechanics*, 173:387–429, 1986.
- [53] J. Epiney. 3D XY model near criticality. Technical Report 90-08, Interdisciplinary Project Center of Supercomputing, ETH-Zentrum CH-8092 Zurich, 1990.
- [54] D. Evans and G. Morriss. *Statistical Mechanics of Non-equilibrium Liquids*. Academic, 1990.
- [55] G. L. Eyink and H. Spohn. Negative temperature states and equivalence of ensembles for the vortex model of a two-dimensional ideal fluid. *Journal of Statistical Physics*, 70:833–886, 1993.
- [56] A. M. Ferrenberg and R. H. Swendsen. New Monte Carlo technique for studying phase transitions. *Physical Review Letters*, 61(23):2635 – 2638, 1988.
- [57] A. M. Ferrenberg and R. H. Swendsen. Optimized Monte Carlo data analysis. *Physical Review Letters*, 63(12):1195 – 1198, 1989.
- [58] J. H. Ferziger. *Numerical Methods for Engineering Application*. Wiley, 1981.
- [59] R. P. Feynman. Application of quantum mechanics to liquid helium. In C. J. Gorter, editor, *Progress in Low Temperature Physics*, 1955.
- [60] E. Fradkin, B. A. Huberman, and S. H. Shenker. Gauge symmetries in random magnetic systems. *Physical Review B*, 18(9):4789–4814, 1978.
- [61] J. Frohlich and T. Spencer. The Kosterlitz-Thouless transition in two dimensional abelian spin systems and the Coulomb gas. *Communications in Mathematical Physics*, 81:527–602, 1971.
- [62] P. G. Gennes. *The Physics of Liquid Crystals*. Clarendon, 1974.
- [63] P. G. Gennes. *Scaling Concepts in Polymer Physics*. Cornell University Press, 1979.

- [64] N. Goldenfeld. *Lectures on Phase Transitions and the Renormalization Group*, volume 85 of *Frontiers in physics*. Addison-Wesley, 1992.
- [65] C. Greengard. Convergence of the vortex filament method. *Mathematics of Computation*, 47:387–398, 1986.
- [66] G. Grimmett. *Percolation*. Springer, 1989.
- [67] K. E. Gustafson and J. A. Sethian, editors. *Vortex Methods and Vortex Motion*. SIAM, 1991.
- [68] O. H. Hald. Convergence of vortex methods II. *SIAM Journal on Scientific and Statistical Computing*, 16:726–755, 79.
- [69] O. H. Hald. Convergence of vortex methods for Euler's equations III. *SIAM Journal on Numerical Analysis*, 24:538–582, 87.
- [70] H. E. Hall and W. F. Vinen. The rotation of liquid helium II:II the theory of mutual friction in uniformly rotating helium II. *Proceedings of the Royal Society of London. Series A.*, 238:215–234, 1956.
- [71] B. I. Halperin, T. C. Lubensky, and S. K. Ma. First-order phase transitions in superconductors and smectic-A liquid crystals. *Physical Review Letters*, 32:292–295, 1974.
- [72] B. I. Halperin and D. R. Nelson. Theory of two-dimensional melting. *Physical Review Letters*, 41:121–124, 1978.
- [73] B. I. Halperin and D. R. Nelson. Resistive transition in superconducting films. *Journal of Low Temperature Physics*, 36:594–616, 1979.
- [74] J. M. Hammersley and D. C. Handscomb. *Monte Carlo Methods*. Wiley, 1964.
- [75] M. Hasenbusch and S. Meyer. Critical exponents for the 3D XY model from cluster update Monte Carlo. *Physics Letters B*, 241(2):238–242, 1990.
- [76] P. C. Hohenberg. Existence of long-range order in one and two dimensions. *Physical Review*, 158:383–386, 1967.

- [77] E. Hopf. Statistical hydrodynamics and functional calculus. *Journal of Rational Mechanics and Analysis*, 1:87–141, 1952.
- [78] C. Itzykson and J. Drouffe. *Statistical Field Theory*, volume 2. Cambridge, 1989.
- [79] F. John. *Partial Differential Equations*. Springer, 1982.
- [80] G. Joyce and D. Montgomery. Negative temperature states for the two-dimensional guiding center plasma. *Journal of Plasma Physics*, 10(107-121), 73.
- [81] H. Kesten. *Percolation for Mathematicians*. Birkhauser, 1982.
- [82] H. Kesten and Y. Zhang. The tortuosity of occupied crossings of a box in critical percolation. *Journal of Statistical Physics*, 70(3-4):613–634, 1993.
- [83] J. Kim and P. Moin. The structure of the vorticity field in turbulent channel flow. *Journal of Fluid Mechanics*, 162:339–361, 1986.
- [84] R. Klein and A. Majda. Self stretching of perturbed vortex filaments II: Structure of solutions. *Physica D*, 53:267–294, 1991.
- [85] G. Kohring and R. Shrock. Properties of generalized 3D $O(2)$ model with suppression/enhancement of vortex strings. *Nuclear Physics B288*, pages 397–418, 1987.
- [86] G. Kohring, R. E. Shrock, and P. Wills. Role of vortex strings in the three-dimensional $O(2)$ model. *Physical Review Letters*, 57(11):1358–1361, 1986.
- [87] J. Kosterlitz. The critical properties of the two-dimensional XY model. *Journal of Physics C*, 7:1046–1060, 1974.
- [88] J. Kosterlitz and D. J. Thouless. Order, metastability and phase transitions in two-dimensional systems. *Journal of Physics C*, 6:1181–1203, 1973.
- [89] B. Kuchta and R. D. Eppers. Features of the histogram Monte Carlo method: Application to N_2 monolayer melting on graphite. *Journal of Computational Physics*, 108:353–356, 1993.
- [90] J. M. F. Labastida, E. Sanchez-Velasco, R. E. Shrock, and P. Wills. Monopoles and the phase structure of 4D $U(1)$ lattice gauge theory with unit-charge higgs fields. *Nuclear Physics B*, 264:393–414, 1985.

- [91] H. Lamb. *Hydrodynamics*. Dover, 1932.
- [92] L. D. Landau and E. M. Lifshitz. *Statistical Physics*. Pergamon, 1980.
- [93] J. C. Le Guillou and J. Zinn-Justin. Critical exponents from field theory. *Physical Review B*, 21:3976–3998, 1980.
- [94] M. Lesieur. *Turbulence in Fluids: Stochastic and Numerical Modelling*. Kluwer Academic Publishers, 2nd edition, 1990.
- [95] H. W. Liepmann and G. A. Laguna. Nonlinear interactions in the fluid mechanics of helium II. *Annual Review of Fluid Mechanics*, 16:139, 1984.
- [96] J. A. Lipa and T. C. P. Chiu. Very high-resolution heat-capacity measurements near the lambda point of liquid helium. *Physical Review Letters*, 51:2291–2294, 1983.
- [97] T. Lundgren and Y. Pointin. Statistical mechanics of two-dimensional vortices. *Journal of Statistical Physics*, 17:323–355, 1977.
- [98] N. Madras. *The Self-avoiding Walk*. Birkhauser, 1993.
- [99] N. Madras, A. Orlicsky, and L. A. Shepp. Monte Carlo generation of self-avoiding walks with fixed endpoints and fixed length. *Journal of Statistical Physics*, 58(1-2):159–183, 1990.
- [100] N. Madras and A. D. Sokal. The pivot algorithm: A highly efficient Monte Carlo method for the self-avoiding walk. *Journal of Statistical Physics*, 50(1-2):109–186, 1988.
- [101] A. Majda. Vorticity and the mathematical theory of incompressible fluid flow. *Communications on Pure and Applied Mathematics*, 39:S187–S179, 86.
- [102] W. D. McComb. *Physical Theories of Turbulence*. Cambridge, 1989.
- [103] J. McWilliams. The emergence of isolated coherent vortices in turbulent flow. *Journal of Fluid Mechanics*, 146:21–46, 1984.
- [104] R. Mehrotra and S. R. Shenoy. Voltage turbulence and vortex dynamics in DC-driven 2-dimensional arrays of Josephson junctions. *Physical Review B*, 46(2):1088–1101, 1992.

- [105] N. D. Mermin. Absence of ordering in certain classical systems. *Journal of Mathematical Physics*, 8:1061–1068, 1967.
- [106] N. D. Mermin and H. Wagner. Absence of ferromagnetism or antiferromagnetism in one or two-dimensional isotropic heisenberg models. *Physical Review Letters*, 17:1133–1136, 1966.
- [107] N. Metropolis, A. W. Rosenbluth, M. N. Rosenbluth, and E. Teller. Equations of state calculations by fast computing machines. *Journal of Chemical Physics*, 21:1087–1092, 1953.
- [108] J. Miller. Statistical mechanics of Euler equations in two dimensions. *Physical Review Letters*, 65:2137–2140, 90.
- [109] D. Montgomery and G. Joyce. Statistical mechanics of negative temperature states. *Physics of Fluids*, 17(6):1139–1145, 1974.
- [110] D. R. Nelson. Study of melting in two dimensions. *Physical Review B*, 18:2318–2338, 1979.
- [111] D. R. Nelson. Defect-mediated phase transitions. In C. Domb and J. Lebowitz, editors, *Phase Transitions and Critical Phenomena*, volume 7. Academic, 1983.
- [112] D. R. Nelson and B. I. Halperin. Dislocation-mediated melting in two dimensions. *Physical Review B*, 19:2457–2487, 1979.
- [113] D. R. Nelson and J. M. Kosterlitz. Universal jump in the superfluid density of two-dimensional superfluids. *Physical Review Letters*, 39:1201–1204, 1977.
- [114] J. C. Neu. Vortices in complex scalar fields. *Physica D*, 43(2-3):385–406, 1990.
- [115] L. Onsager. Statistical hydrodynamics. *Il Nuovo Cimento*, supplement to vol. 6:279–287, 1949.
- [116] S. Orzag. Analytical theories of turbulence. *Journal of Fluid Mechanics*, 41:363–386, 1970.
- [117] R. E. Packard and S. Vitale. Some phenomenological theoretical aspects of intrinsic superfluid critical velocities. *Physical Review B*, 45(5):2512–2515, 1992.

- [118] A. Patrascioiu and E. Seiler. Phase structure of 2-dimensional spin models and percolation. *Journal of Statistical Physics*, 69(3-4):573–595, 1992.
- [119] V. Privman. *Finite Size Scaling and Numerical Simulation of Statistical Systems*. World Scientific, 1990.
- [120] E. G. Puckett. Vortex methods: An introduction and survey of selected research topics. In M. D. Gunzburger and R. A. Nicolaides, editors, *Incompressible Computational Fluid Dynamics Trends and Advances*. Cambridge, 1993.
- [121] S. J. Putterman. *Superfluid Hydrodynamics*. North-Holland, 1974.
- [122] F. Reif. *Fundamentals of Statistical and Thermal Physics*. McGraw-Hill, 1965.
- [123] R. Robert. A maximum entropy principle for two-dimensional perfect fluid dynamics. *Journal of Statistical Physics*, 65:531–554, 1991.
- [124] J. Rogiers, M. Ferer, and E. R. Scaggs. Confluent-singularity analysis of high-temperature series for thermodynamic functions of the $s = \frac{1}{2}$ XY model, the $s = \infty$ XY model, and the planar rotator model on the fcc lattice. *Physical Review B*, 19:1644–1649, 1979.
- [125] D. Ron. *Development of Fast Numerical Solvers for Problems in Optimization and Statistical Mechanics*. PhD thesis, Weizmann Institute of Science, Rehovet 76100, Israel, 1989.
- [126] M. Sahimi and S. Arbabi. On correction to scaling for 2-dimensional and 3-dimensional scalar and vector percolation. *Journal of Statistical Physics*, 62(1-2):453–461, 1991.
- [127] R. Savit. Vortices and the low-temperature structure of the XY model. *Physical Review B*, 17(3):1340–1350, 1978.
- [128] R. Savit. Duality in field theory and statistical systems. *Reviews of Modern Physics*, 52(2):453–487, 1980.
- [129] Z.S. She. Intermittency and non-gaussian statistics in turbulence. *Fluid Dynamics Research*, 8(1-4):143–158, 1991.
- [130] S. R. Shenoy. Vortex-loop scaling in the three-dimensional XY ferromagnet. *Physical Review B*, 40(7):5056–5068, 1989.

- [131] S. R. Shenoy. Enhancement and suppression of the transition temperature of a 3-dimensional XY ferromagnet by control of vortex-loop fugacity. *Physical Review B*, 42(13):8595–8600, 1990.
- [132] S. R. Shenoy. Disorder parameter descriptions of phase transitions. *Current Science*, 65(5):392–398, 1993.
- [133] H. E. Stanley. *Introduction to Phase Transitions and Critical Phenomena*. Oxford, 1971.
- [134] D. Stauffer. *Introduction to Percolation Theory*. Taylor and Francis, 1985.
- [135] J. Strain. Fast potential theory II. layer potentials and discrete sums. *Journal of Computational Physics*, 99:251–270, 1992.
- [136] D. Stuart. The dynamics of abelian higgs vortices in the near Berezinskii-Kosterlitz-Thouless regime. *Communications in Mathematical Physics*, 159(1):51–91, 1994.
- [137] R. H. Swendsen and J.-S. Wang. Nonuniversal critical dynamics in Monte-Carlo simulations. *Physical Review Letters*, 58:86–88, 1987.
- [138] C. J. Thompson. *Mathematical Statistical Mechanics*. Princeton, 1979.
- [139] D. R. Tilley and J. Tilley. *Superfluidity and Superconductivity*. Boston, 1986.
- [140] M. Tinkham. *Introduction to Superconductivity*. McGraw-Hill, 1975.
- [141] W. F. Vinen. Mutual friction in a heat current in liquid helium II:II the theory of mutual friction. *Proceedings of the Royal Society of London. Series A.*, 242:493–515, 1957.
- [142] J. D. Weeks. The roughening transition. In T. Riste, editor, *Ordering in Strongly Fluctuating Condensed Matter Systems*. Plenum, 1980.
- [143] F. W. Wiegel. Vortex-ring model of Bose condensation. *Physica*, 65:321–337, 1973.
- [144] G. A. Williams. Vortex-ring model of the superfluid lambda transition. *Physical Review Letters*, 59(17):1926–1929, 1987. Erratum v.61 p.1142.
- [145] G. A. Williams. Vortices and the superfluid 4He phase transition in two and three dimensions. Manuscript, 1990.

- [146] G. A. Williams. Vortex rings and the superfluid lambda-transition. *Journal of Low Temperature Physics*, 89(1-2):91-100, 1992.
- [147] R.J. Zieve, J. D. Close, J.C. Davis, and R. E. Packard. New experiments on quantization of circulation in superfluid He-4. *Journal of Low Temperature Physics*, 90(3-4):243-268, 1993.

LAWRENCE BERKELEY LABORATORY
UNIVERSITY OF CALIFORNIA
TECHNICAL INFORMATION DEPARTMENT
BERKELEY, CALIFORNIA 94720